Low-lying spectra of Λ-hypernuclei within a microscopic particle-rotor model based on beyond relativistic mean-field approach

PhD Thesis

Low-lying spectra of Λ-hypernuclei within a microscopic particle-rotor model based on beyond relativistic mean-field approach

相対論的平均場近似を超える理論に基づく微視的粒子 - 回転子模型によるΛハイパー核の低エネルギースペクトルの記述

Mei Hua

Department of Physics

Graduate School of Science

Tohoku University

September, 2016

Acknowledgements

First and foremost I would like to thank my supervisor, Prof. Kouichi Hagino, not only for his guidance and instruction, but also for his support throughout the various phases of the work presented in this thesis. His understanding and experiences in many areas have made a pleasure working with him. I am particularly grateful to his encouragement.

Many thanks go also to Prof. Toshio Motoba for meaningful discussions and advices. I have learned much through collaborations with him. I would also like to thank Prof. Hiroyuki Sagawa for helpful discussions and suggestions.

In addition, I would like to express my sincere gratitude to Prof. Shoichi Sasaki and Prof. Akira Ono for their valuable comments and suggestions that have helped me to improve this thesis.

I also thank my lab members for their mental and research supports, especially Dr. Guillaume Scamps, Dr. Yusuke Tanimura, Dr. Tomohiro Oishi, Tomohide Akaishi, and Yasuko Urata.

Moreover, I appreciate the Japanese Government (MONBUKAGAKUSHO: MEXT) SCHOLARSHIP provided by the Ministry of Education, Culture, Sports, Science, and Technology, Japan for supporting my study and daily life.

Finally, I should thank my family for their support and constant understanding, especially for my parents. Particularly, I am grateful to Dr. Jiangming Yao for his love, patience and encouragement. And the most important "thanks" goes to my son and my daughter for their love and accompany.

I will take these joyful memories of study in Tohoku University and of life in Japan with me in my whole life.

Abstract

With the development of high-resolution $\gamma-$ray spectroscopy experiments, experimental data on energy spectra and electric multipole transition strengths of light Λ hypernuclei have been accumulated, and more data on those of medium-heavy and heavy hypernuclei are expected to be obtained with next-generation facilities such as J-PARC. The measured energy spectra and electric multipole transition strengths in low-lying energy states provide rich information on the hyperon-nucleon interaction in nuclear medium and on the impurity effect of a Λ particle on nuclear structure. Since information on hyperon-nucleon and hyperon-hyperon interactions can not be extracted from hyperon-nucleon and hyperon-hyperon scattering experiments, which are difficult to perform due to the short lifetime of hyperon and unavailability of hyperon beams, studies of the structure of hypernuclei play a vital role in shedding light on baryon-baryon interactions. Such information is also crucial in order to understand neutron stars, in which hyperons may emerge in the inner part.

Many theoretical methods have been developed to study hypernuclei, such as cluster model, shell model, *ab*-initio method, antisymmetrized molecular dynamics (AMD), and self-consistent mean-field models. Among them, the self-consistent mean-field approach offers a way to study globally the structure of hypernuclei from light to heavy systems, providing an intuitive picture of nuclear deformation. However, a pure mean-field approximation is formulated in the body-fixed frame and violates the rotational symmetry, and thus does not yield (hyper)nuclear spectra. This difficulty can be overcome by going beyond the mean-field approximation introducing quantum-number projection techniques. The quantum fluctuations in nuclear shapes can also be taken into account with the generator coordinate method (GCM).

In this thesis, we combine the state-of-the-art beyond relativistic mean-field approach with the ideas of traditional particle-rotor model, and propose a novel microscopic particle-rotor model for hypernuclear low-lying states. In this model, hypernuclear states are constructed by coupling the hyperon to low-lying states of the core nucleus. The novelity of the method is that the structure of hypernuclei is constructed by taking into account the excitations of the core nucleus, for which we employ the microscopic beyond-mean-field approach, that is, the generator coordinate method (GCM) with the particle number and angular momentum projections onto mean-field states.

This novel method is applied to the low-energy spectra of ${}^{9}_{\Lambda}$Be, ${}^{13}_{\Lambda}$C, ${}^{21}_{\Lambda}$Ne and ${}^{31}_{\Lambda}$Si. Our results show that the low-lying excitation spectra with positive-parity states of the hypernuclei, which are dominated by Λ hyperon in the s orbital coupled to the core states, are similar to that of the corresponding core states. In particular, we find that the configurations of the first $1/2^-$ and $3/2^-$ states depend much on the properties of a core nucleus, in particular on the sign of quadrupole deformation parameter. For example, the energy splitting between the $1/2^-$ and $3/2^-$ states of ${}^{13}_{\Lambda}$C reflects the spin-orbital interaction of p-Λ hyperon, while the situation is different in ${}^{31}_{\Lambda}$Si(oblate), ${}^{9}_{\Lambda}$Be (prolate) and ${}^{21}_{\Lambda}$Ne(prolate), where there are strong configuration mixings in their $1/2^-$ and $3/2^-$ states. We also discuss the impurity effect in these hypernuclei. It is shown that the electric quadrupole transition strength, $B(E2)$, from the first 2^+ state

to the ground states is reduced by adding a Λ particle in the positive-parity states, where the reduction factor depend on the mass number of the hypernuclei. In order to check the interaction dependence for ${}^{21}_{\Lambda}$Ne and ${}^{31}_{\Lambda}$Si, the calculations are carried out based on two different nucleon-nucleon effective interactions, PC-F1 and PC-PK1. A slightly larger impurity effect is obtained with the PC-PK1 force than with PC-F1 force.

In addition to these studies, we also perform a detailed analysis of the impact of each $N\Lambda$ interaction term on hypernuclear low-energy states for ${}^{13}_{\Lambda}$C and ${}^{9}_{\Lambda}$Be. It is shown that the Λ hyperon binding energy decreases monotonically with increasing strengths of the high-order interaction terms. Moreover, we find that the tensor coupling term decreases the energy splitting between the first $1/2^-$ and $3/2^-$ states and increases the energy splitting between the first $3/2^+$ and $5/2^+$ states in ${}^{13}_{\Lambda}$C and ${}^{9}_{\Lambda}$Be.

Finally, we apply the microscopic particle-rotor model to Λ hypernuclei of Sm isotopes and discuss the transition in the low-energy spectrum from vibrational to rotational characters. The configuration mixing becomes increasingly stronger for $1/2^-_1$ and $3/2^-_1$ states as the shape of nuclear core varies from near-spherical to well-deformed prolate deformation.

Some results presented in this thesis have been published in the following publications:

1. Microscopic particle-rotor model for the low-lying spectrum of Λ hypernuclei
   H. Mei, K. Hagino, J. M. Yao, and T. Motoba, Phys. Rev. C **90**, 064302 (2014).

2. Microscopic study of low-lying spectra of Λ hypernuclei based on a beyond-mean-field approach with a covariant energy density functional
   H. Mei, K. Hagino, J. M. Yao, and T. Motoba, Phys. Rev. C **91**, 064305 (2015).

3. Triaxially deformed relativistic point-coupling model for Λ hypernuclei: A quantitative analysis of the hyperon impurity effect on nuclear collective properties
   W. X. Xue, J. M. Yao, K. Hagino, Z. P. Li, H. Mei, and Y. Tanimura, Phys. Rev. C **91**, 024327 (2015).

4. Low-energy hypernuclear spectra within a microscopic particle-rotor model with a relativistic point-coupling hyperon-nucleon interaction
   H. Mei, K. Hagino, J. M. Yao, and T. Motoba, Phys. Rev. C **93**, 044307 (2016).

5. Generator coordinate method for hypernuclear spectroscopy with a covariant density functional
   H. Mei, K. Hagino, and J. M. Yao, Phys. Rev. C **93**, 011301(R) (2016).

Contents

Chapter 1

Introduction

1.1 Importance of hypernuclei

Atomic nuclei – the core of matters in our nature – are self-bound systems of two types of baryons, namely, neutrons and protons. Both of them are called nucleons, made up of two types of quarks, udd and uud, respectively. In principle, the strong interaction that binds nucleons together inside a nucleus can be described by the theory of quantum chromodynamics (QCD) [1]. However, the application of QCD to the low-energy structure and dynamics of atomic nuclei is not straightforward at all because of its non-perturbation nature in the low-energy region, even though there are many efforts in recent years that have been devoted to overcome this difficulty. Understanding the properties of atomic nuclei from a fundamental level has still been a big challenge in nuclear physics.

Besides the neutrons and protons, there are other types of baryon called hyperons, which contain at least one strange s quark. The typical hyperons are Λ, $(\Sigma^+, \Sigma^0, \Sigma^-)$, and (Ξ^0, Ξ^-) with their constituent quark component of uds, (uus, uds, dds), and (uss, dss), respectively. Among them, Λ particle is the lightest hyperon. An atomic nucleus with one or more nucleons replaced by one (or more) hyperons is called a hypernucleus, which provides a unique laboratory suitable not only for studying the hyperon influences on nuclear structure, but also for studying the property of hadrons in nuclear environment.

The Λ particle inside a nucleus has no charge, no isospin, so it does not suffer from Pauli blocking by the other nucleons and can go deeply inside the nucleus. These features allow us to use a Λ hyperon as a sensitive probe to study the interior of the nucleus and deeply bound nuclear states. Investigating a dynamical change of nuclear structure induced by the added Λ hyperon is a particularly interesting problem in hypernuclear physics.

Another important issue in hypernuclear physics is to understand baryon-baryon interactions. Since hyperon-nucleon and hyperon-hyperon scattering experiments are difficult to perform, because of the short lifetimes of hyperons (of the order of 10^{-10}s, e.g., $\tau = 263$ps for Λ), it is not straightforward to extract the hyperon-nucleon and hyperon-hyperon interactions directly from such scattering experiments. In this situation, investigations of hypernuclear observables, includ-

ing hypernuclear spectra and transition strengths, provide an indirect way to explore information on the hyperon-nucleon and hyperon-hyperon interactions.

1.2 Experimental studies on Λ-hypernuclei

1.2.1 History of hypernuclear experiment

Since the serendipitous discovery of a Λ hypernucleus in an emulsion exposed to cosmic rays in 1953 [2], Λ−hypernclei have been studied for more than six decades. The history of the experimental studies of hypernuclei may be classified into four stages. In the first stage (starting from 1953 to the middle of 1970's, so called the emulsion era), the binding energies of the ground states for light Λ hypernuclei were measured. It has been found that the Λ potential depth is about 2/3 of that of nucleons [3].

In the second stage (starting from the early of 1970's to the middle of 1980's), excited states of hypernuclei were studied by the (K^-, π^-) reaction, especially for p-shell hypernuclei. A very important finding in these experiments is that the spin-orbit splitting of hyperon states is rather small [4, 5].

In the third stage (starting from the middle of 1980's), high-quality Λ spectra were measured by the (π^+, K^+) reaction and hypernuclear spectroscopy was established.

In the fourth stage (starting from 2000), the high-resolution γ-ray spectroscopy of hypernuclei with Hyperball [6–11] and the first $(e, e'K^+)$ experiment at Thomas Jefferson National Accelerator Facility (JLab) [12–15] were performed. These opened a new era of hypernuclear physics.

In the past years, many groups, including CERN, GSI, MAMI, BNL, COSY, J-PARC, JLab, KEK, *et al.*, have been working on hypernuclear experiments and have made considerable progress.

1.2.2 Production reactions of hypernuclei

So far, Λ hypernuclei in a wide mass range from ${}^{3}_{\Lambda}$H up to ${}^{208}_{\Lambda}$Pb have been produced as summarized in Figure 1.1. A Λ hypernucleus can be produced by bombarding the nuclei of a target material with a beam of particles (pion or kaon), where the nucleons inside the atomic nuclei are converted into Λ hyperon. Recently, Λ hypernuclei can also be produced by electromagnetic reactions. Three typical reactions, (K^-, π^-), (π^+, K^+), and $(e, e'K^+)$, are shown schematically in Fig.1.2 at the quark level.

In the (K^-, π^-) production reaction (used to produce Λ-hypernuclei at CERN for the first time [17, 18]), whose elementary process is

$$K^- \ + \ n \rightarrow \Lambda \ + \ \pi^-, \tag{1.1}$$

an s quark in the kaon beam is exchanged with a d quark in a neutron resulting in the production of a Λ hyperon. On the other hand, in the (π^+, K^+) and the $(e, e'K^+)$ reactions, whose

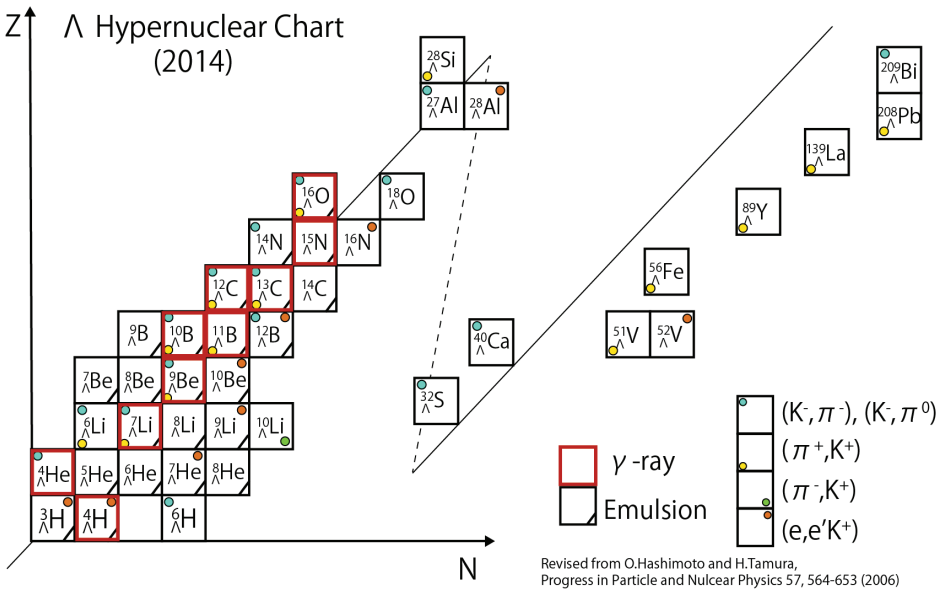

Fig. 1.1 A Λ hypernuclear chart taken from Ref. [16]. The experimentally identified Λ hypernuclei and the experimental methods used to study them (reaction spectroscopies of (K^-, π^-), (π^+, K^+), and $(e, e'K^+)$, γ spectroscopy, and the emulsion method, etc.) are shown.

elementary processes are

$$\pi^+ \ + \ n \rightarrow \Lambda \ + \ K^+ \tag{1.2}$$

$$e^- \ + \ p \rightarrow \Lambda \ + \ e^{-'} \ + \ K^+, \tag{1.3}$$

respectively, an $s\bar{s}$ pair is created associatively, resulting in the production of both a Λ hyperon and a kaon, and thus they are the associated production reaction.

Each reaction has its own advantages. The (K^-, π^-) production reaction is mostly used because of ease of tracking of the reaction products. The (π^+, K^+) reaction is best suited for studying deeply bound states in medium and heavy hypernuclei [19, 20]. The $(e, e'K^+)$ reaction can populate spin-flip hypernuclear states with unnatural parity. Other production reactions, such as (K^-, π^0), could complement our knowledge of hypernuclear spectroscopy.

The energy resolution of hypernuclear levels is very important for studying the fine-structure of hypernuclei. The $(e, e'K^+)$ hypernuclear reaction has the largest advantage in high energy resolution, which is expected to be as good as a few 100keV [15, 22, 23] due to a lower energy spread of primary electron beams than that for secondary meson beams in (K^-, π^-) and (π^+, K^+) reactions. In the (K^-, π^-) and (π^+, K^+) reactions, the energy resolution of hypernuclear levels are limited no better than 1.5MeV due to the inherently limited quality of these secondary hadronic beams [22].

In the past decades, thanks to the development of the HyperBall, many high-resolution γ-ray spectroscopy experiments have been carried out for Λ hypernuclei [6–11]. The experimental data on energy spectra and electric multipole transition strengths have been accumulated, providing

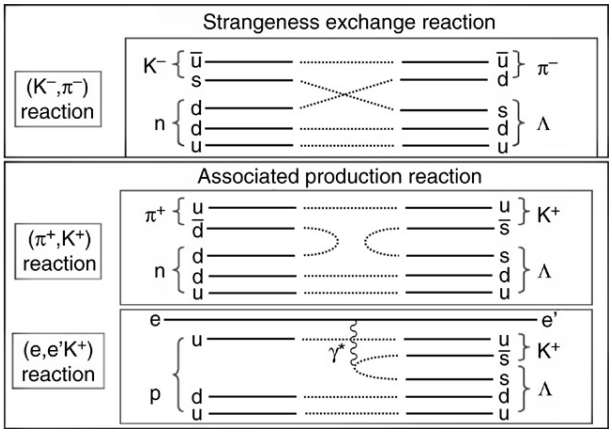

Fig. 1.2 A schematic presentation of three strangeness producing reactions used to study hypernuclei. Taken from Ref. [21].

rich information on a hyperon-nucleon interaction in the nuclear medium as well as the impurity effect of the Λ particle on the structure of atomic nuclei [21, 24]. It is noteworthy that the next-generation facility J-PARC has already been in operation [25], opening up a new opportunity to perform high precision hypernuclear γ-ray spectroscopy studies. Today, many researchers are attempting to achieve more accurate measurement for a variety of hypernuclei in complementary ways, e.g., at J-PARC using hadron beams, GSI using heavy ion beams, MAMI and JLab using electron beams. These experiments will shed light on low-lying states of hypernuclei, especially those of medium and heavy hypernuclei.

1.3 Theoretical methods for hypernuclei

In order to analyze and interpret these experimental data, over the past decades, several different types of theoretical models have been developed. Based on realistic hyperon-nucleon and hyperon-hyperon interactions, *ab*-initio calculations, which establish a direct link between experimental observables and the underlying interactions, have been applied to *p*-shell single-Λ hypernuclei, ${}^{7}_{\Lambda}$Li, ${}^{9}_{\Lambda}$Be and ${}^{13}_{\Lambda}$C [26].

On the other hand, since the lifetime of a Λ hyperon in the nuclear medium ($\sim 10^{-10}s$) is much longer than the time scale of the strong interaction ($\sim 10^{-23}s$), well developed nuclear theory models with an effective Λ-nucleus interaction can be used to study the hypernuclear system.

For instance, a shell model, in which nucleons move independently in an average field (mean-field) and has achieved a great success in describing nuclear structure and magic numbers, has been extended to *p*- and *sd*-shell hypernuclei [27–30].

A cluster model, in which a nucleus is divided into several clusters and nucleons are confined within each cluster, describes successfully an interesting character, that is, the clustering structure of nuclear systems. This model has been applied to study the structure of *p*- and *sd*-shell

hypernuclei with three- and four- body calculations as well as double-Λ hypernuclei ($^{6}_{\Lambda\Lambda}$He and $^{11}_{\Lambda\Lambda}$Be) with five-body calculations [31–37].

Anti-symmetrized molecular dynamics (AMD), which describes a nucleus with antisymmetrized products of Gaussian wave packets of nucleons, has been developed to study the hypernuclear structure up to pf-shell hypernuclei [38–41].

The self-consistent mean-field approach, which has been a powerful tool for studying the properties of normal nuclei, has also been extended to investigate the structure of hypernuclei both on relativistic and non-relativistic frameworks [42–48].

1.4 Impurity effects of Λ hyperon

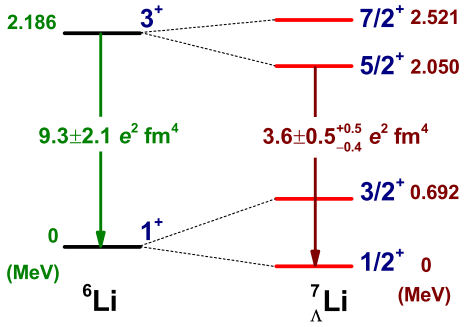

Fig. 1.3 The excitation energy and the E2 transition strength for low-lying states of ^{6}Li and $^{7}_{\Lambda}$Li. The excitation energies are taken from Refs. [6, 21], while the $B(E2)$ strengths are taken from Refs. [7, 21, 49].

One important and interesting question in hypernuclear physics is how an additional Λ particle affects the properties of the nuclear system. Since a Λ particle is located deeply inside the atomic nuclei, the presence of a hyperon as an impurity may significantly change nuclear properties. In particular, the additional Λ hyperon introduces an attractive force between the Λ particle and the nucleons, and may cause a shrinkage of the nuclei. This is the so-called "glue-like" effect.

The cluster model has been used to study the structure change after including a Λ hyperon. Motoba *et al.* were the first to point out that the inter-cluster distance and the E2 transition strengths are drastically reduced in the p-shell and sd-shell Λ hypernuclei (including $^{5}_{\Lambda}$He, $^{7}_{\Lambda}$Li, $^{9}_{\Lambda}$Be, $^{13}_{\Lambda}$C, $^{21}_{\Lambda}$Ne, etc.) compared to those of the core nuclei [31, 32, 50, 51]. AMD and mean-field calculations also show the shrinkage of the intercluster distance by adding a Λ particle [42, 43, 38]. The theoretical prediction for such appreciable shrinkage of the nuclei after adding a Λ particle has been clearly confirmed in the experiment by measuring the B(E2) value in $^{7}_{\Lambda}$Li. Notice that B(E2) value is sensitive to a size contraction as it is approximately proportional to the fourth power of the nuclear size. The measured reduced transition probabilities are $B(E2;^{7}_{\Lambda}\mathrm{Li}\ 5/2^{+} \rightarrow 3/2^{+}) = 3.6 \pm 0.5^{+0.5}_{-0.4} e^2$ fm^4 [21, 7] and $B(E2;^{6}\mathrm{Li}\ 3^{+} \rightarrow 1^{+}) = 9.3 \pm 2.1 e^2$ fm^4 [49], as shown in Fig. 1.3, indicating that the size of ^{6}Li in $^{7}_{\Lambda}$Li is smaller than that in the free space.

Due to the "glue-like" effect, when a Λ particle is added to a very weakly bound nuclear system, the resultant hypernuclei will become more stable against nucleon or cluster decay and

it is expected that the neutron-drip line and proton-drip line are extended from those in ordinary nuclei. ${}^{6}_{\Lambda}$He and ${}^{7}_{\Lambda}$Be [52] are the typical examples for the change of the neutron and proton drip line, respectively, in which ^{5}He is unbound by 0.89 MeV above the $\alpha + n$ breakup threshold and ^{6}Be is located at 1.37 MeV above the $\alpha + p + p$ breakup threshold. Meanwhile, an interesting phenomena concerning neutron halo has been observed in neutron-rich nuclei, in which the neutron density distribution extends to large distance. Three-body and four-body cluster models have been used to study such halo structure influenced by adding a Λ particle. It has been found that the additional Λ hyperon stabilizes these unstable nuclei and the halo structure disappear [53, 54]. The same conclusion is also made with non-relativistic and relativistic mean-field calculations [55, 56]. Moreover, the relativistic Hartree-Bogoliubov method found that the spin-orbit potential plays an important role in stabilizing neutron-rich nuclei [56]. On the experimental side, many neutron-rich hypernuclei have been or will be produced, such as ${}^{6}_{\Lambda}$H [57], ${}^{9}_{\Lambda}$He and ${}^{12}_{\Lambda}$Be at J-PARC, ${}^{10}_{\Lambda}$Li at KEK.

The shape polarization effect of Λ hyperon has been investigated with both non-relativistic mean field and relativistic mean field calculations. It has been found that the addition of the Λ particle in s-orbit changes the deformation of the core nucleus [42, 43] and makes the energy surface somewhat softer along the quadrupole deformation degree of freedom [44]. The potential energy surface of hypernuclei with Λ hyperon in s-orbit (p-orbit) have smaller (larger) deformation of energy minimum than that of the core nucleus. A dramatic change of the deformation has been found in ^{28,30,32}Si and ^{12}C after adding a Λ particle with relativistic mean field [43] and AMD [58] calculations.

The investigation of the impurity effect of Λ hyperon on nuclear collective excitation with a five-dimensional collective Bohr Hamiltonian [46, 59] have shown that Λ hyperon in s-orbit increases the excitation energy of the 2^+_1 state and decreases the $B(E2; 2^+_1 \rightarrow 0^+_1)$ value of the core nuclei inside ${}^{25}_{\Lambda}$Mg, ${}^{27}_{\Lambda}$Mg and ${}^{31}_{\Lambda}$Si hypernuclei.

1.5 Aims of this work

1.5.1 Successes and limitations of mean-field approaches for hypernuclear structure

Among the theoretical methods mentioned in Sec.1.3, the self-consistent mean-field model is the only microscopic method which can be globally applied from light to heavy hypernuclei. Moreover, the mean-field approach has an advantage in that it can automatically lead to the optimized deformation of a nuclear system, which is one of the important features of atomic nuclei. Many nuclei are deformed in their ground states and exhibit characteristic collective excitation spectra, such as rotational band. In the mean-field model, which is defined in the body-fixed frame, the optimized deformation is yielded by minimizing the total energy of a system through the mechanism of the spontaneous symmetry breaking in a self-consistent way. The mean-field model is suitable to study the change of nuclear shape induced by the addition of a Λ hyperon. These kinds of studies have been performed in recent years and it has been found

that the potential energy surface of a hypernucleus is generally softer against deformation than that of the corresponding core nucleus [44].

On the other hand, pure mean-field approximation does not yield a spectrum of nuclei due to the broken symmetries. Furthermore, one can not directly connect mean-field results to spectroscopic observable, such as $B(E2)$ values. To overcome the deficient of mean-field models, one has to transform from the intrinsic frame to the laboratory frame. One way to restore the broken symmetries is by introducing projection techniques. Such kind of development has been carried out with the Skyrme density functional [60]. A further improvement has been made by taking into account configuration mixing with the generator coordinator method (GCM) based on a relativistic point-coupling energy density functional (see Appendix F). Notice that the shape fluctuation effect, which is not included in the pure mean-field approximation, will be more important in hypernuclei than in normal nuclei due to a softer energy surface. The GCM approach offers an intuitive way to study the hypernuclear shape fluctuation as well as the nuclear shape polarization due to the Λ hyperon, but the computational cost is quite expensive. Another way to go beyond the pure mean-field approximation is to rely on additional assumptions such as the rigid rotor model, which however would not work for, *e.g.,* nuclei with small deformation or with shape coexistence.

1.5.2 Aims of this thesis

Given this situation, in this thesis, we will propose a novel microscopic particle-rotor model (MPRM) for low-lying spectra of single-Λ hypernuclei. In MPRM, the hypernuclear states are constructed by coupling a hyperon to low-lying states of the nuclear core through a Λ hyperon interacting with the nucleons inside the core nucleus. The novel feature of our method is that we combine the motion of the Λ particle with the core nucleus states, which are described by the state-of-the-art covariant density functional approach; that is, the generator coordinate method (GCM) based on the relativistic mean-field (RMF) approach supplemented with the particle number and the angular momentum projections.

In contrast to the conventional particle-rotor-model, which usually describes the deformed core nucleus with a rigid rotor, the low-lying states of the core nucleus are constructed microscopically in MPRM. That is, we superpose many quadrupole deformed RMF+BCS states, after both the particle-number and the angular-momentum projections are carried out. In this way, the shape fluctuation effect is naturally taken into account in our approach.

Compared with the GCM approach for hypernuclei, the MPRM provides a more convenient way to analyze the components of hypernuclear wave function and also it significantly reduces the computation costs.

The thesis is organized as follows. In Chapter 2, theoretical framework of the mean-field and the beyond-mean-field methods are introduced based on relativistic point-coupling model by taking ^{12}C as an example. In Chapter 3, the $N\Lambda$ effective interaction based on the relativistic point-coupling model for single-Λ hypernuclei is introduced. In Chapter 4, the microscopic particle-rotor model (MPRM) for the low-lying states of single-Λ hypernuclei is proposed. In

Chapter 5, the microscopic particle-rotor model is applied to ${}^{13}_{\Lambda}$C, ${}^{9}_{\Lambda}$Be, ${}^{21}_{\Lambda}$Ne, ${}^{31}_{\Lambda}$Si and Sm Λ hypernuclei. Low-lying states of ${}^{13}_{\Lambda}$C and the impact of each $N\Lambda$ interaction term on hypernuclear low-lying states are also discussed in details. Finally the summary of this thesis and a brief outlook for future investigations are given in Chapter 6.

Chapter 2

Beyond relativistic mean-field approach for even-even nuclei

2.1 The relativistic mean-field theory with point coupling interaction (RPC)

2.1.1 Introduction

Before we introduce the microscopic particle-rotor model for hypernuclei, we first review the beyond relativistic mean-field approach for their even-even core nucleus. Atomic nuclei are composed of protons and neutrons, which are the bound states of quarks and gluons. These are treated as a quantum mechanical many-body sysyem of Fermions in low energies nuclear theory. Since the nucleon-nucleon interaction derived from the QCD of quarks and gluons is very complicated, one usually takes a phenomenological approach, which extracts the nucleon-nucleon interaction from the nucleon-nucleon scattering data, and makes prediction for nuclei using such interactions. Yet, the NN interaction derived in this way is strongly repulsive at short distances and difficult to handle. In order to remedy this, an effective interaction (G-matrix) in the nuclear medium has been derived with a Brueckner type calculation [61]. Since the Brueckner theory has been possible only for nuclear matter so far [62], more phenomenological concept has been developed. That is, the most successful method starts from an effective density dependent energy functional with the parameters fitted to experimental data, which are understood as a phenomenological parametrization of the G-matrix.

One such approach is the relativistic mean-field (RMF) theory, which starts from relativistic quantum field theory, using a Lagrangian to describe point-like nucleons interaction through the Finite-Range meson exchange (RMF-FR) [63, 64]. This model based upon a coupled field theory of Dirac nucleons and effective meson fields treated at the mean-field level, where density dependence is modeled by nonlinear meson self-couplings. This procedure is completely phenomenological and the parameters are adjusted specifically for mean field applications. This relativistic model has been quite successful, providing a natural explanation of large spin-orbit splitting needed for the understanding of magic numbers in finite nuclei, a new saturation mech-

anism by the relativistic quenching of the attractive scalar field, and pseudo-spin symmetry [65, 66], etc. The relativistic mean-field theory has achieved a great success in describing the bulk properties of both finite nuclei and nuclear matter and in understanding the nucleonic shell structure and magic numbers.

A zero-range version, i.e. point-coupling, of RMF (RMF-PC) has also been proposed [67–72]. In this model, a nucleus is described as a system of Dirac nucleons that interact in a relativistic covariant manner with point couplings. The interaction used in RMF-PC model are composed of zero range and derivative terms, which is to account for the finite ranges of the meson. This model can be viewed as an approach that lies in between the RMF-FR approach and the non-relativistic Skyrme-Hartree-Fock (SHF) approach [73–75], which is also based upon density-dependent contact interactions with extensions to gradient terms, kinetic terms, and the spin-orbit interactions.

In the RMF-PC model, the energy functional is a simple functional of particle density and its derivative, which makes RMF-PC model much easier to be implemented for numerical calculations compared to SHF. Throughout this thesis, we will base our discussions on the relativistic point coupling model.

2.1.2 The lagrangian

The Lagrangian density of the relativistic point-coupling model is constructed as a power series in $(\bar{\psi}\mathcal{O}\Gamma\psi)$ and their derivatives, where $\mathcal{O}$ is either 1 or $\boldsymbol{\tau}$, $\boldsymbol{\tau}$ being the isospin vector, $\Gamma \in \{1, \gamma_\mu, \gamma_5, \gamma_5\gamma_\mu, \sigma_{\mu\nu}\}$ is one of the 4×4 Dirac matrices and ψ is the Dirac field of nucleon. In this work, we use the following Lagrangian density introduced by Büervenich *et al.* in Refs. [76, 77]:

$$\mathscr{L} =: \mathscr{L}_{free} + \mathscr{L}_{4f} + \mathscr{L}_{hot} + \mathscr{L}_{der} + \mathscr{L}_{em} : \tag{2.1}$$

Here the colons :: denote a normal ordering with respect to the vacuum state. In Eq.(2.1), $\mathscr{L}_{free}$ is the Lagrangian density for free nucleons given by

$$\mathscr{L}_{free} = \bar{\psi}(i\gamma_\mu\partial^\mu - m)\psi. \tag{2.2}$$

The Lagrangian density for four fermions coupling term, $\mathscr{L}_{4f}$, is given by

$$\mathscr{L}_{4f} = -\frac{1}{2}\alpha_S(\bar{\psi}\psi)(\bar{\psi}\psi) - \frac{1}{2}\alpha_V(\bar{\psi}\gamma_\mu\psi)(\bar{\psi}\gamma^\mu\psi) - \frac{1}{2}\alpha_{TS}(\bar{\psi}\boldsymbol{\tau}\psi)\cdot(\bar{\psi}\boldsymbol{\tau}\psi) - \frac{1}{2}\alpha_{TV}(\bar{\psi}\boldsymbol{\tau}\gamma_\mu\psi)\cdot(\bar{\psi}\boldsymbol{\tau}\gamma^\mu\psi). \tag{2.3}$$

The derivative terms, $\mathscr{L}_{der}$, which simulate in a simple way the finite range of the nucleon-nucleon forces are

$$\begin{aligned}\mathscr{L}_{der} = &-\frac{1}{2}\delta_S(\partial_\nu\bar{\psi}\psi)(\partial^\nu\bar{\psi}\psi) - \frac{1}{2}\delta_v(\partial_\nu\bar{\psi}\gamma_\mu\psi)(\partial^\nu\bar{\psi}\gamma^\mu\psi)\\ &-\frac{1}{2}\delta_{TS}(\partial_\nu\bar{\psi}\boldsymbol{\tau}\psi)\cdot(\partial^\nu\bar{\psi}\boldsymbol{\tau}\psi) - \frac{1}{2}\delta_{TV}(\partial_\nu\bar{\psi}\boldsymbol{\tau}\gamma_\mu\psi)\cdot(\partial^\nu\bar{\psi}\boldsymbol{\tau}\gamma^\mu\psi).\end{aligned} \tag{2.4}$$

The higher order interaction term, $\mathscr{L}_{hot}$, which corresponds to the self-couplings of the scalar and vector mesons, is written as:

$$\mathscr{L}_{hot} = -\frac{1}{3}\beta_S(\bar{\psi}\psi)^3 - \frac{1}{4}\gamma_S(\bar{\psi}\psi)^4 - \frac{1}{4}\gamma_V[(\bar{\psi}\gamma_\mu\psi)(\bar{\psi}\gamma^\mu\psi)]^2. \tag{2.5}$$

The electromagnetic field, $\mathscr{L}_{em}$, is also introduced to provide the electromagnetic interaction between protons as

$$\mathscr{L}_{em} = -e\bar{\psi}\gamma^\mu\frac{1-\tau_3}{2}\psi A_\mu - \frac{1}{4}F^{\mu\nu}F_{\mu\nu}, \tag{2.6}$$

where e is the charge unit for protons and A_μ is the electromagnetic field. The isospin of neutron and proton are associated with $\tau_3 = +1$ and $\tau_3 = -1$, respectively, so that $\mathscr{L}_{em}$ vanishes for neutrons. The electromagnetic field tensor reads $F_{\mu\nu} = \partial_\mu A_\nu - \partial_\nu A_\mu$.

The total Lagrangian (2.1) contains eleven coupling constants $\alpha_S, \alpha_V, \alpha_{TS}, \alpha_{TV}$, β_S, γ_S, γ_V, δ_S, δ_V, δ_{TS} and δ_{TV}, where the subscripts S, V and T indicate scalar, vector and isovector fields, respectively. Here, the symbol α stands for the four-fermion terms, δ for the derivative couplings, and β for the third-order term as well as γ for the fourth-order terms.

2.1.3 Energy density functional

The Hamiltonian density $\mathscr{H}$ can be derived from the 00 component of the energy-momentum tensor $T_{\mu\nu}$,

$$\mathscr{H} = T_{00} = \frac{\partial\mathscr{L}}{\partial\dot{\psi}}\dot{\psi} + \frac{\partial\mathscr{L}}{\partial\dot{A}_\mu}\dot{A}_\mu - \mathscr{L}. \tag{2.7}$$

Substituting the Lagrangian (2.1) to Eq.(2.7), one obtains the explicit expression for the Hamiltonian as

$$\hat{H} = \int d\boldsymbol{r} : [\mathscr{H}_{free} + \mathscr{H}_{4f} + \mathscr{H}_{hot} + \mathscr{H}_{der} + \mathscr{H}_{em}] :, \tag{2.8}$$

where

$$\mathscr{H}_{free} = \bar{\psi}(i\boldsymbol{\gamma}\cdot\boldsymbol{\partial} + m)\psi, \tag{2.9a}$$

$$\begin{aligned}\mathscr{H}_{4f} = {} & \frac{1}{2}\alpha_S(\bar{\psi}\psi)(\bar{\psi}\psi) + \frac{1}{2}\alpha_V(\bar{\psi}\gamma_\mu\psi)(\bar{\psi}\gamma^\mu\psi) \\ & + \frac{1}{2}\alpha_{TS}(\bar{\psi}\boldsymbol{\tau}\psi)\cdot(\bar{\psi}\boldsymbol{\tau}\psi) + \frac{1}{2}\alpha_{TV}(\bar{\psi}\boldsymbol{\tau}\gamma_\mu\psi)\cdot(\bar{\psi}\boldsymbol{\tau}\gamma_\mu\psi),\end{aligned} \tag{2.9b}$$

$$\begin{aligned}\mathscr{H}_{der} = {} & \frac{1}{2}\delta_S(\partial_\nu\bar{\psi}\psi)(\partial^\nu\bar{\psi}\psi) + \frac{1}{2}\delta_v(\partial_\nu\bar{\psi}\gamma_\mu\psi)(\partial^\nu\bar{\psi}\gamma^\mu\psi) \\ & + \frac{1}{2}\delta_{TS}(\partial_\nu\bar{\psi}\boldsymbol{\tau}\psi)\cdot(\partial^\nu\bar{\psi}\boldsymbol{\tau}\psi) + \frac{1}{2}\delta_{TV}(\partial_\nu\bar{\psi}\boldsymbol{\tau}\gamma_\mu\psi)\cdot(\partial^\nu\bar{\psi}\boldsymbol{\tau}\gamma^\mu\psi),\end{aligned} \tag{2.9c}$$

$$\mathscr{H}_{hot} = \frac{1}{3}\beta_S(\bar{\psi}\psi)^3 + \frac{1}{4}\gamma_S(\bar{\psi}\psi)^4 + \frac{1}{4}\gamma_V[(\bar{\psi}\gamma_\mu\psi)(\bar{\psi}\gamma^\mu\psi)]^2, \tag{2.9d}$$

$$\mathscr{H}_{em} = eA_\mu\bar{\psi}[(1-\tau_3)/2]\gamma^\mu\psi - F^{0\mu}\partial_0 A_\mu + \frac{1}{4}F_{\mu\nu}F^{\mu\nu}. \tag{2.9e}$$

No-sea approximation

The field operator $\psi(\boldsymbol{r})$ can be written in a second quantization form

$$\psi(\boldsymbol{r}) = \sum_k \psi_k(\boldsymbol{r}) a_k + \sum_{\bar{k}} \psi_{\bar{k}}(\boldsymbol{r}) a^\dagger_{\bar{k}} \tag{2.10a}$$

$$\bar{\psi}(\boldsymbol{r}) = \sum_k \bar{\psi}_k(\boldsymbol{r}) a^\dagger_k + \sum_{\bar{k}} \bar{\psi}_{\bar{k}}(\boldsymbol{r}) a_{\bar{k}} \tag{2.10b}$$

where $a^\dagger_k$ is the creation operator for a nucleon in state k and $a^\dagger_{\bar{k}}$ is the creation operator for an antinucleon in antinucleon state $\bar{k}$. In the mean-field calculations, the so-called *no-sea* approximation is adopted, which means the levels in the Dirac-sea of anti-particles are assumed to be all occupied and thus are not taken into account. Only the positive energy states are considered explicitly in this approximation. With this approximation, the Dirac field operator $\psi(\boldsymbol{r})$ is simplified as

$$\psi(\boldsymbol{r}) = \sum_k \psi_k(\boldsymbol{r}) a_k, \qquad \bar{\psi}(\boldsymbol{r}) = \sum_k \bar{\psi}_k(\boldsymbol{r}) a^\dagger_k \tag{2.11}$$

where $\psi_k(\boldsymbol{r})$ (Dirac spinor) is the single-particle wave function with large and small components

$$\psi_k(\boldsymbol{r}) = \begin{pmatrix} f_k(\boldsymbol{r}) \\ i g_k(\boldsymbol{r}) \end{pmatrix}, \tag{2.12}$$

and $\bar{\psi}(\boldsymbol{r})$ is defined as $\psi^\dagger(\boldsymbol{r})\gamma_0$.

With Eq.(2.11), the normal ordering of $(\bar{\psi}\psi)^2$ in Eq.(2.8) is given as

$$\begin{aligned} :(\bar{\psi}\psi)^2: &= :\sum_{kk'} \bar{\psi}_k(\boldsymbol{r}) a^\dagger_k \psi_{k'}(\boldsymbol{r}) a_{k'} \sum_{ll'} \bar{\psi}_l(\boldsymbol{r}) a^\dagger_l \psi_{l'}(\boldsymbol{r}) a_{l'} : \\ &= \sum_{kk'} \bar{\psi}_k(\boldsymbol{r}) \psi_{k'}(\boldsymbol{r}) \sum_{ll'} \bar{\psi}_l(\boldsymbol{r}) \psi_{l'}(\boldsymbol{r}) : a^\dagger_k a_{k'} a^\dagger_l a_{l'} : . \end{aligned} \tag{2.13}$$

Hartree approximation

The nuclear many-body wave function at mean-field level is a Slater determinant of single-particle wave functions

$$|\Phi\rangle = \prod_{k=1}^{A} a^\dagger_k |0\rangle, \tag{2.14}$$

where $|0\rangle$ is the vacuum state. With the above wave function, we can calculate the energy corresponding to the Hamiltonian in Eq. (2.8) with the Wick's theorem. The expectation value of $\hat{H}$ turns out to be the expectation values of two field operators. Neglecting the Fock-term as

done in the covariant density functional theory, namely, only the direct-term is kept as

$$\begin{aligned}\langle\Phi|:(\bar{\psi}\psi)^2:|\Phi\rangle =& \sum_{kk'}\bar{\psi}_k(\boldsymbol{r})\psi_{k'}(\boldsymbol{r})\sum_{ll'}\bar{\psi}_l(\boldsymbol{r}')\psi_{l'}\langle\Phi|(a_k^\dagger a_{k'})|\Phi\rangle\langle\Phi|(a_l^\dagger a_{l'})|\Phi\rangle \\ =& \sum_{kk'}\bar{\psi}_k(\boldsymbol{r})\psi_{k'}(\boldsymbol{r})\sum_{ll'}\bar{\psi}_l(\boldsymbol{r}')\psi_{l'}(\boldsymbol{r}')\delta_{kk'}\delta_{ll'} \\ =& \sum_{k}\bar{\psi}_k(\boldsymbol{r})\psi_{k}(\boldsymbol{r})\sum_{l}\bar{\psi}_l(\boldsymbol{r}')\psi_{l}(\boldsymbol{r}')\end{aligned} \tag{2.15}$$

Similarly, we can derive expectation values of other terms in the Hamiltonian. The final energy functional is expressed in terms of the corresponding local densities and currents as

$$\begin{aligned}E_{\mathrm{DF}}[\rho,j_i^\mu,A_\mu] =& \sum_k\int d\boldsymbol{r}[\psi_k^\dagger(\boldsymbol{r})(\boldsymbol{\alpha}\cdot\boldsymbol{p}+\beta m-m)\psi_k(\boldsymbol{r})] \\ &+\int d\boldsymbol{r}\left\{\frac{\alpha_S}{2}\rho_S^2(\boldsymbol{r})+\frac{\beta_S}{3}\rho_S^3(\boldsymbol{r})+\frac{\gamma_s}{4}\rho_S^4(\boldsymbol{r})+\frac{\delta_S}{2}\rho_S(\boldsymbol{r})\nabla^2\rho_S(\boldsymbol{r})+\frac{\alpha_V}{2}j_\mu(\boldsymbol{r})j^\mu(\boldsymbol{r})\right. \\ &+\frac{\gamma_V}{4}[j_\mu(\boldsymbol{r})j^\mu(\boldsymbol{r})]^2+\frac{\delta_V}{2}j_\mu(\boldsymbol{r})\nabla^2 j^\mu(\boldsymbol{r})+\frac{\alpha_{TS}}{2}\rho_{TS}^2(\boldsymbol{r})+\frac{\delta_{TS}}{2}\rho_{TS}(\boldsymbol{r})\nabla^2\rho_{TS}(\boldsymbol{r}) \\ &\left.+\frac{\alpha_{TV}}{2}j_{TV}(\boldsymbol{r})_\mu j_{TV}^\mu(\boldsymbol{r})+\frac{\delta_{TV}}{2}j_{TV}(\boldsymbol{r})_\mu\nabla^2 j_{TV}^\mu(\boldsymbol{r})+\frac{1}{2}\rho_V^{(p)}(\boldsymbol{r})eA^0(\boldsymbol{r})\right\},\end{aligned} \tag{2.16}$$

where the local densities are given by

$$\rho_S(\boldsymbol{r}) = \langle\Phi|\bar{\psi}(\boldsymbol{r})\psi(\boldsymbol{r})|\Phi\rangle = \sum_k\bar{\psi}_k(\boldsymbol{r})\psi_k(\boldsymbol{r}), \tag{2.17a}$$

$$\rho_V(\boldsymbol{r}) = \langle\Phi|\bar{\psi}(\boldsymbol{r})\gamma_0\psi(\boldsymbol{r})|\Phi\rangle = \sum_k\bar{\psi}_k(\boldsymbol{r})\gamma_0\psi_k(\boldsymbol{r}), \tag{2.17b}$$

$$\rho_{TS}(\boldsymbol{r}) = \langle\Phi|\bar{\psi}(\boldsymbol{r})\boldsymbol{\tau}\psi(\boldsymbol{r})|\Phi\rangle = \sum_k\bar{\psi}_k(\boldsymbol{r})\boldsymbol{\tau}\psi_k(\boldsymbol{r}), \tag{2.17c}$$

and currents are given by

$$j_\mu(\boldsymbol{r}) = \langle\Phi|\bar{\psi}(\boldsymbol{r})\gamma_\mu\psi(\boldsymbol{r})|\Phi\rangle = \sum_k\bar{\psi}_k(\boldsymbol{r})\gamma_\mu\psi_k(\boldsymbol{r}), \tag{2.18a}$$

$$j_{TV_\mu}(\boldsymbol{r}) = \langle\Phi|\bar{\psi}(\boldsymbol{r})\boldsymbol{\tau}\gamma_\mu\psi(\boldsymbol{r})|\Phi\rangle = \sum_k\bar{\psi}_k(\boldsymbol{r})\boldsymbol{\tau}\gamma_\mu\psi_k(\boldsymbol{r}). \tag{2.18b}$$

Here, the space-like component of the photon field is neglected due to the Maxwellian magnetic field $\boldsymbol{A}$ having a small electromagnetic coupling [78].

2.1.4 Equation of motion for nucleons

For the ground state of an even-even nucleus, one has time-reversal symmetry. In this case, the time-odd space-like components of the currents $\boldsymbol{j}^\mu$ vanish and only the zero-components exist. The equation of motion for nucleons can be obtained by minimizing the energy functional in

Eq.(2.16) with respect to the single-particle wave functions ψ_k, that is

$$\frac{\delta}{\delta\psi_k^\dagger}\Big(E_{\rm DF}[\rho, j_i^\mu, A_\mu] - \varepsilon_k\langle\psi_k|\psi_k\rangle\Big) = 0, \tag{2.19}$$

which leads to the Dirac equation for nucleons,

$$\{\boldsymbol{\alpha}\cdot\boldsymbol{p} + \beta[m + S(\boldsymbol{r})] + V(\boldsymbol{r})\}\psi_k = \varepsilon_k\psi_k, \tag{2.20}$$

where the scalar potential is given by $S(\boldsymbol{r}) = V_S(\boldsymbol{r}) + \tau_3\cdot V_{TS}(\boldsymbol{r})$ and the vector potential is given by $V(\boldsymbol{r}) = V_V^0(\boldsymbol{r}) + \tau_3\cdot V_{TV}^0(\boldsymbol{r})$ with

$$V_S(\boldsymbol{r}) = \alpha_S\rho_S(\boldsymbol{r}) + \beta_S\rho_S^2(\boldsymbol{r}) + \gamma_S\rho_S^3(\boldsymbol{r}) + \delta_S\nabla^2\rho_S(\boldsymbol{r}), \tag{2.21a}$$

$$V_V^0(\boldsymbol{r}) = \alpha_V\rho_V(\boldsymbol{r}) + \gamma_V\rho_V^3(\boldsymbol{r}) + \delta_V\nabla^2\rho_V(\boldsymbol{r}) + e\frac{1-\tau_3}{2}A^0(\boldsymbol{r}), \tag{2.21b}$$

$$V_{TS}(\boldsymbol{r}) = \alpha_{TS}\rho_{TS}(\boldsymbol{r}) + \delta_{TS}\nabla^2\rho_{TS}(\boldsymbol{r}), \tag{2.21c}$$

$$V_{TV}^0(\boldsymbol{r}) = \alpha_{TV}\rho_{TV}(\boldsymbol{r}) + \delta_{TV}\nabla^2\rho_{TV}(\boldsymbol{r}). \tag{2.21d}$$

2.1.5 Pairing correlation

In addition to the self-consistent mean-field potentials, pairing correlations, which is one of the most important complements in nuclear shell structure, have to be included in order to describe deformed nuclei as well as open-shell nuclei. For this purpose, the BCS (Bardeen-Coorper-Schrieffer) approximation has been often used to treat the pairing correlation [79–82], except for nuclei close to the neutron and proton drip-lines [83]. In this approximation, the ground-state of nuclear system is approximated

$$|BCS\rangle = \prod_{k>0}(u_k + v_k c_k^\dagger c_{-k}^\dagger)|0\rangle, \tag{2.22}$$

where v_k and $u_k = \sqrt{1-v_k^2}$ are the pairing amplitudes.

In this thesis, we employ a density-independent δ force for the pairing interaction

$$V_\tau^{pair}(\boldsymbol{r}, \boldsymbol{r}') = V_\tau\delta(\boldsymbol{r} - \boldsymbol{r}') \tag{2.23}$$

with a smooth cutoff factor f_k [84] to simulate the effects of finite range

$$f_k = \frac{1}{1 + \exp[(\epsilon_k - \epsilon_F - \Delta E_\tau)/\mu_\tau]}, \tag{2.24}$$

where V_τ is the pairing strength for protons or neutrons (V_p or V_n) and ϵ_k ($\epsilon_k = \varepsilon_k - m$) is the single-particle energy. The chemical potential ϵ_F is determined by the constraint on average particle number $\langle\Phi|\hat{N}_\tau|\Phi\rangle = N_\tau$, where N_τ is the correct particle number of neutron or proton.

Following Ref.[84], the cutoff energy ΔE_τ is chosen from the condition

$$2\sum_{k>0} f_k = N_\tau + 1.65 N_\tau^{2/3}, \tag{2.25}$$

with $\mu_\tau = \Delta E_\tau/10$. The contribution of pairing interaction to the ground state energy is expressed in terms of the pairing tensor κ

$$E_{\rm pair}[\kappa,\kappa^*] = \sum_{\tau=n,p} \frac{V_\tau}{4} \int d\boldsymbol{r} \kappa_\tau^*(\boldsymbol{r})\kappa_\tau(\boldsymbol{r}) \tag{2.26}$$

where the pairing tensor $\kappa(\boldsymbol{r})$ (the pair density) is given by

$$\kappa(\boldsymbol{r}) = -2\sum_{k>0} f_k u_k v_k |\psi_k(\boldsymbol{r})|^2. \tag{2.27}$$

The occupation probabilities are determined by the gap equation as

$$v_k^2 = \frac{1}{2}\left(1 - \frac{\epsilon_k - \epsilon_F}{\sqrt{(\epsilon_k-\epsilon_F)^2 + f_k^2\Delta_k^2}}\right), \qquad v_k^2 + u_k^2 = 1. \tag{2.28}$$

Here, the single-particle gaps Δ_k are state dependent and are determined as

$$\Delta_k = \int d\boldsymbol{r} \psi_k^\dagger(\boldsymbol{r})\Delta_\tau(\boldsymbol{r})\psi_k(\boldsymbol{r}), \tag{2.29}$$

where $\Delta_\tau(\boldsymbol{r})$ is the local pair potential determined as

$$\Delta_\tau(\boldsymbol{r}) = \frac{\partial E_{pair}}{\partial \kappa_\tau(\boldsymbol{r})} = \frac{1}{2} V_\tau \kappa_\tau(\boldsymbol{r}). \tag{2.30}$$

The pairing strength parameters V_τ have been adjusted by fitting the average single-particle pairing gap

$$< \Delta > \equiv \frac{\sum_k f_k v_k^2 \Delta_k}{\sum_k f_k v_k^2} \tag{2.31}$$

to the experimental odd-even mass differences [84]. The pairing strength parameters and the coupling constants appearing in the Lagrangian, Eq.(2.1), are fitted to experiment data simultaneously. The values of these parameters are shown in Table 2.1 for two parameter sets, PC-PK1 [72] and PC-F1 [68].

2.1.6 Center-of-mass correction

The mean-field approximation violates the translational symmetry. In order to correct this, the center-of-mass correction, which has been found very important in predictions for light nuclei [84] and exotic nuclei, should also be taken into account. In this thesis, we adopt the same microscopic estimate as in Ref. [68], in which the center-of-mass correction is calculated through

Table 2.1 Coupling constants for PC-F1 [68] and PC-PK1 [72] sets.

	PC-F1	PC-PK1
α_S (MeV^{-2})	-3.83577×10^{-4}	-3.96291×10^{-4}
β_S (MeV^{-5})	7.68567×10^{-11}	8.6653×10^{-11}
γ_S (MeV^{-8})	-2.90443×10^{-17}	-3.80724×10^{-17}
δ_S (MeV^{-4})	-4.1853×10^{-10}	-1.09108×10^{-10}
α_V (MeV^{-2})	2.59333×10^{-4}	2.6904×10^{-4}
γ_V (MeV^{-8})	-3.879×10^{-18}	-3.64219×10^{-18}
δ_V (MeV^{-4})	-1.1921×10^{-10}	-4.32619×10^{-10}
α_{TV} (MeV^{-2})	3.4677×10^{-5}	2.95018×10^{-5}
δ_{TV} (MeV^{-4})	-4.2×10^{-11}	-4.11112×10^{-10}
V_p (MeV fm^3)	-321	-330
V_n (MeV fm^3)	-308	-349.5

the expectation value of the kinetic energy for the center-of-mass motion with respect to the mean-field wave function as:

$$E_{\rm cm} = -\sum_{\tau=n,p} \frac{\langle \hat{\boldsymbol{P}}^2_{\rm cm} \rangle}{2m_\tau A_\tau}, \tag{2.32}$$

where m_τ and A_τ are the mass and the particle number of neutron or proton, respectively, and $\hat{\boldsymbol{P}}_{\rm cm} = \sum_i^A \hat{\boldsymbol{p}}_i$ is the total momentum of the system.

2.1.7 Total energy of nuclear system

The total energy for the nuclear system includes the energy corresponding to the Lagrangian (2.1) and the pairing energy (2.26) as well as the center-of-mass correction (2.32):

$$E_{\rm tot} = E_{\rm DF}[\rho, j_i^\mu, A_\mu] + E_{\rm pair}[\kappa, \kappa^*] + E_{\rm cm}. \tag{2.33}$$

The express of energy $E_{\rm DF}$ after introducing the pairing correlation reads:

$$\begin{aligned} E_{\rm DF}[\rho, j_i^\mu, A_\mu] = & \sum_k \int d\boldsymbol{r} v_k^2 [\psi_k^\dagger(\boldsymbol{r})(\boldsymbol{\alpha}\cdot\boldsymbol{p} + \beta m - m)\psi_k(\boldsymbol{r})] \\ & + \int d\boldsymbol{r} \left\{ \frac{\alpha_S}{2}\rho_S^2(\boldsymbol{r}) + \frac{\beta_S}{3}\rho_S^3(\boldsymbol{r}) + \frac{\gamma_s}{4}\rho_S^4(\boldsymbol{r}) + \frac{\delta_S}{2}\rho_S(\boldsymbol{r})\nabla^2\rho_S(\boldsymbol{r}) + \frac{\alpha_V}{2}j_\mu(\boldsymbol{r})j^\mu(\boldsymbol{r}) \right. \\ & + \frac{\gamma_V}{4}[j_\mu(\boldsymbol{r})j^\mu(\boldsymbol{r})]^2 + \frac{\delta_V}{2}j_\mu(\boldsymbol{r})\nabla^2 j^\mu(\boldsymbol{r}) + \frac{\alpha_{TS}}{2}\rho_{TS}^2(\boldsymbol{r}) + \frac{\delta_{TS}}{2}\rho_{TS}(\boldsymbol{r})\nabla^2\rho_{TS}(\boldsymbol{r}) \\ & \left. + \frac{\alpha_{TV}}{2}j_{TV}(\boldsymbol{r})_\mu j_{TV}^\mu(\boldsymbol{r}) + \frac{\delta_{TV}}{2}j_{TV}(\boldsymbol{r})_\mu\nabla^2 j_{TV}^\mu(\boldsymbol{r}) + \frac{1}{2}\rho_V^{(p)}(\boldsymbol{r})eA^0(\boldsymbol{r}) \right\}, \end{aligned} \tag{2.34}$$

Here, the local densities and currents are sumed up all occupied states in the Fermi sea with the occupation factor v_k^2 of each orbit determined in the BCS approximation with δ-pairing force:

$$\text{isoscalar} - \text{scalar density}: \qquad \rho_S(\boldsymbol{r}) = \sum_{k>0} v_k^2 \bar{\psi}_k(\boldsymbol{r})\psi_k(\boldsymbol{r}), \tag{2.35a}$$

$$\text{isoscalar} - \text{vector density}: \qquad \rho_V(\boldsymbol{r}) = \sum_{k>0} v_k^2 \bar{\psi}_k(\boldsymbol{r})\gamma_0\psi_k(\boldsymbol{r}), \tag{2.35b}$$

$$\text{isovector} - \text{scalar density}: \qquad \rho_{TS}(\boldsymbol{r}) = \sum_{k>0} v_k^2 \bar{\psi}_k(\boldsymbol{r})\boldsymbol{\tau}\psi_k(\boldsymbol{r}), \tag{2.35c}$$

$$\text{isovector} - \text{vector density}: \qquad \rho_{TV}(\boldsymbol{r}) = \sum_{k>0} v_k^2 \bar{\psi}_k(\boldsymbol{r})\boldsymbol{\tau}\gamma_0\psi_k(\boldsymbol{r}), \tag{2.35d}$$

$$\text{isoscalar} - \text{vector current density}: \qquad j^\mu(\boldsymbol{r}) = \sum_{k>0} v_k^2 \bar{\psi}_k(\boldsymbol{r})\gamma^\mu\psi_k(\boldsymbol{r}), \tag{2.35e}$$

$$\text{isovector} - \text{vector current density}: \qquad j^\mu_{TV}(\boldsymbol{r}) = \sum_{k>0} v_k^2 \bar{\psi}_k(\boldsymbol{r})\boldsymbol{\tau}\gamma^\mu\psi_k(\boldsymbol{r}). \tag{2.35f}$$

2.1.8 Quadrupole deformation constrained calculation

RMF-PC calculations often lead to a deformed ground state with a finite value of quadrupole operator. While the unrestricted RMF-PC calculation can only give the local minimum on the energy surface, a constrained RMF-PC calculation can be performed in order to obtain the energy surface as a function of quadrupole moments $\langle\hat{q}_{20}\rangle$ and $\langle\hat{q}_{22}\rangle$. The quadrupole moments $\langle\hat{q}_{20}\rangle$ and $\langle\hat{q}_{22}\rangle$ are related to the Hill-Wheeler [85] coordinates $\beta, \gamma(\beta > 0)$ by the following relations:

$$\langle\hat{q}_{20}\rangle = \sqrt{\frac{5}{16\pi}}\langle 2z^2 - x^2 - y^2\rangle = \frac{3}{4\pi}AR_0^2\beta\cos\gamma \tag{2.36a}$$

$$\langle\hat{q}_{22}\rangle = \sqrt{\frac{15}{32\pi}}\langle x^2 - y^2\rangle = \frac{3}{4\pi}AR_0^2\frac{1}{\sqrt{2}}\beta\sin\gamma, \tag{2.36b}$$

with R_0 and A being the nuclear radius and the mass number, respectively. In this thesis, we take $R_0 = 1.2A^{1/3}$ (fm). The deformation parameters β, γ are related to the quadrupole moments by

$$\beta = \frac{4\pi}{3AR_0^2}\sqrt{\langle\hat{q}_{20}\rangle^2 + 2\langle\hat{q}_{22}\rangle^2}, \qquad \gamma = \tan^{-1}\left(\sqrt{2}\frac{\langle\hat{q}_{22}\rangle}{\langle\hat{q}_{20}\rangle}\right). \tag{2.37a}$$

In this thesis, we adopt the quadratic constraint on the quadrupole moments by minimizing the following energy with respect to single-particle wave function [81],

$$E' = E_{\text{tot}} + \sum_{\mu=0,2} C_{2\mu}(\langle\hat{q}_{2\mu}\rangle - q_{2\mu})^2, \tag{2.38}$$

where $C_{2\mu}$ is a stiffness parameter and $q_{2\mu}$ is the quadrupole moment to be obtained.

In this thesis, for simplicity, we assume axial symmetry and a constraint only on the axial mass quadrupole moment $\langle\hat{q}_{20}\rangle$ is used to generate a set of mean-field states $|\Phi(\beta)\rangle$ with different intrinsic deformation $\beta = \frac{4\pi}{3AR_0^2}\langle\hat{q}_{20}\rangle$ ($\langle\hat{q}_{22}\rangle = 0$).

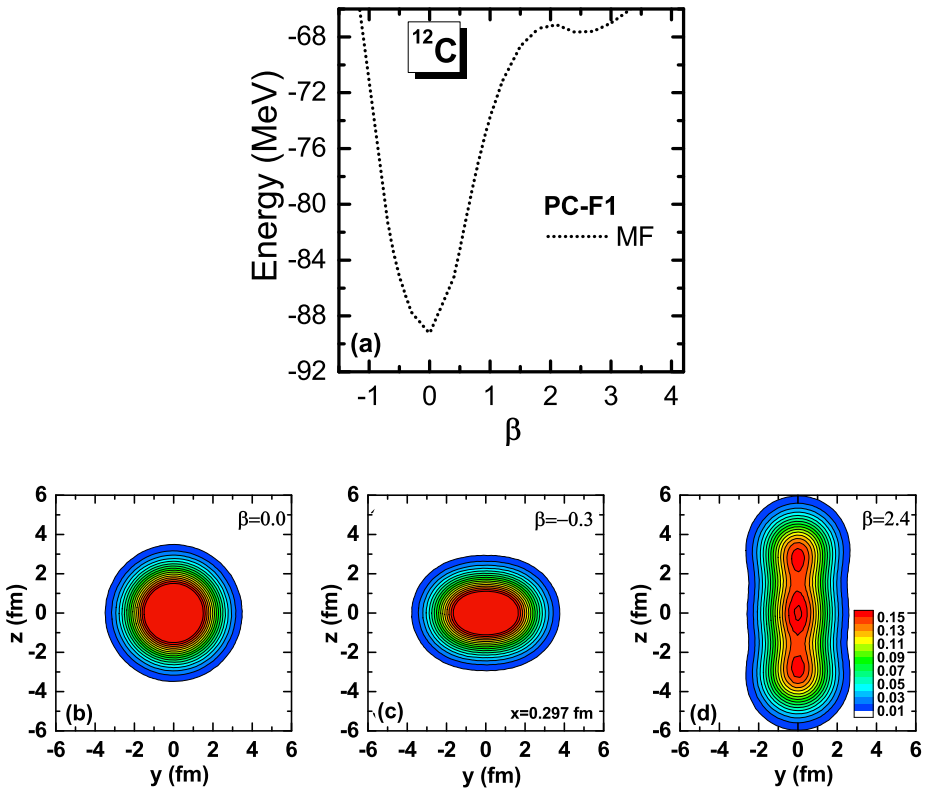

Fig. 2.1 (a):The energy curve of the mean-field state for ^{12}C as a function of the intrinsic quadrupole deformation β generated with the PC-F1 force. (b), (c) and (d): The intrinsic nuclear densities for $\beta = 0.0$, $\beta = -0.3$ and $\beta = 2.4$ on the $y - z$ plane with $x = 0.297$ fm.

As an example, Fig. 2.1(a) shows the total energy of ^{12}C as a function of deformation parameter β from the calculation with the PC-F1 force [68]. In this calculation, the Dirac spinor for each nucleon state is expanded on the basis of a three-dimensional harmonic oscillator (3DHO) with $N_{\rm sh} = 10$ major shells. The oscillator length parameters are chosen as $b_x = b_y = b_z = \sqrt{\hbar/m\omega_0}$, where m is the nucleon mass and the oscillator frequency is taken to be $\hbar\omega_0 = 41A^{-1/3}$ (MeV).

In this calculation, the energy minimum is found at the spherical shape with deformation parameter $\beta = 0$ and energy -89.26 MeV. The experimental data for the binding energy of the ground state of ^{12}C is 92.16 MeV. The energy curve increases dramatically with deformation β. The second minimum in the mean-field energy curve appears around $\beta = 2.4$ and the corresponding density distribution is shown in Fig. 2.1(d) with $3\alpha-$linear structure. This 3α linear-chain structure has also been found in Ref. [86]. For comparison, the density profile of the state at $\beta = 0.0$ and $\beta = -0.3$ are also shown in Fig. 2.1(b) and (c), respectively.

2.2 Restoration of broken symmetries

2.2.1 Symmetry violations in the mean-field approximation

The mean-field approach has been the only microscopic approach that is able to describe all kinds of nuclei throughout the nuclear chart, in particular heavy and open-shell nuclei. In fact, this approach has been widely used for studying the structure properties of nuclei. One advantage of this method is that nuclei are described in terms of a simple many-body wave function, e.g., a single Slater determinant of quasi-particle wave functions or the corresponding density functional. Many kinds of important correlations among nucleons can be taken into account in this framework in a simple manner. This includes, e.g., the long range particle-hole correlations responsible for static deformations and the particle-particle correlations that induce superfluidity. In the mean-field approximation, these correlations can be taken into account at the price of breaking several symmetries of the underlying many-body Hamiltonian. Deformed mean-field and a pairing field breaks the $SO(3)$ rotational symmetry in the Euler space and $U(1)$ symmetry in the gauge space, respectively, in the mean field wave function. While this is a good advantage of the mean-field theory, it results in the ground state wave function which is not an eigenstate of the angular momentum ($\boldsymbol{J}^2$, $\boldsymbol{J}_z$) and the particle number operators. These deficiencies may give rise to some serious problems in the description of nuclear properties, including missing correlations associated with the symmetry restoration, mixing of low-lying excited states into the ground state, a difficulty in connection to the lab frame for spectroscopic observables, and an absence of selection rules for transitions, etc. In order to compare properly with the experimental data, one has to go beyond the mean-field approximation. To this end, the projection method provides an effective tool to restore the spontaneously broken symmetries [81]. In this approach, a suitable linear combinations of the superfluid or rotated deformed intrinsic states will recover the particle or angular momentum quantum numbers of the nuclear wave function. Such procedures are known as the Particle Number Projection (PNP) and Angular Momentum Projection (AMP) methods, respectively.

2.2.2 Projection methods

Let us first discuss a general structure of the projection methods. Suppose that the Hamiltonian $\hat{H}$ of a nucleus has some symmetry S, the element of which is labeled by $\hat{R}(\Omega)$, Ω being the group parameter of S. It means that $\hat{H}$ is invariant under the transformation of an arbitrary group element $\hat{R}(\Omega)$ in S, that is,

$$[\hat{H}, \hat{R}(\Omega)] = 0. \tag{2.39}$$

If the wave function $|\Phi\rangle$ is an eigenstate of $\hat{H}$ with eigenvalue E, then all the wave function generated as

$$|\Phi(\Omega)\rangle = \hat{R}(\Omega)|\Phi\rangle \tag{2.40}$$

are also eigenstates of $\hat{H}$ with the same energy E:

$$\hat{H}|\Phi(\Omega)\rangle = \hat{H}\hat{R}(\Omega)|\Phi\rangle = \hat{R}(\Omega)\hat{H}|\Phi\rangle = E\hat{R}(\Omega)|\Phi\rangle \tag{2.41}$$

with non-zero overlap $\langle\Phi|\Phi(\Omega)\rangle = \langle\Phi|\hat{R}(\Omega)|\Phi\rangle$. Therefore, a set of such kind of wave functions $|\Phi(\Omega)\rangle$ can be used as a generator function and in general we have

$$|\Psi\rangle = \int d\Omega f(\Omega)|\Phi(\Omega)\rangle. \tag{2.42}$$

The generating functions $|\Phi(\Omega)\rangle$ span a subspace, so called the "collective subspace". The basic idea of projection methods is to diagonalize the Hamiltonian $\hat{H}$ in this collective subspace to determine the function $f(\Omega)$ in Eq.(2.42).

Incidentally, this subspace is invariant under the transformation of the symmetry group S,

$$\hat{R}(\Omega)|\Psi\rangle = \int d\Omega' f(-\Omega+\Omega')|\Phi(\Omega')\rangle, \tag{2.43}$$

which means that the projector $\hat{P}$ onto this subspace commutes with the symmetry operation $[\hat{P}, \hat{R}(\Omega)] = 0$ and thus we may find simultaneous eigenstates of $\hat{P}\hat{H}\hat{P}$ and $\hat{R}(\Omega)$. This implies that there exists a function $f(\Omega)$ which minimizes the energy and makes $|\Psi\rangle$ have the proper symmetry. The function $f(\Omega)$ can be found by expanding in a complete set of eigenfunctions of the symmetry operators expressed in the group parameters Ω. If S is an Abelian group, then it corresponds to a Fourier decomposition.

Particle number projection

Let us now discuss the particle number projection. We first notice that the gauge group is connected with the particle number violation. In this case, $\Omega = \varphi$, and $\hat{R}(\varphi) = e^{i\hat{N}\varphi}$, where φ is the gauge angle and $\hat{N}$ is the number operator. The function $f(\Omega)$ becomes

$$f(\varphi) = \sum_n \frac{1}{2\pi} e^{-in\varphi} \cdot g_n \tag{2.44}$$

and the wave function of the system is given by

$$|\Phi^A\rangle = \sum_n g_n \hat{P}^A|\Phi\rangle \tag{2.45}$$

with the projection operator $\hat{P}^A$ defined as

$$\hat{P}^A = \frac{1}{2\pi}\int_0^{2\pi} e^{i\varphi(\hat{N}-A)} d\varphi, \tag{2.46}$$

which projects onto the subspace with particle number A. The coefficient g_n is a normalization constant and is zero for $2n \neq A$.

Angular momentum projection

We next discuss the angular momentum projection. In reality, a nucleus is rotational invariant and the total Hamiltonian for it has $SO(3)$ symmetry, characterized by the Euler angles $\Omega = (\phi, \theta, \psi)$ as the group parameters. The rotation operator $\hat{R}(\Omega)$, according to the notation in the Edmonds's book [87], is given by,

$$\hat{R}(\Omega) = e^{i\phi\hat{I}_z} e^{i\theta\hat{I}_y} e^{i\psi\hat{I}_z}. \tag{2.47}$$

The weight function $f(\Omega)$ in Eq.(2.42) is expanded into a complete set of eigenfunctions of the corresponding symmetry operators, i.e., the representation of the rotation group given by the Wigner functions D^{I*}_{MK},

$$f(\Omega) = \frac{2I+1}{8\pi^2} \sum_{IMK} g_{IMK} D^{I*}_{MK}(\Omega). \tag{2.48}$$

The Wigner functions D^{I*}_{MK} is defined as the matrix elements of the rotation operator $\hat{R}(\Omega)$ in the IM-representation and is related with the Wigner small-d functions by:

$$D^{I}_{MK}(\Omega) = \langle IM|\hat{R}(\Omega)|IK\rangle = e^{i\phi M} d^{I}_{MK}(\theta) e^{i\psi K}, \quad d^{I}_{MK}(\theta) = \langle IM|e^{i\theta\hat{I}_y}|IK\rangle. \tag{2.49}$$

The three-dimensional angular momentum projection operator is then given by:

$$\hat{P}^{I}_{MK} = \frac{2I+1}{8\pi^2} \int d\Omega D^{I*}_{MK}(\Omega) \hat{R}(\Omega), \tag{2.50}$$

which extracts from the intrinsic mean filed state $|\Phi(q)\rangle$, $q \equiv (\beta, \gamma)$ being the deformation parameter, the component with an eigenvalue K and the component with an eigenvalue M of the angular momentum. The volume element of the integration over the Euler angles is given by $d\Omega = d\phi \sin\theta d\theta d\psi$.

For an arbitrary deformed mean-field wave function $|\Phi(q)\rangle$, the projected state can be written as a superposition of states with different K quantum numbers

$$|\Phi^{IM}(q)\rangle = \sum_{K} g_K \frac{2I+1}{8\pi^2} \int d\Omega D^{I*}_{MK}(\Omega) \hat{R}(\Omega) |\Phi(q)\rangle, \tag{2.51}$$

with the coefficient g_K determined by the normalization.

In the case of axial symmetric approximation, for the ground state of even-even nuclei only the $K = 0$ component can be picked up by $\hat{P}^{I}_{MK}$ from an intrinsic state $\Phi(\beta)$. In this case, the integral of ϕ and ψ are trivial, and only the integral over θ has to be carried out numerically. In the applications shown in this thesis, the Gauss-Legendre quadrature is used for the integration over the Euler angle θ and the number of mesh points in the interval $[0, \pi]$ is chosen to be 14 for ^{12}C. In the case of even number of particles, the integration interval for gauge angle φ can be reduced to $[0, \pi]$ due to the symmetries of the integrand. By using the Fomenko's expression

[88–90], the integrals of Eq. (2.46) can be written as

$$\hat{P}^N = \frac{1}{L}\sum_{n=1}^{L} e^{i(\hat{N}-N)\varphi_n}, \qquad \varphi_n = \frac{\pi}{L}n, \tag{2.52}$$

where L is the point number of $\varphi \in [0,\pi]$ and L must be odd number in order to avoid numerical instabilities which might arise at $\varphi = \pi/2$. In this thesis, for ^{12}C, the number of gauge angle φ in the interval $[0,\pi]$ is chosen to be 7 both for protons and neutrons in the Fomenko's expansion.

Figure 2.2 shows the projected energy curves, $E_I(\beta) = \dfrac{\langle\Phi^{IM}(\beta)|\hat{H}|\Phi^{IM}(\beta)\rangle}{\langle\Phi^{IM}(\beta)|\Phi^{IM}(\beta)\rangle}$, after angular momentum and particle number projection procedures, as a function of the axial deformation parameter β for ^{12}C. The first and second minima in the mean-field energy curve found at $\beta = 0.0$ and $\beta = 2.4$, respectively, (see Fig.2.1(a) and the dotted line in Fig.2.2), are shifted to $\beta = -0.3$ and $\beta = 2.7$ in the projected energy curve for $I^\pi = 0^+$. The lowest and the second lowest minima of the projected energy curve with $I^\pi = 0^+$ appear at the oblate side around $\beta = -0.3$ and the prolate side around $\beta = 0.39$ with a small barrier of about 0.44MeV, which indicates the necessity of considering the shape fluctuation effect.

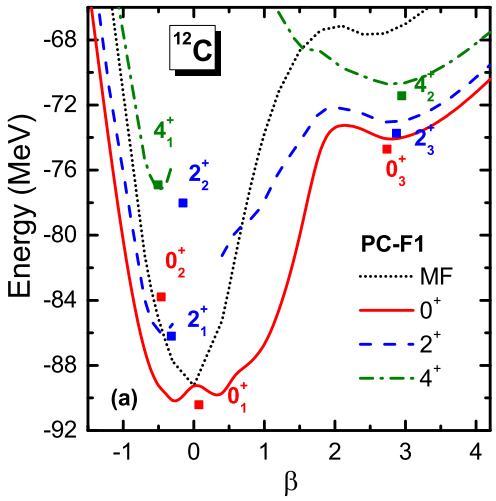

Fig. 2.2 The projected energy curve for ^{12}C as a function of the axial deformation parameter β. The mean-field energy curve (the dotted line) is also shown for a comparison. The filled squares indicate the three lowest GCM solutions for each I^π, which are plotted at their average deformation $\bar{\beta} \equiv \sum_\beta |g_n^I(\beta)|^2\beta$, where $g_n^I(\beta)$ is the collective wave functions defined by Eq. (2.60).

2.3 Generator coordinate method

For transitional nuclei, the energy surface changes very slowly with the deformation, which means that there are many near-degenerate states. For some nuclei, the mean-field energy surface as a function of deformation shows two or more minima which are practically degenerate in energy, e.g., the so-called shape coexistence phenomena. The generator coordinate method

(GCM) constructs a linear superposition of many different wave functions and is classified as a part of beyond the mean-field method. GCM is a simple and flexible variational method and can address a wide range of collective phenomena as well as provide both excitation spectra and transition strengths to be compared with experimental data. The generator coordinate method provides a way to understand the connection between phenomenological models and microscopic descriptions for collective motions. This method has rapidly become a popular tool in nuclear structure studies in recent years, for instance, GCM with Skyrme energy density functionals [91, 75], with the density-dependent Gogny force [92, 93], and with relativistic density functionals [94, 95]. In this work, the GCM is employed to perform configuration mixing calculations of angular momentum and particle number projected mean-field wave functions. This framework is also called multi-reference covariant density functional theory (MR-CDFT).

2.3.1 The Hill-Wheeler-Griffin equation

The generator coordinate method (GCM) is based on the assumption that the GCM state $|\Phi_n\rangle$ is written as a superposition of the generating functions $|\Phi(q)\rangle$, which are labeled by the parameter q, that is,

$$|\Phi_n\rangle = \sum_q F_n(q)|\Phi(q)\rangle, \tag{2.53}$$

where n labels the different eigenstates of $\hat{H}$. The parameter q is referred to as a generator coordinate.

In this work, the generating functions and the generator coordinate are projected mean field wave functions and the quadrupole moment q, respectively. Thus, the wave function of nuclear states are constructed as a superposition of quantum-number projected mean field states with different quadrupole deformation q,

$$|\Phi_n^{IM}\rangle = \sum_{K,q} F_n^{IK}(q)\hat{P}^I_{MK}\hat{P}^N\hat{P}^Z|\Phi(q)\rangle. \tag{2.54}$$

The weight function $F_n^{IK}(q)$ is assumed to be a well behaved function of the variable q and is determined by requiring that the enery expectation value

$$E_n^{IM} = \frac{\langle\Phi_n^{IM}|\hat{H}|\Phi_n^{IM}\rangle}{\langle\Phi_n^{IM}|\Phi_n^{IM}\rangle}, \tag{2.55}$$

be stationary with respect to an arbitrary variation, i.e., $\dfrac{\delta E_n^{IM}}{\delta F_n^{IK}} = 0$. This leads to the Hill-Wheeler-Griffin equation [96]

$$\sum_{K',q'} \left[\mathcal{H}^I_{KK'}(q,q') - E_{nI}\mathcal{N}^I_{KK'}(q,q')\right] F_n^{IK'}(q') = 0. \tag{2.56}$$

where the norm kernel $\mathcal{N}^I(q,q')$ and the Hamiltonian kernel $\mathcal{H}^I(q,q')$ are given by,

$$\mathcal{N}^I_{KK'}(q,q') = \langle\Phi(q)|\hat{P}^I_{KK'}\hat{P}^N\hat{P}^Z|\Phi(q')\rangle, \tag{2.57a}$$

$$\mathcal{H}^I_{KK'}(q,q') = \langle\Phi(q)|\hat{H}\hat{P}^I_{KK'}\hat{P}^N\hat{P}^Z|\Phi(q')\rangle, \tag{2.57b}$$

respectively. Substituting the particle number projector (2.46) and the angular momentum projector (2.50) into Eq.(2.57), those kernels read

$$\begin{aligned}\mathcal{O}^I_{KK'}(q,q') = & \frac{2I+1}{8\pi^2}\int d\Omega D^{I*}_{KK'}(\Omega)\int_0^{2\pi}\frac{e^{-iN\varphi_N}}{2\pi}d\varphi_N\int_0^{2\pi}\frac{e^{-iZ\varphi_Z}}{2\pi}d\varphi_Z \\ & \times\langle\Phi(q)|\hat{O}e^{i\hat{N}\varphi_N}e^{i\hat{Z}\varphi_Z}\hat{R}(\Omega)|\Phi(q')\rangle,\end{aligned} \tag{2.58}$$

where $\hat{O}$ stands for 1 and $\hat{H}$ for the norm kernel and the Hamiltonian kernel, respectively. The energy overlap $\langle\Phi(q)|\hat{H}e^{i\hat{N}\varphi_N}e^{i\hat{Z}\varphi_Z}\hat{R}(\Omega)|\Phi(q')\rangle$ in the Hamiltonian kernel is taken to be the same functional form as in the nuclear mean-field energy Eq.(2.34) but with replacements of the densities and currents with mixed ones, that is, off-diagonal components of the density and current matrices [97]:

$$\tilde{\rho}^{q,q'}_{ij}(\Omega) = \frac{\langle\Phi(q)|c^\dagger_j c_i e^{i\hat{N}\varphi_N}e^{i\hat{Z}\varphi_Z}\hat{R}(\Omega)|\Phi(q')\rangle}{\langle\Phi(q)|e^{i\hat{N}\varphi_N}e^{i\hat{Z}\varphi_Z}\hat{R}(\Omega)|\Phi(q')\rangle}. \tag{2.59}$$

Notice that, since the projected mean-field states do not form an orthogonal basis and the weights $F^{IK}_n(\beta)$ in Eq. (2.54) are not orthogonal functions, $F^{IK}_n(\beta)$ cannot be taken as weights of the state $|\Phi(q)\rangle$ in the state $|\Phi^{IM}_n\rangle$. It is therefore convenient to construct a set of orthonormal collective wave functions g^{IM}_n as [81]

$$g^{IK}_n(q) = \sum_{q'}\left[\mathcal{N}^I_{KK'}\right]^{1/2}(q,q')F^{IK'}_n(q'). \tag{2.60}$$

Notice that the modulus square of $g^{IK}_n(q)$ does not represent the probability to find the state with deformation q in the GCM state. However, in the case of the axial symmetric state, $g^{IK}_n(q)$ provides a good indication about the dominant configurations in the GCM state.

We apply the GCM calculation to ^{12}C and show the low-lying spectrum in Fig. 2.3 (see also Fig. 2.2), in comparison with the experiment data [98, 99]. One can see that the low-lying spectrum is reproduced rather well with this GCM+RMF calculation, although the excitation energies are systematically overestimated.

The distribution of the collective wave functions $g^I_n(\beta)$ for the three lowest states with $I = 0, 2, 4$, and 6 are displayed in Fig. 2.4. The ground state of ^{12}C is dominated by the spherical configuration. The collective wave functions and the energy spectrum indicate that there is a coexistence of an anharmonic spherical vibrator and an oblate deformed band at low excitation energies of ^{12}C. Both structures are not pure and distorted by their strong mixing. The high-lying $0^+_3, 2^+_3$ and 4^+_2 states seem to form a rotational band dominated by the 3α-linear configuration,

in which the collective wave functions are much extended to a large deformation region. Similar rotational band corresponding to a 4α-linear configuration has also been found in the high-lying states of ^{16}O [100].

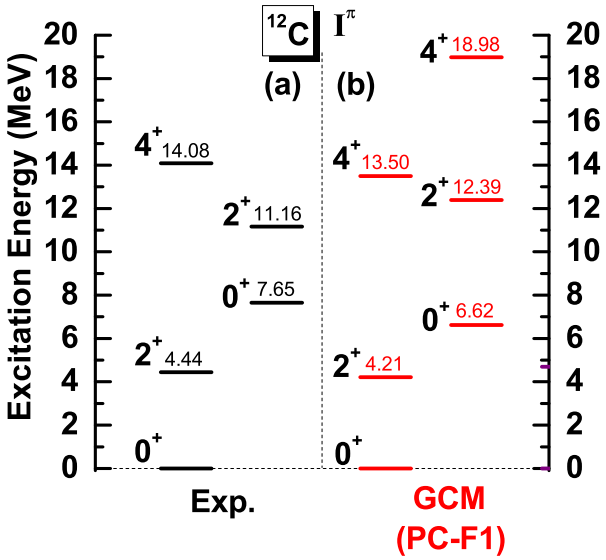

Fig. 2.3 The spectrum of ^{12}C obtained with the GCM with the PC-F1 interaction. The excitation energies are given in units of MeV. The experimental data are taken from Refs. [98, 99].

2.3.2 Transition density between GCM states

The reduced transition density from the initial state $|I_i M_i n_i\rangle$ to the final state $|I_f M_f n_f\rangle$ can be calculated with the wave function of GCM state [101, 102]. For axially deformed states, it is given as follows (see Appendix B for the derivation):

$$\begin{aligned}
\rho_{\lambda,V}^{n_f I_f n_i I_i}(r) &= \hat{I}_i^{-1}\langle n_f I_f||\hat{\rho}_V(\boldsymbol{r})Y_\lambda||n_i I_i\rangle \\
&= (-1)^{I_i-I_f}\frac{\hat{I}_f^2}{\hat{I}_i^2}\sum_{\beta,\beta'}F_{n_f}^{I_f*}(\beta)F_{n_i}^{I_i}(\beta')\sum_K\langle I_f 0\lambda K|I_i K\rangle \\
&\quad\times\int d\hat{\boldsymbol{r}}Y_{\lambda K}^*(\hat{\boldsymbol{r}})\langle\Phi(\beta)|\hat{\rho}_V(\boldsymbol{r})\hat{P}_{K0}^{I_i}\hat{P}^N\hat{P}^Z|\Phi(\beta')\rangle, \qquad (2.61a)\\
\rho_{\lambda,S}^{n_f I_f n_i I_i}(r) &= \hat{I}_i^{-1}\langle n_f I_f||\hat{\rho}_S(\boldsymbol{r})Y_\lambda||n_i I_i\rangle \\
&=(-1)^{I_i-I_f}\frac{\hat{I}_f^2}{\hat{I}_i^2}\sum_{\beta,\beta'}F_{n_f}^{I_f*}(\beta)F_{n_i}^{I_i}(\beta')\sum_K\langle I_f 0\lambda K|I_i K\rangle \\
&\quad\times\int d\hat{\boldsymbol{r}}Y_{\lambda K}^*(\hat{\boldsymbol{r}})\langle\Phi(\beta)|\hat{\rho}_S(\boldsymbol{r})\hat{P}_{K0}^{I_i}\hat{P}^N\hat{P}^Z|\Phi(\beta')\rangle, \qquad (2.61b)
\end{aligned}$$

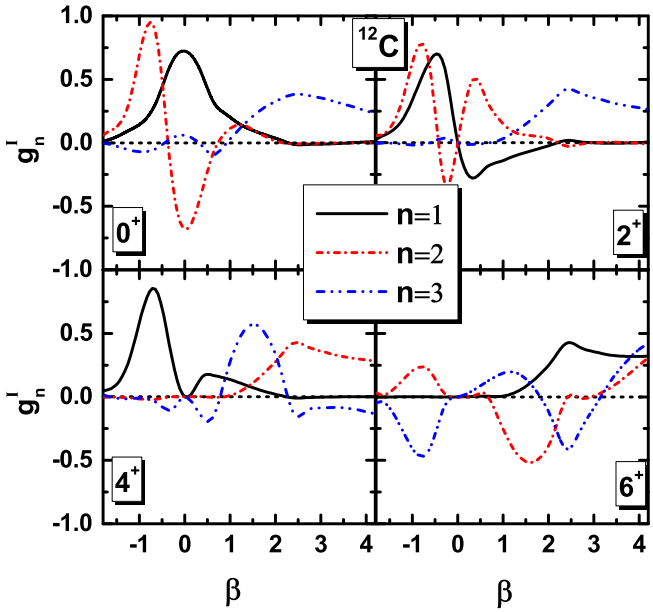

Fig. 2.4 The collective wave functions g_n^I [cf. Eq.(2.60)] for the first three states in ^{12}C with spin-parity of $0^+, 2^+, 4^+$ and 6^+ as functions of deformation parameter β.

where the notation $\hat{I} = \sqrt{2I+1}$ is introduced for simplicity. The vector and scalar density operators are defined as

$$\hat{\rho}_V(\boldsymbol{r}) = \sum_{i=1}^{A_c} \delta(\boldsymbol{r} - \boldsymbol{r}_i), \qquad \hat{\rho}_S(\boldsymbol{r}) = \sum_{i=1}^{A_c} \delta(\boldsymbol{r} - \boldsymbol{r}_i)\gamma_N^0, \tag{2.62}$$

where A_c is the mass number of the nucleus.

Figures 2.5 (a), (b) and (c) show the vector (the solid lines) and scalar (the dashed lines) transition densities $\rho_\lambda^{0\lambda}$ in the low-lying yrast states ($n = 1$) of ^{12}C for the multipolarity $\lambda = 0,\ 2,$ and 4, respectively. The vector $\rho_0^{00}(r)$ is nothing but the total nucleon density for the 0_1^+ ground state multiplied by a factor $\sqrt{4\pi}$. It is shown that the transition density $\rho_\lambda^{0\lambda}$ decreases by one order-of-magnitude as λ increases from 0 to 2, and from 2 to 4. Besides, we also plot the transition densities ρ_λ^{22} (Fig. 2.5(d)) with $\lambda = 0, 2,$ and 4, ρ_λ^{24} (Fig. 2.5(e)) with $\lambda = 2, 4,$ and 6, and ρ_λ^{26} (Fig. 2.5(f)) with $\lambda = 4, 6,$ and 8. Notice that the vector and scalar transition densities are similar to one another.

2.3.3 Form factor in electron scattering

Using the transition densities presented in the previous section, the form factor $F_\lambda(q)$ for electron scattering with an angular momentum transfer λ and the momentum transfer $q = |\boldsymbol{k}_f - \boldsymbol{k}_i|$ is given by the following relation [101],

$$F_\lambda(q) = \frac{\sqrt{4\pi}}{Z} \int_0^\infty dr r^2 \rho_{\lambda,\mathrm{ch}}^{n_f I_f n_i I_i}(r) j_\lambda(qr), \tag{2.63}$$

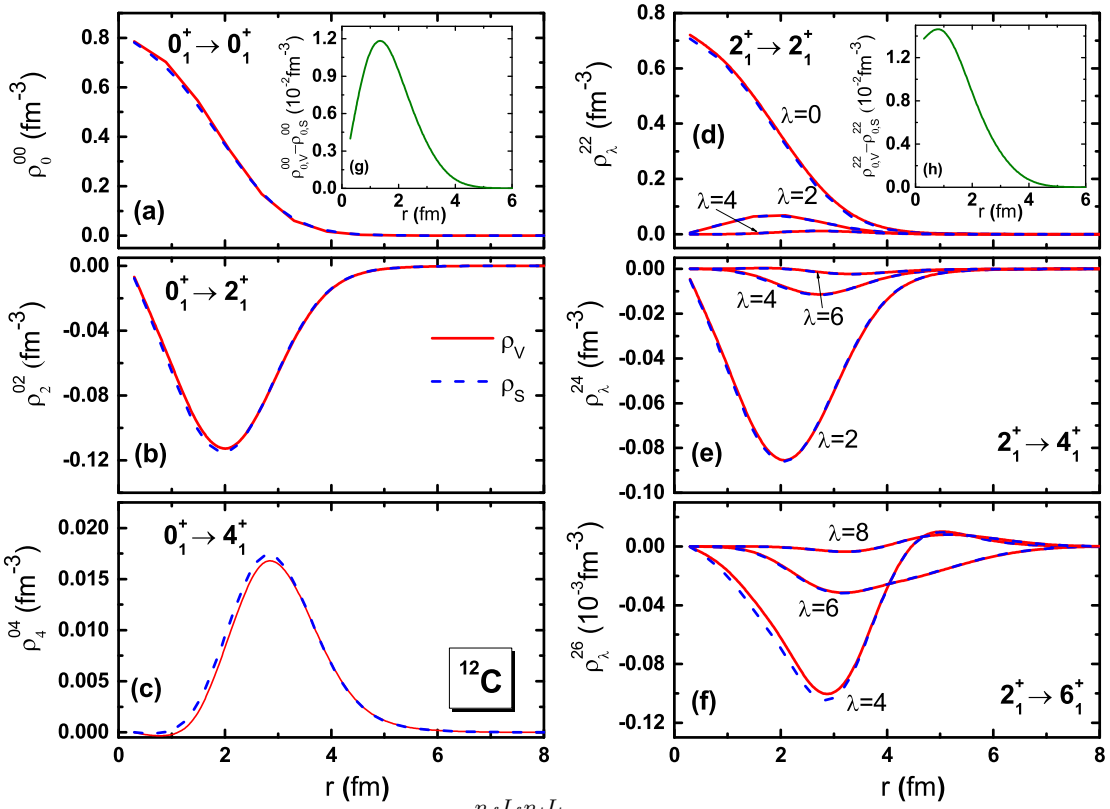

Fig. 2.5 The vector transition density, $\rho_{\lambda,V}^{n_f I_f n_i I_i}$, given by Eq. (2.61a), and the scalar transition density, $\rho_{\lambda,S}^{n_f I_f n_i I_i}$, given by Eq. (2.61b), in the low-lying states ($n = 1$) of ^{12}C. These are plotted by the solid and the dashed lines, respectively. The insets show the difference of the vector and scalar transition densities.

where $j_\lambda(qr)$ is the spherical Bessel function. Here, the $\rho_{\lambda,\mathrm{ch}}^{n_f I_f n_i I_i}(r)$ is the charge transition density, which can be calculated from the convolution of the proton vector transition densities with a Gaussian form factor for a finite proton size [61],

$$\rho_{\lambda,\mathrm{ch}}^{n_f I_f n_i I_i}(\boldsymbol{r}) = \left(\frac{1}{a\sqrt{\pi}}\right)^3 \int d\boldsymbol{r}' \exp\left[-\frac{(\boldsymbol{r}-\boldsymbol{r}')^2}{a^2}\right] \rho_{\lambda,V_p}^{n_f I_f n_i I_i}(\boldsymbol{r}'), \tag{2.64}$$

with $a = \sqrt{3/2}\langle r^2\rangle_p^{1/2} = 0.65$ fm.

The calculated charge form factors for ^{12}C are shown in Fig. 2.6 and are compared with the experiment data. One can see that the form factors $F_\lambda(q)$ are in rather good agreement with the data except for the underestimation of the elastic form factor after the first minimum, as was found also in the recent studies for ^{12}C [106] and ^{24}Mg [107] based on the Skyrme forces. This may be because the spreading of the collective wave function in quadrupole deformation space is somewhat overestimated in the calculations, decreasing the weights of the large-q components of the transition density [106, 107].

The charge form factors for the interband transitions between the two bands with $n = 1$ and $n = 2$ in ^{12}C are shown in Figs. 2.6(d)-(f). The inelastic form factor $F_0(q)$ corresponding to the transition from the 0_1^+ to the 0_2^+ states is significantly underestimated in the high-q region beyond

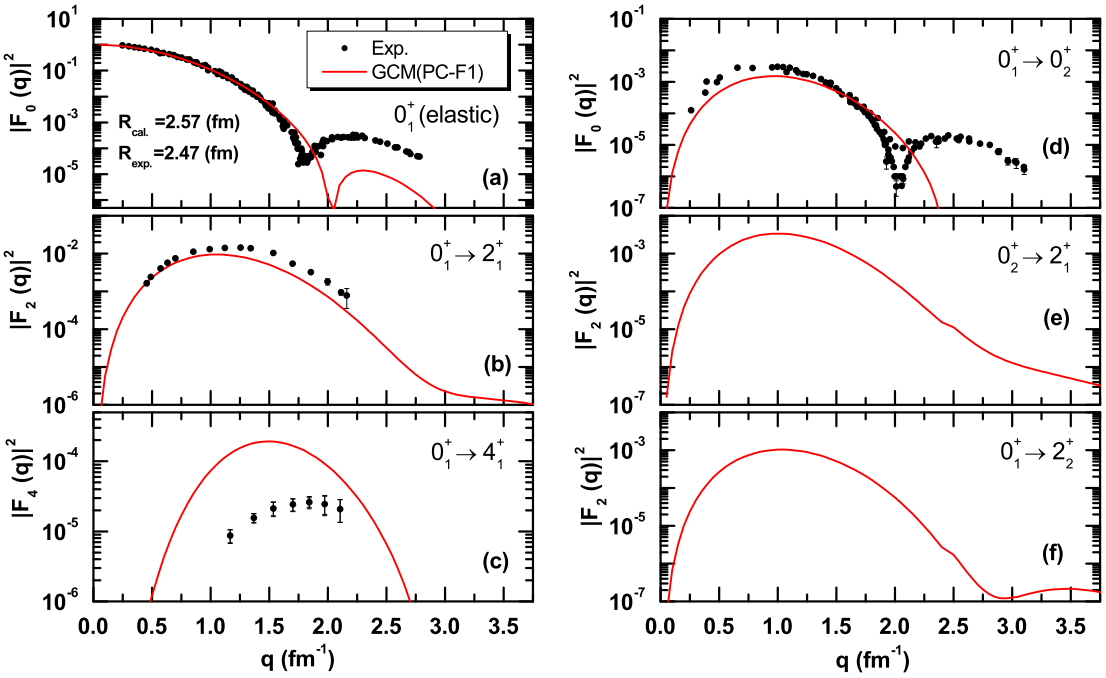

Fig. 2.6 The charge form factor for ^{12}C for the transition from the ground state to (a) the ground state, (b) the excited 2^+_1 state, and (c) the excited 4^+_1 state calculated with the GCM method with the PC-F1 force. The figure also shows those for the transition between the two bands with $n = 1$ and $n = 2$ (d)-(f). These are compared with the available data [103–105]. R on the top panel is the root-mean-square charge radius of ^{12}C.

the first minimum. This is because the 0^+_2 state is the Hoyle state with dilute 3α structure, which is beyond the model space of the present calculation.

2.3.4 Charge radius

In the GCM, the proton radius for the nI state can be calculated as

$$\langle r^2_p \rangle_{nI} = \frac{1}{Z} \sum_{\beta,\beta'} F^I_n(\beta) F^I_n(\beta') \langle nI||er^2||nI\rangle. \tag{2.65}$$

Then the charge radius, which is a fundamental property of the atomic nucleus and can be measured by electron scattering, reads

$$\langle r^2_{\rm ch} \rangle^{1/2} = \sqrt{\langle r^2_p \rangle_{nI} + 0.64({\rm fm}^2)}. \tag{2.66}$$

The calculated charge radii of ^{12}C are shown in Table 2.2. The charge radius of ^{12}C for the ground state by the present GCM calculation is 2.57 fm, which is larger than the empirical value of 2.47 fm. This trend is consistent with the calculated charge form factor shown in Fig. 2.6(a). The α-cluster model calculation gives the charge radius of 0^+_1 state to be 2.54 fm [108]. For the 0^+_2 state, our calculated charge radii is 2.69 fm in comparison with other model calculations, such

as 3.27 fm by the antisymmetrized molecular dynamics [109], 3.38 fm by the fermionic molecular dynamics [108] and 3.83 fm by the alpha-condensation model [110].

Table 2.2 Charge radii of the ground and excited states of ^{12}C. The experimental data is taken from Ref. [111].

I^π_n	Exp. (fm)	GCM(PC-F1)	I^π_n	Exp.	GCM(PC-F1)
0^+_1	2.47	2.57	0^+_2		2.69
2^+_1		2.65	2^+_2		2.71
4^+_1		2.71	4^+_2		3.49

2.3.5 Electric multipole transition strengths

The multipole transition matrix elements, which are related to the vector transition density (2.61a), can be calculated directly in the laboratory frame as

$$\begin{aligned} M_\lambda^{n_f I_f n_i I_i} &= \int dr r^{\lambda+2} \rho_{\lambda,V}^{n_f I_f n_i I_i}(r) \\ &= \frac{1}{\sqrt{2I_i+1}} \sum_{\beta,\beta'} F_{n_f}^{I_f *}(\beta') F_{n_i}^{I_i}(\beta) \langle n_f I_f || \hat{Q}_\lambda || n_i I_i \rangle, \end{aligned} \tag{2.67}$$

where the multipole operator is given as $\hat{Q}_{\lambda M} = \sum_i r_i^\lambda Y_{\lambda M}(\hat{\boldsymbol{r}_i})$.

The reduced transition matrix element $\langle n_f I_f || \hat{Q}_\lambda || n_i I_i \rangle$ is related to the proton vector transition density as

$$\langle n_f I_f || \hat{Q}_\lambda || n_i I_i \rangle = \hat{I}_i \int dr r^{2\lambda} \rho_{\lambda,V}^{n_f I_f n_i I_i}(r). \tag{2.68}$$

The electric transition strength is then given by

$$B(E\lambda; I_i, n_i \to I_f, n_f) = |e M_\lambda^{n_f I_f n_i I_i; p}|^2. \tag{2.69}$$

Table 2.3 shows the calculated transition strengths for ^{12}C. One can see that the E2 transition strengths of the low-energy states are reproduced rather well. The electric monopole transition matrix element $|M(E0: 0^+_2 \to 0^+_1)| = 4.12$ $e$fm^2 is in good agreement with the results (4.5 ± 0.2 $e$fm^2) of the recent configuration mixing calculation based on a Skyrme force [106]. This value should be compared with the experimental data $|M(E0: 0^+_2 \to 0^+_1)| = 5.4(2)$ $e$fm^2 [112].

Table 2.3 The calculated $B(E2)$ and $|M(E0)|$ for ^{12}C with the GCM calculations. The experiment data are taken from Refs. [112, 113].

Transitions	Exp.	GCM(PC-F1)
$B(E2: 2^+_1 \to 0^+_1)$ (e^2 fm^4)	7.6(4)	6.62
$B(E2: 4^+_1 \to 2^+_1)$ (e^2 fm^4)		14.60
$B(E2: 2^+_2 \to 0^+_2)$ (e^2 fm^4)		6.65
$B(E2: 2^+_1 \to 0^+_2)$ (e^2 fm^4)	2.6(4)	2.93
$\lvert M(E0: 0^+_2 \to 0^+_1)\rvert$ (e fm^2)	5.4(2)	4.12

Chapter 3

$N\Lambda$ effective interaction

3.1 Introduction

In order to extend the beyond mean-field approach presented in the previous chapter to hypernuclei, we need a hyperon-nucleon interaction. The understanding of hyperon-nucleon interaction may provide rich information on baryon-baryon interaction. Hypernuclei, consisting of one or more hyperons bound within a nucleus, have been used as a natural laboratory to study hyperon-nucleon and hyperon-hyperon interactions [114–120]. The Λ particle is weakly bound in nuclear medium [121] and the empirical Λ-nuclear spin-orbit coupling is quite weak compared to that of a nucleon in the nucleus [121]. Many theoretical attempts have been done to understand this small spin-orbit splitting in Λ-hypernuclei [3, 122–125].

From the viewpoint of the quark model, $N\Lambda$ interactions are treated at quark level (udd, uud, uds for proton, neutron and Λ hyperon, respectively.). Because the couplings of s-u and s-d quarks are suppressed, the $N\Lambda$ interaction should be 2/3 of that in NN interactions [3].

In the meson exchange picture, Brockmann and Weise were the first who derived the $N\Lambda$ interaction by taking into account the 2π and 3π exchanges and their correlations [126]. They constructed the $N\Lambda$ interaction in the isoscalar-scalar and isovector-vector channels with a reduction factor of about 1/3 of the corresponding NN interaction. Taking into account the tensor coupling gives larger values of the meson couplings and consistent with SU(3). The tensor coupling for Λ is much stronger than that for nucleon and has turned out to be important to reproduce a small hyperon spin-orbit splitting in Λ hypernuclei [124].

As in the NN interaction, an effective $N\Lambda$ interaction has been used in shell model, cluster model, AMD and mean-field theories to study the properties of Λ hypernuclei. These $N\Lambda$ interactions include the effective $N\Lambda$ interaction derived from G-matrix, density-dependent Λ-nuclear interaction derived from chiral SU(3) effective field theory [127, 128], and Skyrme-type $N\Lambda$ interactions [129].

In this chapter, we will briefly review the $N\Lambda$ effective interactions for the relativistic point coupling (RPC) energy density functional which we shall employ. Relativistic mean-field models generate the spin-orbit coupling by the coherent interplay of scalar and vector mean fields.

3.2 $N\Lambda$ effective interaction for relativistic point coupling model

3.2.1 From EDF to $N\Lambda$ effective interaction

As in the case for NN interaction given by Eq.(2.1), in the relativistic point-coupling model, the Lagrangian for $N\Lambda$ interaction is constructed as [130]:

$$\mathscr{L}_{\rm int}^{N\Lambda} =: \mathscr{L}_{\rm 4f}^{N\Lambda} + \mathscr{L}_{\rm der}^{N\Lambda} + \mathscr{L}_{\rm ten}^{N\Lambda} :, \tag{3.1}$$

with

$$\mathscr{L}_{\rm 4f}^{N\Lambda} = -\alpha_S^{N\Lambda}(\bar\psi^N\psi^N)(\bar\psi^\Lambda\psi^\Lambda) - \alpha_V^{N\Lambda}(\bar\psi^N\gamma_\mu\psi^N)(\bar\psi^\Lambda\gamma^\mu\psi^\Lambda), \tag{3.2a}$$

$$\mathscr{L}_{\rm der}^{N\Lambda} = -\delta_S^{N\Lambda}(\partial_\mu\bar\psi^N\psi^N)(\partial^\mu\bar\psi^\Lambda\psi^\Lambda) - \delta_V^{N\Lambda}(\partial_\mu\bar\psi^N\gamma_\nu\psi^N)(\partial^\mu\bar\psi^\Lambda\gamma^\nu\psi^\Lambda), \tag{3.2b}$$

$$\mathscr{L}_{\rm ten}^{N\Lambda} = -\alpha_T^{N\Lambda}(\bar\psi^\Lambda\sigma^{\mu\nu}\psi^\Lambda)(\partial_\nu\bar\psi^N\gamma_\mu\psi^N). \tag{3.2c}$$

The four-fermion point coupling term $\mathscr{L}_{\rm 4f}^{N\Lambda}$ is the leading order of zero-range approximation to the meson exchange interaction and is made up of the operator of scalar and vector densities. The derivative terms $\mathscr{L}_{\rm der}^{N\Lambda}$ simulate to some extent the finite-range character of $N\Lambda$ interaction and these terms are expected to be more pronounced in light hypernuclei [131]. The vector-meson-like tensor coupling term $\mathscr{L}_{\rm ten}^{N\Lambda}$ simulates the Λ-ω tensor coupling $\frac{f_{\Lambda\omega}}{2m_\Lambda}(\bar\psi^\Lambda\sigma^{\mu\nu}\psi^\Lambda)(\partial_\nu\omega_\mu)$. According to the quark model, the ratio of N-ω tensor-to-vector coupling constants, $f_{N\omega}/g_{N\omega}$, is -0.09 [132], which may justify an omission of the tensor coupling terms for nucleons. In contrast, the ratio of Λ-ω tensor-to-vector coupling constants, $f_{\Lambda\omega}/g_{\Lambda\omega}$, is given as -1 [132]. This makes the tensor coupling terms significantly important for Λ hypernuclei, especially to reproduce the smallness of spin-orbit splittings in Λ single-particle spectra.

The energy functional for the $N\Lambda$ interaction in the mean-field and no-sea approximations is given by:

$$\begin{aligned} E_{\rm int}^{(N\Lambda)}[\rho] = \int d\boldsymbol{r}\Big[&\alpha_S^{N\Lambda}\rho_S(\boldsymbol{r})\rho_S^\Lambda(\boldsymbol{r}) + \alpha_V^{N\Lambda}\rho_V(\boldsymbol{r})\rho_V^\Lambda(\boldsymbol{r}) + \delta_S^{N\Lambda}\rho_S(\boldsymbol{r})\Delta\rho_S^\Lambda(\boldsymbol{r}) \\ &+ \delta_V^{N\Lambda}\rho_V(\boldsymbol{r})\Delta\rho_V^\Lambda(\boldsymbol{r}) + \alpha_T^{N\Lambda}\rho_T^\Lambda(\boldsymbol{r})\rho_V(\boldsymbol{r})\Big]. \end{aligned} \tag{3.3}$$

Here ρ_S, ρ_V and ρ_T are the scalar, the vector and the tensor densities defined as:

$$\rho_S(\boldsymbol{r}) = \sum_{i=1}^{A_c}\bar\psi_i(\boldsymbol{r})\psi_i(\boldsymbol{r}), \quad \rho_S^\Lambda(\boldsymbol{r}) = \bar\psi_\Lambda(\boldsymbol{r})\psi_\Lambda(\boldsymbol{r}), \tag{3.4a}$$

$$\rho_V(\boldsymbol{r}) = \sum_{i=1}^{A_c}\psi_i^\dagger(\boldsymbol{r})\psi_i(\boldsymbol{r}), \quad \rho_V^\Lambda(\boldsymbol{r}) = \psi_\Lambda^\dagger(\boldsymbol{r})\psi_\Lambda(\boldsymbol{r}), \tag{3.4b}$$

$$\rho_T^\Lambda(\boldsymbol{r}) = \nabla\cdot(\bar\psi_\Lambda(\boldsymbol{r})i\boldsymbol{\alpha}\psi_\Lambda(\boldsymbol{r})). \tag{3.4c}$$

Taking the second functional derivative of Eq. (3.3) with respect to the densities [81],

$$\hat{V}^{N\Lambda}(\boldsymbol{r},\boldsymbol{r}_i) = \frac{\delta^2 E_{\rm int}^{(N\Lambda)}[\rho]}{\delta\rho_V^{\Lambda}(\boldsymbol{r})\delta\rho_V(\boldsymbol{r}_i)} \tag{3.5}$$

we obtain the following form for the $N\Lambda$ effective interaction

$$\hat{V}^{N\Lambda} = \hat{V}_{\rm S}^{N\Lambda} + \hat{V}_{\rm V}^{N\Lambda} + \hat{V}_{\rm Ten}^{N\Lambda}, \tag{3.6}$$

where the scalar, vector and tensor types of coupling terms read

$$\hat{V}_{\rm S}^{N\Lambda}(\boldsymbol{r},\boldsymbol{r}_i) = \alpha_S^{N\Lambda}\gamma_\Lambda^0\delta(\boldsymbol{r}-\boldsymbol{r}_i)\gamma_N^0 + \delta_S^{N\Lambda}\gamma_\Lambda^0\Big[\overleftarrow{\nabla}^2\delta(\boldsymbol{r}-\boldsymbol{r}_i) + \delta(\boldsymbol{r}-\boldsymbol{r}_i)\overrightarrow{\nabla}^2 + 2\overleftarrow{\nabla}\cdot\delta(\boldsymbol{r}-\boldsymbol{r}_i)\overrightarrow{\nabla}\Big]\gamma_N^0, \tag{3.7a}$$

$$\hat{V}_{\rm V}^{N\Lambda}(\boldsymbol{r},\boldsymbol{r}_i) = \alpha_V^{N\Lambda}\delta(\boldsymbol{r}-\boldsymbol{r}_i) + \delta_V^{N\Lambda}\Big[\overleftarrow{\nabla}^2\delta(\boldsymbol{r}-\boldsymbol{r}_i) + \delta(\boldsymbol{r}-\boldsymbol{r}_i)\overrightarrow{\nabla}^2 + 2\overleftarrow{\nabla}\cdot\delta(\boldsymbol{r}-\boldsymbol{r}_i)\overrightarrow{\nabla}\Big], \tag{3.7b}$$

$$\hat{V}_{\rm Ten}^{N\Lambda}(\boldsymbol{r},\boldsymbol{r}_i) = i\alpha_T^{N\Lambda}\gamma_\Lambda^0\Big[\overleftarrow{\nabla}\delta(\boldsymbol{r}-\boldsymbol{r}_i) + \delta(\boldsymbol{r}-\boldsymbol{r}_i)\overrightarrow{\nabla}\Big]\cdot\boldsymbol{\alpha}. \tag{3.7c}$$

Here, $\overrightarrow{\nabla}$ and $\overleftarrow{\nabla}$ are understood to act on the right- and left-hand sides of the Λ hyperon coordinates, respectively. Vice versa, Eq. (3.3) can be obtained from the above effective $N\Lambda$ interaction (see Appendix C).

3.2.2 $N\Lambda$ interaction parameter sets

Four parameter sets have been determined for the $N\Lambda$ interaction, Eq.(3.1), by fitting to the experimental data of Λ binding energies of hypernuclei from light to heavy mass region [130]. We list these parameter sets, PCY-S1, PCY-S2, PCY-S3 and PCY-S4, in Table 3.1. Notice that the PCY-S2 and PCY-S4 do not include the tensor and the derivative terms, respectively. Notice also that the PCY-S3 was obtained by excluding the spin-orbit splitting of the $1p$ state of Λ in ${}^{16}_{\Lambda}$O from the fitting, and the strength of the tensor coupling is considerably smaller than that in PCY-S1.

Table 3.1 Four parameter sets of relativistic point-coupling $N\Lambda$ interaction proposed in Ref. [130].

	PCY-S1	PCY-S2	PCY-S3	PCY-S4
$\alpha_S^{N\Lambda}$ (MeV^{-2})	-2.0305×10^{-4}	-4.2377×10^{-5}	-2.0197×10^{-4}	-1.8594×10^{-4}
$\alpha_V^{N\Lambda}$ (MeV^{-2})	1.6548×10^{-4}	1.4268×10^{-5}	1.6449×10^{-4}	1.4981×10^{-4}
$\delta_S^{N\Lambda}$ (MeV^{-4})	2.2929×10^{-9}	1.2986×10^{-9}	2.3514×10^{-9}	-1.9958×10^{-10}
$\delta_V^{N\Lambda}$ (MeV^{-4})	-2.3872×10^{-9}	-1.3850×10^{-9}	-2.4993×10^{-9}	0
$\alpha_T^{N\Lambda}$ (MeV^{-3})	-1.0603×10^{-7}	0	-4.082×10^{-9}	-5.5322×10^{-8}

3.3 Mean-field approach for Λ hypernuclei

We now show the results of mean-field calculations for hypernuclei using the point coupling $N\Lambda$ interaction given by Eq.(3.1). Adding the energy of the core nucleus (Eq.(2.33)) with a replacement of the center-of-mass correction with $E_{\rm cm} = -\sum_{\tau=n,p,\Lambda} \frac{\langle \hat{\boldsymbol{P}}_\tau^2 \rangle}{2m_\tau A_\tau}$ to the energy (Eq.(3.3)) due to the additional Λ, one obtains the total energy of a Λ hypernucleus in RMF-PC model. The Dirac equations for nucleons and Λ hyperon are solved on harmonic oscillator basis with 10 major shells. In the following, we adopt the PC-F1 force for the NN interaction and the PCY-S1 force for the $N\Lambda$ interaction.

Figure 3.1 shows the potential energy surfaces for ${}^{25}_{\Lambda}$Mg, ${}^{27}_{\Lambda}$Mg, ${}^{21}_{\Lambda}$Ne and ${}^{31}_{\Lambda}$Si hypernuclei as a function deformation parameter β so obtained, where the notations Λs and Λp correspond to putting the Λ particle in the lowest positive parity state and the lowest negative parity state, respectively. The energy minimum of ${}^{25}_{\Lambda}$Mg and ${}^{21}_{\Lambda}$Ne with Λs and Λp are slightly shifted to a smaller and larger deformation, respectively, compared with that of ^{24}Mg and ^{20}Ne. For ^{26}Mg, Λs hyperon lowers down the barrier at the spherical shape, and the energy minima at prolate side and oblate side are significantly shifted to smaller deformation region. Moreover, the Λ hyperon in the p-orbit inverts the energy ordering of the oblate and prolate minima in ^{26}Mg. For ^{30}Si, a significant change of the deformation parameter β of energy minimum is found by adding a Λ hyperon. The Λs particle shifts the energy minimum from oblate side to spherical shape, while Λp particle shifts the energy minimum to a larger oblate deformation. Similar conclusions are also found in other calculations [43, 45, 133]. One can see that the potential energy surface of ${}^{27}_{\Lambda}$Mg and ${}^{31}_{\Lambda}$Si with Λs particle is much softer against deformation than that of ^{26}Mg and ^{30}Si, respectively. This can also be seen in the potential energy surfaces in the (β, γ) plane, as shown in Fig. 3.2. This implies that the shape fluctuation effect is more important in Λ hypernuclei than in normal nuclei.

The density distribution of protons and neutrons in ^{30}Si and ${}^{31}_{\Lambda_{\rm s}}$Si corresponding to the minimum of energy surface are shown in Fig. 3.3. One can see a central depression in the proton density distribution in ${}^{31}_{\Lambda_{\rm s}}$Si at $\beta = 0.0$, similar to that predicted in "bubble" nucleus, in which the density in the center vanishes or significantly lower than the saturation density, ^{34}Si [102].

We mention that the mean-field approach provides an intuitive picture for nuclear deformation and it is suitable for discussion of the shape polarization effect associated with an additional Λ hyperon. However, this method does not yield a spectrum and connections between the mean-field results and spectroscopic observables are not straight forward. To this end, one has to transform the mean-field results to the laboratory frame and also take into account the shape fluctuation effect. In the next chapter, we will propose a novel method to realize this.

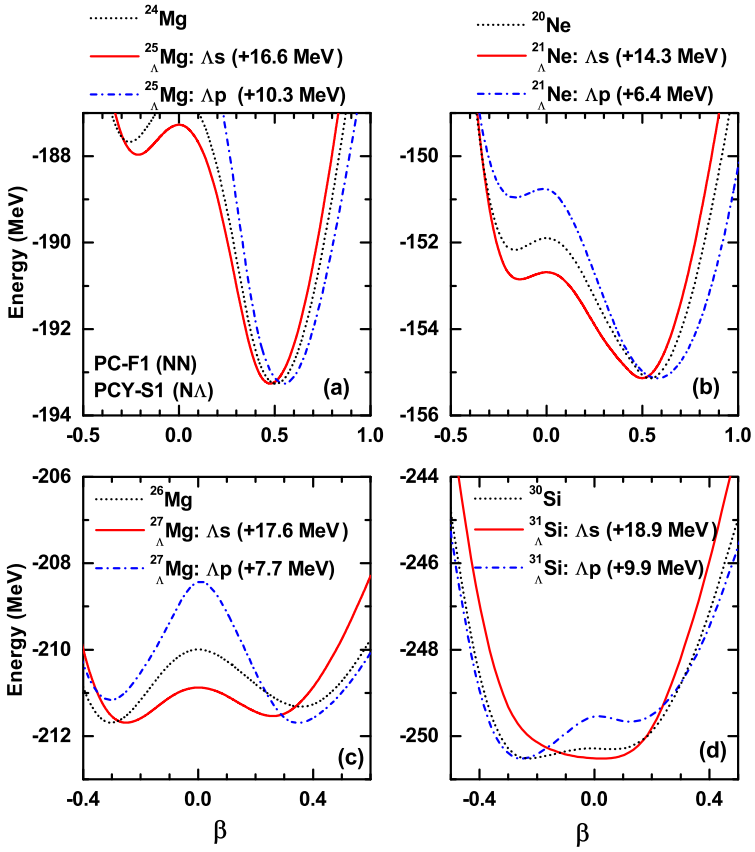

Fig. 3.1 The mean-field potential energy surfaces for hypernuclei obtained as a function of deformations parameter β. The PC-F1 for NN interaction and PCY-S1 force for $N\Lambda$ interaction are used. The energy surfaces for hypernuclei are shifted by a constant amount as indicated in each panel. Λs and Λp indicate putting the Λ particle in the lowest positive parity state and the lowest negative parity state, respectively.

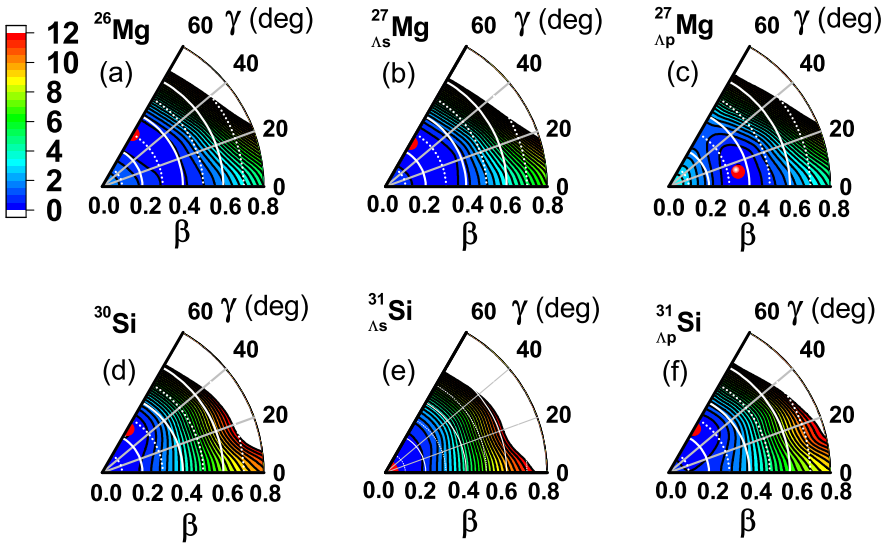

Fig. 3.2 The potential energy surfaces in the (β, γ) plane for ^{26}Mg (a), $^{27}_{\Lambda s}$Mg (b), $^{27}_{\Lambda p}$Mg (c), ^{30}Si (d), $^{31}_{\Lambda s}$Si (e) and $^{31}_{\Lambda p}$Si (f). The energies are normalized to the global minimum. The contour lines are separated by 0.5 MeV.

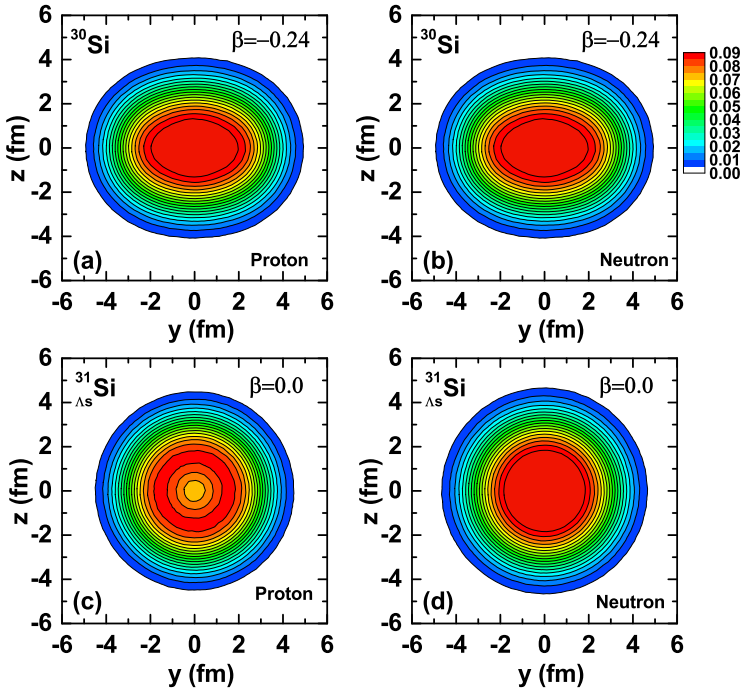

Fig. 3.3 Proton and neutron density distributions at the mean-field minimum for ^{30}Si and $^{31}_{\Lambda s}$Si (in fm^{-3}). These are plotted in the $y-z$ plane at $x = 0.35$ fm.

Chapter 4

Microscopic particle-rotor model

We now propose the novel microscopic particle-rotor model based on the beyond mean-field approach. To this end, we first consider the traditional particle-rotor model and extend it to the microscopic version.

4.1 Particle-rotor model

4.1.1 Rigid rotor

In classical mechanics, it is know that the degrees of freedom of a rigid rotor are the three Euler angles $\Omega = (\phi, \theta, \psi)$, which are used to define the orientation of the body-fixed axes in the laboratory frame. The classical kinetic energy of the rotating rigid rotor body, with the center of mass fixed at the center of coordinates, is

$$E = \sum_{i=1}^{3} \frac{I_i^2}{2\mathcal{J}_i} \tag{4.1}$$

where I_i is the i-th body-fixed angular momentum component and $\mathcal{J}_i$ is the moment of inertia about the i-th axis, which is related to the angular momentum I_i and the angular frequency ω_i as $\mathcal{J}_i = \dfrac{I_i}{\omega_i}$.

The rigid rotor model regards a deformed nucleus as a compact entity. In quantum mechanics, the nucleus has rotational symmetries, and the system can be deformed only in the intrinsic frame. But in the laboratory frame, there is no way to distinguish one of these directions from another, i.e., the angular moment $\boldsymbol{I}$ is conversed in the laboratory frame. Notice that a spherical nucleus does not have rotational excitations and an axially symmetric deformed nucleus cannot rotate around the axis of symmetry.

Corresponding to Eq.(4.1), the Hamiltonian for a rigid rotor can be expressed in terms of three different moments of inertia:

$$\hat{H} = \sum_{i=1}^{3} \frac{\hat{I}_i^2}{2\mathcal{J}_i}. \tag{4.2}$$

We will assume that the rigid rotor has axial symmetry about the 3-axis, then moments of inertia about 1-axis and 2-axis are the same $\mathcal{J}_1 = \mathcal{J}_2 = \mathcal{J}$ and the angular momentum $\boldsymbol{I}$ projected onto the body-fixed 3-axis I_3 is conserved because a nucleus cannot rotate around the axis of symmetry. Then the Hamiltonian for a rigid rotor is given by

$$\hat{H} = \frac{\hat{I}_1^2 + \hat{I}_2^2}{2\mathcal{J}} = \frac{\hat{\boldsymbol{I}}^2 - \hat{I}_3^2}{2\mathcal{J}}. \tag{4.3}$$

Since the energy of the nucleus does not depend on its orientation in space, the quantum state for the nucleus can be label by the laboratory-fixed operators $\hat{\boldsymbol{I}}^2$ and $\hat{I}_z$, which corresponds to quantum numbers I and M, respectively, with the eigenvalues of $\hbar^2 I(I+1)$ and $M\hbar$, respectively. For a nucleus with axially symmetric about the body-fixed 3-axis, $\hat{I}_3$ is also a good quantum number corresponding to the quantum number K, which can be also used to label the rotational states. The relation between the angular momentum $\boldsymbol{I}$ and its projections are shown in Fig. 4.1.

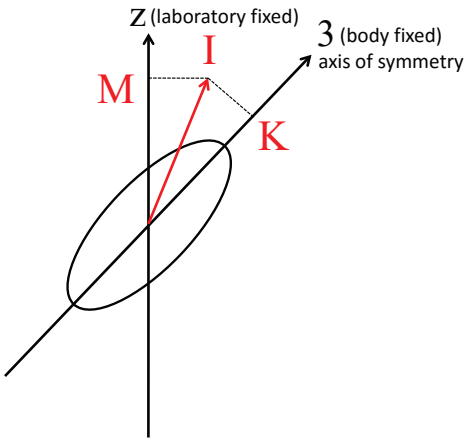

Fig. 4.1 The relation among the total angular momentum $\boldsymbol{I}$, its projection onto the laboratory z axis I_z (M), and its projection onto the body-fixed 3-axis I_3 (K).

The energy of the axially symmetric deformed nucleus corresponding to the Hamiltonian Eq. (4.3) can be written as:

$$E(I,K) = \frac{\hbar^2[I(I+1) - K^2]}{2\mathcal{J}}. \tag{4.4}$$

Notice that the quantum number K is zero for the ground state rotational band for even-even nuclei and the total angular momentum I has to be even because of the requirement of the symmetries for a rigid rotor. The normalized wave functions are therefore given by

$$\Phi_{IMK}(\Omega) = \sqrt{\frac{2I+1}{8\pi^2}} D^I_{MK}(\Omega), \quad I = 0, 2, 4, ..., \quad M = -I, ..., +I, \quad K = 0 \tag{4.5}$$

with eigenenergies of

$$E(I) = \frac{\hbar^2 I(I+1)}{2\mathcal{J}}. \tag{4.6}$$

4.1.2 Particle-rotor model

In order to describe a system with a valence particle with a deformed core nucleus, the particle-rotor model was firstly proposed by Bohr and Mottelson[134]. This model describes the interplay between the valence particle and the collective rotational core. This model provides an approximate description for many properties of the low-lying bands in odd mass nuclei, which is composed of a valence nucleon and an even-even core. The particle-rotor model has been recently used also to study the structure of odd-mass neutron-rich nuclei, for instance, ^{11}Be [135, 136], ^{15,17,19}C [137], and ^{31}Ne [138]. In these calculations, the motion of a valence particle is coupled to the rotational motion of a deformed core nucleus, which is usually described by the rigid rotor model with Wigner D functions, and the Pauli principle between the valence nucleon and the nucleons in the core nucleus is treated approximately.

The Hamiltonian for this system includes two parts, the intrinsic part $H_{\rm intr}$ describing the valence particle and the rotor part $H_{\rm coll}$ for the core nucleus[81]:

$$\hat{H} = \hat{H}_{\rm intr} + \hat{H}_{\rm coll}. \tag{4.7}$$

The intrinsic part includes the kinetic energy of the valence particle and the interaction between the valence particle and the nucleons inside the core, that is,

$$\hat{H}_{\rm intr} = \hat{T} + \sum_i \hat{V}(\boldsymbol{r}, \boldsymbol{r}_i). \tag{4.8}$$

The collective part which describes the rotation of the core is given by

$$\hat{H}_{\rm coll} = \frac{\hat{I}_1^2}{2\mathcal{J}_1} + \frac{\hat{I}_2^2}{2\mathcal{J}_2} + \frac{\hat{I}_3^2}{2\mathcal{J}_3}. \tag{4.9}$$

The total angular momentum of the system $\boldsymbol{J}$ is given by

$$\boldsymbol{J} = \boldsymbol{I} + \boldsymbol{j}, \tag{4.10}$$

where $\boldsymbol{I}$ is the collective angular momentum of the core and $\boldsymbol{j}$ is the angular momentum of the valence particle. The total wave function of the system can be written as

$$\Psi_{JM}(\boldsymbol{r}) = \sum_{j,\ell,I} \mathscr{R}_{j\ell I}(r) \mathscr{F}^{JM}_{j\ell I}(\hat{\boldsymbol{r}}, \Omega), \tag{4.11}$$

where

$$\begin{aligned} \mathscr{F}^{JM}_{j\ell I}(\hat{\boldsymbol{r}}, \Omega) =& [\mathscr{Y}_{j\ell}(\hat{\boldsymbol{r}}) \otimes \Phi_{IM_IK}(\Omega)]^{(JM)} \\ =& \sum_{mM_I} \langle jmIM_I | JM \rangle \mathscr{Y}_{j\ell m}(\hat{\boldsymbol{r}}) \Phi_{IM_IK}(\Omega) \end{aligned} \tag{4.12}$$

is the spin-angular wave function, constructed by coupling spin-angular wave functions of the valence particle $\mathscr{Y}_{j\ell m}$ to the rotational wave function $\Phi_{IM_IK}(\Omega)$ of the rigid rotor. For symmetric rotor, $\Phi_{IM_IK}(\Omega)$ is given by Eq.(4.5).

4.2 Microscopic particle-rotor model

In a spirit very similar to the conventional particle-rotor model described in the previous section, we here propose a novel microscopic particle-rotor model (MPRM) for a single-Λ hypernucleus, which consists of a Λ hyperon and an even-even core nucleus. In contrast to the conventional particle-rotor model, the low-lying states of the nuclear core are constructed microscopically, which are described by the beyond mean-field approach (see Chapter 2); that is, the GCM based on the RMF approach supplemented with the particle number and the angular momentum projections. Moreover, the Pauli principle between the valence Λ hyperon and the nucleons in the core nucleus is absent in Λ-hypernuclei.

4.2.1 Wave functions

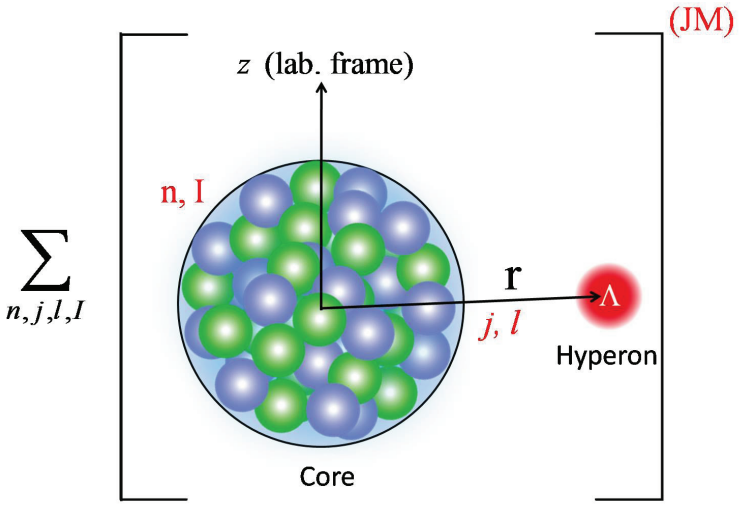

Fig. 4.2 A schematic picture of the microscopic particle-rotor model for Λ hypernucleus in the laboratory frame, in which $\boldsymbol{r}$ denotes the coordinate of the Λ hyperon. In this approach, the low-lying states of the nuclear core are described microscopically with the GCM method.

In the MPRM, the valence Λ hyperon couples to low-lying states of a nuclear core in the laboratory frame, as illustrated in a schematic picture of Fig. 4.2. Then the wave function of the whole Λ hypernucleus with the angular momentum J is constructed as

$$\Psi_{JM}(\boldsymbol{r},\{\boldsymbol{r}_i\}) = \sum_{n,j,\ell,I} \mathscr{R}_{j\ell nI}(r)\mathscr{F}^{JM}_{j\ell nI}(\hat{\boldsymbol{r}},\{\boldsymbol{r}_i\}), \tag{4.13}$$

with

$$\begin{aligned}\mathscr{F}^{JM}_{j\ell nI}(\hat{\boldsymbol{r}},\{\boldsymbol{r}_i\}) =&[\mathscr{Y}_{j\ell}(\hat{\boldsymbol{r}})\otimes\Phi_{nI}(\{\boldsymbol{r}_i\})]^{(JM)}\\ =&\sum_{mM_I}\langle jmIM_I|JM\rangle\mathscr{Y}_{j\ell m}(\hat{\boldsymbol{r}})\Phi_{nIM_I}(\{\boldsymbol{r}_i\})\end{aligned}\tag{4.14}$$

where $\boldsymbol{r}$ and $\boldsymbol{r}_i$ are the coordinates of the Λ hyperon and the nucleons, respectively. Here, M is the projection of the angular momentum J onto the z-axis in the laboratory frame. $|\Phi_{nI}\rangle$ is the wave functions of the low-lying states of the nuclear core, where I represent the angular momentum of the core state and $n = 1, 2, \ldots$ distinguish different core states with the same angular momentum I. The core states $|\Phi_{nI}\rangle$ are constructed with the quantum-number projected GCM approach, which has been introduced in Chapter II (see Eq.(2.54)). $\mathscr{Y}_{j\ell m}(\hat{\boldsymbol{r}})$ is the spin-angular wave function for the Λ hyperon, which is described by the spinor spherical harmonics,

$$\mathscr{Y}_{j\ell m}(\hat{\boldsymbol{r}}) = \sum_{m_l m_s}\langle lm_l\frac{1}{2}m_s|jm\rangle Y_{lm_l}(\theta,\varphi)\chi_{m_s},\tag{4.15}$$

where $Y_{lm_l}(\theta,\varphi)$ is the spherical harmonic and χ_{m_s} is the spin wave function (see Appendix D). For convenience, hereafter we introduce a shorthanded notation $k = \{j\ell nI\}$ to represent different channels. In Eq. (4.13), $\mathscr{R}_k(r)$ is the radial wave function for the Λ-particle. In the relativistic approach, it is given as a four-component Dirac spinor

$$\mathscr{R}_k(r) = \begin{pmatrix} f_k(r) \\ ig_k(r)\boldsymbol{\sigma}\cdot\hat{\boldsymbol{r}}\end{pmatrix}.\tag{4.16}$$

The probability P_k of the channel k in the hypernuclear state Ψ_{JM} is determined by the radial wave function $\mathscr{R}_k(r)$

$$P_k = \int r^2dr\,|\mathscr{R}_k(r)|^2 = \int r^2dr\,\left[|f_k(r)|^2 + |g_k(r)|^2\right].$$

The radial wave function is normalized as $\sum_k P_k = 1$.

We assume that the Hamiltonian $\hat{H}$ for the whole Λ hypernucleus is given as (see Eqs.(4.7) and (4.8))

$$\hat{H} = \hat{T}_\Lambda + \hat{H}_{\rm c} + \sum_{i=1}^{A_c}\hat{V}^{N\Lambda}(\boldsymbol{r},\boldsymbol{r}_i).\tag{4.17}$$

Here $\hat{T}_\Lambda = -i\boldsymbol{\alpha}\cdot\nabla_\Lambda + \gamma^0_\Lambda m_\Lambda$ is the relativistic kinetic energy of Λ hyperon, where m_Λ is the mass of Λ particle, and $\boldsymbol{\alpha}$ and γ^0 are the Dirac matrices. $\hat{H}_c$ is the many-body Hamiltonian for the core nucleus, with which the core state $|\Phi_{nI}\rangle$ satisfies $\hat{H}_c|\Phi_{nI}\rangle = E_{nI}|\Phi_{nI}\rangle$. The last term in Eq. (4.17) represents the interaction term between the valence Λ particle and the nucleons in the core nucleus, where A_c is the mass number of the core nucleus. The $N\Lambda$ interaction term is chosen as the contact coupling forms as shown in Eq.(3.7).

Substituting the wave function Eq.(4.13) to the total Dirac equation, $\hat{H}|\Psi_{JM}\rangle = E_J|\Psi_{JM}\rangle$, leads to

$$\Big\{ -i\boldsymbol{\alpha}\cdot\nabla_\Lambda + i\alpha_T^{N\Lambda}\gamma_\Lambda^0 \sum_{i=1}^{A_c}\Big[\overleftarrow{\nabla}\delta(\boldsymbol{r}-\boldsymbol{r}_i)+\delta(\boldsymbol{r}-\boldsymbol{r}_i)\overrightarrow{\nabla}\Big]\cdot\boldsymbol{\alpha} + \hat{H}_c +$$
$$\gamma_\Lambda^0\big\{m_\Lambda + \sum_{i=1}^{A_c}[\alpha_S^{N\Lambda}\delta(\boldsymbol{r}-\boldsymbol{r}_i)\gamma_N^0 + \delta_S^{N\Lambda}[\overleftarrow{\nabla}^2\delta(\boldsymbol{r}-\boldsymbol{r}_i)+\delta(\boldsymbol{r}-\boldsymbol{r}_i)\overrightarrow{\nabla}^2 + 2\overleftarrow{\nabla}\cdot\delta(\boldsymbol{r}-\boldsymbol{r}_i)\overrightarrow{\nabla}]\gamma_N^0]\big\}$$
$$+\sum_{i=1}^{A_c}[\alpha_V^{N\Lambda}\delta(\boldsymbol{r}-\boldsymbol{r}_i) + \delta_V^{N\Lambda}[\overleftarrow{\nabla}^2\delta(\boldsymbol{r}-\boldsymbol{r}_i)+\delta(\boldsymbol{r}-\boldsymbol{r}_i)\overrightarrow{\nabla}^2 + 2\overleftarrow{\nabla}\cdot\delta(\boldsymbol{r}-\boldsymbol{r}_i)\overrightarrow{\nabla}]\Big\}\sum_k \mathscr{R}_k(r)\mathscr{F}_k^{JM}(\hat{\boldsymbol{r}},\{\boldsymbol{r}_i\})$$
$$= E_J\sum_k \mathscr{R}_k(r)\mathscr{F}_k^{JM}(\hat{\boldsymbol{r}},\{\boldsymbol{r}_i\}). \tag{4.18}$$

For simplicity, we define

$$\hat{V}(\boldsymbol{r}) = \sum_{i=1}^{A_c}\Big\{\alpha_V^{N\Lambda}\delta(\boldsymbol{r}-\boldsymbol{r}_i) + \delta_V^{N\Lambda}[\overleftarrow{\nabla}^2\delta(\boldsymbol{r}-\boldsymbol{r}_i)+\delta(\boldsymbol{r}-\boldsymbol{r}_i)\overrightarrow{\nabla}^2 + 2\overleftarrow{\nabla}\cdot\delta(\boldsymbol{r}-\boldsymbol{r}_i)\overrightarrow{\nabla}]\Big\}, \tag{4.19}$$

$$\hat{S}(\boldsymbol{r}) = \sum_{i=1}^{A_c}\Big\{\alpha_S^{N\Lambda}\delta(\boldsymbol{r}-\boldsymbol{r}_i)\gamma_N^0 + \delta_S^{N\Lambda}[\overleftarrow{\nabla}^2\delta(\boldsymbol{r}-\boldsymbol{r}_i)+\delta(\boldsymbol{r}-\boldsymbol{r}_i)\overrightarrow{\nabla}^2 + 2\overleftarrow{\nabla}\cdot\delta(\boldsymbol{r}-\boldsymbol{r}_i)\overrightarrow{\nabla}]\gamma_N^0\Big\}, \tag{4.20}$$

and

$$\hat{V}_T(\boldsymbol{r}) = \sum_{i=1}^{A_c}\hat{V}_T^{N\Lambda}(\boldsymbol{r},\boldsymbol{r}_i), \qquad \text{with} \qquad \hat{V}_T^{N\Lambda}(\boldsymbol{r},\boldsymbol{r}_i) \equiv \alpha_T^{N\Lambda}\Big[\overleftarrow{\nabla}\delta(\boldsymbol{r}-\boldsymbol{r}_i)+\delta(\boldsymbol{r}-\boldsymbol{r}_i)\overrightarrow{\nabla}\Big]. \tag{4.21}$$

The equation (4.18) then becomes

$$\Big\{ -i\boldsymbol{\alpha}\cdot\nabla_\Lambda + i\hat{V}_T\cdot\boldsymbol{\gamma} + \gamma_0[m_\Lambda+\hat{S}] + \hat{H}_c + \hat{V} - E_J\Big\}\sum_k \mathscr{R}_k(r)\mathscr{F}_k^{JM}(\hat{\boldsymbol{r}},\{\boldsymbol{r}_i\}) = 0 \tag{4.22}$$

with $\boldsymbol{\alpha} = \begin{pmatrix} 0 & \boldsymbol{\sigma} \\ \boldsymbol{\sigma} & 0 \end{pmatrix}$, $\gamma^0 = \beta = \begin{pmatrix} I & 0 \\ 0 & -I \end{pmatrix}$ and $\boldsymbol{\gamma} = \beta\boldsymbol{\alpha} = \begin{pmatrix} 0 & \boldsymbol{\sigma} \\ -\boldsymbol{\sigma} & 0 \end{pmatrix}$.

Substituting Eq.(4.16) into the above equation, we obtain

$$\sum_k \begin{pmatrix} m_\Lambda + \hat{S} + \hat{V} - E_J + E_{nI} & \boldsymbol{\sigma}\cdot\boldsymbol{p} + i\hat{V}_T\cdot\boldsymbol{\sigma} \\ \boldsymbol{\sigma}\cdot\boldsymbol{p} - i\hat{V}_T\cdot\boldsymbol{\sigma} & -m_\Lambda - \hat{S} + \hat{V} - E_J + E_{nI} \end{pmatrix}\begin{pmatrix} f_k(r) \\ ig_k(r)\boldsymbol{\sigma}\cdot\hat{\boldsymbol{r}} \end{pmatrix}\mathscr{F}_k^{JM}(\hat{\boldsymbol{r}},\{\boldsymbol{r}_i\}) = 0, \tag{4.23}$$

from which we obtain two coupled equations

$$\sum_k \Big\{[m_\Lambda + \hat{S} + \hat{V} - E_J + E_{nI}]f_k(r) + [\boldsymbol{\sigma}\cdot\boldsymbol{p} + i\hat{V}_T\cdot\boldsymbol{\sigma}][ig_k(r)\boldsymbol{\sigma}\cdot\hat{\boldsymbol{r}}]\Big\}\mathscr{F}_k^{JM}(\hat{\boldsymbol{r}},\{\boldsymbol{r}_i\}) = 0 \tag{4.24}$$

$$\sum_k \Big\{[\boldsymbol{\sigma}\cdot\boldsymbol{p} - i\hat{V}_T\cdot\boldsymbol{\sigma}]f_k(r) + [-m_\Lambda - \hat{S} + \hat{V} - E_J + E_{nI}][ig_k(r)\boldsymbol{\sigma}\cdot\hat{\boldsymbol{r}}]\Big\}\mathscr{F}_k^{JM}(\hat{\boldsymbol{r}},\{\boldsymbol{r}_i\}) = 0. \tag{4.25}$$

Notice that with the relation of $(\boldsymbol{\sigma}\cdot\hat{\boldsymbol{r}})\mathscr{Y}_{jlm} = -\mathscr{Y}_{j\tilde{l}m}$, $(\boldsymbol{\sigma}\cdot\hat{\boldsymbol{r}})\mathscr{Y}_{j\tilde{l}m} = -\mathscr{Y}_{jlm}$ and $\hat{\kappa}\mathscr{Y}_{jlm} = -\kappa\mathscr{Y}_{jlm}$, $\hat{\kappa}\mathscr{Y}_{j\tilde{l}m} = \kappa\mathscr{Y}_{j\tilde{l}m}$ (see Appendix D), one has

$$(\boldsymbol{\sigma}\cdot\boldsymbol{p})[ig_k(r)\boldsymbol{\sigma}\cdot\hat{\boldsymbol{r}}]\mathscr{F}_k^{JM} = \left(\frac{d}{dr} - \frac{\kappa-1}{r}\right) g_k(r)[\mathscr{Y}_{j\ell}(\hat{\boldsymbol{r}})\otimes\Phi_{nI}(\{\boldsymbol{r}_i\})]^{(JM)} \tag{4.26}$$

$$(\boldsymbol{\sigma}\cdot\boldsymbol{p})f_k(r)\mathscr{F}_k^{JM} = i\left(\frac{d}{dr} + \frac{\kappa+1}{r}\right) f_k(r)[\mathscr{Y}_{j\tilde{\ell}}(\hat{\boldsymbol{r}})\otimes\Phi_{nI}(\{\boldsymbol{r}_i\})]^{(JM)}. \tag{4.27}$$

In order to obtain the radial wave function $\mathscr{R}_k(r)$ given by Eq. (4.16) and the energy E_J for each hypernuclear low-lying states, we multiply $\langle\mathscr{F}_k^{JM}|$ to the total equation, $\hat{H}|\Psi_{JM}\rangle = E_J|\Psi_{JM}\rangle$, from the left and integrate it over $\hat{\boldsymbol{r}}$ and $\{\boldsymbol{r}_i\}$. This leads to the following coupled-channels equations,

$$\left(\frac{d}{dr} - \frac{\kappa-1}{r}\right) g_k(r) + (E_{nI} - E_J)f_k(r) + \sum_{k'} U_T^{kk'}(r)g_{k'}(r) + \sum_{k'}\Big[U_V^{kk'}(r) + U_S^{kk'}(r)\Big] f_{k'}(r) = 0, \tag{4.28a}$$

$$\left(\frac{d}{dr} + \frac{\kappa+1}{r}\right) f_k(r) - (E_{nI} - 2m_\Lambda - E_J)g_k(r) - \sum_{k'} U_T^{kk'}(r)f_{k'}(r) - \sum_{k'}\Big[U_V^{kk'}(r) - U_S^{kk'}(r)\Big] g_{k'}(r) = 0, \tag{4.28b}$$

where κ is defined as $\kappa = (-1)^{j+\ell+1/2}(j+1/2)$. In these coupled-channel equations, the coupling potentials between different channels are given by

$$U_{\rm S}^{kk'}(r) \equiv \langle\mathscr{F}_{jlnI}^{JM}|\sum_{i=1}^{A_c}\hat{V}_{\rm S}^{N\Lambda}(\boldsymbol{r},\boldsymbol{r}_i)|\mathscr{F}_{j'l'n'I'}^{JM}\rangle, \tag{4.29a}$$

$$U_{\rm V}^{kk'}(r) \equiv \langle\mathscr{F}_{jlnI}^{JM}|\sum_{i=1}^{A_c}\hat{V}_{\rm V}^{N\Lambda}(\boldsymbol{r},\boldsymbol{r}_i)|\mathscr{F}_{j'l'n'I'}^{JM}\rangle, \tag{4.29b}$$

$$U_T^{kk'}(r) \equiv \langle\mathscr{F}_{jlnI}^{JM}|\sum_{i=1}^{A_c}\hat{V}_{\rm T}^{N\Lambda}(\boldsymbol{r},\boldsymbol{r}_i)\cdot\boldsymbol{\sigma}|\mathscr{F}_{j'\tilde{l}'n'I'}^{JM}\rangle. \tag{4.29c}$$

In order to solve the equations, the large $f_k(r)$ and small $g_k(r)$ components of the Dirac spinors, Eq.(4.16), are expanded in terms of the radial function $R_{\alpha l}(r)$ of a spherical harmonic

oscillator, that is,

$$f_k(r) = \sum_{\alpha=1}^{f_{max}^{(k)}} F_{k\alpha} R_{\alpha l}^k(r), \tag{4.30a}$$

$$g_k(r) = \sum_{\alpha=1}^{g_{max}^{(k)}} G_{k\alpha} R_{\alpha \tilde{l}}^k(r). \tag{4.30b}$$

The orbital angular momenta l and $\tilde{l}$ are determined by angular momenta j and the parity π as

$$l = j + \frac{1}{2}, \qquad \tilde{l} = j - \frac{1}{2} \qquad \text{for} \qquad \pi = (-)^{j+1/2} \tag{4.31a}$$

$$l = j - \frac{1}{2}, \qquad \tilde{l} = j + \frac{1}{2} \qquad \text{for} \qquad \pi = (-)^{j-1/2}. \tag{4.31b}$$

The coupled-channels equations (4.28a), (4.28b) are then transformed into a real symmetric matrix equation,

$$\sum_{\alpha',k'} \begin{pmatrix} A_{\alpha\alpha'}^{kk'} + V_{\alpha\alpha'}^{kk'} + S_{\alpha\alpha'}^{kk'} & B_{\alpha\alpha'}^{kk'} + T_{\alpha\alpha'}^{kk'} \\ B_{\alpha\alpha'}^{kk'} + T_{\alpha\alpha'}^{kk'} & C_{\alpha\alpha'}^{kk'} + V_{\alpha\alpha'}^{kk'} - S_{\alpha\alpha'}^{kk'} \end{pmatrix} \begin{pmatrix} F_{\alpha'}^{k'} \\ G_{\alpha'}^{k'} \end{pmatrix} = E_J \begin{pmatrix} F_{\alpha}^{k} \\ G_{\alpha}^{k} \end{pmatrix}. \tag{4.32}$$

The dimension of the matrix is $\sum_k f_{max}^{(k)} + g_{max}^{(k)}$, where k represents different channels. With the multipole expansion for the δ function in the coordinate space

$$\delta(\boldsymbol{r} - \boldsymbol{r}_i) = \frac{\delta(r - r_i)}{r r_i} \sum_{\lambda,\mu} Y_{\lambda\mu}(\hat{\boldsymbol{r}}) Y_{\lambda\mu}^*(\hat{\boldsymbol{r}_i}), \tag{4.33}$$

the matrix elements in Eq. (4.32) are given by

$$A_{\alpha\alpha'}^{kk'} = \langle R_{\alpha l}^k(r) | E_{nI} | R_{\alpha' l'}^{k'}(r) \rangle \delta_{k,k'} \tag{4.34a}$$

$$B_{\alpha\alpha'}^{kk'} = \langle R_{\alpha l}^k(r) | \frac{d}{dr} - \frac{\kappa - 1}{r} | R_{\alpha' \tilde{l}'}^{k'}(r) \rangle \delta_{k,k'} \tag{4.34b}$$

$$C_{\alpha\alpha'}^{kk'} = \langle R_{\alpha \tilde{l}}^k(r) | (E_{nI} - 2m_\Lambda) | R_{\alpha' \tilde{l}'}^{k'}(r) \rangle \delta_{k,k'} \tag{4.34c}$$

$$\begin{aligned} V_{\alpha\alpha'}^{kk'} =& \langle R_{\alpha l}^k(r) | U_V^{kk'}(r) | R_{\alpha' l'}^{k'}(r) \rangle \\ =& (-1)^{j'+I+J} \sum_\lambda \begin{Bmatrix} J & I & j \\ \lambda & j' & I' \end{Bmatrix} \langle j\ell || Y_\lambda || j'\ell' \rangle \int r^2 dr \varrho_{\lambda,V}^{nIn'I'}(r) \\ & \times \left\{ \alpha_V^{N\Lambda} R_{\alpha l}^k(r) R_{\alpha' l'}^{k'}(r) + \delta_V^{N\Lambda} \left[\frac{1}{r^2} \frac{d}{dr} (r^2 \frac{d}{dr}) - \frac{\lambda(\lambda+1)}{r^2} \right] \left[R_{\alpha l}^k(r) R_{\alpha' l'}^{k'}(r) \right] \right\} \end{aligned} \tag{4.34d}$$

$$\begin{aligned} S_{\alpha\alpha'}^{kk'} =& \langle R_{\alpha l}^k(r) | U_S^{kk'}(r) | R_{\alpha' l'}^{k'}(r) \rangle \\ =& (-1)^{j'+I+J} \sum_\lambda \begin{Bmatrix} J & I & j \\ \lambda & j' & I' \end{Bmatrix} \langle j\ell || Y_\lambda || j'\ell' \rangle \int r^2 dr \varrho_{\lambda,S}^{nIn'I'}(r) \\ & \times \left\{ \alpha_S^{N\Lambda} R_{\alpha l}^k(r) R_{\alpha' l'}^{k'}(r) + \delta_S^{N\Lambda} \left[\frac{1}{r^2} \frac{d}{dr} (r^2 \frac{d}{dr}) - \frac{\lambda(\lambda+1)}{r^2} \right] \left[R_{\alpha l}^k(r) R_{\alpha' l'}^{k'}(r) \right] \right\} \end{aligned} \tag{4.34e}$$

and

$$\begin{aligned}
T^{kk'}_{\alpha\alpha'} =& \langle R^{k}_{\alpha l}(r)|U^{kk'}_{T}(r)|R^{k'}_{\alpha'\tilde{l}'}(r)\rangle \\
=& -\alpha_T^{N\Lambda}(-1)^{j+I'+J}\sum_{\lambda}\begin{Bmatrix} J & I & j \\ \lambda & j' & I' \end{Bmatrix}\int r^2 dr\, \varrho^{nIn'I'}_{\lambda,V}(r) \\
&\times\Big\{\Big[\frac{dR^{k}_{\alpha l}(r)}{dr}+\frac{\kappa+1}{r}R^{k}_{\alpha l}(r)\Big]R^{k'}_{\alpha'\tilde{l}'}(r)\langle j\tilde{\ell}||Y_\lambda||j'\tilde{\ell}'\rangle \\
&+\Big[\frac{dR^{k'}_{\alpha'\tilde{l}'}(r)}{dr}-\frac{\kappa'-1}{r}R^{k'}_{\alpha'\tilde{l}'}(r)\Big]R^{k}_{\alpha l}(r)\langle j\ell||Y_\lambda||j'\ell'\rangle\Big\}. \qquad (4.35)
\end{aligned}$$

See Appendices E.1 and E.2 for the derivation of the matrix elements of the vector derivative coupling term and the tensor coupling term of Eqs. (4.34d) and (4.35), respectively.

The reduced vector $\varrho^{nIn'I'}_{\lambda,V}(r)$ and scalar $\varrho^{nIn'I'}_{\lambda,S}(r)$ transition densities between the nuclear state $|\Phi_{n'I'}\rangle$ and the state $|\Phi_{nI}\rangle$ of the core are defined as

$$\varrho^{nIn'I'}_{\lambda,V}(r) = \langle nI||\sum_{i=1}^{A_c}\frac{\delta(r-r_i)}{r_i r}Y_\lambda(\hat{\boldsymbol{r}}_i)||n'I'\rangle, \qquad (4.36a)$$

$$\varrho^{nIn'I'}_{\lambda,S}(r) = \langle nI||\sum_{i=1}^{A_c}\gamma_i^0\frac{\delta(r-r_i)}{r_i r}Y_\lambda(\hat{\boldsymbol{r}}_i)||n'I'\rangle, \qquad (4.36b)$$

which are related to the transition densities $\rho^{nIn'I'}_{\lambda,V}(r)$ and $\rho^{nIn'I'}_{\lambda,S}(r)$ defined in section (2.3.2) by

$$\varrho^{nIn'I'}_{\lambda,V}(r) = \hat{I}_i\rho^{nIn'I'}_{\lambda,V}(r), \qquad \varrho^{nIn'I'}_{\lambda,S}(r) = \hat{I}_i\rho^{nIn'I'}_{\lambda,S}(r). \qquad (4.37)$$

A simple approximation to MPRM is to restrict the Λ-hyperon to a specific orbit (l,j) coupled to a single core state (n,I), which means that $k=\{jlnI\}$ has a definite value and so we call it a single-channel calculation. In this case, the summation in Eq.(4.13) is absent, and the coupled-channels equations Eqs. (4.28a) and (4.28b) become

$$\left(\frac{d}{dr}-\frac{\kappa-1}{r}\right)g_k(r)+U^{kk}_T(r)g_k(r)+(E_{nI}-E_J)f_k(r)+\Big[U^{kk}_V(r)+U^{kk}_S(r)\Big]f_k(r)=0, \qquad (4.38)$$

$$\left(\frac{d}{dr}+\frac{\kappa+1}{r}\right)f_k(r)-U^{kk}_T(r)g_k(r)-(E_{nI}-2m_\Lambda-E_J)g_k(r)-\Big[U^{kk}_V(r)-U^{kk}_S(r)\Big]g_k(r)=0. \qquad (4.39)$$

In the single-channel calculation, only the diagonal couplings are present. The matrix equation (4.32) then becomes

$$\sum_{\alpha'}\begin{pmatrix} A^{kk}_{\alpha\alpha'}+V^{kk}_{\alpha\alpha'}+S^{kk}_{\alpha\alpha'} & B^{kk}_{\alpha\alpha'}+T^{kk}_{\alpha\alpha'} \\ B^{kk}_{\alpha\alpha'}+T^{kk}_{\alpha\alpha'} & C^{kk}_{\alpha\alpha'}+V^{kk}_{\alpha\alpha'}-S^{kk}_{\alpha\alpha'}\end{pmatrix}\begin{pmatrix} F^k_{\alpha'} \\ G^k_{\alpha'}\end{pmatrix}=E_J\begin{pmatrix} F^k_{\alpha} \\ G^k_{\alpha}\end{pmatrix}. \qquad (4.40)$$

4.2.2 Electric quadrupole transition strengths between hypernuclear states

The electric quadrupole ($E2$) transition strength from an initial state $|J_i\rangle$ to a final state $|J_f\rangle$ in Λ hypernuclei is given by

$$B(E2; J_i \to J_f) = \frac{1}{2J_i+1} \left| \langle J_f || \hat{Q}_2 || J_i \rangle \right|^2, \tag{4.41}$$

where $\hat{Q}_{2\mu} = e \sum_{i \in p} r_i^2 Y_{2\mu}(\hat{r}_i)$ is the $E2$ operator. Notice that we use the bare charge in evaluating the $B(E2)$ strengths, that is, $+e$ for protons and 0 for neutrons and a Λ particle, since our microscopic calculations are in the full configuration space. Substituting the wave function for the hypernuclear states Eq.(4.13) to this equation, one finds the reduced matrix element to be

$$\begin{aligned}
\langle J_f || \hat{Q}_2 || J_i \rangle =& \langle \sum_{k_f} \mathscr{R}_{k_f}(r) [\mathcal{Y}_{j_f l_f}(\hat{\boldsymbol{r}}) \otimes \Phi_{n_f I_f}(\{\boldsymbol{r}_i\})]^{J_f} || \hat{Q}_2 || \sum_{k_i} \mathscr{R}_{k_i}(r) [\mathcal{Y}_{j_i l_i}(\hat{\boldsymbol{r}}) \otimes \Phi_{n_i I_i}(\{\boldsymbol{r}_i\})]^{J_i} \rangle \\
=& \sum_{k_i, k_f} \int dr r^2 \mathscr{R}^\dagger_{k_f}(r) \mathscr{R}_{k_i}(r) \langle [\mathcal{Y}_{j_f l_f}(\hat{\boldsymbol{r}}) \otimes \Phi_{n_f I_f}(\{\boldsymbol{r}_i\})]^{J_f} || \hat{Q}_2 || [\mathcal{Y}_{j_i l_i}(\hat{\boldsymbol{r}}) \otimes \Phi_{n_i I_i}(\{\boldsymbol{r}_i\})]^{J_i} \rangle.
\end{aligned}$$

With the relation of (see Eq. (7.1.8) in Ref. [87])

$$\langle \gamma' j_1' j_2 J' || T(k) || \gamma j_1 j_2 J \rangle = (-1)^{(j_1'+j_2+J+k)} [(2J+1)(2J'+1)]^{1/2} \langle \gamma' j_1' || T(k) || \gamma j_1 \rangle \begin{Bmatrix} j_1' & J' & j_2 \\ J & j_1 & k \end{Bmatrix},$$

we have

$$\begin{aligned}
&\langle [\mathcal{Y}_{j_f l_f}(\hat{\boldsymbol{r}}) \otimes \Phi_{n_f I_f}(\{\boldsymbol{r}_i\})]^{J_f} || \hat{Q}_2 || [\mathcal{Y}_{j_i l_i}(\hat{\boldsymbol{r}}) \otimes \Phi_{n_i I_i}(\{\boldsymbol{r}_i\})]^{J_i} \rangle \\
&= \delta_{j_f j_i} \delta_{\ell_f \ell_i} (-1)^{I_f + j_i + J_i} \hat{J}_i \hat{J}_f \begin{Bmatrix} I_f & J_f & j_i \\ J_i & I_i & 2 \end{Bmatrix} \langle n_f I_f || \hat{Q}_2 || n_i I_i \rangle.
\end{aligned} \tag{4.42}$$

Here, $\langle n_f I_f || \hat{Q}_2 || n_i I_i \rangle$ is the reduced $E2$ transition matrix element between the nuclear core states $|I_f, n_f\rangle$ and $|I_i, n_i\rangle$, which has been given by Eq. (2.68) with $\lambda = 2$. Then the $E2$ transition strengths in hypernucleus can be rewritten as

$$B(E2; J_i \to J_f) = \hat{J_f}^2 \left| \sum_{k_i, k_f} \langle \mathscr{R}_{k_f}(r) | \mathscr{R}_{k_i}(r) \rangle \delta_{j_f j_i} \delta_{\ell_f \ell_i} \begin{Bmatrix} I_f & J_f & j_i \\ J_i & I_i & 2 \end{Bmatrix} \langle n_f I_f || \hat{Q}_2 || n_i I_i \rangle \right|^2. \tag{4.43}$$

4.2.3 Charge radius of hypernuclei

According to the definition of hypernuclear wave function (see Eqs.(4.13) and (4.14)),

$$\Psi_{JM}(\boldsymbol{r}, \{\boldsymbol{r}_i\}) = \sum_{n,j,\ell,I} \sum_{m M_I} \langle j m I M_I | J M \rangle \mathscr{R}_{jlnI}(r) \mathscr{Y}_{j\ell m}(\hat{\boldsymbol{r}}) \Phi_{nIM_I}(\{\boldsymbol{r}_i\}) \tag{4.44}$$

the proton radius of hypernuclei can be calculated as

$$\langle r_p^2\rangle_J = \sum_{n,j,\ell,I}\sum_{mM_I}\langle jmIM_I|JM\rangle^2\langle\mathscr{R}_{jlnI}(r)\mathscr{Y}_{j\ell m}(\hat{\boldsymbol{r}})|\mathscr{R}_{jlnI}(r)\mathscr{Y}_{j\ell m}(\hat{\boldsymbol{r}})\rangle\langle r_p^2\rangle_{nI}, \tag{4.45}$$

where $\langle r_p^2\rangle_{nI}$ is the proton radius of nI state for the core nucleus given by Eq.(2.65). With the relation of $\sum_{m_1m_2}\langle j_1m_1j_2m_2|JM\rangle^2 = 1$, we have

$$\langle r_p^2\rangle_J = \sum_{n,j,\ell,I} P_{j\ell I_n}\langle r_p^2\rangle_{nI}. \tag{4.46}$$

Then the charge radius of hypernuclear state with angular momenta J reads

$$\langle r_{\rm ch}^2\rangle_J^{1/2} = \sqrt{\langle r_p^2\rangle_J + 0.64(\mathrm{fm}^2)}. \tag{4.47}$$

Chapter 5

Low-lying spectrum of Λ hypernuclei

Let us now apply the microscopic particle-rotor model (MPRM) systematically to study the low-lying spectra of single-Λ hypernuclei from light to heavy mass region, which include ${}^{13}_{\Lambda}$C, ${}^{9}_{\Lambda}$Be, ${}^{21}_{\Lambda}$Ne, ${}^{31}_{\Lambda}$Si and hypernuclei of Sm isotopes. To this end, we will first outline the procedure of the MPRM calculations.

5.1 Calculation procedure

The MPRM calculations are composed of the following four steps:

(i) **Self-consistent deformation constrained RMF+BCS calculation for an even-even core nucleus:**

In this step, a set of deformed mean-field states $|\varphi(\beta)\rangle$ with different quadrupole deformation β is generated (see section(2.1.8)). The Dirac spinor for each nucleon state is expanded on the harmonic oscillator (HO) basis with $N_{\rm sh} = 10$ major shells for ^{8}Be, ^{12}C ,^{20}Ne and ^{30}Si, and with $N_{\rm sh} = 12$ for Sm isotopes. The oscillator length parameter in the HO is chosen as $b_x = b_y = b_z = \sqrt{\hbar/m\omega_0}$, where m is the nucleon mass and the oscillator frequency is determined as $\hbar\omega_0 = 41A_c^{-1/3}$ MeV. We adopt the non-linear point-coupling EDF with the PC-F1 set for the effective nucleon-nucleon interaction. In order to study the parameter set dependence, we also use the PC-PK1 set for ^{20}Ne and ^{30}Si. A density independent δ force supplemented with an energy-dependent cutoff is used in the pairing channel for the nucleons. Axial symmetry and time-reversal invariance are imposed in the mean-field calculations.

(ii) **MR-CDFT calculation for low-lying states of the nuclear core:**

The wave functions Φ_{nI} and the energy E_{nI} for the core state I_n as well as the transition density between the states $|nI\rangle$ and $|n'I'\rangle$ are obtained in this step (see section (2.2) and (2.3)).

(ii-1) **Angular momentum and particle number projections**

The mean-field wave functions $|\varphi(\beta)\rangle$ are projected onto a state with the proton number Z and neutron number N as well as the angular momentum I. For the ^{8}Be and ^{12}C nuclei, the number of mesh points for Euler angle θ is chosen to be 14 in the interval $[0, \pi]$, and the number of gauge angle φ for the particle number projection is chosen to be 7. For ^{20}Ne and ^{30}Si as well as

Sm isotopes, we enlarge the mesh points and use 16 and 9 for the angular momentum and the particle number projections, respectively.

(ii-2) **GCM calculation**

Configuration mixing calculations with projected mean-field states is performed in this step to take into account the fluctuation effect of collective coordinates. By solving the HWG equation, Eq.(2.56), we obtain the energy and wave function of the core state I_n. With the wave functions of nuclear core states so obtained, the transition densities, which are used to determine the coupling potentials in the coupled-channels equations, are calculated according to Eq.(2.61).

(iii) **Coupled-channels calculation for low-lying states of Λ hypernuclei:**

With the coupling potentials so obtained, the coupled-channels equations, Eq.(4.28), are solved by expanding the radial part of the hypernuclear wave function $\mathscr{R}_{j\ell nI}(r)$ on the spherical harmonic oscillator basis with 18 major shells. The cutoff of the core states $n_{\rm cut}$ and of the core angular momentum $I_{\rm cut}$ are chosen as $n_{\rm cut} = 1$ and $I_{\rm cut} = 4$ for ^{8}Be, $n_{\rm cut} = 2$ and $I_{\rm cut} = 4$ for ^{12}C, $n_{\rm cut} = 2$ and $I_{\rm cut} = 6$ for ^{20}Ne and ^{30}Si, $n_{\rm cut} = 3$ and $I_{\rm cut} = 8$ for Sm isotopes. From the solutions of the coupled-channels equations, we construct the spectrum of hypernucleus and calculate the $B(E2)$ transition strengths between the hypernuclear states.

(iv) **Projected energy curves for hypernuclei:**

The potential energy curve for hypernuclei can be also calculated with a similar procedure by ignoring the configuration mixing in the core states, that is, by using the projected MF states rather than GCM states.

The inter-relation among each step is illustrated in Fig. 5.1.

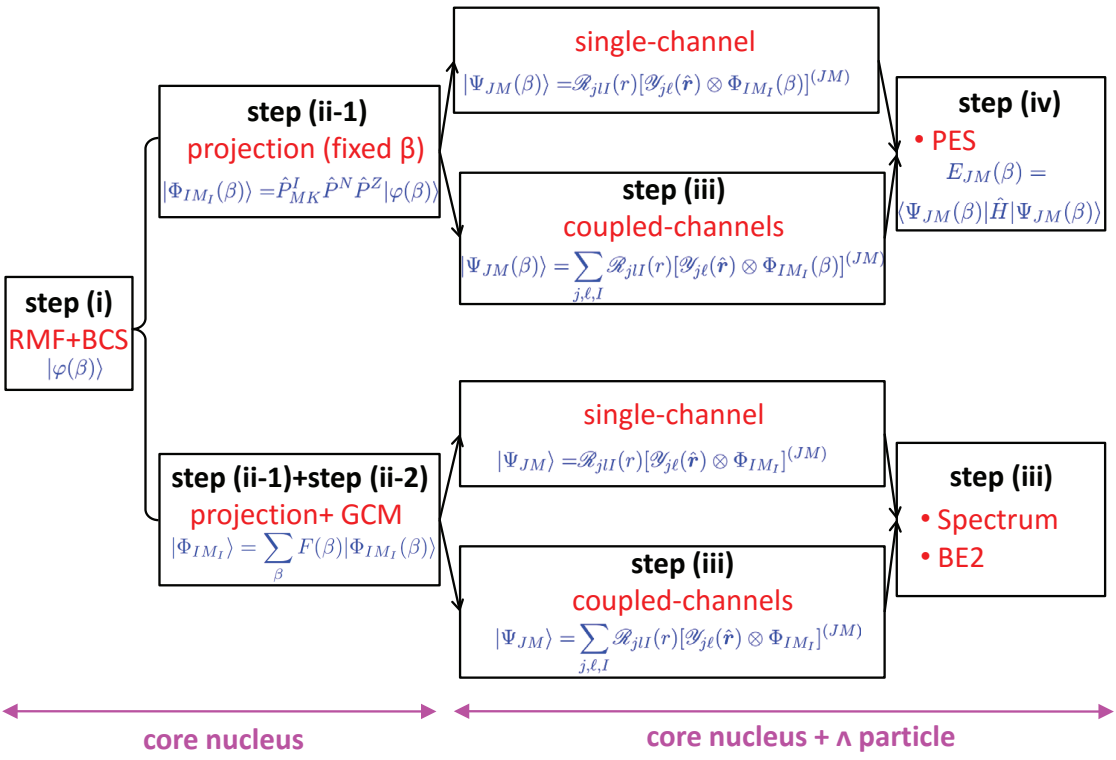

Fig. 5.1 Calculation procedures for microscopic particle-rotor model.

5.2 Illustrative calculations for ${}^{13}_{\Lambda}$C

In this section, we will take ${}^{13}_{\Lambda}$C as an example to give an illustrative calculation for MPRM. The low-lying states of the nuclear core ^{12}C and the transition densities between the core states have been discussed in section 2.3. We couple the Λ hyperon to those core states to carry out the MPRM calculations. To this end, we use the PCY-S4 parameter set for the $N\Lambda$ interaction.

5.2.1 Projected potential energy surface of ${}^{13}_{\Lambda}$C

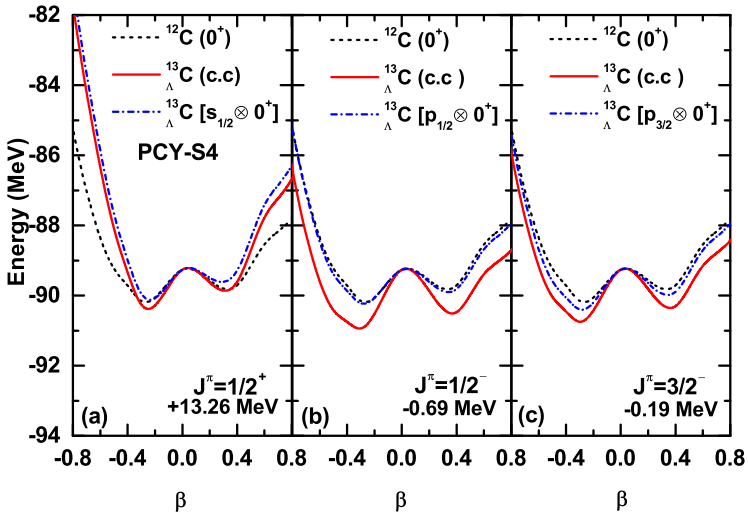

Fig. 5.2 The potential energy surfaces of hypernucleus ${}^{13}_{\Lambda}$C obtained with the single-channel calculation (the dot-dashed lines) and the coupled-channel (c.c) calculation (the solid lines) with spin-parity of (a) $J^\pi = 1/2^+$, (b) $J^\pi = 1/2^-$ and (c) $J^\pi = 3/2^-$ as a function of intrinsic deformation β. For comparison, the energy surface for the nuclear core ^{12}C with spin-parity of $I^\pi = 0^+$ (the dashed lines) is also shown. The energy surfaces for ${}^{13}_{\Lambda}$C hypernuclei are shifted by a constant amount as indicated in each panel.

As the first step (step (i) and (ii-1) in section (5.1)), we construct the wave function of the nuclear core state as the projected mean-field state with the intrinsic deformation β as follow:

$$|\Phi_{IM_I}(\beta)\rangle = \hat{P}^I_{M_I K}\hat{P}^N\hat{P}^Z|\varphi(\beta)\rangle, \tag{5.1}$$

where $P^I_{M_I K}$ and $\hat{P}^N(Z)$ are the angular momentum projector and the neutron (proton) number projector, respectively. The mean-field wave functions $|\varphi(\beta)\rangle$ with the intrinsic deformation β are determined by the deformation constrained RMF calculation. In order to draw the potential energy surface of ${}^{13}_{\Lambda}$C as a function of β, the wave function of Λ hypernuclei is then constructed as:

$$|\Psi_{JM}(\beta)\rangle = \sum_{j,\ell,I} \mathscr{R}_{jlI}(r;\beta)\mathscr{F}^{JM}_{jlI}(r;\{\hat{\boldsymbol{r}}_i\}) \tag{5.2}$$

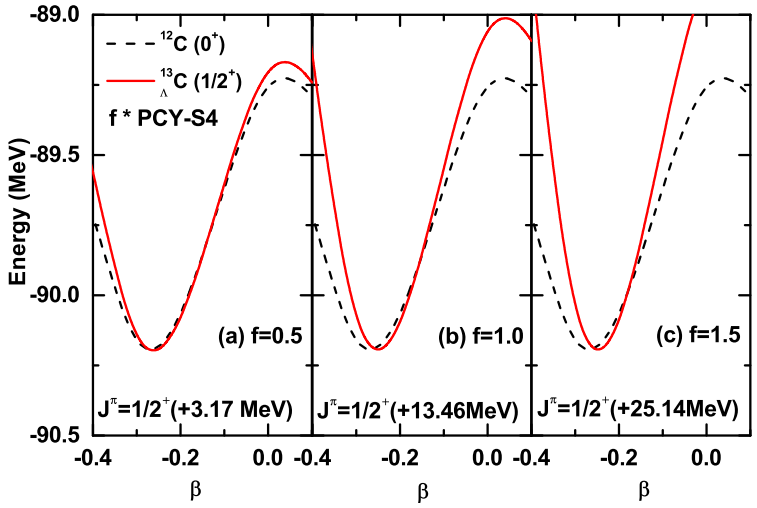

Fig. 5.3 The potential energy surfaces of hypernucleus ${}^{13}_{\Lambda}$C for $J^\pi = 1/2^+$ with the $N\Lambda$ interaction scaled by a factor f as shown in the figure.

with

$$\mathscr{F}^{JM}_{jlI}(r;\{\hat{\boldsymbol{r}}_i\}) = \sum_{mM_I} \langle jmIM_I|JM\rangle \mathscr{Y}_{j\ell m}(\hat{\boldsymbol{r}})\Phi_{IM_I}(\beta). \tag{5.3}$$

With this wave function, we obtain similar couple-channel equations as Eq.(4.28). Using the solutions of the coupled-channels equations, we can then compute the hypernuclear energy curve as $E_J(\beta) = \langle \Psi_{JM}(\beta)|\hat{H}|\Psi_{JM}(\beta)\rangle$.

Figure 5.2 shows the energy $E_J(\beta)$ for the $J^\pi = 1/2^+$, $1/2^-$ and $3/2^-$ states in ${}^{13}_{\Lambda}$C as a function of the intrinsic deformation β of the core nucleus ^{12}C. The potential energy curves obtained by solving the single-channel equations with only taking into account the ground state of the nuclear core 0^+_1 are also shown for comparison (the dot-dashed lines). One can see that the energy surfaces obtained with the single-channel calculation are systematically higher than that with the coupled-channel calculations due to the absence of configuration mixing.

The hypernuclear energy curve with spin-parity of $1/2^+$ has an oblate minimum with $\beta = -0.25$ (see the red curve in Fig.5.2(a)), which is significantly smaller than that of ^{12}C of 0^+ with $\beta = -0.27$, indicating a smaller collectivity in ${}^{13}_{\Lambda}$C. In order to illustrate this point in a more transparent way, the potential energy curves for $1/2^+$ with a scaled $N\Lambda$ interaction, i.e., the PCY-S4 force multiplied by a scaling factor f ($\hat{V}^{N\Lambda}$ in Eq.(3.6) $\rightarrow f \cdot \hat{V}^{N\Lambda}$) are shown in Fig. 5.3 with f =0.5 and 1.5. It is shown that the $N\Lambda$ coupling strength have an influence on the deformation of the energy minimum, i.e., the larger $N\Lambda$ coupling strength yield the smaller value of $|\beta|$ of the energy minimum and the higher barrier at the spherical shape, indicating the larger shrinkage effect.

For $J^\pi = 1/2^-$ and $J^\pi = 3/2^-$, the deformation at the oblate minimum is the same value for both the configurations, i.e., $\beta(1/2^-) = \beta(3/2^-) = -0.30$ (see Figs. 5.2(b) and 5.2(c)). Moreover, both the energy curves have a higher barrier at the spherical shape compared with that of the core nucleus for $I^\pi = 0^+$, from which one may expect a weaker shape mixing between the prolate and oblate configurations.

The main component of the $1/2^+$ $(1/2^-)$ hypernuclear state of ${}^{13}_{\Lambda}$C is the Λ particle in $s_{1/2}$ $(p_{1/2})$ orbit coupled to the ground state 0^+_1 of ^{12}C. This indicates that a Λ particle in the s (p) orbit decreases (increases) the collectivity of ^{12}C, which is consistent with the findings in Refs.[38, 46].

5.2.2 Single-channel calculations

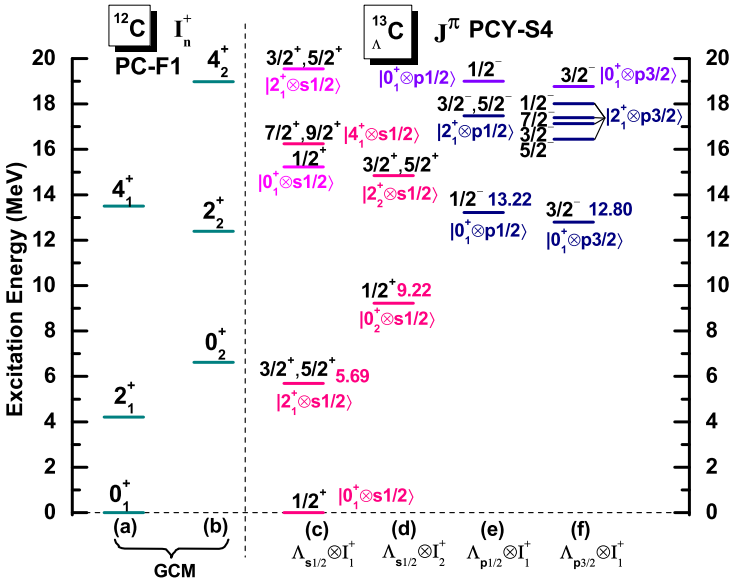

Fig. 5.4 Low-lying states for ${}^{13}_{\Lambda}$C obtained with the single-channel calculation by restricting the Λ particle in the $s_{1/2}$, $p_{1/2}$ and $p_{3/2}$ orbits are shown in the columns (c) and (d), (e) and (f), respectively. For comparison, the low-energy excitation spectrum of ^{12}C is are also plotted in the columns (a) and (b).

We next discuss the spectrum of ${}^{13}_{\Lambda}$C. Before we investigate the hypernuclear spectrum from the full coupled-channels calculations, let us first investigate the results of single-channel calculations. The columns (c) and (d) in Fig. 5.4 show the results for the Λ particle in the $s_{1/2}$ orbit, while the columns (e) and (f) show those in the $p_{1/2}$ and $p_{3/2}$ orbits, respectively. Here, the columns (c) and (d) correspond to the Λ particle in the $s_{1/2}$ orbit coupled to the ground band (the column (a)) and the first excitation band (the column (b)) of the core nucleus ^{12}C, respectively. The spectrum of ^{12}C shown in the columns (a) and (b) is same as the column (b) in Fig. 2.3.

According to the angular momentum coupling algebra, a Λ hyperon with angular momentum (l, j) coupled to the core state with angular momentum I^+ results in several hypernuclear states J^π with $|I - j| \leq J \leq I + j$. The parity of hypernuclear states are determined by the orbital angular momentum l of Λ hyperon to be $\pi = (-1)^\ell$. When the Λ particle is restricted to the $s_{1/2}$ orbit or $p_{1/2}$ orbit, doublet states with $J = (I \pm 1/2)$ are yielded, which are degenerate in energy for $I \neq 0$, as shown in Figs. 5.4(c), (d) and (e). For instance, when the Λ in $s_{1/2}$ and $p_{1/2}$ orbits are coupled to the nuclear core 2^+_1 state, the degenerate doublet states $(3/2^+, 5/2^+)$ and $(3/2^-, 5/2^-)$ are generated, respectively. The case of $[\Lambda_{p3/2} \otimes I^+]$ is more complex. For instance, the $[\Lambda_{p3/2} \otimes 2^+]$ configuration yields multiplet states of $1/2^-, 3/2^-, 5/2^-$ and $7/2^-$.

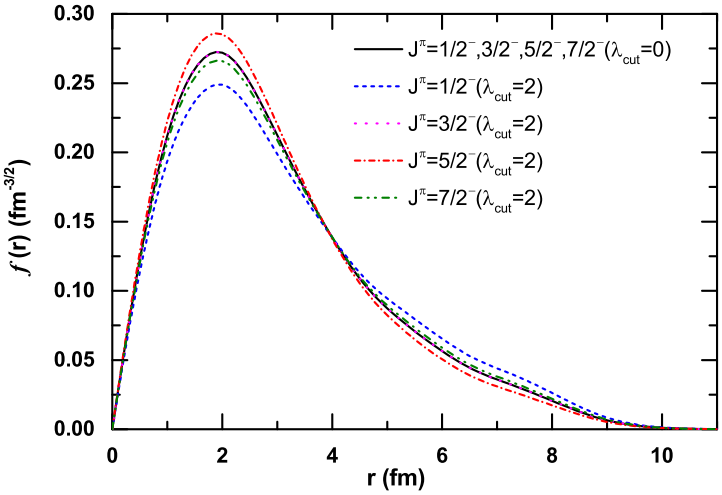

Fig. 5.5 The large component of the radial wave function $\mathscr{R}_{j\ell nI}(r)$ for the $[\Lambda_{p3/2}\otimes 2^+]^{(J)}$ configurations as a function of r.

These multiplet states are ordered in energy according to the properties of the coupling potential in Eq.(4.29), determined by the reduced transition densities $\rho^{nIn'I'}_{\lambda,S}(r)$ and $\rho^{nIn'I'}_{\lambda,V}(r)$. In order to understand this, we perform the single-channel calculation for the cutoff of $\lambda_{\rm cut}=0$ and $\lambda_{\rm cut}=2$ in the multipole expansion in Eq. (4.33) for a δ function in the $N\Lambda$ interaction. The results are given in Table 5.1.

For the cutoff of $\lambda_{\rm cut}=0$, the $1/2^-, 3/2^-, 5/2^-$ and $7/2^-$ states are degenerate in energy at -85.891 MeV and have same wave functions (see the black solid line in Fig. 5.5). Table 5.1 also list the expectation value of $(\hat{V}^{N\Lambda}_{\rm V}+\hat{V}^{N\Lambda}_{\rm S})$ with respect to state Ψ_{JM}

$$
\begin{aligned}
\langle\hat{V}^{N\Lambda}_m\rangle_{J^\pi} =&\langle\mathscr{R}_k(r)\mathscr{F}^{JM}_k(\hat{\boldsymbol{r}},\{\boldsymbol{r}_i\})|\hat{V}^{N\Lambda}_m|\mathscr{R}_k(r)\mathscr{F}^{JM}_k(\hat{\boldsymbol{r}},\{\boldsymbol{r}_i\})\rangle\\
=&\sum_\alpha F^2_{k\alpha}(-1)^{j+I+J}\sum_{\lambda=0}^{\lambda_{\rm cut}}\begin{Bmatrix}J & I & j\\ \lambda & j & I\end{Bmatrix}\langle j\ell||Y_\lambda||j\ell\rangle\int r^2dr\varrho^{nInI}_{\lambda,m}(r)\\
&\times\left\{\alpha^{N\Lambda}_m R^k_{\alpha l}(r)R^k_{\alpha l}(r)+\delta^{N\Lambda}_m\left[\frac{1}{r^2}\frac{d}{dr}(r^2\frac{d}{dr})-\frac{\lambda(\lambda+1)}{r^2}\right]\left[R^k_{\alpha l}(r)R^k_{\alpha l}(r)\right]\right\}\\
&+\sum_\alpha G^2_{k\alpha}(-1)^{j+I+J}\sum_{\lambda=0}^{\lambda_{\rm cut}}\begin{Bmatrix}J & I & j\\ \lambda & j & I\end{Bmatrix}\langle j\tilde{\ell}||Y_\lambda||j\tilde{\ell}\rangle\int r^2dr\varrho^{nInI}_{\lambda,m}(r)\\
&\times\left\{\alpha^{N\Lambda}_m R^k_{\alpha\tilde{\ell}}(r)R^k_{\alpha\tilde{\ell}}(r)+\delta^{N\Lambda}_m\left[\frac{1}{r^2}\frac{d}{dr}(r^2\frac{d}{dr})-\frac{\lambda(\lambda+1)}{r^2}\right]\left[R^k_{\alpha\tilde{\ell}}(r)R^k_{\alpha\tilde{\ell}}(r)\right]\right\}\\
\equiv&\sum_{\lambda=0}^{\lambda_{\rm cut}}\langle\hat{V}^{N\Lambda}_m\rangle_\lambda
\end{aligned}
\tag{5.4}
$$

with the index m representing either S or V. Notice that $\langle\hat{V}^{N\Lambda}_m\rangle_{\lambda=0}$ for $\lambda_{\rm cut}=2$ is different from $\langle\hat{V}^{N\Lambda}_m\rangle_{\lambda=0}$ for $\lambda_{\rm cut}=0$ because the wave function $\mathscr{R}_k(r)$ is different due to a different value of $\lambda_{\rm cut}$ (see the color lines in Fig. 5.5).

Table 5.1 The total energy and the expectation value of $(\hat{V}_V^{N\Lambda} + \hat{V}_S^{N\Lambda})$ for the $[\Lambda_{p3/2} \otimes 2^+]^{(J)}$ configurations.

	$\lambda_{\rm cut} = 0$		$\lambda_{\rm cut} = 2$			
J^π	E	$\langle \hat{V}_V^{N\Lambda} + \hat{V}_S^{N\Lambda} \rangle$	E	$\langle \hat{V}_V^{N\Lambda} + \hat{V}_S^{N\Lambda} \rangle_{\lambda=0}$	$\langle \hat{V}_V^{N\Lambda} + \hat{V}_S^{N\Lambda} \rangle_{\lambda=2}$	$\langle \hat{V}_V^{N\Lambda} + \hat{V}_S^{N\Lambda} \rangle$
$1/2^-$	-85.891	-14.248	-85.014	-13.682	1.231	-12.451
$3/2^-$	-85.891	-14.248	-85.891	-14.248	0.000	-14.248
$5/2^-$	-85.891	-14.248	-86.577	-14.556	-0.949	-15.505
$7/2^-$	-85.891	-14.248	-85.630	-14.103	0.365	-13.738

The expectation value $\langle \hat{V}_m^{N\Lambda} \rangle_{J^\pi}$ is mainly determined by the coefficient

$$(-1)^{j+I+J} \sum_{\lambda=0}^{\lambda_{\rm cut}} \langle j\ell || Y_\lambda || j\ell \rangle \begin{Bmatrix} J & I & j \\ \lambda & j & I \end{Bmatrix} \equiv C_{0\lambda} \sum_{\lambda=0}^{\lambda_{\rm cut}} C_{1\lambda} C_{2\lambda}, \tag{5.5}$$

where $C_{n\lambda}$ with $n = 0, 1, 2$ are defined as,

$$C_{0\lambda} \equiv (-1)^{j+I+J} \equiv C_0, \tag{5.6a}$$

$$C_{1\lambda} \equiv \langle j\ell || Y_\lambda || j\ell \rangle = \frac{(-1)^{j+1/2}}{\sqrt{4\pi}} \hat{j}^2 \hat{\lambda} \begin{pmatrix} j & \lambda & j \\ 1/2 & 0 & -1/2 \end{pmatrix} \delta_{\lambda,even}, \tag{5.6b}$$

$$C_{2\lambda} \equiv \begin{Bmatrix} J & I & j \\ \lambda & j & I \end{Bmatrix}. \tag{5.6c}$$

The values of each coefficients $C_{n\lambda}$ for the $[\Lambda_{p3/2} \otimes 2^+]^{(J)}$ configurations are list in Table 5.2. For $\lambda = 0$, the products of the coefficients, $C_0 C_{10} C_{20}$, are the same for the multiplet states of $1/2^-, 3/2^-, 5/2^-$ and $7/2^-$, which leads to the same expectation value of $\langle \hat{V}_V^{N\Lambda} + \hat{V}_S^{N\Lambda} \rangle_{J^\pi} = -14.248$ MeV (see Table 5.1).

For the cutoff of $\lambda_{\rm cut} = 2$, these multiplets are split and ordered as $5/2^-, 3/2^-, 7/2^-, 1/2^-$ (see Table 5.1). The origin for the splitting of these multiplets is the nonzero $\lambda = 2$ term in the matrix elements and the order of $J^\pi = 1/2^-, 3/2^-, 5/2^-, 7/2^-$ is determined by the transition density $\rho_2^{22}(r)$ and the coefficient C as well as the coupling parameters. One can see that the value of the coefficient $C = C_0 C_{1\lambda} C_{2\lambda}$ for $\lambda = 2$ is the largest for $J = 5/2^-$, and it decreases in the order of $J = 3/2^-, 7/2^-$, and $1/2^-$. Since the product of the other factors is negative, the contribution of these factors results in the value of $\langle \hat{V}_V^{N\Lambda} + \hat{V}_S^{N\Lambda} \rangle_{J^\pi}$ for $\lambda = 2$ increasing in the order of $J = 5/2^-, 3/2^-, 7/2^-$, and $1/2^-$, which is in the same order as the spectrum (see the column (f) in Fig.5.4).

For the configuration $[\Lambda_{p1/2} \otimes 2_1^+]$, the generated doublet states $3/2^-$ and $5/2^-$ are degenerate in energy at -85.55 MeV, since the coefficient $C = C_0 C_{1\lambda} C_{2\lambda}$ is not zero only for $\lambda = 0$, having the same value of $1/\sqrt{20\pi}$ for both the two states (see Table 5.2).

Table 5.2 The coefficients defined in Eq.(5.6) for the $[\Lambda_{lj} \otimes 2^+]^{(J)}$ configurations.

$[\Lambda_{lj} \otimes 2^+]$	J^π	C_0	C_{10}	C_{20}	$C_0C_{10}C_{20}$	C_{12}	C_{22}	$C_0C_{12}C_{22}$
$[\Lambda_{p3/2} \otimes 2^+]$	$1/2^-$	1.00	$\frac{1}{\sqrt{\pi}}$	$\frac{1}{\sqrt{20}}$	$\frac{1}{\sqrt{20\pi}}$	$-\frac{1}{\sqrt{\pi}}$	$\frac{\sqrt{14}}{20}$	$-\frac{\sqrt{14/\pi}}{20}$
$[\Lambda_{p3/2} \otimes 2^+]$	$3/2^-$	-1.00	$\frac{1}{\sqrt{\pi}}$	$-\frac{1}{\sqrt{20}}$	$\frac{1}{\sqrt{20\pi}}$	$-\frac{1}{\sqrt{\pi}}$	0.00	0.00
$[\Lambda_{p3/2} \otimes 2^+]$	$5/2^-$	1.00	$\frac{1}{\sqrt{\pi}}$	$\frac{1}{\sqrt{20}}$	$\frac{1}{\sqrt{20\pi}}$	$-\frac{1}{\sqrt{\pi}}$	$-\frac{\sqrt{14}}{28}$	$\frac{\sqrt{14/\pi}}{28}$
$[\Lambda_{p3/2} \otimes 2^+]$	$7/2^-$	-1.00	$\frac{1}{\sqrt{\pi}}$	$-\frac{1}{\sqrt{20}}$	$\frac{1}{\sqrt{20\pi}}$	$-\frac{1}{\sqrt{\pi}}$	$-\frac{\sqrt{14}}{70}$	$-\frac{\sqrt{14/\pi}}{70}$
$[\Lambda_{p1/2} \otimes 2^+]$	$3/2^-$	1.00	$\frac{1}{\sqrt{2\pi}}$	$\frac{1}{\sqrt{10}}$	$\frac{1}{\sqrt{20\pi}}$	0.00	0.00	0.00
$[\Lambda_{p1/2} \otimes 2^+]$	$5/2^-$	-1.00	$\frac{1}{\sqrt{2\pi}}$	$-\frac{1}{\sqrt{10}}$	$\frac{1}{\sqrt{20\pi}}$	0.00	0.00	0.00

5.2.3 Coupled-channels calculations

Convergence check

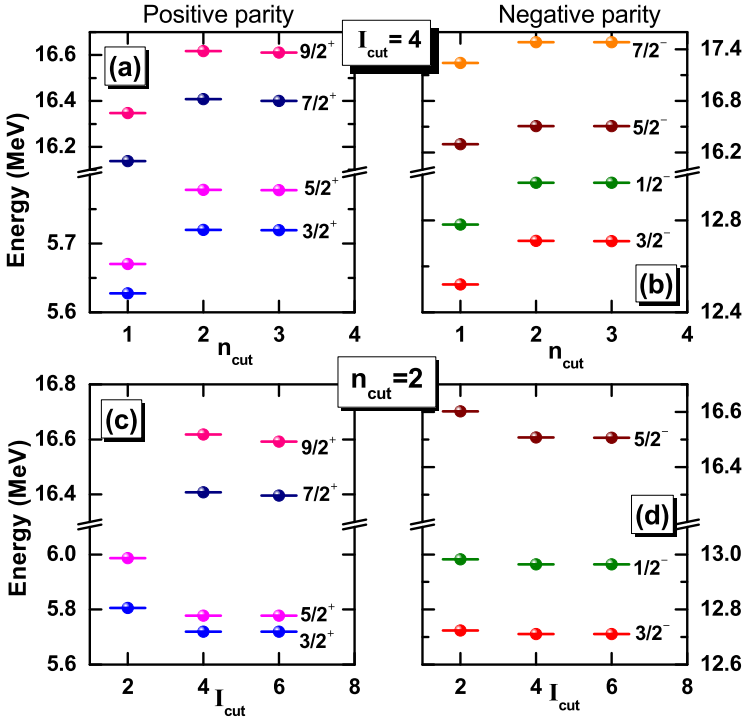

Fig. 5.6 Excitation energies of positive parity and negative parity yrast states in ${}^{13}_{\Lambda}$C as a function of the cutoff of the core states n ((a) and (b)) and the cutoff of the core angular momentum I ((c) and (d)) in the coupled-channels calculations.

We now show in this section the full coupled-channels calculations for ${}^{13}_{\Lambda}$C by mixing all single-channel configurations. We first check the convergence feature of the excitation energies with respect to the number of basis. Figure 5.6 shows the low-lying states in ${}^{13}_{\Lambda}$C obtained by solving the coupled-channels equations for different values for the cutoff of the core states $n_{\rm cut}$ and the cutoff of the core angular momentum $I_{\rm cut}$. When the cutoff of the core angular momentum is $I_{\rm cut} = 4$, there is a large difference in the low-excitation energy between the calculations with

$n_{\rm cut} = 1$ and $n_{\rm cut} = 2$ (see Figs. 5.6 (a) and (b)). However, there is no much change in the low-excitation energy between $n_{\rm cut} = 2$ and $n_{\rm cut} = 3$. On the other hand, when the cutoff of core states is $n_{\rm cut} = 2$, the excitation energy of the first $1/2^-$ state and $3/2^-$ state do not change much for $I_{\rm cut} = 2, 4, 6$, while the excitation energies of the low-lying states $3/2^+, 5/2^+, 7/2^+$ and $5/2^-$ converge after $I_{\rm cut} \geq 4$. All these show that $n_{\rm cut} = 2$ and $I_{\rm cut} = 4$ is enough to yield a good convergence for the low-lying excited states for $^{13}_{\Lambda}$C, although the excitation energy of $9/2^+$ state has a small difference between $I_{\rm cut} = 4$ and $I_{\rm cut} = 6$. Form these consideration, we will use the cut-offs of $I_{\rm cut} = 4$ and $n_{\rm cut} = 2$ in the following calculations for $^{13}_{\Lambda}$C.

Low-lying spectrum

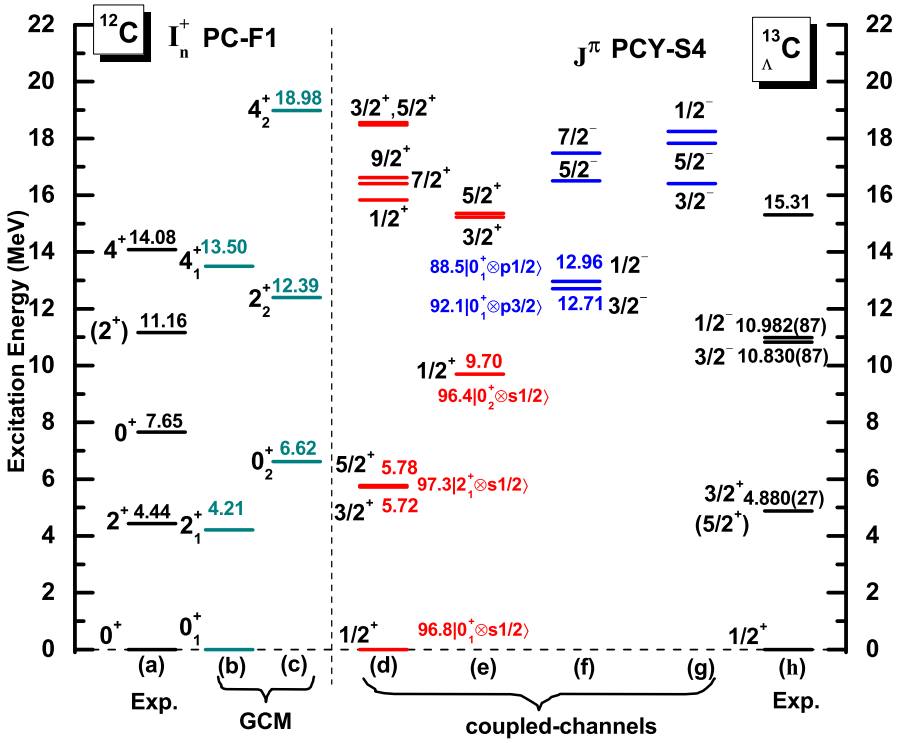

Fig. 5.7 The low-energy excitation spectra of ^{12}C ((b)-(c)) and $^{13}_{\Lambda}$C ((d)-(g)) obtained from the full GCM calculation with PC-F1 and from the MPRM calculation with PCY-S4, respectively. The columns (d) and (e) show the positive-parity states in $^{13}_{\Lambda}$C, while the columns (f) and (g) show the negative-parity states. The experimental data shown in (a) and (h) are taken from Ref. [139] and Refs. [21, 140, 141], respectively. The weight of dominant components for several states are given in percent.

With these cut-off parameters, the calculated low-energy spectrum of $^{13}_{\Lambda}$C is shown in the columns (d), (e), (f), and (g) in Fig. 5.7, in comparison with the experimental data [21, 140, 141]. In these calculations, the state of J^π is obtained by mixing all the configurations of $[\Lambda_{lj} \otimes I^\pi]^{J^\pi}$ with the coupled-channels method. One observes that the low-lying spectra for $^{13}_{\Lambda}$C are reasonably well reproduced, although the excitation energies are slightly overestimated.

Table 5.3 The probability P_{jlI_n} for the dominant components in the wave function for low-lying states of ${}^{13}_{\Lambda}$C obtained by the MPRM calculation with PCY-S4 force. E is the energy of each state obtained by solving the coupled-channels equations, while $E^{(0)}_{\rm 1ch}$ is the unperturbed energy obtained with the single-channel calculations. The energies are listed in units of MeV.

J^π	E	$(l\ j)\otimes I^\pi_n$	P_{jlI_n}	$E^{(0)}_{\rm 1ch}$	J^π	E	$(l\ j)\otimes I^\pi_n$	P_{jlI_n}	$E^{(0)}_{\rm 1ch}$
$1/2^+_1$	0.00	$s_{1/2}\otimes 0^+_1$	0.97	0.00	$1/2^-_1$	12.96	$p_{1/2}\otimes 0^+_1$	0.89	13.22
							$p_{3/2}\otimes 2^+_1$	0.11	18.01
$3/2^+_1$	5.72	$s_{1/2}\otimes 2^+_1$	0.97	5.69	$3/2^-_1$	12.71	$p_{3/2}\otimes 0^+_1$	0.92	12.79
							$p_{1/2}\otimes 2^+_1$	0.05	17.48
$5/2^+_1$	5.78	$s_{1/2}\otimes 2^+_1$	0.98	5.69	$5/2^-_1$	16.51	$p_{3/2}\otimes 2^+_1$	0.79	16.45
							$p_{1/2}\otimes 2^+_1$	0.20	17.48
$7/2^+_1$	16.41	$s_{1/2}\otimes 4^+_1$	0.97	16.25	$7/2^-_1$	17.48	$p_{3/2}\otimes 2^+_1$	0.96	17.40
$9/2^+_1$	16.62	$s_{1/2}\otimes 4^+_1$	0.99	16.25					
$1/2^+_2$	9.70	$s_{1/2}\otimes 0^+_2$	0.96	9.22	$1/2^-_2$	18.24	$p_{1/2}\otimes 0^+_1$	0.45	13.22
							$p_{3/2}\otimes 2^+_1$	0.52	18.01
$3/2^+_2$	15.23	$s_{1/2}\otimes 2^+_2$	0.96	14.84	$3/2^-_2$	16.40	$p_{3/2}\otimes 2^+_1$	0.57	17.14
							$p_{1/2}\otimes 2^+_1$	0.42	17.48
$5/2^+_2$	15.36	$s_{1/2}\otimes 2^+_2$	0.97	14.84	$5/2^-_2$	17.83	$p_{1/2}\otimes 2^+_1$	0.76	17.48
							$p_{3/2}\otimes 2^+_1$	0.19	16.45

The $1/2^+$ states shown in the column (d) and the column(e) are obtained by mixing all $1/2^+$ states shown in Figs. 5.4 (c) and (d) and other configurations $[\Lambda_{lj}\otimes I^\pi]^{1/2^+}$ (not shown). The main component of the first $1/2^+$ state is $[\Lambda s_{1/2}\otimes 0^+_1]^{1/2^+}$, but it also has other components, such as $[\Lambda d_{5/2}\otimes 2^+_1]^{1/2^+}$. See Table 5.3 for the probabilities of the dominant components in each state.

The doublets $(5/2^+, 3/2^+)$ and $(9/2^+, 7/2^+)$ in the column (d) mainly consist of the configurations of $[\Lambda s_{1/2}\otimes 2^+_1]$ and $[\Lambda s_{1/2}\otimes 4^+_1]$, respectively, (see Table 5.3). These doublets are degenerate in the single-channel calculation, as already shown in Fig. 5.4. The energies of the $3/2^+_1$ state and the $5/2^+_1$ state are different from each other by 58 keV due to the weak mixing of other configurations. It has been pointed out that the splitting of the doublet states ($5/2^+_1$, $3/2^+_1$) is dominated by the spin-spin $N\Lambda$ interaction [142], but no experimental data exist yet that resolves the splitting between the $5/2^+_1$ state and $3/2^+_1$ state in ${}^{13}_{\Lambda}$C. The energy difference between $7/2^+_1$ and $9/2^+_1$ states is calculated to be 210 keV.

The levels in Fig.5.7 (e) are dominated by the configuration of $\Lambda s_{1/2}$ coupled to the second band ($n = 2$) in ^{12}C and share similar features as those in the column (d). The splitting of the doublet states ($5/2^+_2$, $3/2^+_2$) is calculated to be 127 keV.

The negative-parity states are shown in the columns (f) and (g) in Fig. 5.7. The first $1/2^-$ and $3/2^-$ states are dominated by the configuration of $\Lambda p_{1/2}$ and $\Lambda p_{3/2}$ coupled to 0^+_1, respectively. That is, the energy splitting between the $3/2^-$ and $1/2^-$ states reflects mainly the spin-orbit splitting of Λ hyperon in the $p_{3/2}$ and $p_{1/2}$ states. The γ rays from the decay of the $3/2^-$

and $1/2^-$ states to the ground state in $^{13}_{\Lambda}$C have been measured and the energy difference was reported to be $152 \pm 54(\text{stat}) \pm 36(\text{syst})$ keV [140, 141]. In the single-channel calculation, the energy difference between the pure configurations of $[\Lambda_{p3/2} \otimes 0^+_1]$ and $[\Lambda_{p1/2} \otimes 0^+_1]$ is 423 keV. In the coupled-channel calculation, the energy splitting between the $3/2^-$ and $1/2^-$ states is as small as 254 keV. The tensor $N\Lambda$ interaction is important to reproduce this small hyperon spin-orbit splitting in Λ hypernuclei [124] and will be discussed in section 5.2.4 in detail.

For the second $1/2^-$ and $3/2^-$ states, one can see a strong configuration mixing (see Table 5.3). The reason for this is that there are two states whose unperturbed energies in the single-channel calculations, $E^{(0)}_{\text{1ch}}$, are close to each other as shown in Table 5.3 and are strongly coupled in the coupled-channels equations by the off-diagonal components of the coupling potentials.

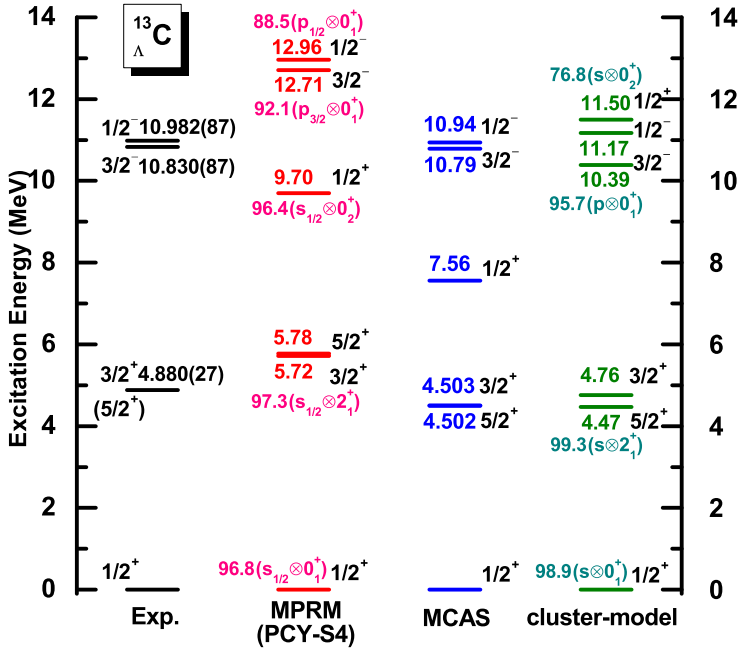

Fig. 5.8 A comparison of low-lying spectra of $^{13}_{\Lambda}$C obtained with the MPRM, the multi-channel algebraic scattering (MCAS) approach [142], the $3\alpha+\Lambda$ cluster model [143], and the experimental data [21, 140, 141].

Figure 5.8 shows a comparison of our calculated low-energy excitation spectra of $^{13}_{\Lambda}$C with results of other approaches, that is, the multi-channel algebraic scattering (MCAS) approach [142], and the $3\alpha + \Lambda$ cluster model [143], together with the experimental data [21]. The basic idea of the MCAS approach for Λ hypernuclei is similar to our MPRM in a sense that the hypernuclear states are constructed by the Λ pariticle coupled to the low-excitation states of a nuclear core. In contrast to our full microscopic model, in which all the inputs are from multi-reference CDFT calculations, the MCAS approach adopts a phenomenological deformed Woods-Saxon potential. It uses the experimental data for the energies of nuclear core states with an assumption of pure collective rotational states. Notice that, the energy ordering of the first $3/2^+$ and $5/2^+$ states obtained with the MCAS approach and the cluster model are different from our MPRM calculation. Except for this, the MPRM and the MCAS approaches give the same structure of spectrum

and energy ordering of the low-lying states. The MPRM and the cluster model calculations give similar results on the main component of each state, while such comparison is impossible between MPRM and MCAS as the components are not shown explicitly in Ref. [142].

E2 transition strengths

We next discuss the $E2$ transition strengths between the low-lying positive-parity yrast states for ${}^{13}_{\Lambda}$C. The low-lying positive parity yrast states of Λ-hypernuclei are dominated by Λ hyperon in $s_{1/2}$ orbit coupled to the ground states band of nuclear core $[\Lambda_{s1/2} \otimes I_1]^{J^+}$, then the relations between the initial state and the final state in hypernuclear transitions are approximately given by $j_f = j_i = 1/2$, $\ell_f = \ell_i = 0$ and $n_f = n_i = 1$. In this approximation, assuming also $\langle \mathscr{R}_{I_f}(r) | \mathscr{R}_{I_i}(r) \rangle \approx 1$, Eq. (4.43) can be rewritten as

$$B(E2; J_i \to J_f) \approx \hat{I_i}^2 \hat{J_f}^2 \begin{Bmatrix} I_f & J_f & 1/2 \\ J_i & I_i & 2 \end{Bmatrix}^2 \frac{1}{\hat{I_i}^2} \left| \langle I_f || \hat{Q}_2 || I_i \rangle \right|^2 . \tag{5.7}$$

(Notice that in the actual calculations shown below, we do not use this approximation but we use Eq. (4.43) as it is.) It is convenient to introduce a new value $cB(E2)$, which reflects the $B(E2)$ value of the core part in hypernuclei (see Eq.(5.7)),

$$\begin{aligned} cB(E2 : I_i \to I_f) \equiv & \frac{1}{\hat{I_i}^2} \left| \langle I_f || \hat{Q}_2 || I_i \rangle \right|^2 \\ \approx & \hat{I_i}^{-2} \hat{J_f}^{-2} \begin{Bmatrix} I_f & J_f & 1/2 \\ J_i & I_i & 2 \end{Bmatrix}^{-2} B(E2 : J_i \to J_f) \\ \equiv & C \cdot B(E2 : J_i \to J_f), \end{aligned} \tag{5.8}$$

where $C = \hat{I_i}^{-2} \hat{J_f}^{-2} \begin{Bmatrix} I_f & J_f & 1/2 \\ J_i & I_i & 2 \end{Bmatrix}^{-2}$. In this way, the trivial factor due to the angular momentum coupling for $s_{1/2}$ for the Λ particle can be removed and the impurity effect of Λ particle on the nuclear collectivity becomes more clearly. That is, the impurity effect of Λ particle can be discussed directly by comparing the $B(E2)$ values for the core nucleus and the $cB(E2)$ values for the corresponding hypernucleus.

Table 5.4 shows the calculated $E2$ transition strengths for low-lying positive-parity states of the ${}^{13}_{\Lambda}$C hypernucleus and those of the core nucleus ^{12}C with three different values of $n_{\rm cut}$ for the core states. Here, Δ is defined as

$$\Delta \equiv \frac{cB(E2; {}^{13}_{\Lambda}\mathrm{C}) - B(E2; {}^{12}\mathrm{C})}{B(E2; {}^{12}\mathrm{C})}. \tag{5.9}$$

Even though the B(E2) value does not change much for $n_{\rm cut} = 1$ by adding a Λ particle, for $n_{\rm cut} = 2$ and $n_{\rm cut} = 3$, the $B(E2)$ value for $2^+_1 \to 0^+_1$ in ^{12}C is significantly reduced by a factor of

$\sim 11.48\%$. One can see that $n_{\rm cut} = 2$ yields a good convergence for the $E2$ transition strengths for the low-lying positive parity states for ${}^{13}_{\Lambda}$C.

According to the definition of B(E2) value, it is approximately proportional to $\beta^2 \times r_p^4$. In our calculation, the proton radius r_p (the average deformation β) is 2.44fm (-0.27) for the $1/2^+_1$ state in ${}^{13}_{\Lambda}$C and is 2.39fm (-0.25) for the 0^+_1 state in ^{12}C. One can see that the change in deformation β is the dominant ingredient of the reduction of the E2 transition strength.

Table 5.4 The calculated $E2$ transition strengths (in units of e^2 fm^4) for low-lying positive parity states of ^{12}C and ${}^{13}_{\Lambda}$C. The $cB(E2)$ value is defined by Eq. (5.8). $\triangle$ is the change in the $B(E2)$ of the core nucleus defined by Eq. (5.9). The experimental data for ^{12}C shown in the parenthesis is taken from Ref. [98].

^{12}C		${}^{13}_{\Lambda}$C									
				$n_{\rm cut}=1$			$n_{\rm cut}=2$			$n_{\rm cut}=3$	
$I^\pi_i \to I^\pi_f$	$B(E2)$	$J^\pi_i \to J^\pi_f$	C	$B(E2)$	$cB(E2)$	$\Delta(\%)$	$B(E2)$	$cB(E2)$	$\Delta(\%)$	$B(E2)$	$cB(E2)$
$2^+_1 \to 0^+_1$	6.62	$3/2^+_1 \to 1/2^+_1$	1	6.606	6.606	-0.21	5.86	5.86	-11.48	5.86	5.86
	(7.6 ± 0.4)	$5/2^+_1 \to 1/2^+_1$	1	6.617	6.617	-0.05	5.86	5.86	-11.48	5.86	5.86
$4^+_1 \to 2^+_1$	14.60	$7/2^+_1 \to 3/2^+_1$	10/9	12.96	14.40	-1.34	11.68	12.98	-11.10	11.64	12.93
		$7/2^+_1 \to 5/2^+_1$	10	1.44	14.38	-1.51	1.30	12.98	-11.10	1.29	12.94
		$9/2^+_1 \to 5/2^+_1$	1	14.41	14.41	-1.30	12.99	12.99	-11.03	12.98	12.98

5.2.4 Sensitivity of low-energy hypernuclear spectra to $N\Lambda$ interaction

The $N\Lambda$ parameters forces

There are four parameter sets of effective $N\Lambda$ interaction for the relativistic point-coupling model (see Table 3.1), which were adjusted at the mean-field level to the Λ binding energy of several Λ hypernuclei. In this subsection, we compare the Λ binding energy and low-lying state obtained with these four $N\Lambda$ forces.

To begin with, Figs. 5.9(b)-(e) show the calculated low-energy spectra of ${}^{13}_{\Lambda}$C in comparison with the experimental data. One can see that the main structures of the low-lying states are similar to each other with the four parameter sets, but the energy splitting between the $1/2^-$ and $3/2^-$ states, as well as that between the $5/2^+$ and $3/2^+$ states, are clearly different. That is, the splitting between the $1/2^-_1$ and $3/2^-_1$ states by PCY-S2 and PCY-S3 are significantly larger than that by PCY-S1 and PCY-S4, which are much closer to the experiment data. The splitting between the $5/2^+$ and $3/2^+$ states with PCY-S1 force is much larger than that with the other $N\Lambda$ parameter forces. It indicates that the fine structure of the hypernuclear low-lying states reflects the impact of the higher-order terms in the $N\Lambda$ interaction. Notice that a good description is still achieved with the PCY-S2 force, in which the tensor term is absent, by largely deviating from the expected relations of a naive quark model, that is, $\alpha^{N\Lambda} = \frac{2}{3}\alpha^{NN}$ etc. [144]. We will further discuss the role of the higher order terms in $N\Lambda$ interaction in the next subsections and will demonstrate that the tensor term plays an important role if the expected

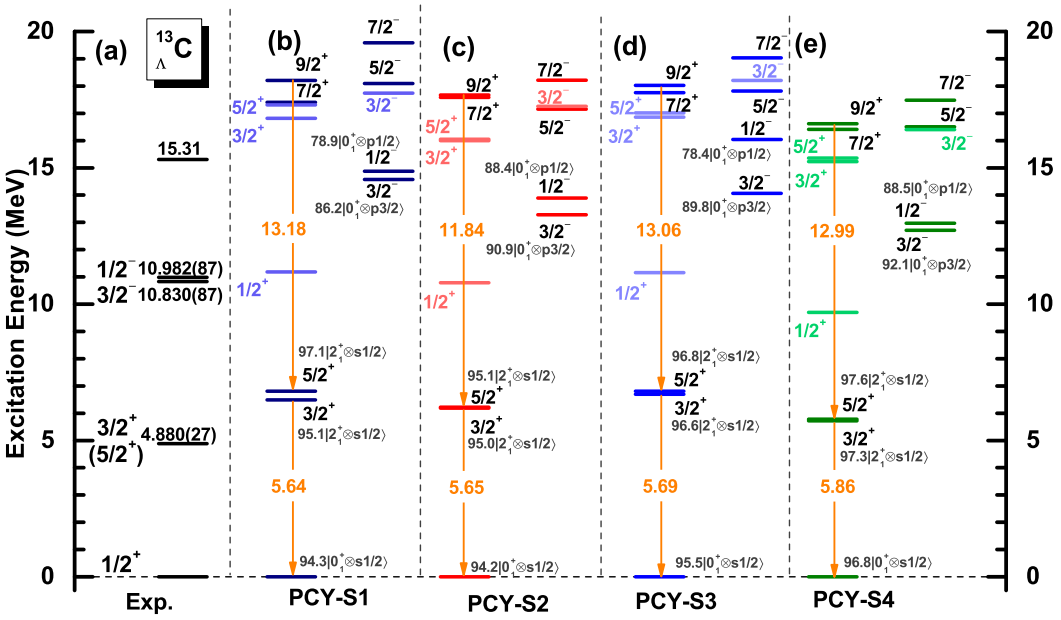

Fig. 5.9 The excitation energies for the first and the second state for each spin-parity (J^π) of $^{13}_{\Lambda}$C obtained with the MPRM with (b)PCY-S1, (c)PCY-S2, (d)PCY-S3 and (e)PCY-S4. The column (a) shows the experimental data taken from Refs. [21, 140, 141]. The numbers with the arrow indicate the B($E2$) value for the $3/2^+_1 \to 1/2^+_1$ and the $9/2^+_1 \to 5/2^+_1$ transitions, given in units of e^2 fm^4.

relation of $\alpha^{N\Lambda} = \frac{2}{3}\alpha^{NN}$ is maintained. The figure also shows that the quadrupole transition strengths $B(E2)$ between the low-lying states of $^{13}_{\Lambda}$C do not much vary with the four $N\Lambda$ effective interactions.

The calculated Λ binding energy of $^{13}_{\Lambda}$C, which is defined as the energy difference between the 0^+_1 state of ^{12}C and the $1/2^+_1$ state of $^{13}_{\Lambda}$C, is 15.72, 13.63, 15.42 and 13.22 MeV with the MPRM with PCY-S1, PCY-S2, PCY-S3 and PCY-S4, respectively. Comparing with the empirical value, $B_\Lambda^{\rm exp.} = 11.38 \pm 0.05$ MeV [21], our MPRM calculations overestimate the Λ binding energy of $^{13}_{\Lambda}$C due to the fact that all these four $N\Lambda$ forces were adjusted to Λ binding energy of hypernuclei at the mean-field level [130].

In order to reproduce the Λ binding energy with our model, we scale all the coupling strengths in the parameters of the $N\Lambda$ interaction by 18%, 9%, 16% and 8% for PCY-S1, PCY-S2, PCY-S3 and PCY-S4, respectively. The calculated low-lying spectra obtained with the scaled interactions are shown in Fig. 5.10. It is shown that the predicted low-energy excitation spectrum of $^{13}_{\Lambda}$C is slightly compressed and the $B(E2)$ values are somewhat increased. The energy splitting between the $1/2^-_1$ and $3/2^-_1$ states is reduced from 303.7 keV (253.7 keV) to 161.5 keV(206.3 keV) after scaling the coupling strengths for the PCY-S1 (PCY-S4) interaction, while it still remains large by the scaled PCY-S2 and PCY-S3 forces. The configuration mixing for the $1/2^+_1$, $3/2^+_1$, $5/2^+_1$, $1/2^-_1$ and $3/2^-_1$ states becomes slightly reduced for all the scaled parameter sets due to the slightly weaker $N\Lambda$ coupling strength.

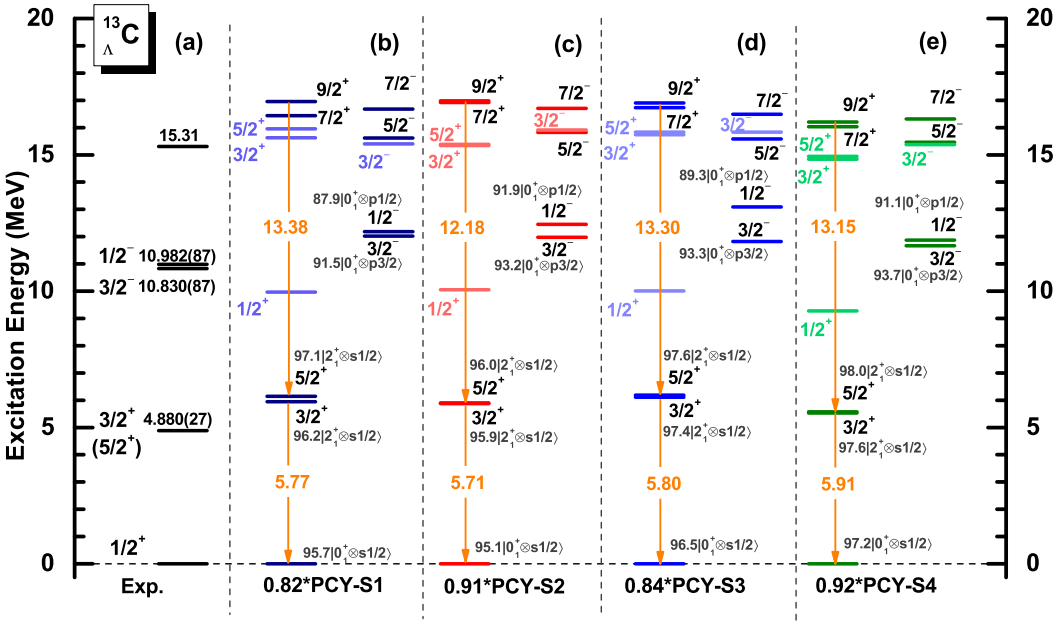

Fig. 5.10 Same as Fig. 5.9, but with scaled $N\Lambda$ interactions, in which the scaling factor is determined for each parameter set to reproduce the empirical Λ binding energy of $^{13}_{\Lambda}$C.

$N\Lambda$ coupling strength

We next examine the effect of the leading-order coupling terms and higher-order derivative coupling terms on the Λ binding energy. First, we check the relation between the parameters $\alpha_S^{N\Lambda}$ and $\alpha_V^{N\Lambda}$ in the $N\Lambda$ interaction which reproduces the Λ binding energy in $^{13}_{\Lambda}$C. To this end, we only include the leading-order coupling terms in the effective $N\Lambda$ interaction, that is, only $\hat{V}_{\rm S}^{N\Lambda}(\boldsymbol{r},\boldsymbol{r}_i) = \alpha_S^{N\Lambda}\gamma_\Lambda^0\delta(\boldsymbol{r}-\boldsymbol{r}_i)\gamma_N^0$ and $\hat{V}_{\rm V}^{N\Lambda}(\boldsymbol{r},\boldsymbol{r}_i) = \alpha_V^{N\Lambda}\delta(\boldsymbol{r}-\boldsymbol{r}_i)$ are adopted in Eq. (3.7) by setting $\delta_S^{N\Lambda} = \delta_V^{N\Lambda} = \alpha_T^{N\Lambda} = 0$. Figure 5.11(a) shows a contour plot of the absolute value of the difference between the calculated and the experimental hyperon binding energies $|B_\Lambda^{\rm th} - B_\Lambda^{\rm exp}|$ as a function of $\alpha_S^{N\Lambda}$ and $\alpha_V^{N\Lambda}$. As illustrated in Fig. 5.11(a), all the parameter sets of ($\alpha_S^{N\Lambda}$, $\alpha_V^{N\Lambda}$) located at the valley can reproduce the Λ binding energy and are linearly correlated. In other words, the two strength parameters cannot be uniquely determined by fitting only to B_Λ, as expected.

Taking four sets of the parameters along the valley with $B_\Lambda^{\rm th} = B_\Lambda^{\rm exp}$ in Fig. 5.11(a), we calculate the energy of the low-excitation states of $3/2^+$, $3/2^-$ and $1/2^-$ in $^{13}_{\Lambda}$C, as shown in Fig. 5.11(b). The excitation energies of $3/2^+$ and $3/2^-$ states depend on the choice of the parameters weakly and the energy of $1/2^-$ state slightly decreases with the decrease of the absolute value of the coupling strengths $\alpha_S^{N\Lambda}$. For all the sets of the parameters $(\alpha_S^{N\Lambda}, \alpha_V^{N\Lambda})$ in the region of concerned, the energy splitting between the first $1/2^-$ and $3/2^-$ states is in a good agreement with the experiment data.

Next, we fix the coupling strengths for the leading order terms $(\alpha_V^{N\Lambda}, \alpha_S^{N\Lambda})$ to be the same values as those in the PCY-S2 force and study the Λ binding energy as a function of the coupling strengths ($\delta_V^{N\Lambda}$, $\delta_S^{N\Lambda}$) of the derivative terms, as shown in Fig. 5.11(c). Since the tensor coupling

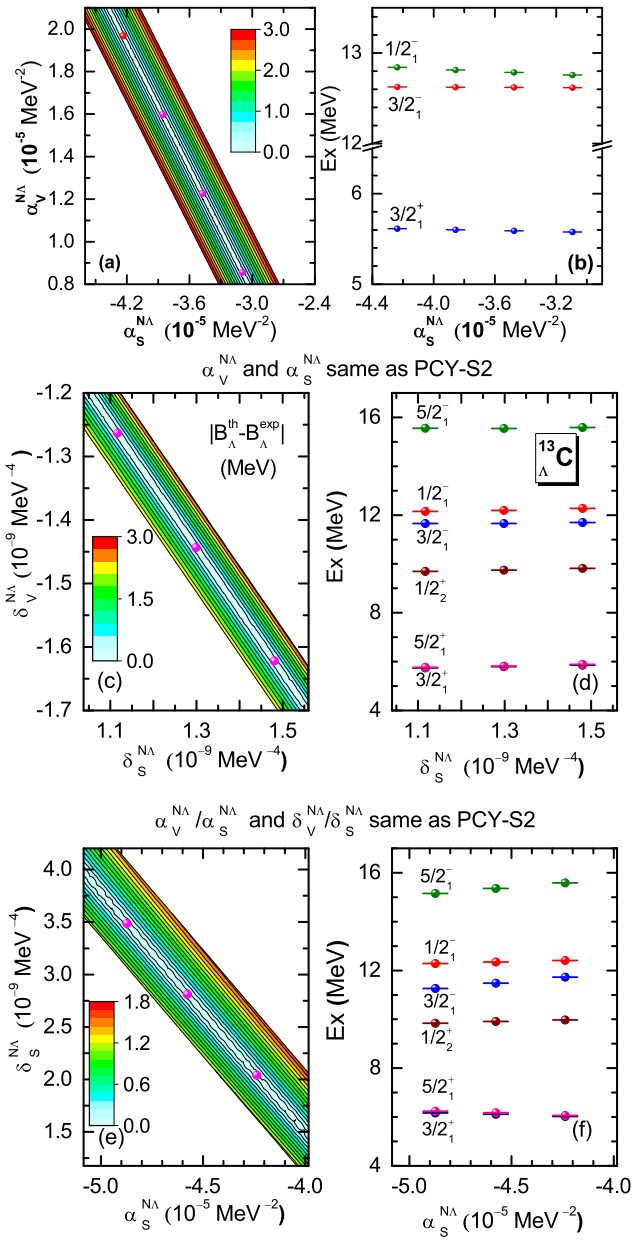

Fig. 5.11 (a), (c) and (e): Contour plots for the absolute value of the difference between the theoretical and the experimental hyperon binding energies of ${}^{13}_{\Lambda}$C hypernucleus as a function of the coupling strength parameters ($\alpha_V^{N\Lambda}$,$\alpha_S^{N\Lambda}$), ($\delta_V^{N\Lambda}$, $\delta_S^{N\Lambda}$) and ($\delta_S^{N\Lambda}$, $\alpha_S^{N\Lambda}$), respectively. In (a), only $\hat{V}_{\rm S}^{N\Lambda}(\boldsymbol{r},\boldsymbol{r}_i) = \alpha_S^{N\Lambda}\gamma_\Lambda^0\delta(\boldsymbol{r}-\boldsymbol{r}_i)\gamma_N^0$ and $\hat{V}_{\rm V}^{N\Lambda}(\boldsymbol{r},\boldsymbol{r}_i) = \alpha_V^{N\Lambda}\delta(\boldsymbol{r}-\boldsymbol{r}_i)$ are used for $N\Lambda$ interaction. In (c), $\alpha_V^{N\Lambda}$ and $\alpha_S^{N\Lambda}$ are fixed to the same values as in PCY-S2. In (e), the value of $\alpha_V^{N\Lambda}$ and $\delta_V^{N\Lambda}$ is determined for each ($\alpha_S^{N\Lambda}$, $\delta_S^{N\Lambda}$) so as to keep the ratios $\alpha_V^{N\Lambda}/\alpha_S^{N\Lambda}$ and $\delta_V^{N\Lambda}/\delta_S^{N\Lambda}$ to be the same as those for PCY-S2. (b), (d) and (f): Low-energy levels in ${}^{13}_{\Lambda}$C calculated with the strength parameters denoted by the dots in the panels (a), (c) and (e), respectively.

is absent in PCY-S2, we can isolate the effect of the derivative terms in this procedure. One can see that a clear linear correlation between $\delta_V^{N\Lambda}$ and $\delta_S^{N\Lambda}$. Selecting three sets of $(\delta_V^{N\Lambda}, \delta_S^{N\Lambda})$ along the valley in Fig. 5.11(c), we calculate the low-excitation energies of ${}^{13}_{\Lambda}$C and show them in Fig. 5.11(d). It is found that the low-lying states are similar to each other with these three sets, which is again a natural consequence of that the coupling strengths $(\delta_V^{N\Lambda}, \delta_S^{N\Lambda})$ can not be uniquely determined by the energies of hypernuclear low-lying states.

Figs. 5.11(a) and (c) illustrate that the vector coupling strengths $\alpha_V^{N\Lambda}$ and $\delta_V^{N\Lambda}$ are linearly correlated with the corresponding scalar coupling strengths $\alpha_S^{N\Lambda}$ and $\delta_S^{N\Lambda}$, respectively. Next, we keep the ratios of $\alpha_V^{N\Lambda}/\alpha_S^{N\Lambda}$ and $\delta_V^{N\Lambda}/\delta_S^{N\Lambda}$ to be the same as those in PCY-S2 force and calculate the Λ binding energy as a function of $\alpha_S^{N\Lambda}$ and $\delta_S^{N\Lambda}$, as shown in Fig. 5.11(e). One observes that the parameters $\delta_S^{N\Lambda}$ and $\alpha_S^{N\Lambda}$ are also linearly correlated when these are fitted to the Λ binding energy in ${}^{13}_{\Lambda}$C (see Fig. 5.11(e)).

Notice that the vector and scalar transition densities have only a small difference from one another in the low-lying states of ^{12}C (see Fig.2.5). Assuming that the vector transition density $\rho_{\lambda,V}^{nIn'I'}(r)$ and the scalar transition density $\rho_{\lambda,S}^{nIn'I'}(r)$ have the same value, in the non-relativistic approximation, the sum of leading order coupling strengths, $\alpha_S^{N\Lambda} + \alpha_V^{N\Lambda}$, and the sum of the derivative coupling strengths, $\delta_S^{N\Lambda} + \delta_V^{N\Lambda}$, can be regarded as the depth of the central potential U_0 and the surface coupling strength D introduced in Ref. [131], respectively. It has been found in Ref. [131] that the pairs of values (U_0, D) that reproduce the empirical B_Λ are also correlated linearly.

Taking three sets of the parameters along the valley with $B_\Lambda^{\rm th} = B_\Lambda^{\rm exp}$ in Fig. 5.11(e), one finds that those three sets yield almost the same excitation energies for the $3/2_1^+$, $5/2_1^+$, $1/2_2^+$ and $1/2_1^-$ states (with differences within around 0.13 MeV), while the difference is much larger for the $3/2_1^-$ and $5/2_1^-$ states (around 0.45 MeV). A comparison between Figs. 5.11 (b), (d) and (f) suggests that the excitation energies of the low-lying states are more sensitive to $\alpha_S^{N\Lambda}$ and $\alpha_V^{N\Lambda}$ than to $\delta_S^{N\Lambda}$ and $\delta_V^{N\Lambda}$.

Derivative coupling terms

The derivative coupling terms, which simulate to some extent the finite-range character of $N\Lambda$ interaction, are expected to be more pronounced in light hypernuclei [131]. We next examine the effect of the derivative terms on the energy of low-lying states. To this end, we fix the values of $\alpha_S^{N\Lambda}$, $\alpha_V^{N\Lambda}$, $\alpha_T^{N\Lambda}$ and the ratio $\delta_S^{N\Lambda}/\delta_V^{N\Lambda}$ to be the same as the original values for each of the four parameter sets, PCY-S1, PCY-S2, PCY-S3, and PCY-S4, and change the value of $\delta_S^{N\Lambda} + \delta_V^{N\Lambda}$. The Λ binding energy so obtained with the four $N\Lambda$ forces are shown in Fig. 5.12(a) as a function of $|\delta_S^{N\Lambda} + \delta_V^{N\Lambda}| = -(\delta_S^{N\Lambda} + \delta_V^{N\Lambda})$. The open circles denote the calculated B_Λ with the original value of each parameter set. One observes that B_Λ decreases with increasing $|\delta_S^{N\Lambda} + \delta_V^{N\Lambda}|$ and approaches to the experimental value denoted by the thin solid line. For PCY-S1 force, the B_Λ decreases from 21.28 MeV to 15.72 MeV, which is close to the experiment data, by including the derivative interaction terms (that is, by varying $|\delta_S^{N\Lambda} + \delta_V^{N\Lambda}|$ from 0 to the original value denoted

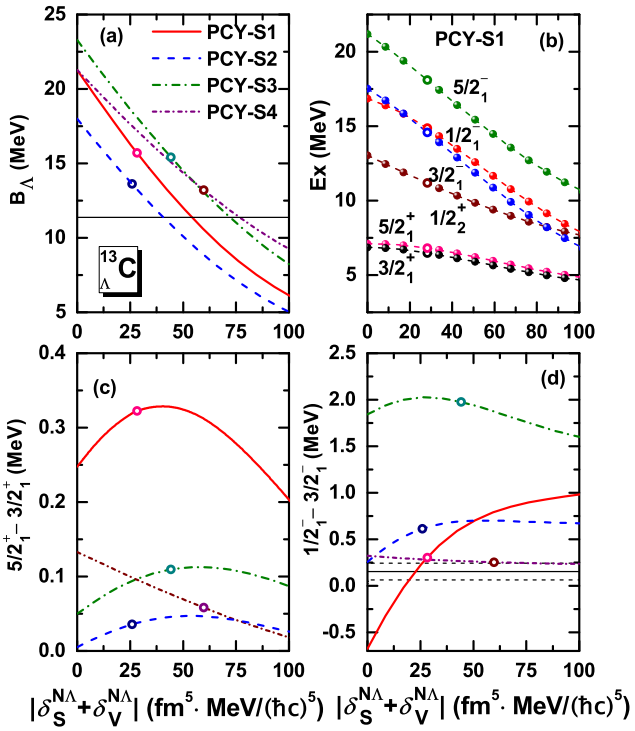

Fig. 5.12 (a): The Λ binding energy in ${}^{13}_{\Lambda}$C as a function of $|\delta_S^{N\Lambda}+\delta_V^{N\Lambda}|$, while keeping the same values of $\alpha_S^{N\Lambda}$, $\alpha_V^{N\Lambda}$, $\alpha_T^{N\Lambda}$ and $\delta_V^{N\Lambda}/\delta_S^{N\Lambda}$ as the original values for the PCY-S1, PCY-S2, PCY-S3, and PCY-S4 parameter sets. B_Λ with the original value of $\delta_S^{N\Lambda}$ and $\delta_V^{N\Lambda}$ is denoted by the open circles for each parameter set. The experimental value is denoted by the thin solid line. (b): The excitation energies of the low-lying states as a function of $|\delta_S^{N\Lambda}+\delta_V^{N\Lambda}|$ for the PCY-S1 parameter set. (c) and (d): The energy splitting between the $5/2^+_1$ and $3/2^+_1$ states and that between the $1/2^-_1$ and $3/2^-_1$ states, respectively, as a function of $|\delta_S^{N\Lambda}+\delta_V^{N\Lambda}|$.

by the open circle). For PCY-S2, PCY-S3, and PCY-S4 forces, the Λ binding energy are shifted from 18.01, 23.29, and 21.27 MeV to 13.63, 15.42, and 13.22 MeV, respectively.

Figure 5.12(b) shows the excitation energies of the low-lying states as a function of the derivative coupling strength $|\delta_S^{N\Lambda}+\delta_V^{N\Lambda}|$, where $\alpha_S^{N\Lambda}$, $\alpha_V^{N\Lambda}$, $\alpha_T^{N\Lambda}$ and $\delta_S^{N\Lambda}/\delta_V^{N\Lambda}$ are kept to be the same as those for PCY-S1. One can see that the excitation energies decrease with the increase of $|\delta_S^{N\Lambda}+\delta_V^{N\Lambda}|$. Notice that the change of the $3/2^+$ and $5/2^+$ states are much smaller compared to the change in the other states. Similar behaviors are also found for the PCY-S2, PCY-S3 and PCY-S4 forces (not shown). The energy splittings of $(3/2^+_1, 5/2^+_1)$ and $(1/2^-_1, 3/2^-_1)$ states are shown in Figs. 5.12(c) and (d), respectively, as a function of $|\delta_S^{N\Lambda}+\delta_V^{N\Lambda}|$. One observes that the $3/2^+_1$ state is always slightly lower than the $5/2^+_1$ state, which is by less than 150 keV except for PCY-S1 in the range of $|\delta_S^{N\Lambda}+\delta_V^{N\Lambda}|$ shown in the figure, although this may not be conclusive as the spin-spin $N\Lambda$ interaction [142] is not included in these calculations.

For the doublet states of $(1/2^-, 3/2^-)$, the $3/2^-$ state is predicted to be lower than the $1/2^-$ state for all the forces except for the PCY-S1, with which the $3/2^-$ state is higher than the $1/2^-$ state in the region of $|\delta_S^{N\Lambda}+\delta_V^{N\Lambda}| < 17.56$ fm$^5\cdot$MeV. The energy splitting between the $1/2^-$ and

$3/2^-$ states reflects the spin-orbit splitting of the p_Λ hyperon in ${}^{13}_{\Lambda}$C (as discussed in section 5.2.3) and is mainly governed by the tensor coupling term, which will be discussed in the next subsection.

Tensor coupling term

It has been point out by Noble that the tensor $N\Lambda$ interaction is important to reproduce a small hyperon spin-orbit splitting in Λ hypernuclei [124]. In order to understand the effect of tensor coupling, we first discuss the Dirac equation for Λ hyperon in the mean-field approximation, that is,

$$[\boldsymbol{\alpha}\cdot\boldsymbol{p}+\beta(m_\Lambda+S)+V+T]\psi=\varepsilon\psi, \tag{5.10}$$

where S, V and T are the scalar potential, the vector potential and the tensor coupling potential, respectively. The Dirac equation can be written as the Schrödinger equivalent equation for the large component of the Dirac spinor ψ as

$$\left\{-\frac{1}{2M}\left[\frac{d^2}{dr^2}-\frac{V_-'}{2M}\frac{d}{dr}-\frac{l(l+1)}{r^2}\right]+\left(\frac{V_-'}{4M^2}+\frac{T}{M}\right)\frac{\kappa}{r}+\frac{1}{2M}\left(T^2-T'+\frac{V_-'}{2M}T\right)+V_+\right\}f_\kappa(r)$$
$$=\varepsilon f_\kappa(r), \tag{5.11}$$

where $M=\frac{1}{2}(m_\Lambda+\varepsilon+S-V)$, $V_\pm=m_\Lambda+S\pm V$, $V_-'=\frac{dV_-}{dr}$, $T'=\frac{dT}{dr}$, and $\kappa=(-1)^{j+l+1/2}(j+1/2)$. Notice that the spin-orbit potential is given by

$$V_{ls}=\left(\frac{V_-'}{4M^2}+\frac{T}{M}\right)\frac{\kappa}{r}=\left(\frac{d(S-V)/dr}{4M^2}+\frac{T}{M}\right)\frac{\kappa}{r}. \tag{5.12}$$

That is, the spin-orbit splitting is originated from the contributions of the central spin-orbit term $\frac{d(S-V)/dr}{4M^2}\frac{\kappa}{r}$ and the tensor coupling term $\frac{T}{M}\frac{\kappa}{r}$.

For Λ hyperon, the contribution of the tensor coupling term almost cancels with the central spin-orbit term, resulting in a small spin-orbit splitting in Λ hypernuclei. This can be seen from the Nilsson diagram of the single-particle energy for Λ hyperon in hypernuclei with mean-field calculation. Figure 5.13 shows the single-particle energy for Λ hyperon in ${}^{13}_{\Lambda}$C. In order to draw this, we have constructed the mean-field potential by assuming that the Λ hyperon occupies the lowest state. The results with and without the tensor potential are shown in Figs. 5.13 (a) and 5.13 (b), respectively. One can see that the tensor potential pushes up the energy of the $1s_{1/2}$ and $1p_{3/2}$ orbitals and pulls down the $1p_{1/2}$ orbital, resulting in a significant reduction in the spin-orbit splitting between the partner states $1p_{3/2}$ and $1p_{1/2}$ for the spherical shape.

Notice that the contribution of the tensor coupling for different hyperons to the spin-orbit term are different in their magnitude and sign [125]. For instance, the contribution of the tensor coupling term for Σ hyperon has the same sign as the central spin-orbit term and results in an almost double enhancement of the spin-orbit term. On the other hand, for Ξ hyperon, the contribution of the tensor coupling term to the spin-orbit term has the same sign as that in Λ hyperon but with larger magnitude.

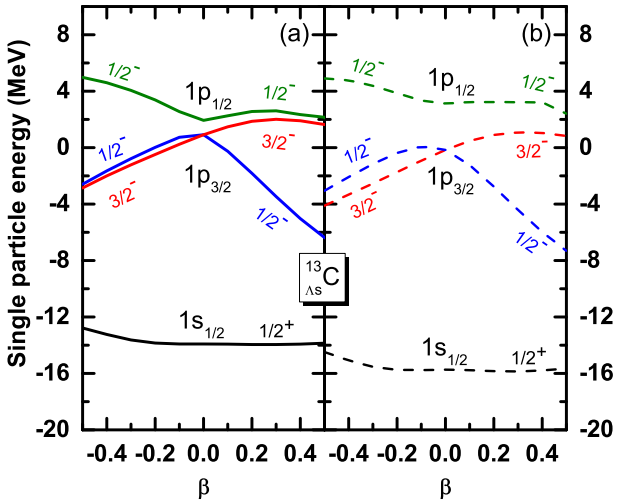

Fig. 5.13 (a) The single-particle energies of Λ hyperon in ${}^{13}_{\Lambda}$C as a function of deformation parameters β obtained with a relativistic mean-field calculation with PC-F1 force for NN interaction and PCY-S1 force for $N\Lambda$ interaction. These are obtained with the mean-field potential which is by putting the Λ particle in the lowest parity state. (b)The energy levels from the calculation without the tensor potential.

We now examine the effects of the tensor coupling term on Λ-hypernuclear low-lying states with MPRM. For this purpose, we adopt the PCY-S1 and PCY-S4 sets for $N\Lambda$ interaction and change the strength $\alpha_T^{N\Lambda}$ for the tensor coupling term. Figure 5.14 shows the energy of low-lying states for ${}^{13}_{\Lambda}$C as a function of $|\alpha_T^{N\Lambda}| = -\alpha_T^{N\Lambda}$, in which the energy for the original value of $\alpha_T^{N\Lambda}$ for the PCY-S1 and PCY-S4 forces are indicated by the open circles. One can see that the effect of tensor coupling term on the low-lying state energies are significant. The tensor coupling term increases the energy of the $1/2_1^+$ state resulting in that the Λ binding energy gradually decreases from 17.71 MeV (14.12 MeV) for $\alpha_T^{N\Lambda} = 0$ to 15.72 MeV (13.22 MeV) for the original value of $\alpha_T^{N\Lambda}$ for the PCY-S1 (PCY-S4) force, which is indicated by the open circle in Fig. 5.15(a). This is consistent with the previous mean-field studies [46, 125, 144] that the tensor coupling term makes the s_Λ hyperon less bound by increasing the energy of the $s_{1/2}$ level (see also Fig. 5.13). As a result, the Λ binding energy is reduced by 0.9 MeV for the PCY-S1 and 1.99 MeV for the PCY-S4 after turning on the tensor coupling term.

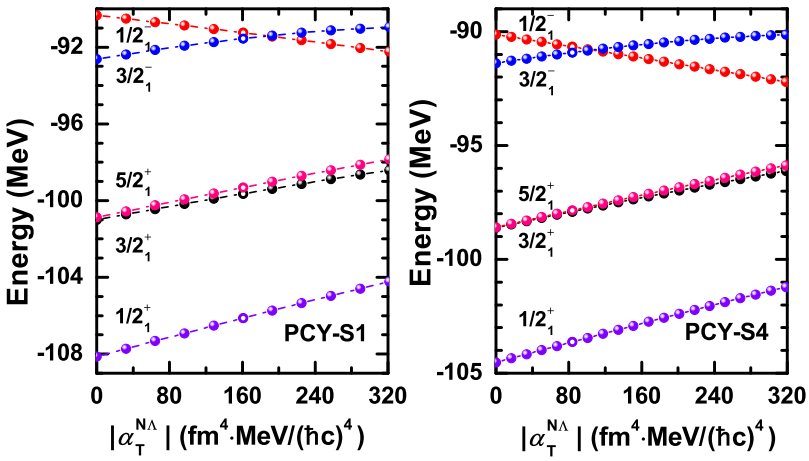

Fig. 5.14 The energy of the low-lying states of ${}^{13}_{\Lambda}$C as a function of the tensor coupling strength $|\alpha_T^{N\Lambda}|(=-\alpha_T^{N\Lambda})$ for the PCY-S1 and PCY-S4 forces. The open circles denote the original value of $\alpha_T^{N\Lambda}$ for PCY-S1 and PCY-S4 forces.

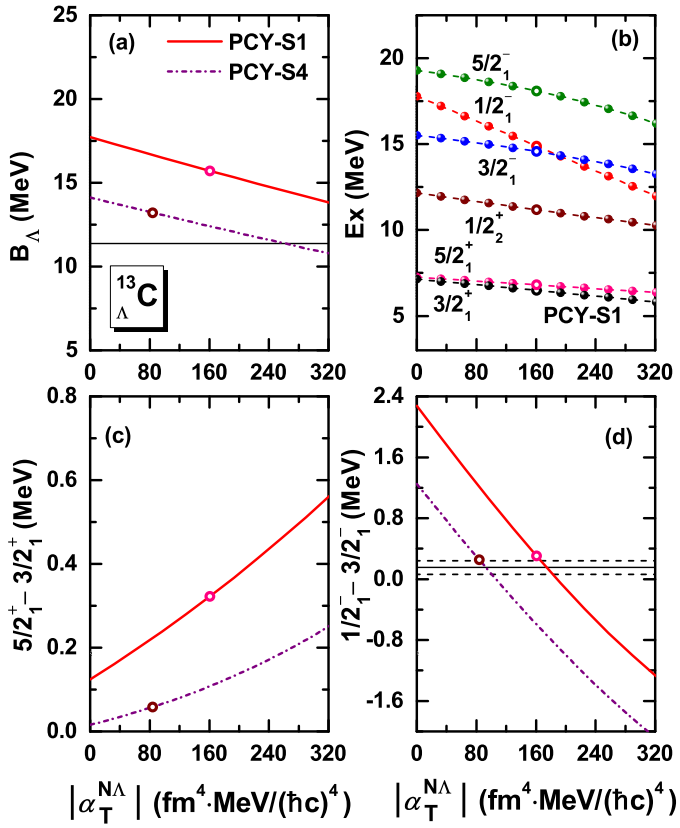

Fig. 5.15 Same as Fig. 5.12, but as a function of the tensor coupling strength $|\alpha_T^{N\Lambda}|(=-\alpha_T^{N\Lambda})$ for the PCY-S1 and PCY-S4 forces.

At the same time, the tensor coupling term increases (decreases) the energy of the $3/2^-$ ($1/2^-$) state, which mainly consists of the $p_{3/2}$ ($p_{1/2}$) hyperon coupled to the ground state (0^+) of ^{12}C. Because the change of these two states are smaller than that in $1/2^+_1$, the excitation energy for both the $3/2^-$ and $1/2^-$ states decrease with increasing $|\alpha_T^{N\Lambda}|$, as shown in Fig. 5.15(b).

Moreover, the excitation energy of the $1/2^-$ state changes more significantly than the $3/2^-$ state, resulting in that the higher lying $1/2^-$ state approaches the $3/2^-$ state and even becomes lower than the $3/2^-$ state for large values of the tensor coupling strength. This clearly indicates that the energy splitting bewteen the $1/2^-$ and $3/2^-$ states is sensitive to the tensor coupling strength. The energy difference between the $1/2^-_1$ and $3/2^-_1$ states decreases from 2.28 MeV to 0.31 MeV, and from 1.25 MeV to 0.25 MeV for the PCY-S1 and PCY-S4 forces, respectively, while turning on the tensor coupling term, as shown in Fig. 5.15(d).

For the $3/2^+_1$ and $5/2^+_1$ states, the energy changes are comparable with that in $1/2^+_1$ (see Fig. 5.14), resulting in that the excitation energy of these two states change slowly with respect to $|\alpha_T^{N\Lambda}|$ (see Fig. 5.15(b)). The energy gap between the $3/2^+_1$ and $5/2^+_1$ states increases with an increasing value of $|\alpha_T^{N\Lambda}|$, as shown in Fig. 5.15(c), and therefore the tensor coupling term does not invert the energy ordering of the $3/2^+_1$ and $5/2^+_1$ states.

5.3 Application to ${}^{9}_{\Lambda}$Be

The ${}^{9}_{\Lambda}$Be is a typical light hypernucleus and has been measured with many reactions, such as ${}^{9}\mathrm{Be}(K^-,\pi^-){}^{9}_{\Lambda}\mathrm{Be}$ [8] and ${}^{9}\mathrm{Be}(\pi^+,K^+){}^{9}_{\Lambda}\mathrm{Be}$ [21]. Many theoretical methods, including the cluster model and *ab*-initio method as well as AMD, have been applied to discuss the spectra of ${}^{9}_{\Lambda}$Be. In this section, we investigate the ${}^{9}_{\Lambda}$Be hypernucleus with the MPRM.

5.3.1 Properties of the nuclear core ^{8}Be

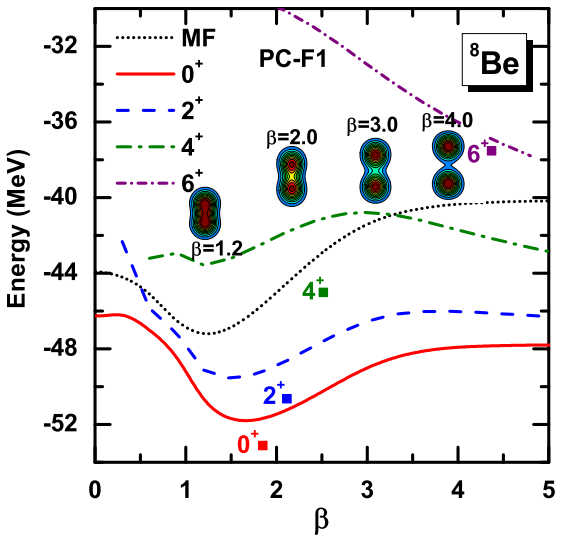

Fig. 5.16 Same as Fig. 2.2, but for ^{8}Be.

We first discuss properties of the core nucleus, ^{8}Be. Figure 5.16 displays the energy of mean-field states and the energy after projections onto good angular momentum for ^{8}Be as a function of the intrinsic quadrupole deformation β. The 2α cluster structure can be seen for deformations

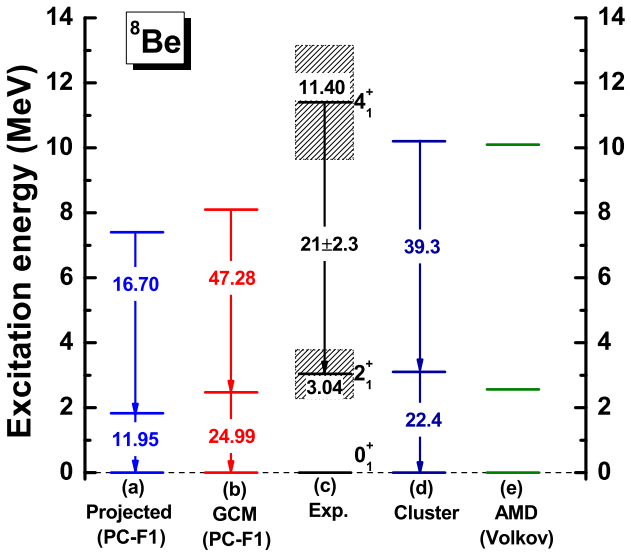

Fig. 5.17 The spectrum of ^{8}Be obtained with several methods, that is, the full GCM calculation, the projected calculation based on one single-configuration (β= 1.2), the alpha cluster model [31], and anti-symmetrized molecular dynamics (AMD) [145]. The PC-F1 interaction is used for the GCM and the projected calculations. The excitation energies are given in units of MeV. The solid arrows are the quadrupole transition strength $B(E2)$ (e^2 fm^4). The experimental data are taken from Refs. [146, 147].

larger than the minimum ($\beta = 1.2$) of mean-field energy curve. After restoration of rotational symmetry ($I = 0$), the energy minimum is found at $\beta = 1.5$. With the increase of angular momentum I, the minimum on the energy curve becomes shallower and eventually disappears at $I = 6$. It implies that the 6^+ state in ^{8}Be is unstable against the 2α fission, which is consistent with the experimental data.

The results of the full GCM calculation for ^{8}Be are shown in Fig. 5.17(b), which are compared with those of the projected calculation based on one single configuration (β= 1.2) as shown in Fig. 5.17(a). These energies are in a reasonable agreement with the experimental data shown in Fig. 5.17(c) [146], although they are slightly smaller than the observed energies as well as cluster model [31] and AMD [145] calculations (see Fig. 5.17 (d) and (e)). Notice that both the 2^+ and 4^+ states in ^{8}Be are resonance states having large widths in the continuum spectrum. A proper treatment of the scattering boundary condition, instead the harmonic oscillator expansion which we employ, would be necessary to describe them in a consistent manner. For the GCM calculation, we show the ^{8}Be energy levels calculated by superposing mean-field states within the range of deformation parameters of $\beta \in [-0.9, 5.1]$, which better describes the $^{9}_{\Lambda}$Be, even though we could reproduce the excitation energy of the 2^+ state of ^{8}Be by choosing different mesh points in the deformation parameter in the range of $\beta \in [-0.9, 4.2]$.

The calculated E2 transition strengths for $2^+ \to 0^+$ and $4^+ \to 2^+$ in ^{8}Be are 25.0 e^2fm^4 and 47.3 e^2fm^4, respectively, which are slightly larger than the values 22.4 e^2fm^4 and 39.3 e^2fm^4 obtained with the cluster model calculation [31]. Both our method and the cluster model calcu-

lations overestimate the recently measured $B(E2:4^+ \to 2^+)$ value, $21 \pm 2.3\ e^2\mathrm{fm}^4$ [147], by a factor of about 2.

5.3.2 Projected potential energy surface of ${}^{9}_{\Lambda}$Be

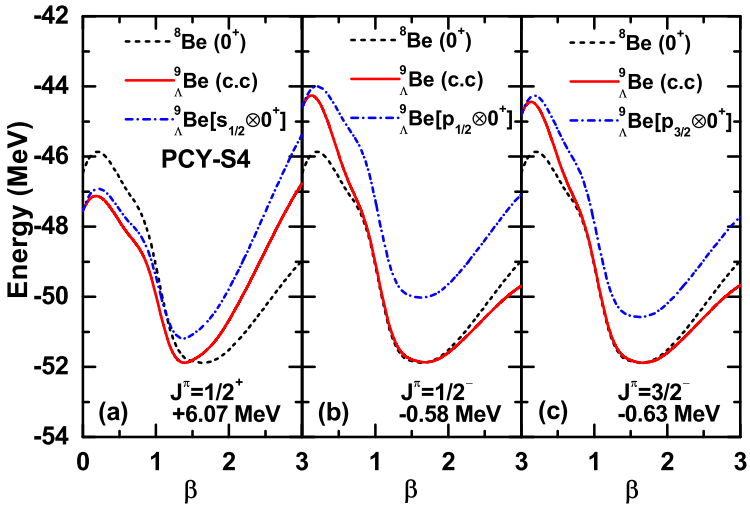

Fig. 5.18 Same as Fig. 5.2 but for ^{8}Be and ${}^{9}_{\Lambda}$Be.

We next consider the structure of ${}^{9}_{\Lambda}$Be. Figure 5.18 shows the projected potential energy surface of hypernucleus ${}^{9}_{\Lambda}$Be for $J^\pi = 1/2^+, 1/2^-$ and $3/2^-$ obtained with the single-channel calculation (the dot-dashed lines) and the coupled-channel calculation (the solid lines) with the PCY-S4 force for the $N\Lambda$ effective interaction. The impurity effect of Λ hyperon on the potential energy curves in ${}^{9}_{\Lambda}$Be is similar to that in ${}^{13}_{\Lambda}$C. That is, the potential energy surfaces with the coupled-channel calculation are lower than that with the single-channel calculation due to the effect of configuration mixing. The deformation parameter β for the potential energy minimum is altered from 1.64 to 1.39 by adding a Λ particle in the positive-parity state, $J^\pi = 1/2^+$. For the negative parity states $J^\pi = 1/2^-$ and $3/2^-$, the energy curves have a prolate minimum with β larger than that of ^{8}Be. The shift in the deformation parameter is more significant for ${}^{9}_{\Lambda}$Be than for ${}^{13}_{\Lambda}$C due to the smaller mass number.

5.3.3 Low-lying spectrum of ${}^{9}_{\Lambda}$Be

Single-channel calculation

The low-lying spectra of ${}^{9}_{\Lambda}$Be obtained with the single-channel calculation, in which the Λ particle is restricted to the $s_{1/2}$, $p_{1/2}$, and $p_{3/2}$ orbitals, are shown in the columns (c), (d), and (e) in Fig. 5.19, respectively. When the Λ hyperon in the $s_{1/2}$ orbit couples to the core excitation states of 2^+_1 and 4^+_1, the degenerate $(3/2^+, 5/2^+)$ and $(7/2^+, 9/2^+)$ doublet states are yielded in ${}^{9}_{\Lambda}$Be, respectively. One finds that the excitation energies of these two doublet states are slightly larger than those of the corresponding excited states of the core nucleus. This is due to the fact

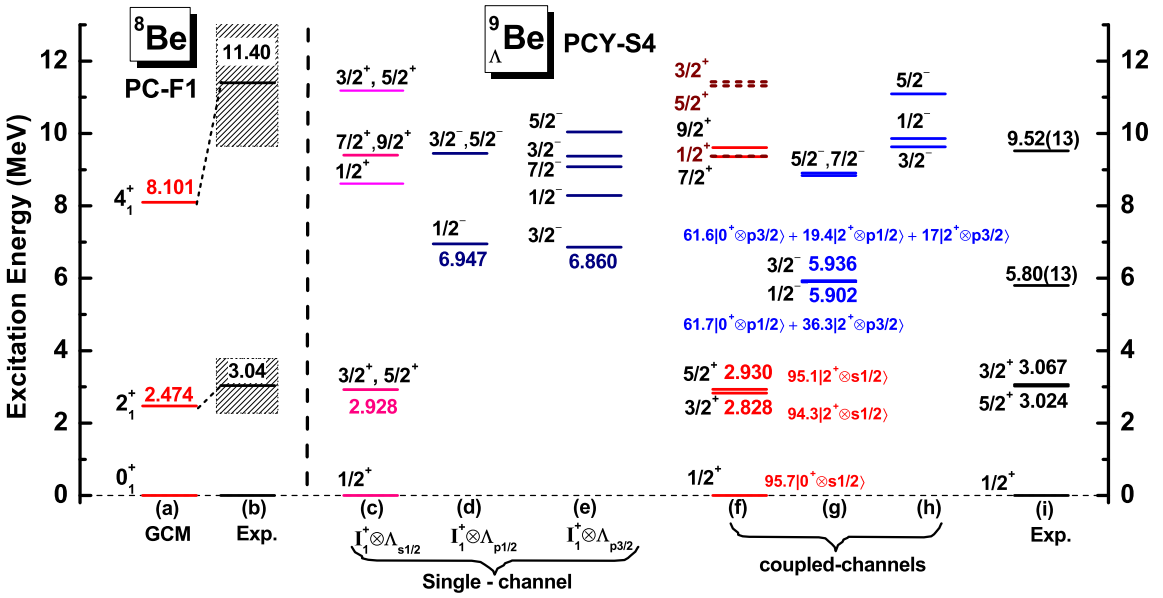

Fig. 5.19 Same as Fig. 5.7, but for ^{8}Be and ${}^{9}_{\Lambda}$Be. The experimental data for ^{8}Be shown in the column (b) are taken from Ref. [146]. The experimental data for ${}^{9}_{\Lambda}$Be shown in the column (i) are taken from Refs. [8, 21, 148]. The results of single-channel calculation for ${}^{9}_{\Lambda}$Be with the Λ particle in the $s_{1/2}$, $p_{1/2}$ and $p_{3/2}$ orbitals are plotted in the columns (c), (d), and (e), respectively. The dashed lines shown in the column (f) represent the second states for each spin-parity J^{π}.

that the ground state gains more energy from the $N\Lambda$ interaction than the other excited states. For the Λ particle in the $p_{1/2}$ and $p_{3/2}$ orbitals, one obtains the lowest negative parity $1/2^{-}$ and $3/2^{-}$ states in ${}^{9}_{\Lambda}$Be, with the $1/2^{-}$ state being higher than the $3/2^{-}$ state by 87 keV.

In the column (e) in Fig. 5.19, the $1/2^{-}_{1}$, $7/2^{-}_{1}$, $3/2^{-}_{2}$, and $5/2^{-}_{1}$ states around 10 MeV are generated from the $[\Lambda_{p3/2} \otimes 2^{+}_{1}]$ configuration. One can see that the order of these states is opposite to that in ${}^{13}_{\Lambda}$C (see Fig. 5.4 (f)). As we have discussed in section 5.2.2 for ${}^{13}_{\Lambda}$C, the order of these states is due to the reorientation effect, that is, the diagonal component for the quardupole term in the coupling potential in the coupled-channels equations. Different ordering of the $[\Lambda_{p3/2} \otimes 2^{+}_{1}]$ multiple states in these two hypernuclei is due to the different properties of the core nuclei, i.e., ^{8}Be and ^{12}C. That is, ^{8}Be is well-deformed with a much larger transition density $\rho^{02}_{2}(r)$, as shown in Fig. 5.20(a), than that in ^{12}C, shown in Fig. 2.5(b). The transition density $\rho^{22}_{2}(r)$ in ^{8}Be (see Fig. 5.20(b)) has an opposite sign to that in ^{12}C (see Fig. 2.5(d)), reflecting the fact that the sign of quadrupole moment is opposite (that is, prolate deformation for ^{8}Be and oblate deformation for ^{12}C). This results in the ordering of the $[\Lambda_{p3/2} \otimes 2^{+}_{1}]$ multiplet states in ${}^{9}_{\Lambda}$Be which is opposite to that in ${}^{13}_{\Lambda}$C. Notice that, because the $1/2^{-}$ state is lowered down within the $[\Lambda_{p3/2} \otimes 2^{+}_{1}]$ multiplets, the $1/2^{-}$ state in Fig. 5.19(d) and the $1/2^{-}$ state in Fig. 5.19(e) are close to each other, inducing a large configuration mixture in $1/2^{-}$ state with the coupled-channel calculation, as we discuss in the next sub-section.

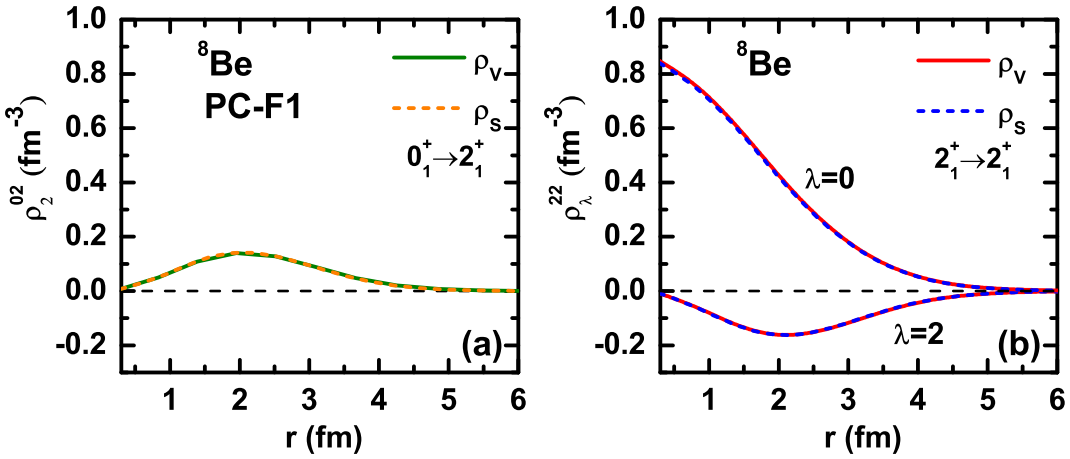

Fig. 5.20 The vector transition density, given by Eq.(2.61a), and the scalar transition density, given by Eq.(2.61b), for ^{8}Be.

In contrast to the $[\Lambda_{p3/2} \otimes 2^+_1]$ multiplets, when the Λ particle in the $p_{1/2}$ orbit couples to the 2^+_1 state of the core nucleus, the quadrupole term does not contribute, and the degenerate doublet states $(3/2^-, 5/2^-)$ are obtained (see Fig. 5.19(d) and also Fig. 5.4 (e)).

Coupled-channel calculation

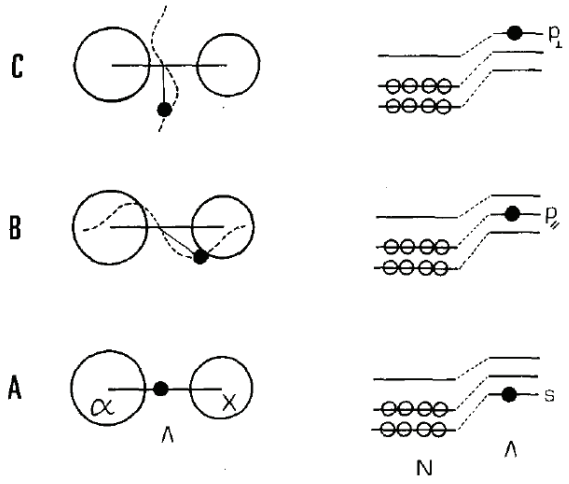

Fig. 5.21 A schematic picture taken from Ref. [31] for Λ particle occupying the $s-$orbit(A), the p-orbit parallel to the $\alpha - \alpha$ deformation axis (B) and the p-orbit perpendicular to the $\alpha - \alpha$ deformation axis. Here x means the α cluster.

The low-energy spectra of $^{9}_{\Lambda}$Be obtained with the coupled-channels calculations are shown in the columns (f), (g), and (h) in Fig. 5.19. They are compared with the available data [21, 148] shown in the column (i) in Fig. 5.19. A good agreement with the experiment data is obtained with our MPRM calculations. According to our calculations, the experimentally observed level

Table 5.5 Same as Table 5.3, but for ${}^{9}_{\Lambda}$Be with PCY-S4 force.

J^π	E	$(l\ j)\otimes I^\pi_n$	P_{jlI_n}	$E^{(0)}_{\rm 1ch}$	J^π	E	$(l\ j)\otimes I^\pi_n$	P_{jlI_n}	$E^{(0)}_{\rm 1ch}$
$1/2^+_1$	0.000	$s_{1/2}\otimes 0^+_1$	0.957	0.000	$1/2^-_1$	5.902	$p_{1/2}\otimes 0^+_1$	0.617	6.947
							$p_{3/2}\otimes 2^+_1$	0.363	8.284
$3/2^+_1$	2.828	$s_{1/2}\otimes 2^+_1$	0.943	2.928	$3/2^-_1$	5.936	$p_{3/2}\otimes 0^+_1$	0.616	6.860
							$p_{1/2}\otimes 2^+_1$	0.194	9.451
							$p_{3/2}\otimes 2^+_1$	0.170	9.375
$5/2^+_1$	2.930	$s_{1/2}\otimes 2^+_1$	0.951	2.928	$5/2^-_1$	8.836	$p_{3/2}\otimes 2^+_1$	0.214	10.041
$7/2^+_1$	9.362	$s_{1/2}\otimes 4^+_1$	0.903	9.404			$p_{1/2}\otimes 2^+_1$	0.658	9.451
$9/2^+_1$	9.609	$s_{1/2}\otimes 4^+_1$	0.922	9.404			$p_{3/2}\otimes 4^+_1$	0.103	14.299
$1/2^+_2$	9.376	$s_{1/2}\otimes 0^+_1$	0.994	8.617	$1/2^-_2$	9.858	$p_{1/2}\otimes 0^+_1$	0.427	6.947
							$p_{3/2}\otimes 2^+_1$	0.569	8.284
$3/2^+_2$	11.427	$d_{3/2}\otimes 0^+_1$	0.958	10.647	$3/2^-_2$	9.633	$p_{3/2}\otimes 0^+_1$	0.426	6.860
							$p_{1/2}\otimes 2^+_1$	0.255	9.451
							$p_{3/2}\otimes 2^+_1$	0.314	9.375
$5/2^+_2$	11.317	$d_{5/2}\otimes 0^+_1$	0.920	10.617	$5/2^-_2$	11.091	$p_{1/2}\otimes 2^+_1$	0.234	9.451
							$p_{3/2}\otimes 2^+_1$	0.761	10.041

at excitation energy of 5.80(13) MeV is actually a mixture of two negative-parity states with $J^\pi = 3/2^-$ and $1/2^-$.

The low-lying states of ${}^{9}_{\Lambda}$Be can be categorized into three rotational bands according to the calculated $B(E2)$ values. Figure 5.21 shows the intrinsic structures of hypernuclear states for these three rotational bands based on the cluster model [31]. The states shown in Fig. 5.19 (g) correspond to Λ particle occupying the p-orbit parallel to the $\alpha-\alpha$ deformation axis (see Fig. 5.21(B)). They do not have corresponding states in the ordinary nucleus due to the Pauli principle of the valence neutron, so these rotational state are called "genuine hypernuclear" states [31]. The states shown in Fig. 5.19(h) correspond to the Λ particle occupying the p-orbit perpendicular to the $\alpha-\alpha$ deformation axis, as shown in Fig. 5.21(C). The band for these states shares a similar structure as the ground band of ^{9}Be, except for the spin-orbit splitting, so we call it the "^{9}Be-analog band". The first positive-parity states for each spin J, that is the solid lines shown in Fig. 5.19(f), are dominated by the Λ hyperon occupying the s-orbit, corresponding to Fig. 5.21(A). Since the structure of these states is similar as the ground band of the core nucleus ^{8}Be, we call the band for these states the "^{8}Be-analog band".

Table 5.5 lists the values of the probability of the dominant components for a few low-lying states of ${}^{9}_{\Lambda}$Be. One obvious thing is that the states in the "^{8}Be-analog band" are almost pure with the $[\Lambda_{s1/2}\otimes I^+_1]$ configuration. On the other hand, appreciable configuration mixings are found for the negative-parity states. In the second positive parity states (J^+_2), except for the $1/2^+_2$ state, the Λ_d state is admixed appreciably. Also, there is a strong mixing between the $[\Lambda_{p_{1/2}}\otimes 0^+]$ and the $[\Lambda_{p_{3/2}}\otimes 2^+]$ configurations with similar weights for the first negative-parity state $1/2^-_1$. This large configuration mixing is because the reorientation effect brings the $[\Lambda_{p_{3/2}}\otimes 2^+]$ configuration close to the $[\Lambda_{p_{1/2}}\otimes 0^+]$ configuration in energy due to the prolate nature of the 2^+ state of ^{8}Be (see the discussion in the previous subsection). After mixing single-channel configurations, the

obtained $1/2^-_1$ state is slightly lower than the $3/2^-_1$ state by 34 keV. Our calculation reconfirms an interesting prediction of the cluster model, that is, the strong coupling of a hyperon to the collective rotation is realized when the Λ is in the p-orbit [31]. We also point out that the values of $P_{j\ell I}$ obtained in the present calculations are similar to those with the cluster model calculations shown in Fig. 2 of Ref. [31].

In our calculation, the excitation energy of the $3/2^+_1$ and $5/2^+_1$ states of ${}^{9}_{\Lambda}$Be is significantly larger than that of the 2^+ state of ^{8}Be, whereas the experimental data and the cluster model calculations indicate that this energy shift is negligibly small [149]. This discrepancy between the present calculation and the cluster model calculations might be due to the effects of higher members of the core excited states, which are not included in present calculations.

E2 transition strengths

Table 5.6 shows the calculated $E2$ transition strengths for low-lying states of ^{8}Be and ${}^{9}_{\Lambda}$Be. One can see that the E2 transition strengths in ${}^{9}_{\Lambda}$Be are not converged yet with the cut-off of core states $n_{\rm cut} = 1$. The second excitation states of 0^+, 2^+ and 4^+ have a large influence on the B(E2) value with our model. However, with the present implementation of GCM, we have a

Table 5.6 Same as Table 5.4, but for ^{8}Be and ${}^{9}_{\Lambda}$Be. The value in the parenthesis for ^{8}Be is the experimental data taken from Ref. [147]. The results of the cluster model are taken from Ref.[31].

^{8}Be		${}^{9}_{\Lambda}$Be							
			$n_{\rm cut}=1$			$n_{\rm cut}=2$			Cluster model
$I^\pi_i \to I^\pi_f$	$B(E2)$	$J^\pi_i \to J^\pi_f$	$B(E2)$	$cB(E2)$	$\Delta(\%)$	$B(E2)$	$cB(E2)$	$\Delta(\%)$	$\Delta(\%)$
$2^+_1 \to 0^+_1$	24.99	$3/2^+_1 \to 1/2^+_1$	25.09	25.09	+0.40	17.94	17.94	−28.21	−49.55
		$5/2^+_1 \to 1/2^+_1$	25.11	25.11	+0.48	17.91	17.91	−28.33	−49.55
$4^+_1 \to 2^+_1$	47.28	$7/2^+_1 \to 3/2^+_1$	40.82	45.36	−4.06	22.19	24.66	−47.84	−65.65
	(21 ± 2.3)	$7/2^+_1 \to 5/2^+_1$	4.56	45.56	−3.64	2.47	24.65	−47.86	−65.65
		$9/2^+_1 \to 5/2^+_1$	45.24	45.24	−4.31	24.46	24.46	−48.27	−65.65

limitation to construct the wave functions for the non-resonant core states (that is, the second and the third 0^+, 2^+, and 4^+ states), which extend up to large values of deformation parameter β.

In the experiment, the upper limit for the lifetime of 0.1 ps has been deduced for the first $3/2^+$ and $5/2^+$ states of ${}^{9}_{\Lambda}$Be[148], which corresponds to the B(E2) value larger than 29.07 e^2fm^4 [148, 8]. In our calculation, the E2 transition strength of $2^+ \to 0^+$ for the core nucleus in ${}^{9}_{\Lambda}$Be, that is $cB(E2)$, is slightly increased for $n_{\rm cut} = 1$ and is significantly reduced for $n_{\rm cut} = 2$, although the calculations with $n_{\rm cut} = 2$ may not be reasonable. We mention that the reduction in $B(E2)$ value with the present model is much smaller than the results of the cluster model calculations [31, 149].

5.3.4 Dependence on $N\Lambda$ interaction

The spectra of ${}^{9}_{\Lambda}$Be by the four parameter sets of $N\Lambda$ interaction are shown in Fig. 5.22. As one can see, the four parameter sets yield qualitatively similar low-lying spectra for ${}^{9}_{\Lambda}$Be. One important quantity is the energy splitting between the positive-parity $5/2^+_1$ and $3/2^+_1$ levels, which can be used to study the $N\Lambda$ spin-orbit splitting. The splitting between the $5/2^+_1$ and the $3/2^+_1$ states in ${}^{9}_{\Lambda}$Be has been measured by high-resolution γ-ray experiments, which have reported that the $5/2^+_1$ state is lower than $3/2^+_1$ state by 43 ± 5keV [8]. In our calculation, the $5/2^+_1$ state is higher than the $3/2^+_1$ state for all the four parameter sets. It has been pointed out that the splitting of the doublet states ($5/2^+_1$ and $3/2^+_1$) is dominated by the spin-spin coupling [142], which is missing in the present calculations. The splitting between the positive parity doublet states $5/2^+_1$ and $3/2^+_1$ in ${}^{9}_{\Lambda}$Be are larger than that in ${}^{13}_{\Lambda}$C due to the light mass number for ${}^{9}_{\Lambda}$Be.

The energy ordering of the first $1/2^-$ and the first $3/2^-$ states depends on the parameter sets, that is, the first $1/2^-$ state is lower than the first $3/2^-$ state with the PCY-S1 and PCY-S4 forces, while the first $1/2^-$ state is higher than the first $3/2^-$ state with the PCY-S2 and PCY-S3 forces. A small splitting between the $3/2^-_1$ and $1/2^-_1$ states is found in our calculation for ${}^{9}_{\Lambda}$Be, although it does not directly reflect the $N\Lambda$ spin-orbit splitting because of a strong mixing between the $[\Lambda_{p_{1/2}} \otimes 0^+]$ and the $[\Lambda_{p_{3/2}} \otimes 2^+]$ configurations in the $1/2^-_1$ state.

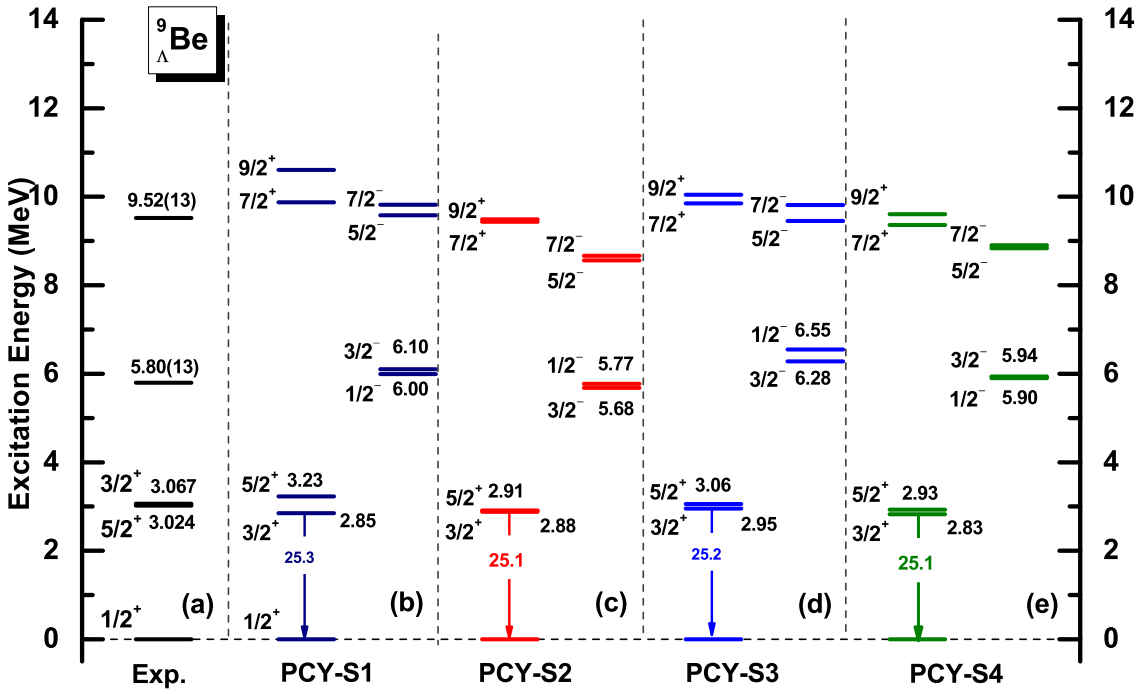

Fig. 5.22 Same as Fig. 5.9, but for ${}^{9}_{\Lambda}$Be. The experimental data for ${}^{9}_{\Lambda}$Be are taken from Refs. [8, 21, 148].

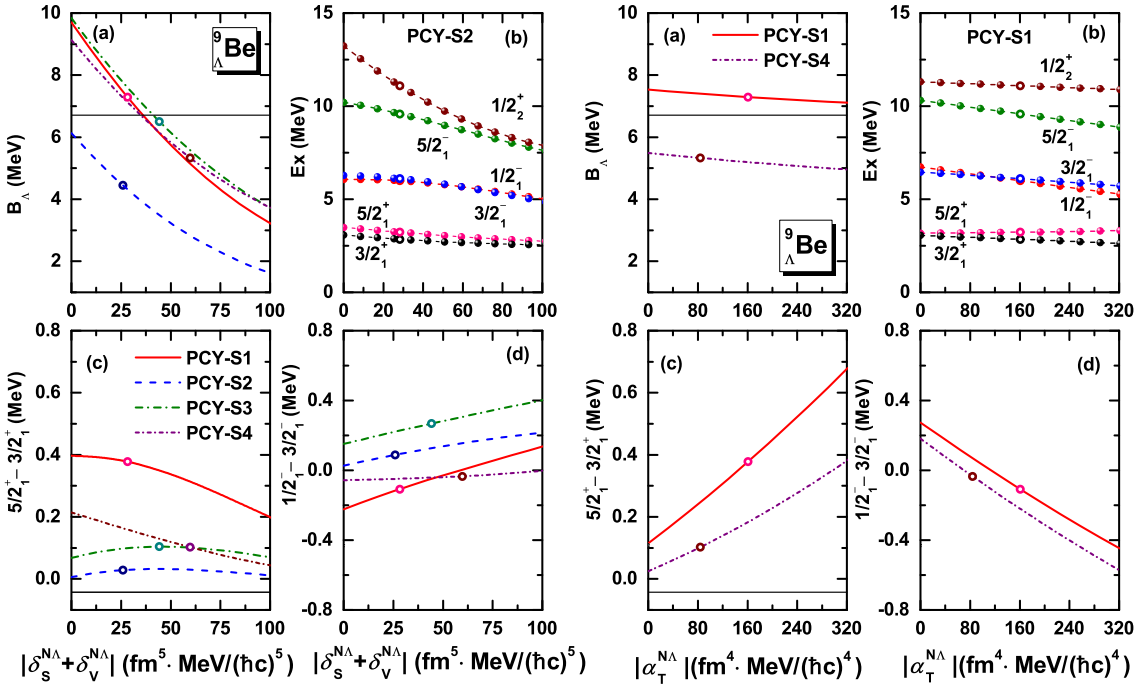

Fig. 5.23 Same as Figs. 5.12 and 5.15 but for $^{9}_{\Lambda}$Be.

Figure 5.23 shows the impact of the higher-order derivative and the tensor terms on the low-lying states of $^{9}_{\Lambda}$Be. The effects of the derivative and the tensor terms on the spectrum of $^{9}_{\Lambda}$Be are similar to those in $^{13}_{\Lambda}$C shown in Figs. 5.12 and 5.15. Moreover, the energy ordering of the $3/2^+_1$ and $5/2^+_1$ states in $^{9}_{\Lambda}$Be cannot be reproduced by the present effective $N\Lambda$ interaction. In order to reproduce it, the four-fermion coupling terms $(\bar{\psi}_N\Gamma_i\psi_N)(\bar{\psi}_\Lambda\Gamma_i\psi_\Lambda)$ with $\Gamma_i = \sigma_{\mu\nu}$ and $\gamma_\mu\gamma^5$, which provides the spin-spin $N\Lambda$ interaction [150] $(\bar{\psi}_N\boldsymbol{\sigma}\psi_N)(\bar{\psi}_\Lambda\boldsymbol{\sigma}\psi_\Lambda)$, would have to be taken into account. This term is not included in the present study, and it is an interesting future work to study the influence on the energy ordering of the $3/2^+_1$ and $5/2^+_1$ states.

5.4 Application to $^{21}_{\Lambda}$Ne

We next consider hypernuclei in the *sd*-shell region. In particular, we intend to study the $^{21}_{\Lambda}$Ne hypernucleus. In order to study the nucleon-nucleon interaction parameter set dependence, we employ both the PC-F1 and PC-PK1 sets for ^{20}Ne.

5.4.1 Properties of the nuclear core ^{20}Ne

The mean-field energy and the projected energy curves for ^{20}Ne obtained with the PC-F1 and PC-PK1 parameter sets are shown in Fig. 5.24(a) and Fig. 5.24(b), respectively. One can see that the mean-field energy curve for the PC-F1 force has a higher barrier at the spherical shape than that for the PC-PK1 force. The energy minimum of the mean-field energy curves are located at deformation $\beta = 0.53$ for both PC-F1 and PC-PK1 sets, while two prolate minima appear in the

projected energy curve for $I^\pi = 0^+$. Both PC-F1 and PC-PK1 sets yield almost the same β for the minima for $I^\pi = 0^+$, that is $\beta = 0.39$ and $\beta = 0.67$.

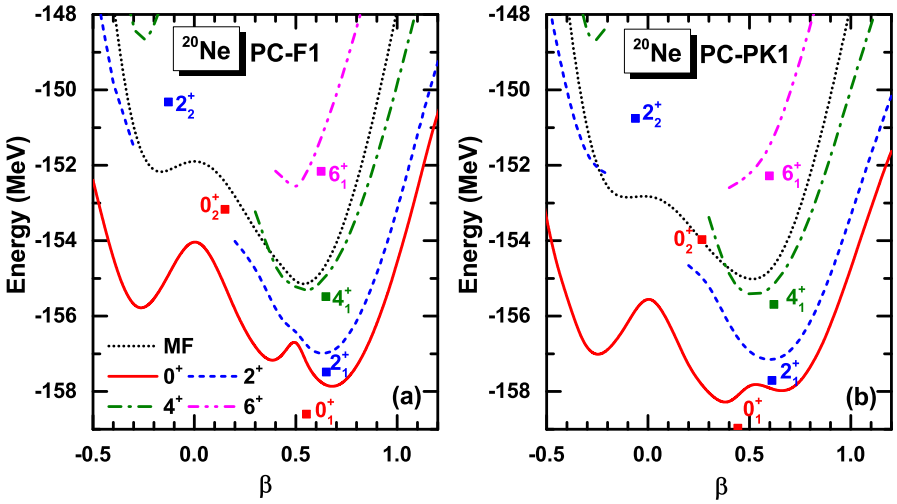

Fig. 5.24 Same as Fig. 2.1, but for ^{20}Ne with PC-F1 and PC-PK1 parameter sets.

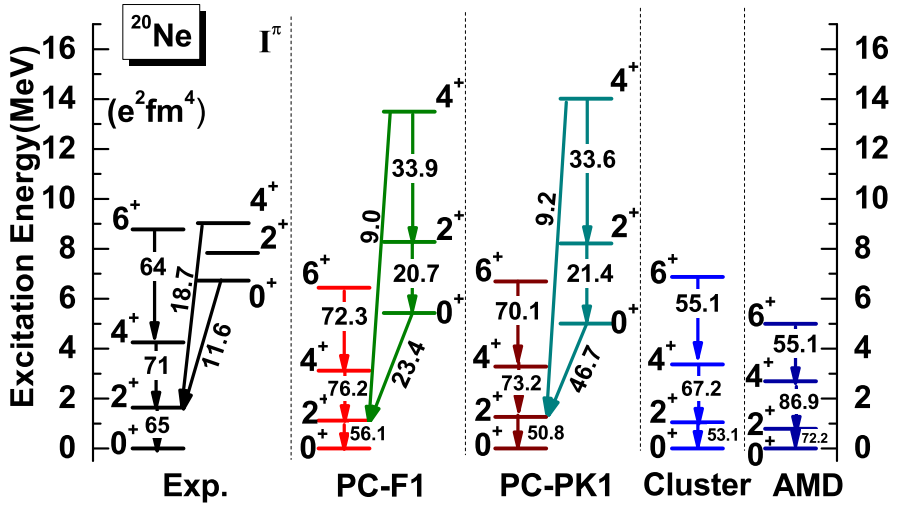

Fig. 5.25 A comparison of the excitation energy of low-lying states of ^{20}Ne obtained with several methods. The results of the cluster model and the AMD are taken from Refs. [151] and [38], respectively. The experimental data for ^{20}Ne are taken from Ref. [139].

Figure 5.25 shows the calculated low-lying states of ^{20}Ne, in comparison with the results of α+^{16}O cluster model [151] and the AMD model [38]. One can see that all these models reproduce the rotational character of the yrast states, although they overestimate the moment of inertia. The experimental data of the second excited states of each angular momentum exhibits vibrational feature, $\dfrac{E(4_2^+) - E(0_2^+)}{E(2_2^+) - E(0_2^+)} = 2.08$, which can only be described by exciting the ^{16}O cluster itself [151]. This character was not obtained in AMD model and is not reproduced in our GCM calculation, either. Notice that, for simplicity, in the present calculations, we have

assumed reflection symmetry for ^{20}Ne, even though the ^{20}Ne nucleus has prominent negative-parity bands originated from the α+^{16}O structure. The inclusion of these negative parity states in the coupled-channels calculations is thus beyond the scope of the present thesis.

5.4.2 Projected potential energy surface of ${}^{21}_{\Lambda}$Ne

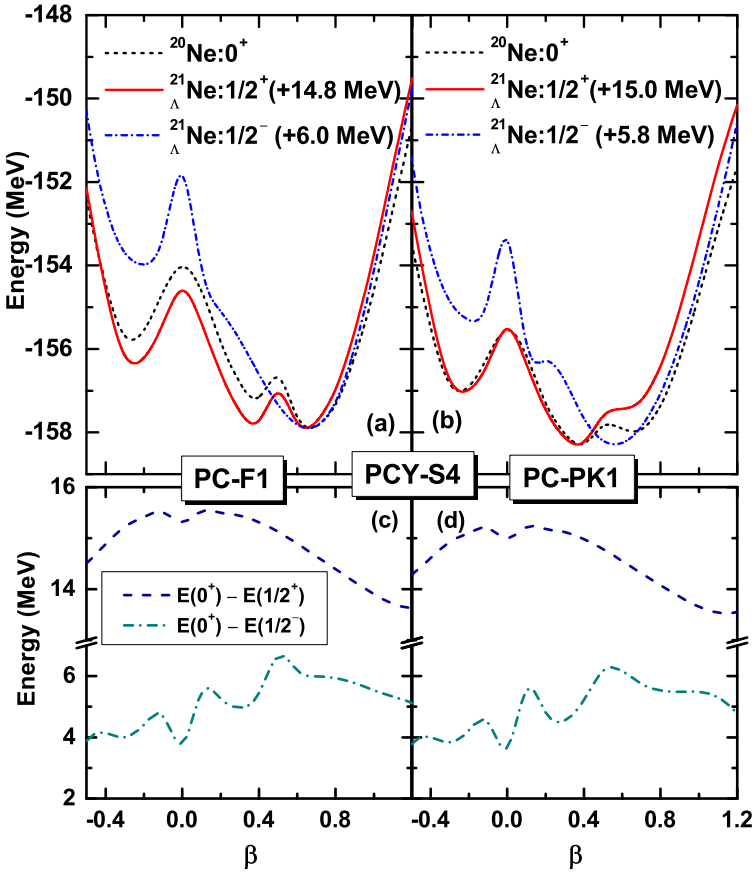

Fig. 5.26 (a) and (b): The potential energy surface $E_J(\beta)$ for the $J^\pi = 1/2^+$ (the solid line) and $1/2^-$ (the dot-dashed line) states in ${}^{21}_{\Lambda}$Ne as a function of the deformation β obtained with the PC-F1 force (Fig. 5.26 (a)) and the PC-PK1 force (Fig. 5.26 (b)) for the NN interaction. These are obtained with the PCY-S4 force for the $N\Lambda$ interaction. In order to make a comparison easy, each hypernuclear curve is shifted by a constant value so that the energy at the absolute minimum coincides with that for ^{20}Ne with I^π =0^+. (c) and (d): The difference between the energy curve of ${}^{21}_{\Lambda}$Ne and that of ^{20}Ne for the PC-F1 and PC-PK1 forces, respectively.

Figure 5.26 shows the obtained energy curve $E_J(\beta)$ for the PCY-S4 force for $N\Lambda$ interaction for the $J^\pi = 1/2^+$ and $1/2^-$ states in ${}^{21}_{\Lambda}$Ne as a function of the deformation β of the core nucleus. The left and the right panels show the result with the PC-F1 and PC-PK1 forces for NN interaction, respectively. For PC-F1, the hypernuclear energy curve for spin-parity of $1/2^+$ and $1/2^-$ has a prolate minimum with a smaller β compared to the 0^+ state of ^{20}Ne. On the other hand, for PC-PK1, the value of β at the energy minimum decreases for the $1/2^+$ configuration while that for the $1/2^-$ configuration increases as compared to the deformation for ^{20}Ne with

0^+. Notice that the energy surface for $1/2^-$ has a higher barrier at the spherical shape than the barrier for ^{20}Ne for both the interactions. This indicates that $^{21}_{\Lambda}$Ne with $1/2^+$ and $1/2^-$ has a smaller and a larger collectivity than that of ^{20}Ne. The energy differences between the $1/2^+$ state in $^{21}_{\Lambda}$Ne and the ground state of ^{20}Ne, as well as the $1/2^-$ state in $^{21}_{\Lambda}$Ne and the ground state of ^{20}Ne, are shown in Figs. 5.26 (c) and 5.26 (d), respectively. Those energy curves are qualitatively similar to each other, even though the PC-F1 and PC-PK1 forces predict somewhat different energy curves.

5.4.3 Low-lying spectrum of $^{21}_{\Lambda}$Ne

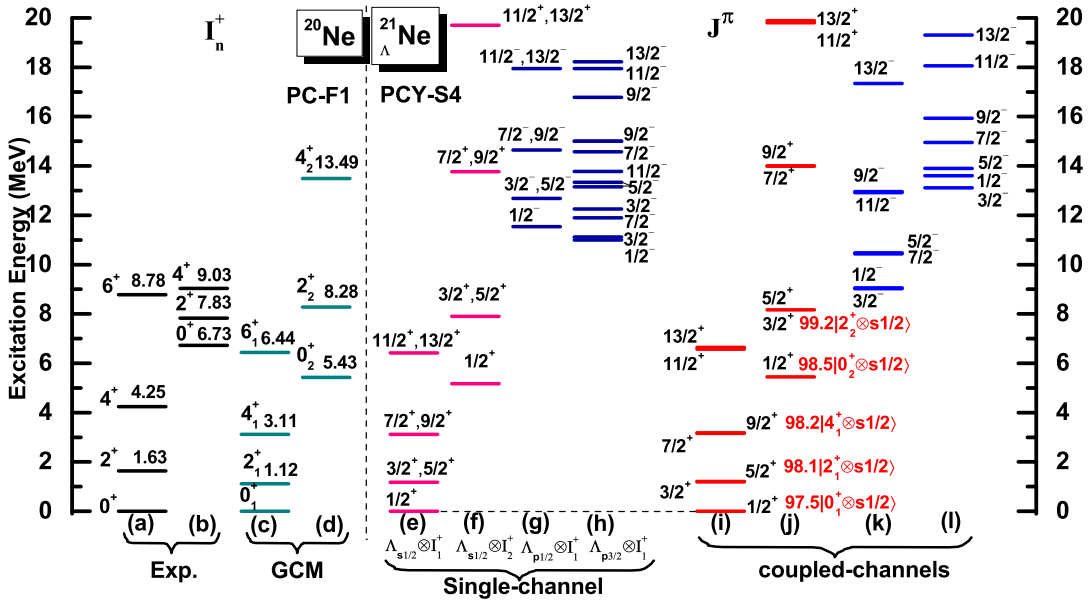

Fig. 5.27 Same as Fig. 5.7, but for ^{20}Ne and $^{21}_{\Lambda}$Ne. The experimental data for ^{20}Ne are taken from Ref. [139].

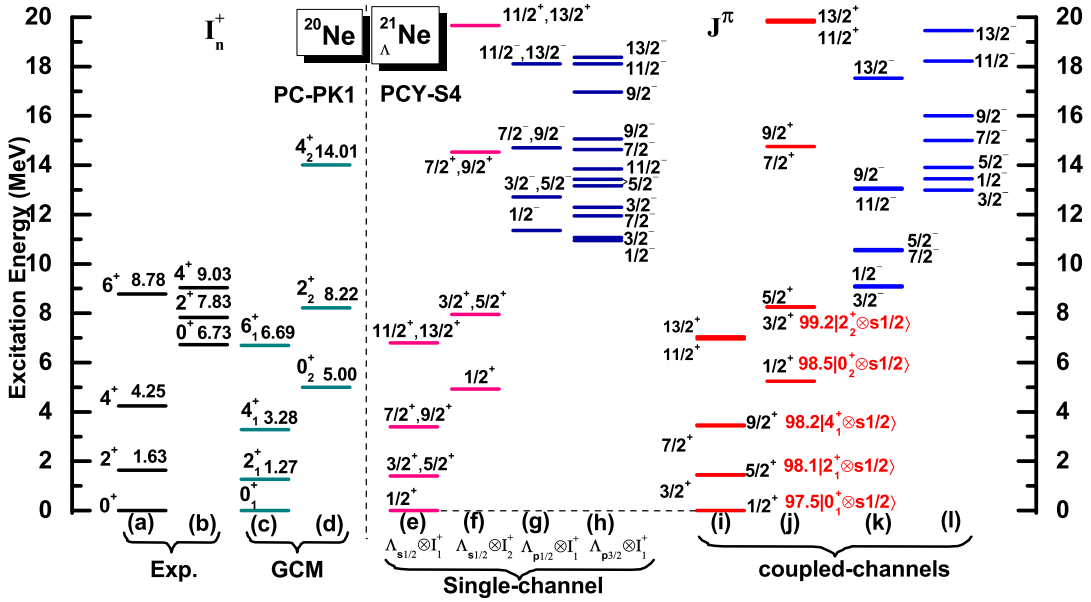

Fig. 5.28 Same as Fig. 5.27, but with PC-PK1 instead of PC-F1 for the NN interaction.

The Λ binding energy of ${}^{21}_{\Lambda}$Ne obtained by the MPRM calculation is 14.92 MeV and 15.10 MeV for the PC-F1 and PC-PK1 force, respectively. Figure 5.27 and 5.28 show the low-lying states of ${}^{21}_{\Lambda}$Ne with the PC-F1 and PC-PK1 forces, respectively. In order to investigate the channel-coupling effect on hypernuclear states, we also show the results obtained with the single-channel calculations. One can see that the results of the coupled-channels calculations for the positive parity states plotted in the columns (i) and (j) are close to the results of the single-channel calculation shown in the columns (e) and (f) both in Figs. 5.27 and 5.28.

From the probability of the main components for each states, shown in Table 5.7, one can see that these states are dominated by the configuration of $\Lambda_{s1/2}$ coupled to the state I in the first ($n = 1$) and the second ($n = 2$) bands in ^{20}Ne with the weight larger than 97% . Moreover, it is seen that the spectrum of the positive-parity states in ${}^{21}_{\Lambda}$Ne is close to that of ^{20}Ne with similar excitation energies. This means that for the positive parity states the presence of an s orbit Λ hyperon does not change significantly the low-energy structure of the core nucleus ^{20}Ne.

Table 5.7 Same as Table 5.3, but for the ${}^{21}_{\Lambda}$Ne hypernucleus with the PC-F1 and PC-PK1 forces for NN interaction and the PCY-S4 force for $N\Lambda$ interaction.

		PC-F1			PC-PK1		
J^π	$(l\ j)\otimes I^\pi_n$	E	P_{jlI_n}	$E^{(0)}_{\rm 1ch}$	E	P_{jlI_n}	$E^{(0)}_{\rm 1ch}$
$1/2^+_1$	$s_{1/2}\otimes 0^+_1$	0.000	0.975	0.000	0.000	0.971	0.000
$3/2^+_1$	$s_{1/2}\otimes 2^+_1$	1.198	0.980	1.173	1.444	0.980	1.407
$5/2^+_1$	$s_{1/2}\otimes 2^+_1$	1.210	0.981	1.173	1.454	0.980	1.407
$7/2^+_1$	$s_{1/2}\otimes 4^+_1$	3.157	0.980	3.123	3.437	0.980	3.394
$9/2^+_1$	$s_{1/2}\otimes 4^+_1$	3.184	0.982	3.123	3.465	0.982	3.394
$1/2^+_2$	$s_{1/2}\otimes 0^+_2$	5.447	0.985	5.169	5.243	0.981	4.924
$3/2^+_2$	$s_{1/2}\otimes 2^+_2$	8.164	0.992	7.898	8.245	0.991	7.956
$5/2^+_2$	$s_{1/2}\otimes 2^+_2$	8.172	0.992	7.898	8.260	0.992	7.956
$1/2^-_1$	$p_{3/2}\otimes 2^+_1$	9.055	0.559	10.996	9.104	0.532	11.064
	$p_{1/2}\otimes 0^+_1$		0.416	11.541		0.442	11.357
$3/2^-_1$	$p_{3/2}\otimes 0^+_1$	9.022	0.460	11.117	9.064	0.489	10.942
	$p_{3/2}\otimes 2^+_1$		0.263	12.258		0.247	12.297
	$p_{1/2}\otimes 2^+_1$		0.252	12.680		0.240	12.711
$5/2^-_1$	$p_{1/2}\otimes 2^+_1$	10.474	0.455	12.680	10.578	0.459	12.711
	$p_{3/2}\otimes 4^+_1$		0.360	13.342		0.356	13.425
	$p_{3/2}\otimes 2^+_1$		0.159	13.149		0.160	13.167
$7/2^-_1$	$p_{3/2}\otimes 2^+_1$	10.436	0.648	11.899	10.539	0.652	11.946
	$p_{1/2}\otimes 4^+_1$		0.192	14.647		0.191	14.711
	$p_{3/2}\otimes 4^+_1$		0.136	14.573		0.134	14.640

The columns (k) and (l) show the negative-parity states in ${}^{21}_{\Lambda}$Ne. Comparing the columns (k,l) with the columns (g,h) for the single-channel calculations, one sees that the channel-coupling effect plays an important role in their excitation energies. Moreover, we note that the energy difference between the first $1/2^-$ and $3/2^-$ states is about 33keV and 40keV for the PC-F1 and the PC-PK1, respectively. For the $1/2^-$ state, there is a strong admixture of the configurations

$[\Lambda_{p1/2} \otimes 0^+_1]$ and $[\Lambda_{p3/2} \otimes 2^+_1]$. On the other hand, the $3/2^-$ state is a strong admixture of the configurations $[\Lambda_{p3/2} \otimes 0^+_1]$, $[\Lambda_{p3/2} \otimes 2^+_1]$ and $[\Lambda_{p1/2} \otimes 2^+_1]$. Similar to ${}^{9}_{\Lambda}$Be, the splitting of the $1/2^-$ and $3/2^-$ levels in ${}^{21}_{\Lambda}$Ne does not reflect the strength of the Λ spin-orbit splitting, which is different from the case in ${}^{13}_{\Lambda}$C. The underlying reason for this strong mixing in ${}^{21}_{\Lambda}$Ne is similar to what we have discussed in ${}^{9}_{\Lambda}$Be, i.e., ^{20}Ne is prolately deformed with a large transition density $\rho_2^{02}(r)$, see Figs. 5.29 and 5.30. Notice also that the energy ordering of the $[\Lambda_{p3/2} \otimes 2^+_1]$ multiplet states is the same as that in ${}^{9}_{\Lambda}$Be and opposite to that in ${}^{13}_{\Lambda}$C, reflecting the fact that the sign of quadrupole moment is the same as ^{8}Be and opposite to ^{12}C.

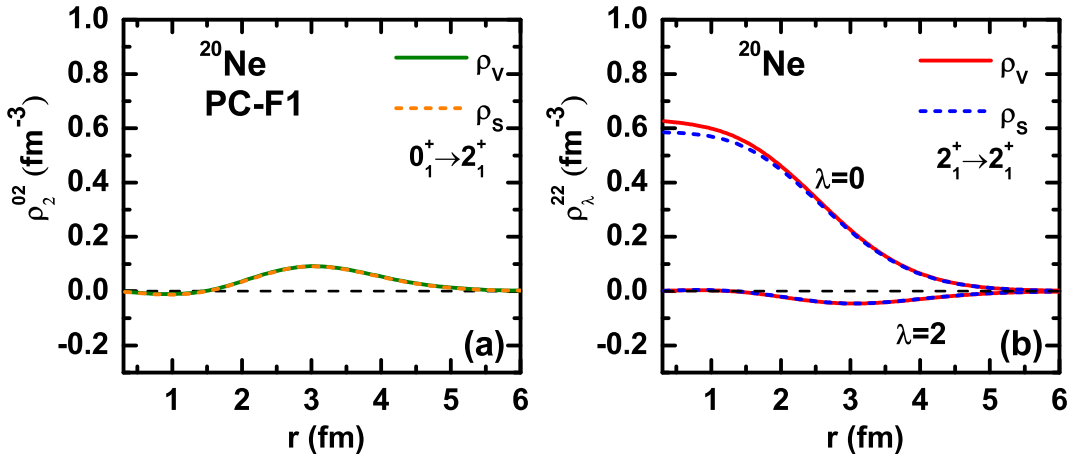

Fig. 5.29 The same as in Fig. 5.20, but for ^{20}Ne.

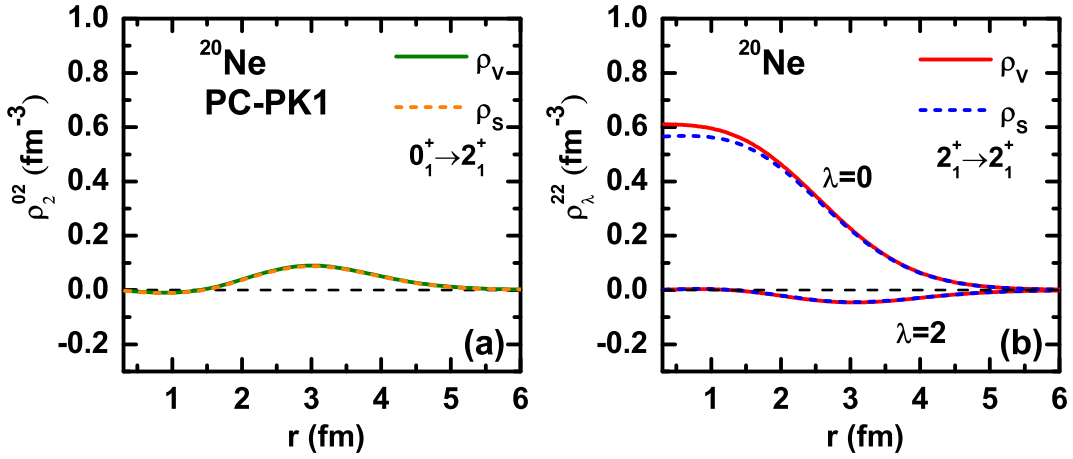

Fig. 5.30 Same as Fig. 5.29, but with PC-PK1 instead of PC-F1 for the NN interaction.

Figure 5.31 shows a comparison of the low-energy excitation spectra of ${}^{21}_{\Lambda}$Ne obtained with the cluster model [151], the AMD [38], and the present MPRM calculations based on the PC-F1 and PC-PK1 interactions. The positive-parity band in the MPRM is closer to the result of the cluster model as compared to the result of AMD, which has a slightly larger moment of inertia. The negative-parity states are similar to the AMD results but with lower excitation energies,

which might be due to the large channel-coupling effect taken explicitly into account in the present work, see Figs. 5.27 and 5.28 as well as Table 5.7.

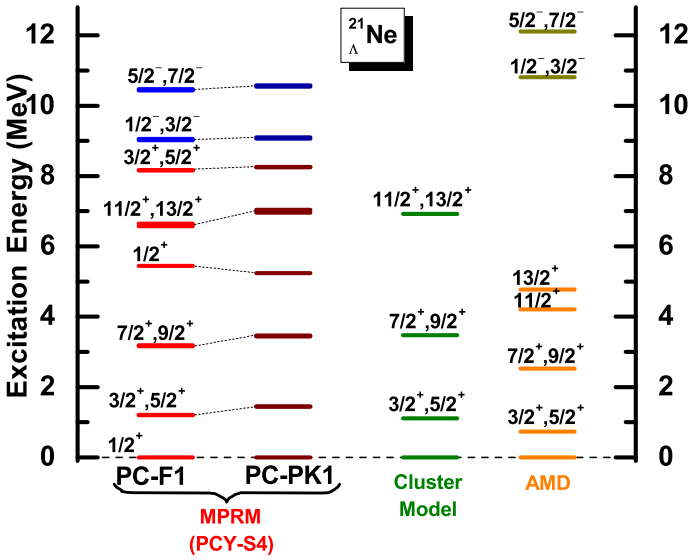

Fig. 5.31 A comparison of the low-energy excitation spectra of $^{21}_{\Lambda}$Ne obtained with the cluster model [151], the AMD [38], and the present MPRM calculations with the PC-F1 and PC-PK1 forces.

E2 transition strengths

Table 5.8 lists the $E2$ transition strengths for the low-lying states of $^{21}_{\Lambda}$Ne with the PC-F1 and PC-PK1 forces. For comparison, the table also shows the change in $B(E2)$ from ^{20}Ne to $^{21}_{\Lambda}$Ne obtained with the cluster model [151], and the AMD [38]. The $B(E2)$ value decreases by adding a Λ hyperon in s-orbit in all of these calculations. However, the cluster model and the AMD model predict larger reductions compared to the MPRM. The shrinkage effect with the PC-PK1 force is more significantly than that with the PC-F1 force.

Table 5.8 The calculated $B(E2)$ values (in units of e^2 fm^4) for the low-lying states of $^{21}_{\Lambda}$Ne with the PC-F1 and the PC-PK1 forces for NN interaction and the PCY-S4 force for $N\Lambda$ interaction. The results for the change in the $B(E2)$ value from ^{20}Ne to $^{21}_{\Lambda}$Ne is compared with the results with the cluster model [151] and the AMD [38] calculations.

^{20}Ne			$^{21}_{\Lambda}$Ne								
	PC-F1	PC-PK1		PC-F1			PC-PK1			AMD	Cluster
$I_i^\pi \to I_f^\pi$	$B(E2)$	$B(E2)$	$J_i^\pi \to J_f^\pi$	$B(E2)$	$cB(E2)$	$\Delta(\%)$	$B(E2)$	$cB(E2)$	$\Delta(\%)$	$\Delta(\%)$	$\Delta(\%)$
$2_1^+ \to 0_1^+$	56.07	50.79	$3/2_1^+ \to 1/2_1^+$	52.67	52.67	−6.06	45.68	45.68	−10.07	−11.8	−23.9
			$5/2_1^+ \to 1/2_1^+$	52.66	52.66	−6.08	45.66	45.66	−10.10	−11.5	
$4_1^+ \to 2_1^+$	76.23	73.22	$7/2_1^+ \to 3/2_1^+$	65.77	73.08	−4.13	62.84	69.82	−4.64	−17.8	−22.6
			$7/2_1^+ \to 5/2_1^+$	7.31	73.08	−4.13	6.98	69.83	−4.64		
			$9/2_1^+ \to 5/2_1^+$	73.01	73.02	−4.21	69.78	69.78	−4.70	−13.0	

Parameter set dependence for the $N\Lambda$ interaction

Figure 5.32 shows the low-lying spectrum of the ${}^{21}_{\Lambda}$Ne hypernucleus obtained with the four force for $N\Lambda$ interaction and with the PC-F1 force for NN interaction. The four parameter sets give similar spectrum and E2 transition strength to each other, except for the fine structure of the hypernuclear spectrum. The positive parity doublets are almost degenerate due to the large mass number of ${}^{21}_{\Lambda}$Ne. The first $1/2^-$ state is higher than the first $3/2^-$ state except for the PCY-S1 force due to the large tensor coupling strength in the PCY-S1 force.

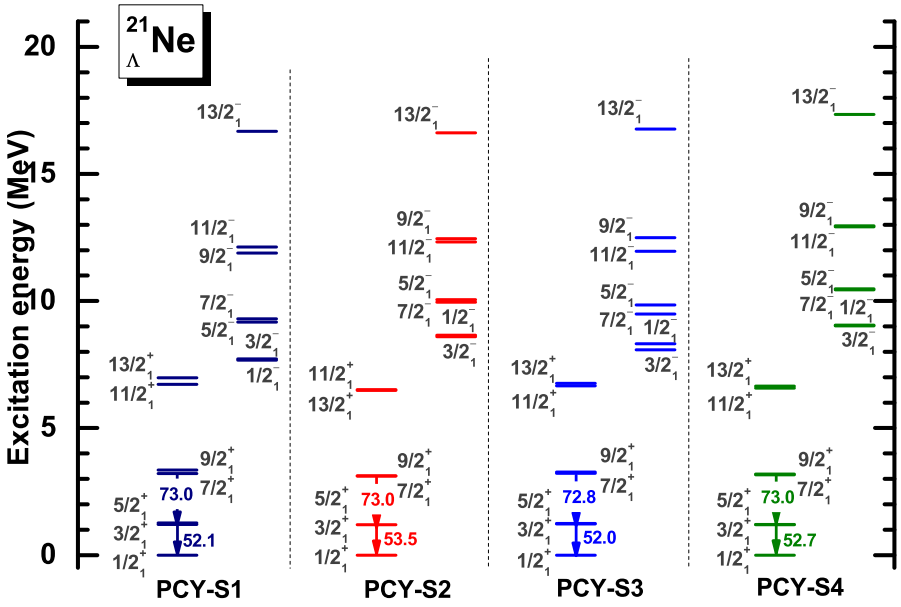

Fig. 5.32 Same as Fig. 5.9, but for ${}^{21}_{\Lambda}$Ne hypernucleus.

5.5 Application to ${}^{31}_{\Lambda}$Si

5.5.1 Properties of the nuclear core ^{30}Si

We next discuss an oblately deformed hypernucleus ${}^{31}_{\Lambda}$Si in the *sd*-shell region. Figure 5.33 shows the mean-field and the projected energy curves for ^{30}Si obtained with PC-F1 (the left panel) and PC-PK1 (the right panel) forces. It is shown that the mean-field energy with PC-F1 force has a minimum at $\beta = -0.22$ with a soft energy curve around the spherical shape, while the energy curve with PC-PK1 force has a prolate minimum around $\beta = 0.07$ (see the dotted lines). Even though these two forces predict different mean-field energy curves, the projected energy curves are quite similar. The projected energy curves for 0^+ with the PC-F1 and PC-PK1 forces have an oblate minimum at $\beta = -0.33$ and $\beta = -0.29$, respectively.

The results of the GCM calculation for the low-lying states of ^{30}Si are shown in Fig. 5.34, in comparison with the measured data. Both the PC-F1 and PC-PK1 forces describe successfully the ground-state band and the yare band, except for the overestimation of the intraband B($E2$)

value and the underestimation of the interband B($E2$) value, in addition to the underestimate of the 2^+_1 energy.

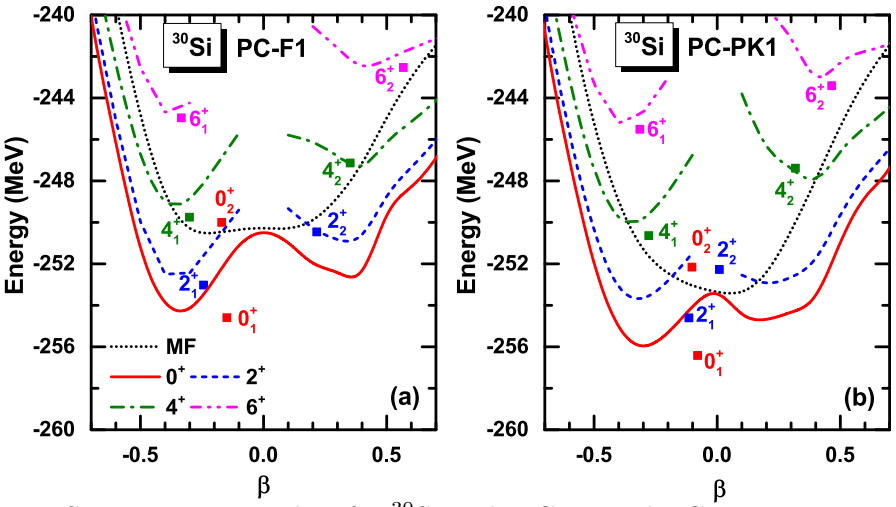

Fig. 5.33 Same as Fig. 2.1, but for ^{30}Si with PC-F1 and PC-PK1 parameter sets.

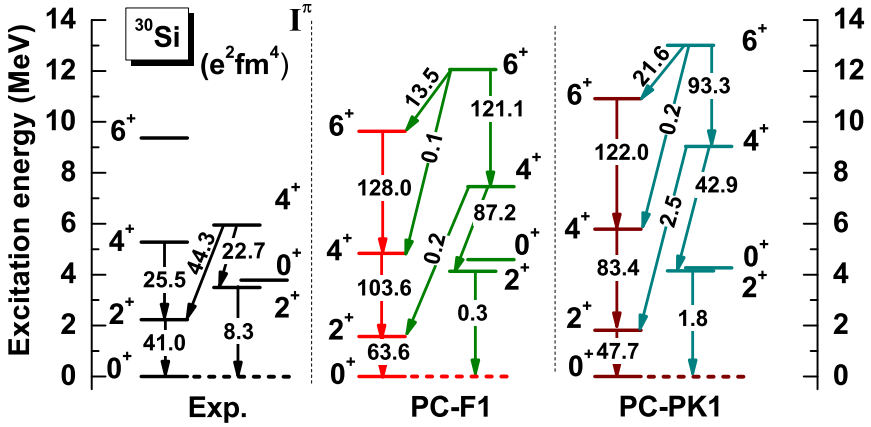

Fig. 5.34 Comparison between the (left) experimental data, (middle) by the PC-F1 force, and (right) by the PC-PK1 force for the low-lying states in ^{30}Si. The electric quadrupole (E2) transition strength is indicated with the value in units of e^2fm^4. The experimental data for ^{30}Si are taken from Ref. [139].

5.5.2 Projected potential energy surface of $^{31}_{\Lambda}$Si

Figures 5.35 (a) and (b) show the obtained energy $E_J(\beta)$ for the $J^\pi = 1/2^+$ and $1/2^-$ states of $^{31}_{\Lambda}$Si as a function of the deformation β with the PC-F1 and PC-PK1 forces, respectively. Similarly to Fig. 5.26 for ^{20}Ne and $^{21}_{\Lambda}$Ne, the energy surface of hypernucleus with $1/2^+$ and $1/2^-$ has a lower and higher barrier than that of core nucleus with 0^+ at the spherical shape, respectively. The deformation at the energy minimum for ^{30}Si with 0^+ is located at $\beta = -0.35$ ($\beta = -0.30$), which is altered to $\beta = -0.30$ ($\beta = -0.26$) for $^{31}_{\Lambda}$Si with $1/2^+$ for the PC-F1 (PC-PK1) force, indicating a smaller collectivity in $^{31}_{\Lambda}$Si with $J^\pi = 1/2^+$ than that in ^{30}Si with

$I^\pi = 0^+$. On the other hand, for $1/2^-$ configuration, the deformation at the minimum becomes $\beta = -0.35$ ($\beta = -0.32$) for PC-F1 (PC-PK1) force.

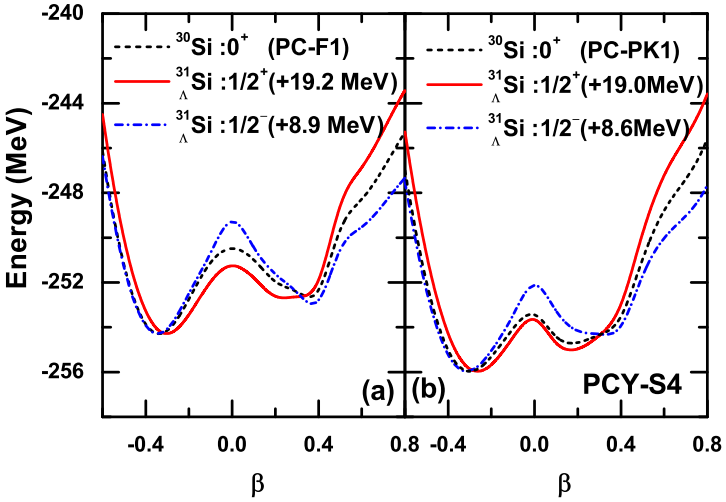

Fig. 5.35 Same as Figs. 5.26 (a) and (b), but for ^{30}Si and ${}^{31}_{\Lambda}$Si.

5.5.3 Low-lying states of ${}^{31}_{\Lambda}$Si

Figure 5.36 displays the low-lying excitation spectra of ${}^{31}_{\Lambda}$Si obtained with the PC-F1 and PC-PK1 forces for the NN interaction. As we have discussed, the four parameter sets of $N\Lambda$ interaction yield a qualitatively similar spectra for ${}^{9}_{\Lambda}$Be, ${}^{13}_{\Lambda}$C and ${}^{21}_{\Lambda}$Ne, and we have adopted the PCY-S4 force for $N\Lambda$ interaction. The positive parity states shown in the column (a),(b) and (f),(g) are almost the same as their core states. These states are dominated by the Λ hyperon in s-orbit coupled to the core states I^π. For the negative parity states, shown in the column (c-e) and (h-j), the energy ordering of the states is the same between the two NN interactions, although the gap among these levels are different. The yrast negative parity states, shown in the column (c) and column (h), are dominated by Λ hyperon in p-orbit coupled to the ground band of the nuclear core, see Table 5.9. On the other hand, there is a large mixture of the first and the second $0^+, 2^+$ states of the nuclear core for the $1/2^-_2, 1/2^-_3$ states.

The ratio $E(4^+_1)/E(2^+_1)$ provides an idea on the nature of collective excitations. For a well deformed rigid rotor, the ratio is 3.33, while it is 2 for a harmonic vibration of spherical nuclei. For the ^{30}Si nucleus, this ratio is 3.083 with PC-F1 force (see Fig. 5.34), which is consistent with a rigid rotor. The ratio is changed to 2.829 for ${}^{31}_{\Lambda}$Si after adding a Λ particle (that is, $E(9/2^+_1)/E(5/2^+_1) = 2.829$, see Fig. 5.36). This indicates that the nature of collective excitation is modified from a rigid rotor towards a spherical harmonic oscillator. This trend is in fact qualitatively consistent with the previous result based on the mean-field approximation, which has predicted that the deformation disappears in ^{30}Si after adding a Λ particle (see Fig.3.1(d)). However, the ratio $E(9/2^+_1)/E(5/2^+_1)$ for ${}^{31}_{\Lambda}$Si is still close to 3, and the deformation remains a finite value. That is, the present beyond-mean-field calculation does not completely support the previous mean-field calculation, even though some signature of disappearance of deformation

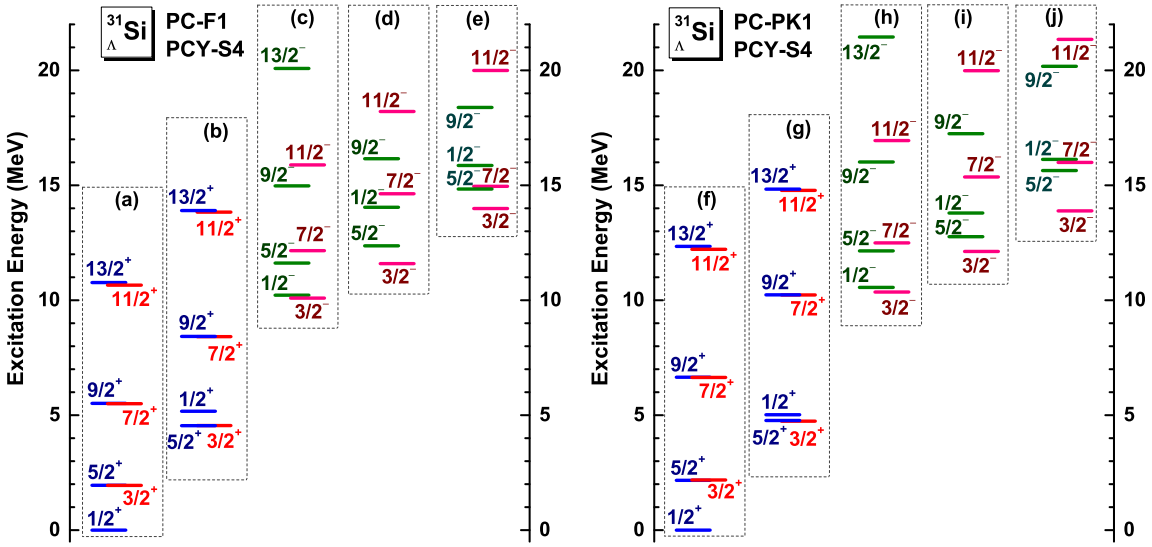

Fig. 5.36 The low-lying spectra of $^{31}_{\Lambda}$Si obtained with the microscopic particle-rotor model. The PC-F1 and PC-PK1 forces are used for the NN interaction for the left and right panels, respectively, together with the PCY-S4 interaction for the $N\Lambda$ interaction.

can still be seen in the spectrum. One of the main reasons for this difference is due to the shape fluctuation effect. That is, the mean-field energy surface is very flat both for ^{30}Si and $^{31}_{\Lambda}$Si(red line in Fig.3.1(d)), and the difference between the two energy surfaces becomes significantly small after the shape fluctuation effect is taken into account, even if the minimum appears at different deformations (notice that only the minimum matters in the mean-field approximation). The angular momentum projection also plays a role in making the difference between ^{30}Si and $^{31}_{\Lambda}$Si much smaller than in the mean-field approximation. All of these indicate that the beyond-mean-field effects play an important role in discussing spectra of hypernuclei.

E2 transition strengths

Compared with the $B(E2 : 2^+_1 \rightarrow 0^+_1)$ value in ^{30}Si, the $B(E2)$ transition strength from the $3/2^+_1$ to $1/2^+_1$ state in $^{31}_{\Lambda}$Si is decreased by 10.38% and 16.38% for the PC-F1 and PC-PK1 forces, respectively, as shown in Table 5.10. The E2 transition strength for $4^+_1 \rightarrow 2^+_1$ in ^{30}Si is reduced by a factor of $\sim 1\%$ and $\sim 8\%$ for the PC-F1 and PC-PK1 forces, respectively. The PC-PK1 force predicts larger changes in E2 transition strength than the PC-F1, that indicates that the structure of ^{30}Si is more influenced with PC-PK1 than with PC-F1 to an addition of a Λ particle.

Table 5.9 The largest component in each positive parity state and the two largest components in each negative parity state of ${}^{31}_{\Lambda}$Si hypernucleus obtained with the PC-F1 and PC-PK1 forces for NN interaction and the PCY-S4 force for $N\Lambda$ interaction.

	PC-F1				PC-PK1			
J^π	$[(lj)\otimes I_n^\pi]$	P_{jlI_n}	$[(lj)\otimes I_n^\pi]$	P_{jlI_n}	$[(lj)\otimes I_n^\pi]$	P_{jlI_n}	$[(lj)\otimes I_n^\pi]$	P_{jlI_n}
$1/2_1^+$	$[s_{1/2}\otimes 0_1^+]$	0.963			$[s_{1/2}\otimes 0_1^+]$	0.972		
$3/2_1^+$	$[s_{1/2}\otimes 2_1^+]$	0.977			$[s_{1/2}\otimes 0_1^+]$	0.973		
$5/2_1^+$	$[s_{1/2}\otimes 2_1^+]$	0.977			$[s_{1/2}\otimes 0_1^+]$	0.970		
$7/2_1^+$	$[s_{1/2}\otimes 4_1^+]$	0.979			$[s_{1/2}\otimes 0_1^+]$	0.978		
$1/2_2^+$	$[s_{1/2}\otimes 0_2^+]$	0.972			$[s_{1/2}\otimes 0_1^+]$	0.981		
$3/2_2^+$	$[s_{1/2}\otimes 2_2^+]$	0.985			$[s_{1/2}\otimes 0_1^+]$	0.977		
$5/2_2^+$	$[s_{1/2}\otimes 2_2^+]$	0.984			$[s_{1/2}\otimes 0_1^+]$	0.975		
$7/2_2^+$	$[s_{1/2}\otimes 4_2^+]$	0.985			$[s_{1/2}\otimes 0_1^+]$	0.985		
$1/2_1^-$	$[p_{1/2}\otimes 0_1^+]$	0.704	$[p_{3/2}\otimes 2_1^+]$	0.273	$[p_{1/2}\otimes 0_1^+]$	0.760	$[p_{3/2}\otimes 2_1^+]$	0.230
$3/2_1^-$	$[p_{3/2}\otimes 0_1^+]$	0.772	$[p_{1/2}\otimes 2_1^+]$	0.115	$[p_{3/2}\otimes 0_1^+]$	0.828	$[p_{1/2}\otimes 2_1^+]$	0.089
$5/2_1^-$	$[p_{3/2}\otimes 2_1^+]$	0.796	$[p_{1/2}\otimes 2_1^+]$	0.170	$[p_{3/2}\otimes 2_1^+]$	0.807	$[p_{1/2}\otimes 2_1^+]$	0.128
$7/2_1^-$	$[p_{3/2}\otimes 2_1^+]$	0.798	$[p_{1/2}\otimes 4_1^+]$	0.108	$[p_{3/2}\otimes 2_1^+]$	0.841	$[p_{1/2}\otimes 4_1^+]$	0.077
$1/2_2^-$	$[p_{3/2}\otimes 2_2^+]$	0.706	$[p_{1/2}\otimes 0_1^+]$	0.104	$[p_{3/2}\otimes 2_1^+]$	0.431	$[p_{3/2}\otimes 2_2^+]$	0.435
$3/2_2^-$	$[p_{3/2}\otimes 2_1^+]$	0.555	$[p_{1/2}\otimes 2_1^+]$	0.407	$[p_{3/2}\otimes 2_1^+]$	0.559	$[p_{1/2}\otimes 2_1^+]$	0.365
$5/2_2^-$	$[p_{1/2}\otimes 2_1^+]$	0.615	$[p_{3/2}\otimes 4_1^+]$	0.206	$[p_{1/2}\otimes 2_1^+]$	0.691	$[p_{3/2}\otimes 4_1^+]$	0.147
$7/2_2^-$	$[p_{3/2}\otimes 2_2^+]$	0.805	$[p_{1/2}\otimes 4_2^+]$	0.097	$[p_{3/2}\otimes 2_2^+]$	0.897	$[p_{1/2}\otimes 4_2^+]$	0.038
$1/2_3^-$	$[p_{3/2}\otimes 2_1^+]$	0.515	$[p_{1/2}\otimes 0_2^+]$	0.279	$[p_{1/2}\otimes 0_2^+]$	0.712	$[p_{3/2}\otimes 2_1^+]$	0.143
$3/2_3^-$	$[p_{3/2}\otimes 2_2^+]$	0.398	$[p_{1/2}\otimes 2_2^+]$	0.279	$[p_{3/2}\otimes 2_2^+]$	0.280	$[p_{1/2}\otimes 2_1^+]$	0.276
$5/2_3^-$	$[p_{1/2}\otimes 2_2^+]$	0.541	$[p_{3/2}\otimes 2_2^+]$	0.235	$[p_{3/2}\otimes 2_2^+]$	0.610	$[p_{1/2}\otimes 2_2^+]$	0.281
$7/2_3^-$	$[p_{3/2}\otimes 4_1^+]$	0.636	$[p_{1/2}\otimes 4_1^+]$	0.333	$[p_{3/2}\otimes 4_1^+]$	0.641	$[p_{1/2}\otimes 4_1^+]$	0.335

Table 5.10 Same as Table 5.8, but for ^{30}Si and $^{31}_{\Lambda}$Si.

^{30}Si			$^{31}_{\Lambda}$Si						
	PC-F1	PC-PK1		PC-F1			PC-PK1		
$I_i^\pi \to I_f^\pi$	$B(E2)$	$B(E2)$	$J_i^\pi \to J_f^\pi$	$B(E2)$	$cB(E2)$	$\Delta(\%)$	$B(E2)$	$cB(E2)$	$\Delta(\%)$
$2_1^+ \to 0_1^+$	63.60	47.68	$3/2_1^+ \to 1/2_1^+$	57.00	57.00	−10.38	39.87	39.87	−16.38
			$5/2_1^+ \to 1/2_1^+$	57.06	57.06	−10.28	39.59	39.59	−16.97
$4_1^+ \to 2_1^+$	103.59	83.42	$7/2_1^+ \to 3/2_1^+$	92.14	102.38	− 1.17	69.24	76.94	−7.77
			$7/2_1^+ \to 5/2_1^+$	10.22	102.24	− 1.30	7.60	76.02	−8.87
			$9/2_1^+ \to 5/2_1^+$	102.36	102.36	− 1.19	76.14	76.14	−8.73

5.6 Application to Sm Λ hypernuclei

In the microscopic particle-rotor model, the core excited states are given by the full microscopic beyond mean-field calculations, where the collective motions of both rotations and vibrations, as well as their couplings, are taken into account automatically with the angular momentum projection and GCM. In this section, we apply the present method to study a transition in low-lying spectrum from a vibrational to a rotational characters. To this end, we discuss how the structure of Sm isotopes evolves after including a Λ hyperon, as the rapid transition from spherical shape to well deformed shape in Sm isotopes around $N = 90$ has been studied extensively in the past decades [152–155].

5.6.1 Properties of Sm isotopes

Figure 5.37 shows the mean-field and the projected energies of Sm isotopes as functions of the deformation parameter β. The prolate minimum in the mean-field energy curve gradually shifts from $\beta = 0.14$ in ^{148}Sm to a larger deformation $\beta = 0.32$ in ^{154}Sm. It has been found that the mean-field potential energy surface displays a flat minimum in Nd isotopes with $N = 90$, i.e., ^{150}Nd [156, 157]. For Sm isotopes with $N = 90$, i.e., ^{152}Sm, this flat prolate minimum does not appear in the mean-field energy curve but it exhibits only in the projected energy curve with $I^\pi = 0^+$. For projected energy curves, one can see that the deformation of the prolate minimum increases with increasing neutron number.

Figure 5.38 shows the calculated ground-state band of Sm isotopes, in comparison with the empirical data. The ground-state band in Sm isotopes are reasonably reproduced, although the spectra are somewhat stretched. The levels scaled with a factor $E_{I^+}^{\rm Scaled} = E_{2^+}^{\rm GCM}/E_{2^+}^{\rm exp.}$ are also shown in Fig. 5.38, displayed by the blue lines.

The ratio of the excitation energies of 2_1^+ to that of 4_1^+, $R_{4/2} \equiv E(4_1^+)/E(2_1^+)$, is one significant feature of shape transitions. For vibrational nuclei, which have a spherical ground-state shape and exhibit small amplitude quadrupole oscillations about the spherical equilibrium shape, the excitation energies of one-phonon state and two-phonon state are $\hbar\omega$ and $2\hbar\omega$, respectively.

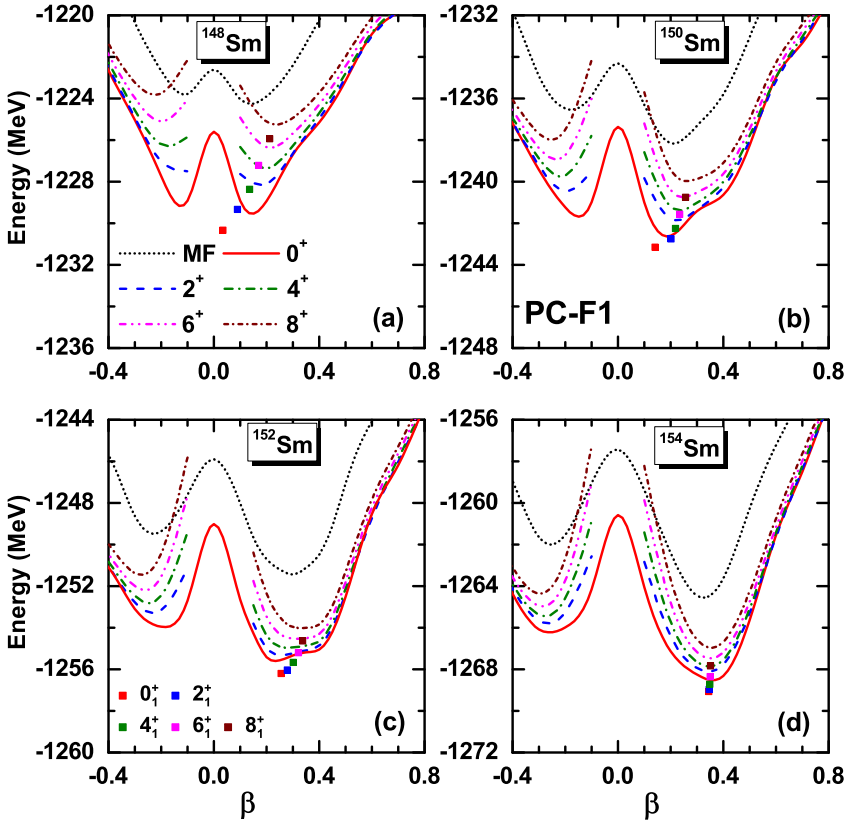

Fig. 5.37 Same as Fig. 2.1, but for Sm isotopes.

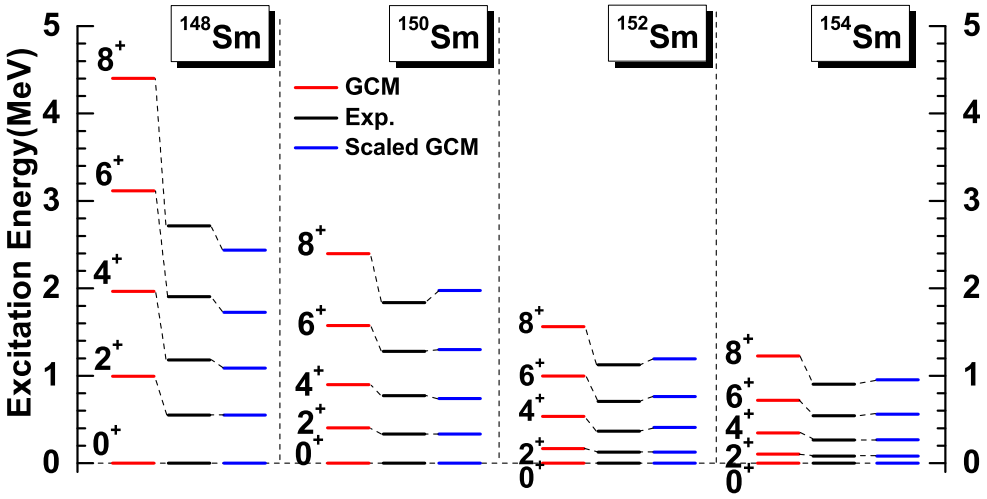

Fig. 5.38 The yrast levels of Sm isotopes calculated with GCM (red lines) and the scaled levels (blue lines) with a factor $E^{\rm Scaled}_{I^+} = E^{\rm GCM}_{2^+}/E^{\rm exp.}_{2^+}$, in comparison with the experiment data(black lines) taken from Ref. [139].

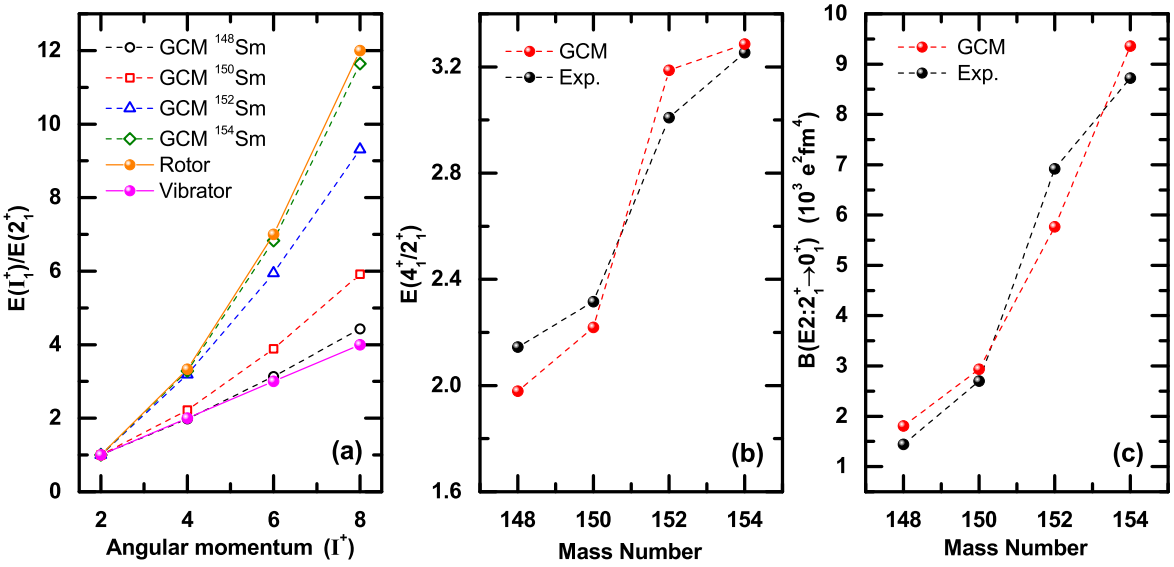

Fig. 5.39 (a)The ratio of $E(I_1^+)/E(2_1^+)$ for the yrast states in Sm isotopes calculated with the GCM. These are compared with those predicted by the spherical vibrator and a well-deformed axial rotor. (b) Evolution of the ratio of $E(4_1^+)/E(2_1^+)$ as function of the mass number in Sm isotopes. (c) Evolution of the $B(E2:2_1^+\rightarrow 0_1^+)$ values in $e^2\text{fm}^4$ as function of the mass number in Sm isotopes. The experiment data are taken from Ref. [139].

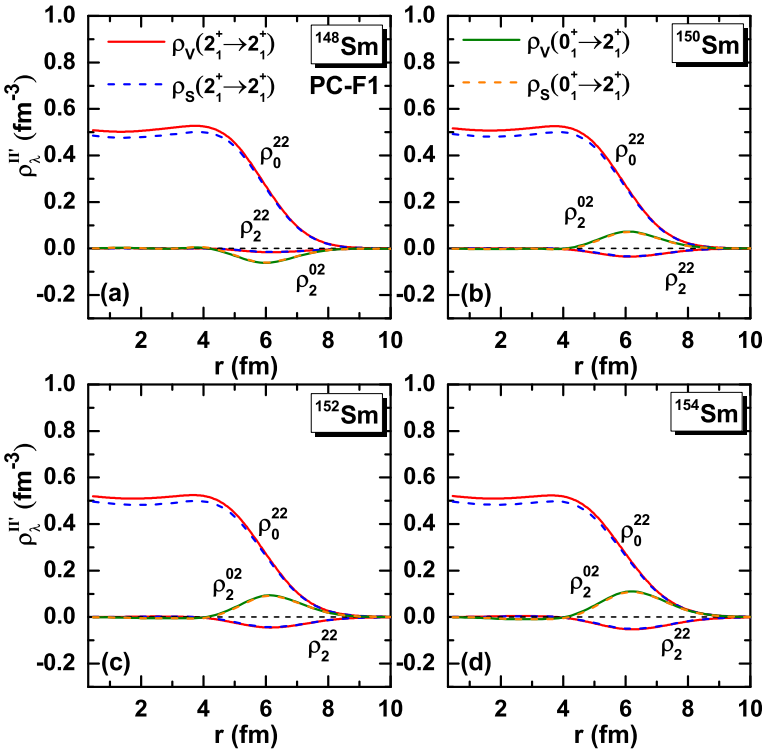

Fig. 5.40 The vector and the scalar transition densities in the low-lying states (n=1) of Sm isotopes.

Considering the residual interactions of phonons gives the $R_{4/2}$ values between 2.2 and 2.4. For ^{148}Sm, the calculated value of $R_{4/2}$ is 1.98, while the experimental value is $R_{4/2} = 2.15$, both of which are very close to a value expected for a characteristic spherical vibrator.

On the other hand, the dominant collective motion becomes the rotational one for rotational nuclei, although the surface vibrations still exist as collective modes. For axially deformed even-even nuclei, the excitation energies for rotational spectra reads $E_I = \frac{\hbar^2 I(I+1)}{2\mathcal{J}}$ and one find $R_{4/2} = 3.33$. For ^{154}Sm, the GCM results of $R_{4/2} = 3.29$ is in a good agreement with the experimental data 3.25, and show a clear rotational character.

In Fig. 5.39(a), we compare the $E(I_1^+)/E(2_1^+)$ values calculated with GCM and those with the analytic expressions for vibrator and rotor. This figure clearly indicates a transition between spherical and axially deformed shapes as the mass number increases.

The calculated energy ratios of $E(4_1^+)/E(2_1^+)$ are compared with the experiment data, as shown in Fig. 5.39(b). The tendency of GCM calculation is similar as the experimental data. Figure 5.39(c) displays the calculated $B(E2 : 2_1^+ \to 0_1^+)$ values as a function of the mass number of Sm isotopes. It is shown that the overall tendency and the sudden rise in B(E2) values from $N = 88$ to $N = 90$ observed in the available data are reproduced rather well in the GCM calculations, although the GCM results predict a smoother evolutionary trend for this shift. This sudden rise can be understood in terms of shape change, i.e., from predominantly spherical shape to prolate shape, to which the electric quadrupole transition strength $B(E2 : 2_1^+ \to 0_1^+)$ is sensitive.

The vector and scalar transition densities ρ_λ^{22} of Sm isotopes are shown in Fig. 5.40. The transition densities ρ_0^{22} of Sm isotopes are almost similar to each other, while an obvious evolution is found in the transition densities ρ_2^{22} and ρ_2^{02}. That is, the transition density ρ_2^{22} for ^{148}Sm is almost close to zero and gradually becomes more pronounced as the number of neutrons increases. The transition density ρ_2^{02} changes its sigh from negative to positive after $N \geq 88$ and the peak of ρ_2^{02} curves becomes more and more prominent as the number of neutrons increases.

5.6.2 Projected potential energy surface of Sm Λ hypernuclei

Figure 5.41 shows the projected energy curves for Sm isotopes and the corresponding Λ hypernculei obtained with PCY-S4 for the $N\Lambda$ interaction together with PC-F1 for the NN interaction. The polarization effect of Λ in s orbit and p orbit on the properties of the core nuclei is much smaller than that on ^{12}C, ^{20}Ne and ^{30}Si due to the large mass number. Compared with the $1/2^+$ state, the effect is large for the $1/2^-$ state due to the strong channel coupling effects. For ^{152}Sm, the extended energy minimum on the prolate side becomes flatter after including a Λ particle in s-orbit and the minimum is shiftted from $\beta = 0.23$ to $\beta = 0.37$ by adding a Λ particle in p-orbit.

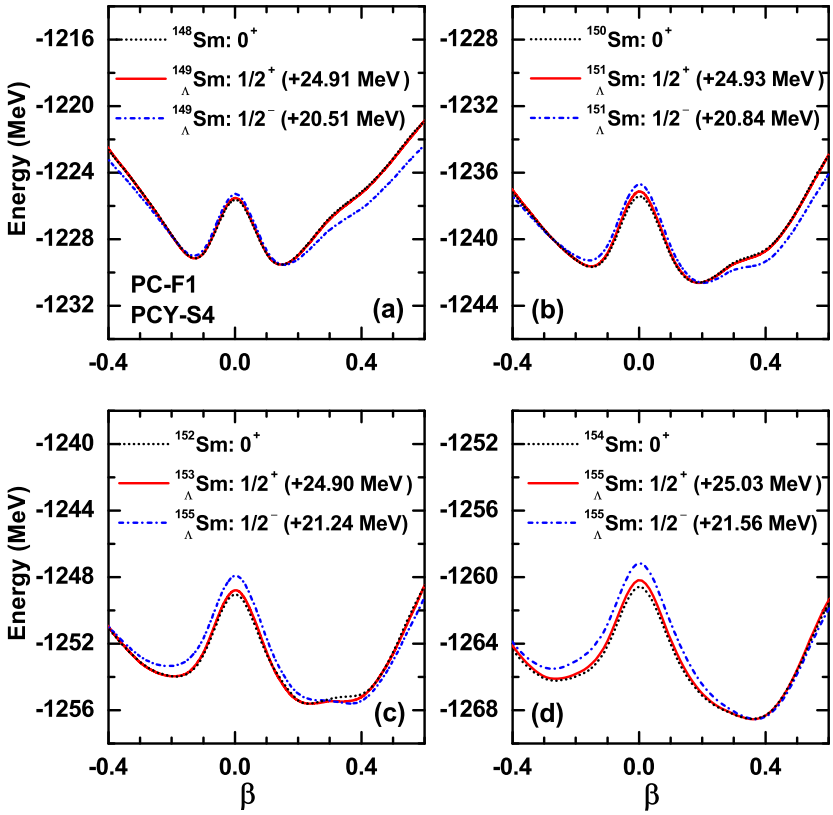

Fig. 5.41 Same as Fig. 5.26, but for Sm isotopes and corresponding Λ-hypernuclei.

5.6.3 Low-lying spectrum of Sm Λ hypernuclei

Figure 5.42 shows the calculated low-energy spectra of Sm hyper-isotopes with the PC-F1 force together with the PCY-S4 force. The low-lying positive-parity states J^π in Sm hyper-isotopes are dominated by the single-configuration of $[\Lambda_{s_{1/2}} \otimes I^+]$ with the weight around 99% (see Table 5.11) and have similar excitation energies as that of the nuclear core state with I^+. The positive-parity states J^+, except for $1/2^+$, are nearly two-fold degenerate. These characters are similar to the hypernuclei in the lighter-mass region. The negative-parity yrast states, which are formed by the Λ hyperon in the p-orbital coupled to the ground-state band of the nuclear core, are also nearly two-fold degenerate and share a similar structure of the positive-parity ground band, even though there are strong configuration mixings in these states. Table 5.11 also lists the probabilities for the dominant components in the negative party states. The second negative-parity states of each angular momentum J in Fig. 5.42 are dominated by the configuration of Λ particle in p-orbit coupled to the ground band of the nuclear core. These levels, except for $1/2^-_2$, form two bands having $\Delta J = 2$.

The evolution of the probability of the dominant components for the $1/2^-_1$ state and $3/2^-_1$ state in Λ-hypernuclei for Sm isotopes are shown in Fig. 5.43. For $^{149}_{\Lambda}$Sm, the $1/2^-_1$ state and $3/2^-_1$ state are dominated by Λ hyperon in $p_{1/2}$ and $p_{3/2}$ coupled to the 0^+ state of ^{148}Sm, respectively. A weaker configuration mixing in these two states of $^{149}_{\Lambda}$Sm is due to the near-

spherical components in the 0_1^+ state and 2_1^+ state of ^{148}Sm, which are $\beta = 0.03$ and $\beta = 0.09$, respectively. The configuration mixing becomes stronger as the mass number increases, e.g., the mixing between 0_1^+ and 2_1^+ becomes almost half-to-half for $^{151}_{\Lambda}$Sm. With increasing the mass number, the probability for the $[\Lambda_p \otimes 2_1^+]$ configuration increases leading to a large configuration mixture in $^{155}_{\Lambda}$Sm, for which the deformation of the 0_1^+ state and 2_1^+ state in the core nucleus is $\beta = 0.34$ and $\beta = 0.35$, respectively.

Table 5.11 The probability for the dominant components in the first and the second negative states of each angular momentum J of Sm isotopes Λ-hypernuclei.

J^π	$(lj) \otimes I_n^\pi$	$^{149}_{\Lambda}$Sm	$^{151}_{\Lambda}$Sm	$^{153}_{\Lambda}$Sm	$^{155}_{\Lambda}$Sm	J^π	$(lj) \otimes I_n^\pi$	$^{149}_{\Lambda}$Sm	$^{151}_{\Lambda}$Sm	$^{153}_{\Lambda}$Sm	$^{155}_{\Lambda}$Sm
$1/2_1^+$	$s_{1/2} \otimes 0_1^+$	0.997	0.994	0.988	0.982	$1/2_2^+$	$s_{1/2} \otimes 0_2^+$	0.993	0.992	0.987	0.990
$3/2_1^+$	$s_{1/2} \otimes 2_1^+$	0.996	0.993	0.988	0.982	$3/2_2^+$	$s_{1/2} \otimes 2_2^+$	0.995	0.992	0.986	0.989
$5/2_1^+$	$s_{1/2} \otimes 2_1^+$	0.996	0.993	0.988	0.982	$5/2_2^+$	$s_{1/2} \otimes 2_2^+$	0.995	0.991	0.986	0.989
$7/2_1^+$	$s_{1/2} \otimes 4_1^+$	0.996	0.993	0.987	0.982	$7/2_2^+$	$s_{1/2} \otimes 4_2^+$	0.994	0.987	0.985	0.986
$1/2_1^-$	$p_{1/2} \otimes 0_1^+$	0.859	0.484	0.348	0.322	$1/2_2^-$	$p_{1/2} \otimes 0_1^+$	0.133	0.498	0.635	0.654
	$p_{3/2} \otimes 2_1^+$	0.136	0.503	0.627	0.639		$p_{3/2} \otimes 2_1^+$	0.813	0.472	0.351	0.330
$3/2_1^-$	$p_{3/2} \otimes 0_1^+$	0.876	0.545	0.395	0.363	$3/2_2^-$	$p_{3/2} \otimes 0_1^+$	0.113	0.435	0.583	0.605
	$p_{1/2} \otimes 2_1^+$	0.054	0.204	0.271	0.281		$p_{3/2} \otimes 2_1^+$	0.583	0.322	0.266	0.258
	$p_{3/2} \otimes 2_1^+$	0.064	0.238	0.309	0.318		$p_{1/2} \otimes 2_1^+$	0.252	0.210	0.136	0.119
$5/2_1^-$	$p_{3/2} \otimes 4_1^+$	0.154	0.377	0.462	0.504	$5/2_2^-$	$p_{3/2} \otimes 2_1^+$	0.658	0.746	0.764	0.780
	$p_{1/2} \otimes 2_1^+$	0.573	0.453	0.385	0.346		$p_{1/2} \otimes 2_1^+$	0.283	0.221	0.210	0.202
	$p_{3/2} \otimes 2_1^+$	0.262	0.156	0.127	0.112						
$7/2_1^-$	$p_{3/2} \otimes 2_1^+$	0.854	0.653	0.554	0.497	$7/2_2^-$	$p_{3/2} \otimes 2_1^+$	0.124	0.336	0.428	0.472
	$p_{1/2} \otimes 4_1^+$	0.074	0.183	0.232	0.258		$p_{3/2} \otimes 4_1^+$	0.368	0.350	0.294	0.272
	$p_{3/2} \otimes 4_1^+$	0.062	0.150	0.188	0.207		$p_{1/2} \otimes 4_1^+$	0.302	0.307	0.266	0.237

The large configuration mixing in the low-lying negative party states of $^{155}_{\Lambda}$Sm can be qualitatively understood in terms of a Nilsson model, in which the single-particle potential is deformed, that is, $V(\boldsymbol{r}) = V_0(r) - \beta_2 R_0 \frac{dV_0(r)}{dr} Y_{20}(\hat{\boldsymbol{r}}) + \cdots$ for an axially symmetric deformation. Such potential violates the rotational symmetry and thus different quantum numbers of l and j are coupled to each other in single-particle wave functions. If one treats the deformed part of potential, $-\beta_2 R_0 \frac{dV_0(r)}{dr} Y_{20}(\hat{\boldsymbol{r}})$, with the first order perturbation theory, the wave function for the lowest negative parity state is given by $|\psi_\Lambda\rangle = C_1 |\psi_{p3/2,m=1/2}\rangle + C_2 |\psi_{p1/2,m=1/2}\rangle$, where $|\psi_{p3/2,m=1/2}\rangle$ and $|\psi_{p1/2,m=1/2}\rangle$ are single-particle wave functions in the spherical limit. The coefficients C_1 and C_2 are determined by the following eigen-value equation

$$\begin{pmatrix} \langle \mathscr{Y}_{p3/2,m=1/2} | Y_{20} | \mathscr{Y}_{p3/2,m=1/2} \rangle & \langle \mathscr{Y}_{p3/2,m=1/2} | Y_{20} | \mathscr{Y}_{p1/2,m=1/2} \rangle \\ \langle \mathscr{Y}_{p1/2,m=1/2} | Y_{20} | \mathscr{Y}_{p3/2,m=1/2} \rangle & \langle \mathscr{Y}_{p1/2,m=1/2} | Y_{20} | \mathscr{Y}_{p1/2,m=1/2} \rangle \end{pmatrix} \begin{pmatrix} C_1 \\ C_2 \end{pmatrix} = \lambda \begin{pmatrix} C_1 \\ C_2 \end{pmatrix}. \tag{5.13}$$

The solutions of this equation gives two eigenvectors $\begin{pmatrix} \sqrt{2/3} \\ -\sqrt{1/3} \end{pmatrix}$ and $\begin{pmatrix} \sqrt{1/3} \\ \sqrt{2/3} \end{pmatrix}$, with the eigen-values of $\frac{2}{\sqrt{20\pi}}$ and $-\frac{1}{\sqrt{20\pi}}$, respectively. For a positive value of β, the former state is lower in energy. For this state, the probability of each component reads 66.7% for the $p_{3/2}$ component and 33.3% for the $p_{1/2}$ component. A more consistent calculation with the self-consistent deformed RMF method also yields 67% for the $p_{3/2}$ component for ${}^{155}_{\Lambda}$Sm at $\beta = 0.30$. Notice that this value is consistent with the components shown in Table 5.11 for ${}^{155}_{\Lambda}$Sm. For instance, for the first $1/2^-$ state, the component of $[p_{3/2} \otimes 2^+_1]$ is 63.9% while that of $[p_{1/2} \otimes 0^+_1]$ is 32.2%, being close to the expected values of 66.7% and 33.3%, respectively. For the first $3/2^-$ state, the sum of $[p_{3/2} \otimes 0^+_1]$ and $[p_{3/2} \otimes 2^+_1]$ is 68.1% and the $[p_{1/2} \otimes 2^+_1]$ component has 28.1%, which are again consistent with the expected values. This is the case also for the $5/2^-$ and $7/2^-$ states.

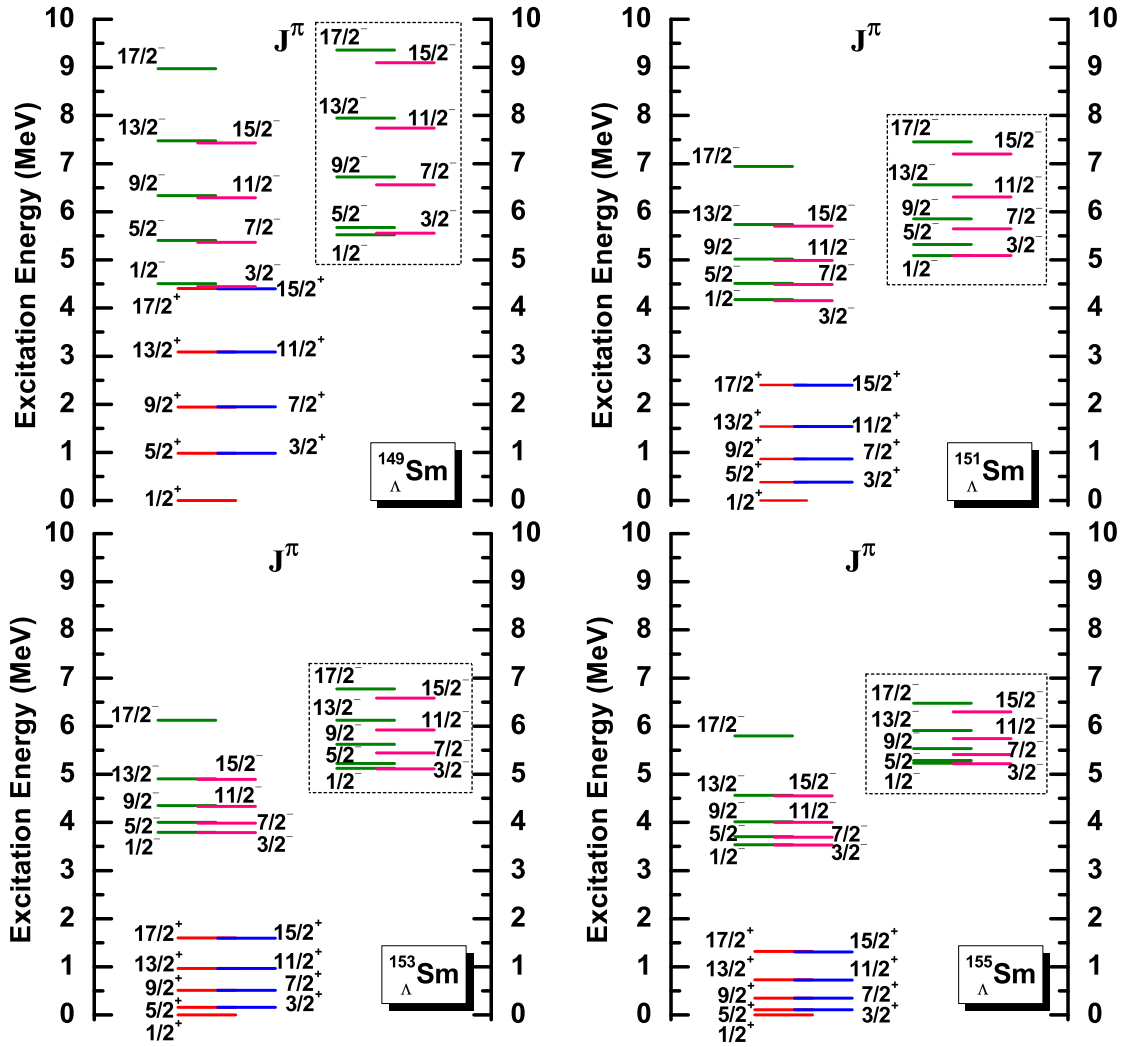

Fig. 5.42 Low-energy excitation spectra of Λ-hypernuclei for Sm isotopes.

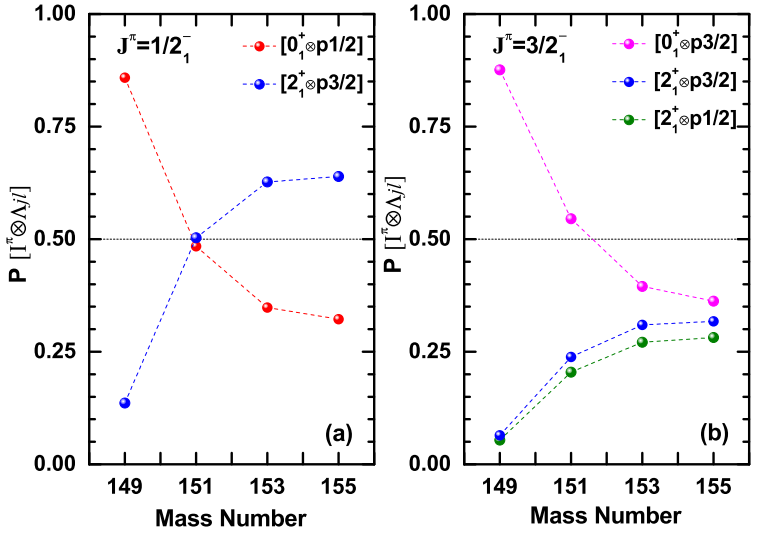

Fig. 5.43 The probability of the dominant components for the $1/2^-_1$ state(a) and $3/2^-_1$ state(b) as a function of mass number in Λ-hypernuclei for Sm isotopes.

Chapter 6

Summary and perspectives

In this thesis, we have proposed a novel method for a low-lying spectrum of single-Λ hypernuclei based on a covariant density functional theory. Since the pure mean-field approximation does not yield a spectrum due to the broken rotational symmetry, we have employed a beyond relativistic mean-field approach by carrying out the angular momentum and the particle number projections as well as the configuration mixing with the generator coordinate method. In this novel method, the beyond-mean-field approach is applied to low-lying states of the core nucleus and the wave functions for hypernuclei is constructed by coupling the Λ hyperon to the low-lying states of the core nucleus in the laboratory frame, and thus we call it the microscopic particle-rotor model. In this model, the radial wave functions for a Λ particle are obtained by solving the corresponding coupled-channel equations, in which the coupling potentials are provided in terms of the transition densities of the nuclear core states. We have employed the $N\Lambda$ effective interaction which are constructed based on the relativistic point-coupling model. We emphasize that this is the first calculation for the spectra of hypernuclei based on a density functional approach.

Taking ${}^{13}_{\Lambda}$C as an example, we have performed the detailed calculation of this new method with the four sets of effective $N\Lambda$ interaction. Our calculation has shown that the four parameter sets yield qualitatively similar low-lying spectra, even though these parameter sets were optimized to the Λ binding energies of the ground states. We have studied the structure of the low-energy states and the corresponding components in the wave functions. The results obtained in this work evidently show that the low-lying excited states with positive parity J^+, except for $1/2^+$, are nearly twofold degenerate and are dominated by a single-configuration of $[\Lambda_{s1/2} \otimes I^+]$, which is the Λ particle in $s-$state couples to the nuclear core states, showing the weak coupling feature. This character is also found in other hypernuclei which we studied in this thesis, that is, ${}^{9}_{\Lambda}$Be, ${}^{21}_{\Lambda}$Ne, ${}^{31}_{\Lambda}$Si, ${}^{149}_{\Lambda}$Sm, ${}^{151}_{\Lambda}$Sm, ${}^{153}_{\Lambda}$Sm, and ${}^{155}_{\Lambda}$Sm.

For the first $3/2^-$ and $1/2^-$ states in ${}^{13}_{\Lambda}$C, the calculations showed that the configuration mixing in these states is rather small and thus the energy splitting between these states reflects the spin-orbit splitting of Λ hyperon in the p-orbit. The energy splitting between the $3/2^-_1$ and $1/2^-_1$ states was found to be large for the PCY-S2 and PCY-S3 forces while it was calculated to be 303.7 keV and 253.7 keV for the PCY-S1 and the PCY-S4 force, respectively, both of which

are close to the empirical data of $152 \pm 54 \pm 36$ keV. These results indicate that the fine structure of the hypernuclear spectra depends on the higher-order derivative and tensor $N\Lambda$ interaction terms.

Subsequently, we have discussed the impact of the higher-order derivative and tensor $N\Lambda$ interaction terms on hypernuclear low-energy levels for ${}^{13}_{\Lambda}$C. It was shown that both the second-order derivative and the tensor coupling terms raise the energy of hypernuclear states and thus reduce the Λ binding energy. With the increase of the tensor coupling strength, the excitation energy of the $1/2^-$ state has been found to decrease faster than that of the $3/2^-$ states. As a result, the energy difference between these states, $E(1/2^-) - E(3/2^-)$, decreases to a small value and even changes its sign for large values of the tensor coupling term. Similar calculations for ${}^{9}_{\Lambda}$Be have also been performed and the effects of the derivative and the tensor terms turned out to be similar to those in ${}^{13}_{\Lambda}$C.

We have applied our method also to another light hypernucleus ${}^{9}_{\Lambda}$Be. A reasonable agreement with the experimental data of low-lying spectrum has been achieved. Our calculation well reproduced the so-called ^{8}Be analog band, the genuine hypernuclear band, and the ^{9}Be analog band, which had been predicted by the cluster model. Moreover, the probability of the dominant components in our calculation was also found to be similar to the cluster model calculation. For the first $3/2^-$ and $1/2^-$ states in ${}^{9}_{\Lambda}$Be, a strong configuration mixing between Λ hyperon in $p_{1/2}$ and $p_{3/2}$ orbitals has been found. This feature of strong mixing has also been found in ${}^{21}_{\Lambda}$Ne and the underlying reason for this strong mixing has been investigated. We have found that the configuration mixing in the negative-parity states is sensitive to the properties of the core nuclei. That is, a spherical or weakly deformed nuclear core gives a smaller mixing in the $3/2^-_1$ and $1/2^-_1$ hypernuclear states than well-deformed prolate nuclei.

We have also applied our method to $sd-$shell hypernuclei ${}^{21}_{\Lambda}$Ne and ${}^{31}_{\Lambda}$Si, chosen as the examples for a prolate and an oblate nucleus, respectively. In order to investigate the parameter dependence for the nucleon-nucleon (NN) interaction force, we have adopted both the PC-F1 and PC-PK1 parameter sets for the NN interaction and found that the structure of hypernuclear spectra is not significantly dependent on the NN interaction force. That is, the two parameter sets lead to similar low-lying excitation spectra to each other for ${}^{21}_{\Lambda}$Ne and ${}^{31}_{\Lambda}$Si. For ${}^{31}_{\Lambda}$Si, a weaker configuration mixing is found in the $1/2^-_1$ and $3/2^-_1$ states due to the weakly oblate deformation of ^{30}Si, as compared to ${}^{21}_{\Lambda}$Ne.

We have applied the MPRM also to heavy hypernuclei, Sm hyper-isotopes, and studied the evolution of nuclear structure after including a Λ hyperon. We have found that the positive parity states share a similar structure as the ground band of the nuclear core, and exhibit a vibrational band for ${}^{149}_{\Lambda}$Sm and a rotational band for ${}^{155}_{\Lambda}$Sm. The configuration mixings in the $1/2^-_1$ and $3/2^-_1$ states were also analyzed and we found that the mixture between the Λ hyperon in $p_{1/2}$ and $p_{3/2}$ becomes stronger as the shape of the nuclear core changes from a nearly spherical shape to a well-deformed prolate shape. For this kind of heavy nuclei, the impurity effect of the embedded Λ hyperon is very small and the projected energy curve for $J = 1/2^+$ is almost the same as that for the corresponding core for $I = 0^+$.

Concerning the electromagnetic transitions, we have found that for all the systems the $B(E2)$ value from the first 2^+ to the ground states in the core nuclei is reduced by adding a Λ particle in the positive-parity states. The reduction factor is about 28.21% for ${}^{9}_{\Lambda}$Be with PC-F1, 11.48% for ${}^{13}_{\Lambda}$C with PC-F1, 6.06%(10.07%) for ${}^{21}_{\Lambda}$Ne with PC-F1(PC-PK1), 10.39%(16.38%) for ${}^{31}_{\Lambda}$Si with PC-F1(PC-PK1), and 0.1% for ${}^{155}_{\Lambda}$Sm with PC-F1. For ${}^{21}_{\Lambda}$Ne and ${}^{31}_{\Lambda}$Si, a slightly larger impurity effect was found with the PC-PK1 force as compared to the PC-F1 force.

In short, the major conclusions of this thesis are as follows,

- The microscopic particle-rotor model based on the concept of a hyperon coupled to nuclear core states, which are described by quantum-number projected generator coordinate method calculations, is capable of describing hypernuclear low-lying states.
- The global features of the hypernuclear low-lying states are mainly determined by the properties of nuclear core states, while the fine structures of the hypernuclear states are dependent on the properties of the $N\Lambda$ interaction. In other words, one can learn both the properties of nuclear core states and the $N\Lambda$ interaction with the data of the hypernuclear γ-ray spectroscopy.

The major findings of the study presented in this thesis are as follows,

- The low-lying positive-parity states of Λ hypernuclei are dominated by the Λ hyperon in the s-orbit coupled to the core states and share similar structure with the core nucleus.
- There is a large configuration mixing in negative-parity state for well-deformed hypernuclei, while it is small for weak deformed hypernuclei. It indicates that in general the splitting of the lowest $1/2^-$ and $3/2^-$ states of deformed hypernuclei cannot be interpreted as the spin-orbit splitting for the p-orbit.
- Shape fluctuation effect is important for soft nuclei and should be taken into account while discussing the shrinkage effect induced by the Λ particle. As expected, the changes on the nuclear structure properties induced by the hyperon is shown to decrease with increasing the mass number of core nucleus. Therefore, the deformation remains almost the same for heavy deformed nuclei such as ^{154}Sm even after adding a Λ particle.

In this thesis, for simplicity, we have assumed the axial deformation for the core nucleus. An obvious extension of our method is to take into account more complicated deformations of the core nucleus. One is the triaxial deformation, even though such kind of calculation will be much more computationally expensive. An interesting candidate for this is ${}^{25}_{\Lambda}$Mg, for which the triaxial degree of freedom has been shown to be important in the core nucleus ^{24}Mg. Another extension is to include octupole deformation of the core nucleus. One candidate for this case is ^{20}Ne, which has a prominent negative-parity band originating from the reflection asymmetric molecular α+^{16}O cluster structure. Moreover, a more careful treatment of high-lying collective states in the core nucleus will also be an important issue. In particular, one way to improve

the description for the nuclear core states is to carry out GCM by mixing the mean-field states cranked to different frequencies [158]. These are all interesting future works.

One more interesting future problem is to apply our method to the production reaction of hypernuclei. To this end, one would need to apply the present method consistently also to ordinary odd-mass nuclei, for which a treatment of the Pauli principle would make it more complicated as compared to hypernuclei studied in this thesis.

Appendix A

From finite-range to zero-range effective nuclear interactions

It is generally believed that the most important part of the two-body nuclear interaction can be represented by a contact potential. The finite-range part can be simulated by a momentum dependence, which can be shown by transforming the potential function $V(\boldsymbol{r})$ of the relative distance $\boldsymbol{r} = \boldsymbol{r}_1 - \boldsymbol{r}_2$ into momentum space

$$\langle \boldsymbol{p}|V|\boldsymbol{p}'\rangle = \frac{1}{(2\pi\hbar)^3}\int e^{-\frac{i}{\hbar}(\boldsymbol{p}-\boldsymbol{p}')\boldsymbol{r}}V(\boldsymbol{r})d^3r \tag{A.1}$$

For a delta-force, Eq. (A.1) is a constant and any p-dependence in Eq. (A.1) represents the effect of finite range of the interaction. To the second order in p, the simplest rotationally invariant one is of the form

$$(2\pi\hbar)^3\langle \boldsymbol{p}|V|\boldsymbol{p}'\rangle = V_0 + V_1\boldsymbol{p}'^2 + V_1\boldsymbol{p}^2 + V_2\boldsymbol{p}\boldsymbol{p}', \tag{A.2}$$

which in coordinate space corresponds to the momentum dependent operator

$$V(\boldsymbol{r}) = V_0\delta(\boldsymbol{r}) + V_1[\hat{\boldsymbol{p}}^2\delta(\boldsymbol{r}) + \delta(\boldsymbol{r})\hat{\boldsymbol{p}}^2] + V_2\hat{\boldsymbol{p}}\delta(\boldsymbol{r})\hat{\boldsymbol{p}}. \tag{A.3}$$

Finite-range effective interaction can be expanded into a zero-range coupling term plus momentum dependent terms.

Appendix B

Transition density between GCM states

The reduced transition density from the initial state $|n_i I_i\rangle$ to the final state $|n_f I_f\rangle$ is defined as

$$\rho_L^{n_f I_f n_i I_i}(r) = \hat{I}_i^{-1} \langle n_f I_f || \hat{\rho}(\boldsymbol{r}) Y_L || n_i I_i \rangle, \tag{B.1}$$

which is related to the transition density with the Wigner-Eckart theorem as

$$\langle n_f I_f || \hat{\rho}(\boldsymbol{r}) Y_L || n_i I_i \rangle = \frac{(-1)^{-2L} \hat{I}_f}{\langle I_i M_i L M | I_f M_f \rangle} \langle n_f I_f M_f | \hat{\rho}(\boldsymbol{r}) Y_{LM} | n_i I_i M_i \rangle, \tag{B.2}$$

where $|nIM\rangle = \sum_{K,q} F_{n,q}^{IK} \hat{P}_{MK}^{I} \hat{P}^N \hat{P}^Z |q\rangle$ is the GCM wave function for the low-lying states. For simplicity, we introduce the shorthand notation α to represent nIM and define

$$\langle n_f I_f M_f | \hat{\rho}(\boldsymbol{r}) Y_{LM} | n_i I_i M_f \rangle = \int d\hat{\boldsymbol{r}} \rho^{\alpha_f \alpha_i}(\boldsymbol{r}) Y_{LM}(\hat{\boldsymbol{r}}), \tag{B.3}$$

where

$$\begin{aligned}
\rho^{\alpha_f \alpha_i}(\boldsymbol{r}) = & \langle n_f I_f M_f | \hat{\rho}(\boldsymbol{r}) | n_i I_i M_i \rangle \\
= & \sum_{K_f, K_i} \sum_{q_f, q_i} F_{n_f, q_f}^{I_f K_f *} F_{n_i, q_i}^{I_i K_i} \langle q_f | \hat{P}_{K_f M_f}^{I_f} \hat{\rho}(\boldsymbol{r}) \hat{P}_{K_i M_i}^{I_i \dagger} \hat{P}^N \hat{P}^Z | q_i \rangle \\
= & \sum_{K_f, K_i} \sum_{q_f, q_i} F_{n_f, q_f}^{I_f K_f *} F_{n_i, q_i}^{I_i K_i} \frac{\hat{I}_i^2 \hat{I}_f^2}{(8\pi^2)^2} \\
& \iint d\Omega' d\Omega \mathcal{D}_{K_f M_f}^{I_f *}(\Omega') \mathcal{D}_{K_i M_i}^{I_i}(\Omega) \langle q_f | \hat{R}(\Omega') \hat{\rho}(\boldsymbol{r}) \hat{P}^N \hat{P}^Z \hat{R}^\dagger(\Omega) | q_i \rangle.
\end{aligned} \tag{B.4}$$

Using $\hat{R}(\Omega) = \hat{R}(\Omega'') \hat{R}(\Omega')$, $\hat{R}^\dagger(\Omega) = \hat{R}^\dagger(\Omega') \hat{R}^\dagger(\Omega'')$ and the properties of Wigner-D function

$$\mathcal{D}_{K_i M_i}^{I_i}(\Omega) = \sum_K \mathcal{D}_{K_i K}^{I_i}(\Omega'') \, \mathcal{D}_{K M_i}^{I_i}(\Omega') \tag{B.5}$$

$\rho^{\alpha_f\alpha_i}(\boldsymbol{r})$ can be simplified as

$$\rho^{\alpha_f\alpha_i}(\boldsymbol{r}) = \sum_{K_f,K_i}\sum_{q_f,q_i} F^{I_fK_f*}_{n_f,q_f}F^{I_iK_i}_{n_i,q_i}\frac{\hat{I}_f^2}{8\pi^2}\int d\Omega' \mathcal{D}^{I_f*}_{K_fM_f}(\Omega')\sum_K \mathcal{D}^{I_i}_{KM_i}(\Omega')\hat{R}^\dagger(\Omega)\rho^{I_iKK_i}_{q_fq_i}(\boldsymbol{r}) \quad \text{(B.6)}$$

with $\rho^{I_iKK_i}_{q_fq_i}(\boldsymbol{r}) \equiv \langle q_f|\hat{\rho}(\boldsymbol{r})\hat{P}^{I_i}_{KK_i}\hat{P}^N\hat{P}^Z|q_i\rangle$. Expanding $\rho^{I_iKK_i}_{q_fq_i}(\boldsymbol{r})$ in terms of spherical harmonics, we have

$$\hat{R}^\dagger(\Omega')\rho^{I_iKK_i}_{q_fq}(\boldsymbol{r}) = \sum_{\lambda\nu\nu'} D^{\lambda*}_{\nu\nu'}(\Omega')\rho^{I_iKK_i}_{q_fq_i;\lambda\nu}(r)Y_{\lambda\nu'}(\hat{\boldsymbol{r}}). \quad \text{(B.7)}$$

Assuming that $I_i + I_f + \lambda$ is integer, one has

$$\int d\Omega' D^{I_f*}_{K_fM_f}(\Omega')D^{I_i}_{KM_i}(\Omega')D^{\lambda*}_{\nu\nu'}(\Omega') = \frac{8\pi^2}{\hat{I}_i^2}\langle I_fK_f\lambda\nu|I_iK\rangle\langle I_fM_f\lambda\nu'|I_iM_i\rangle. \quad \text{(B.8)}$$

Consider the orthogonality condition for spherical harmonics, $\int d\hat{\boldsymbol{r}}Y_{LM}(\hat{\boldsymbol{r}})Y_{\lambda\nu'}(\hat{\boldsymbol{r}}) = (-1)^{-M}\delta_{L\lambda}\delta_{M-\nu'}$, and the symmetry for the CG coefficient

$$\langle I_fM_fL-M|I_iM_i\rangle = (-1)^{2L-M+I_i-I_f}\frac{\hat{I}_i}{\hat{I}_f}\langle I_iM_iLM|I_fM_f\rangle. \quad \text{(B.9)}$$

Then

$$\begin{aligned}\rho_L^{n_fI_fn_iI_i}(r) &= (-1)^{I_i-I_f}\frac{\hat{I}_f^2}{\hat{I}_i^2}\sum_{K_f,K_i}\sum_{q_f,q_i}F^{I_fK_f*}_{n_f,q_f}F^{I_iK_i}_{n_i,q_i}\sum_{K\nu}\langle I_fK_fL\nu|I_iK\rangle\rho^{I_iKK_i}_{q_fq_i;L\nu}(r)\\ &= (-1)^{I_i-I_f}\frac{\hat{I}_f^2}{\hat{I}_i^2}\sum_{K_f,K_i}\sum_{q_f,q_i}F^{I_fK_f*}_{n_f,q_f}F^{I_iK_i}_{n_i,q_i}\sum_{K\nu}\langle I_fK_fL\nu|I_iK\rangle\int d\hat{\boldsymbol{r}}\ \rho^{I_iKK_i}_{q_fq_i}(\boldsymbol{r})Y^*_{L\nu}(\hat{\boldsymbol{r}})\end{aligned} \quad \text{(B.10)}$$

In the case of axial symmetry approximation with $K_f = K_i = 0$, the reduced transition density is given by

$$\begin{aligned}\rho_L^{n_fI_fn_iI_i}(r) &= (-1)^{I_i-I_f}\frac{\hat{I}_f^2}{\hat{I}_i^2}\sum_{q_f,q_i}F^{I_f0*}_{n_f,q_f}F^{I_i0}_{n_i,q_i}\sum_K\langle I_f0LK|I_iK\rangle\int d\hat{\boldsymbol{r}}\ \rho^{I_iK0}_{q_fq_i}(\boldsymbol{r})Y^*_{LK}(\hat{\boldsymbol{r}})\\ &= (-1)^{I_i-I_f}\frac{\hat{I}_f^2}{\hat{I}_i^2}\sum_{q_f,q_i}F^{I_f0*}_{n_f,q_f}F^{I_i0}_{n_i,q_i}\sum_K\langle I_f0LK|I_iK\rangle\int d\hat{\boldsymbol{r}}Y^*_{LK}(\hat{\boldsymbol{r}})\langle q_f|\hat{\rho}(\boldsymbol{r})\hat{P}^{I_i}_{K0}\hat{P}^N\hat{P}^Z|q_i\rangle\end{aligned} \quad \text{(B.11)}$$

Appendix C

From $N\Lambda$ effective interaction to RPC EDF

The energy functional for $N\Lambda$ interaction is given by the expectation value of the effective interaction $\hat{V}^{N\Lambda}$ at the Hartree level,

$$E_{\rm int}^{N\Lambda} = \sum_{i=1}^{A_c} \int d\boldsymbol{r} d\boldsymbol{r}' \psi_\Lambda^\dagger(\boldsymbol{r}) \psi_i^\dagger(\boldsymbol{r}') \hat{V}^{N\Lambda}(\boldsymbol{r}, \boldsymbol{r}') \psi_\Lambda(\boldsymbol{r}) \psi_i(\boldsymbol{r}'). \tag{C.1}$$

The $N\Lambda$ interaction given by Eqs. (3.7a), (3.7b) and (3.7c) lead to the energy functional given by Eq.(3.3) as follows.

Substituting the LO scalar effective interaction term,

$$\hat{V}_S^{N\Lambda}(\boldsymbol{r}, \boldsymbol{r}') = \alpha_S^{N\Lambda} \gamma_\Lambda^0 \delta(\boldsymbol{r} - \boldsymbol{r}') \gamma_N^0 \tag{C.2}$$

to Eq.(C.1), one finds

$$\begin{aligned} E_{\rm S}^{N\Lambda} &= \sum_{i=1}^{A_c} \int d\boldsymbol{r} d\boldsymbol{r}' \psi_\Lambda^\dagger(\boldsymbol{r}) \psi_i^\dagger(\boldsymbol{r}') \alpha_S^{N\Lambda} \gamma_\Lambda^0 \delta(\boldsymbol{r} - \boldsymbol{r}') \gamma_N^0 \psi_\Lambda(\boldsymbol{r}) \psi_i(\boldsymbol{r}') \\ &= \alpha_S^{N\Lambda} \sum_{i=1}^{A_c} \int d\boldsymbol{r} \psi_\Lambda^\dagger(\boldsymbol{r}) \gamma_\Lambda^0 \psi_\Lambda(\boldsymbol{r}) \psi_i^\dagger(\boldsymbol{r}) \gamma_N^0 \psi_i(\boldsymbol{r}) \\ &= \int d\boldsymbol{r} \alpha_S^{N\Lambda} \rho_S^\Lambda(\boldsymbol{r}) \rho_S(\boldsymbol{r}), \end{aligned} \tag{C.3}$$

where ρ_S and ρ_S^Λ are the scalar densities defined as

$$\rho_S(\boldsymbol{r}) = \sum_{i=1}^{A_c} \bar{\psi}_i(\boldsymbol{r}) \psi_i(\boldsymbol{r}), \quad \rho_S^\Lambda(\boldsymbol{r}) = \bar{\psi}_\Lambda(\boldsymbol{r}) \psi_\Lambda(\boldsymbol{r}), \tag{C.4}$$

and the bar indicates the Dirac adjoint $\bar{\psi} = \psi^\dagger \gamma^0$.

A similar derivation holds also for the vector part of the $N\Lambda$ interaction. For the vector LO term,

$$\hat{V}_V^{N\Lambda}(\boldsymbol{r},\boldsymbol{r}') = \alpha_V^{N\Lambda}\delta(\boldsymbol{r}-\boldsymbol{r}'), \tag{C.5}$$

we have

$$\begin{aligned} E_{\rm V}^{N\Lambda} &= \sum_{i=1}^{A_c}\int d\boldsymbol{r}d\boldsymbol{r}'\psi_\Lambda^\dagger(\boldsymbol{r})\psi_i^\dagger(\boldsymbol{r}')\alpha_V^{N\Lambda}\delta(\boldsymbol{r}-\boldsymbol{r}')\psi_\Lambda(\boldsymbol{r})\psi_i(\boldsymbol{r}') \\ &= \alpha_V^{N\Lambda}\sum_{i=1}^{A_c}\int d\boldsymbol{r}\psi_\Lambda^\dagger(\boldsymbol{r})\psi_\Lambda(\boldsymbol{r})\psi_i^\dagger(\boldsymbol{r})\psi_i(\boldsymbol{r}) \\ &= \int d\boldsymbol{r}\alpha_V^{N\Lambda}\rho_V^\Lambda(\boldsymbol{r})\rho_V(\boldsymbol{r}), \end{aligned} \tag{C.6}$$

where ρ_V and ρ_V^Λ are the vector densities defined as

$$\rho_V(\boldsymbol{r}) = \sum_{i=1}^{A_c}\psi_i^\dagger(\boldsymbol{r})\psi_i(\boldsymbol{r}), \quad \rho_V^\Lambda(\boldsymbol{r}) = \psi_\Lambda^\dagger(\boldsymbol{r})\psi_\Lambda(\boldsymbol{r}). \tag{C.7}$$

The effective interaction with the scalar derivative term,

$$\hat{V}_{\rm Der}^{N\Lambda}(\boldsymbol{r},\boldsymbol{r}') = \delta_S^{N\Lambda}\gamma_\Lambda^0\Big[\overleftarrow{\nabla}^2\delta(\boldsymbol{r}-\boldsymbol{r}') + \delta(\boldsymbol{r}-\boldsymbol{r}')\overrightarrow{\nabla}^2 + 2\overleftarrow{\nabla}\cdot\delta(\boldsymbol{r}-\boldsymbol{r}')\overrightarrow{\nabla}\Big]\gamma_N^0, \tag{C.8}$$

leads to

$$\begin{aligned} E_{\rm S}^{N\Lambda} &= \sum_{i=1}^{A_c}\int d\boldsymbol{r}d\boldsymbol{r}'\psi_\Lambda^\dagger(\boldsymbol{r})\psi_i^\dagger(\boldsymbol{r}')\delta_S^{N\Lambda}\gamma_\Lambda^0\Big[\overleftarrow{\nabla}^2\delta(\boldsymbol{r}-\boldsymbol{r}') + \delta(\boldsymbol{r}-\boldsymbol{r}')\overrightarrow{\nabla}^2 + 2\overleftarrow{\nabla}\cdot\delta(\boldsymbol{r}-\boldsymbol{r}')\overrightarrow{\nabla}\Big]\gamma_N^0\psi_\Lambda(\boldsymbol{r})\psi_i(\boldsymbol{r}') \\ &= \delta_S^{N\Lambda}\sum_{i=1}^{A_c}\int d\boldsymbol{r}\Big\{[\nabla^2\psi_\Lambda^\dagger(\boldsymbol{r})\gamma_\Lambda^0]\psi_\Lambda(\boldsymbol{r}) + [\psi_\Lambda^\dagger(\boldsymbol{r})\gamma_\Lambda^0][\nabla^2\psi_\Lambda(\boldsymbol{r})] + 2[\nabla\psi_\Lambda^\dagger(\boldsymbol{r})\gamma_\Lambda^0]\cdot[\nabla\psi_\Lambda(\boldsymbol{r})]\Big\}[\psi_i^\dagger(\boldsymbol{r})\gamma_N^0\psi_i(\boldsymbol{r})] \\ &= \int d\boldsymbol{r}\delta_S^{N\Lambda}\rho_S(\boldsymbol{r})\nabla^2\rho_S^\Lambda(\boldsymbol{r}). \end{aligned} \tag{C.9}$$

The vector derivative term

$$\hat{V}_{\rm Der}^{N\Lambda}(\boldsymbol{r},\boldsymbol{r}') = \delta_V^{N\Lambda}\Big[\overleftarrow{\nabla}^2\delta(\boldsymbol{r}-\boldsymbol{r}') + \delta(\boldsymbol{r}-\boldsymbol{r}')\overrightarrow{\nabla}^2 + 2\overleftarrow{\nabla}\cdot\delta(\boldsymbol{r}-\boldsymbol{r}')\overrightarrow{\nabla}\Big], \tag{C.10}$$

leads to

$$\begin{aligned} \Longrightarrow E_{\rm V}^{N\Lambda} &= \sum_{i=1}^{A_c}\int d\boldsymbol{r}d\boldsymbol{r}'\psi_\Lambda^\dagger(\boldsymbol{r})\psi_i^\dagger(\boldsymbol{r}')\delta_V^{N\Lambda}\Big[\overleftarrow{\nabla}^2\delta(\boldsymbol{r}-\boldsymbol{r}') + \delta(\boldsymbol{r}-\boldsymbol{r}')\overrightarrow{\nabla}^2 + 2\overleftarrow{\nabla}\cdot\delta(\boldsymbol{r}-\boldsymbol{r}')\overrightarrow{\nabla}\Big]\psi_\Lambda(\boldsymbol{r})\psi_i(\boldsymbol{r}') \\ &= \delta_V^{N\Lambda}\sum_{i=1}^{A_c}\int d\boldsymbol{r}\Big\{[\nabla^2\psi_\Lambda^\dagger(\boldsymbol{r})]\psi_\Lambda(\boldsymbol{r}) + [\psi_\Lambda^\dagger(\boldsymbol{r})][\nabla^2\psi_\Lambda(\boldsymbol{r})] + 2[\nabla\psi_\Lambda^\dagger(\boldsymbol{r})]\cdot[\nabla\psi_\Lambda(\boldsymbol{r})]\Big\}[\psi_i^\dagger(\boldsymbol{r})\psi_i(\boldsymbol{r})] \\ &= \int d\boldsymbol{r}\delta_V^{N\Lambda}\rho_V(\boldsymbol{r})\nabla^2\rho_V^\Lambda(\boldsymbol{r}). \end{aligned} \tag{C.11}$$

On the other hand, the tensor effective interaction,

$$\hat{V}_T^{N\Lambda}(\boldsymbol{r},\boldsymbol{r}') = i\alpha_T^{N\Lambda}\Big[\overleftarrow{\nabla}\cdot\boldsymbol{\gamma}\delta(\boldsymbol{r}-\boldsymbol{r}') + \delta(\boldsymbol{r}-\boldsymbol{r}')\overrightarrow{\nabla}\cdot\boldsymbol{\gamma}\Big] \tag{C.12}$$

leads to

$$\begin{aligned}
E_{\mathrm{T}}^{N\Lambda} &= \sum_{i=1}^{A_c}\int d\boldsymbol{r}d\boldsymbol{r}'\psi_\Lambda^\dagger(\boldsymbol{r})\psi_i^\dagger(\boldsymbol{r}')i\alpha_T^{N\Lambda}\Big[\overleftarrow{\nabla}\cdot\boldsymbol{\gamma}\delta(\boldsymbol{r}-\boldsymbol{r}') + \delta(\boldsymbol{r}-\boldsymbol{r}')\overrightarrow{\nabla}\cdot\boldsymbol{\gamma}\Big]\psi_\Lambda(\boldsymbol{r})\psi_i(\boldsymbol{r}') \\
&= \alpha_T^{N\Lambda}\sum_{i=1}^{A_c}\int d\boldsymbol{r}\Big\{[\nabla\psi_\Lambda^\dagger(\boldsymbol{r})\gamma_\Lambda^0]\cdot i\boldsymbol{\alpha}\psi_\Lambda(\boldsymbol{r}) + [\psi_\Lambda^\dagger(\boldsymbol{r})\gamma_\Lambda^0][\nabla\cdot i\boldsymbol{\alpha}\psi_\Lambda(\boldsymbol{r})]\Big\}[\psi_i^\dagger(\boldsymbol{r})\psi_i(\boldsymbol{r})] \\
&= \int d\boldsymbol{r}\alpha_T^{N\Lambda}\rho_V(\boldsymbol{r})[\nabla\cdot(\bar{\psi}_\Lambda(\boldsymbol{r})i\boldsymbol{\alpha}\psi_\Lambda(\boldsymbol{r}))] \\
&= \int d\boldsymbol{r}\alpha_T^{N\Lambda}\rho_V(\boldsymbol{r})\rho_T^\Lambda(\boldsymbol{r}),
\end{aligned} \tag{C.13}$$

where ρ_T^Λ is the tensor densities defined as

$$\rho_T^\Lambda(\boldsymbol{r}) = \nabla\cdot(\bar{\psi}_\Lambda(\boldsymbol{r})i\boldsymbol{\alpha}\psi_\Lambda(\boldsymbol{r})). \tag{C.14a}$$

Putting all these together, we finally obtain

$$\begin{aligned}
E_{\mathrm{int}}^{(N\Lambda)} = \int d\boldsymbol{r}\Big[&\alpha_S^{N\Lambda}\rho_S(\boldsymbol{r})\rho_S^\Lambda(\boldsymbol{r}) + \alpha_V^{N\Lambda}\rho_V(\boldsymbol{r})\rho_V^\Lambda(\boldsymbol{r}) + \delta_S^{N\Lambda}\rho_S(\boldsymbol{r})\Delta\rho_S^\Lambda(\boldsymbol{r}) + \delta_V^{N\Lambda}\rho_V(\boldsymbol{r})\Delta\rho_V^\Lambda(\boldsymbol{r}) \\
&+ \alpha_T^{N\Lambda}\rho_T^\Lambda(\boldsymbol{r})\rho_V(\boldsymbol{r})\Big].
\end{aligned} \tag{C.15}$$

Appendix D

Spinor spherical harmonics

Spinor spherical harmonics are constructed from the spherical harmonics $Y_{lm_l}(\theta,\varphi)$ and the spin wave functions χ_{m_s} ($s=\frac{1}{2}$). In accordance with the coupling scheme of two angular momenta, it is given

$$\mathscr{Y}_{j\ell m}(\theta,\varphi)=\sum_{m_l m_s}\langle lm_l\frac{1}{2}m_s|jm\rangle Y_{lm_l}(\theta,\varphi)\chi_{m_s}, \tag{D.1}$$

where j is a half-integer and $m=-j,-j+1,....,j-1,j$.

The orthonormality condition for $\mathscr{Y}_{j\ell m}(\theta,\varphi)$ is

$$\int_0^\pi \sin\theta d\theta\int_0^{2\pi} d\varphi\mathscr{Y}^\dagger_{j'\ell'm'}(\theta,\varphi)\mathscr{Y}_{j\ell m}(\theta,\varphi)=\delta_{jj'}\delta_{mm'}\delta_{ll'}. \tag{D.2}$$

The relation of the spin operator $\boldsymbol{s}=\boldsymbol{\sigma}/2$, the orbital angular momentum operator $\boldsymbol{l}$ and the total angular momentum operator is $\boldsymbol{j}=\boldsymbol{l}+\boldsymbol{s}$.

The action of operators ∇ and the angular momentum operators on the spinor spherical harmonics has following relations. (In following equations, we use $\hat{\boldsymbol{r}}=\boldsymbol{r}/r$.)

(a)

$$(\boldsymbol{s}\cdot\boldsymbol{r})\mathscr{Y}_{j\ell m}(\theta,\varphi)=-\frac{1}{2}\mathscr{Y}_{j\tilde{\ell}m}(\theta,\varphi) \tag{D.3}$$

$$(\boldsymbol{s}\cdot\boldsymbol{r})\mathscr{Y}_{j\tilde{\ell}m}(\theta,\varphi)=-\frac{1}{2}\mathscr{Y}_{jlm}(\theta,\varphi) \tag{D.4}$$

where $\tilde{\ell}=2j-l$.

$$(\boldsymbol{\sigma}\cdot\hat{\boldsymbol{r}})\mathscr{Y}_{j\ell m}(\theta,\varphi)=-\mathscr{Y}_{j\tilde{\ell}m}(\theta,\varphi) \tag{D.5}$$

$$(\boldsymbol{\sigma}\cdot\hat{\boldsymbol{r}})\mathscr{Y}_{j\tilde{\ell}m}(\theta,\varphi)=-\mathscr{Y}_{jlm}(\theta,\varphi) \tag{D.6}$$

(b)

$$(\boldsymbol{s}\cdot\boldsymbol{l})\mathscr{Y}_{j\ell m}(\theta,\varphi)=\frac{1}{2}[j(j+1)-l(l+1)-\frac{3}{4}]\mathscr{Y}_{j\ell m}(\theta,\varphi) \tag{D.7}$$

$$\frac{1}{2}(\boldsymbol{\sigma}\cdot\boldsymbol{l})\mathscr{Y}_{j\ell m}(\theta,\varphi)=-\frac{1+\kappa}{2}\mathscr{Y}_{j\ell m}(\theta,\varphi) \tag{D.8}$$

$$\kappa=\begin{cases} j+1/2=l & \text{if} \quad l=j+1/2 \\ -(j+1/2)=-(l+1) & \text{if} \quad l=j-1/2 \end{cases} \tag{D.9}$$

$$(\boldsymbol{\sigma}\cdot\boldsymbol{l}+1)\mathscr{Y}_{j\ell m}(\theta,\varphi)=-\kappa\mathscr{Y}_{j\ell m}(\theta,\varphi) \tag{D.10}$$

Introduce $\hat{\kappa}=\boldsymbol{\sigma}\cdot\boldsymbol{l}+1$, which has following relation

$$\hat{\kappa}\mathscr{Y}_{j\ell m}(\theta,\varphi)=-\kappa\mathscr{Y}_{j\ell m}(\theta,\varphi) \tag{D.11}$$

$$\hat{\kappa}\mathscr{Y}_{j\tilde{\ell}m}(\theta,\varphi)=\kappa\mathscr{Y}_{j\tilde{\ell}m}(\theta,\varphi). \tag{D.12}$$

(c)

$$r(\boldsymbol{s}\cdot\nabla)\mathscr{Y}_{j\ell m}(\theta,\varphi)=-\frac{1+\kappa}{2}\mathscr{Y}_{j\tilde{l}m}(\theta,\varphi) \tag{D.13}$$

$$r(\boldsymbol{s}\cdot\nabla)\mathscr{Y}_{j\tilde{l}m}(\theta,\varphi)=-\frac{1-\kappa}{2}\mathscr{Y}_{jlm}(\theta,\varphi) \tag{D.14}$$

$$(\boldsymbol{r}\cdot\nabla)[f(r)\mathscr{Y}_{j\ell m}(\theta,\varphi)]=r\frac{d}{dr}f(r)\mathscr{Y}_{j\ell m}(\theta,\varphi) \tag{D.15}$$

$$(\boldsymbol{r}\cdot\nabla)[f(r)\mathscr{Y}_{j\tilde{l}m}(\theta,\varphi)]=r\frac{d}{dr}f(r)\mathscr{Y}_{j\tilde{\ell}m}(\theta,\varphi) \tag{D.16}$$

$$\boldsymbol{\sigma}\cdot\nabla=(\boldsymbol{\sigma}\cdot\hat{\boldsymbol{r}})(\frac{d}{dr}+\frac{1-\hat{\kappa}}{r}) \tag{D.17}$$

$$(\boldsymbol{\sigma}\cdot\nabla)\left[f(r)\mathscr{Y}_{j\ell m}(\theta,\varphi)\right]=-[\frac{d}{dr}+\frac{1+\kappa}{r}]f(r)\mathscr{Y}_{j\tilde{l}m}(\theta,\varphi) \tag{D.18}$$

$$(\boldsymbol{\sigma}\cdot\nabla)\left[f(r)\mathscr{Y}_{j\tilde{l}m}(\theta,\varphi)\right]=-[\frac{d}{dr}+\frac{1-\kappa}{r}]f(r)\mathscr{Y}_{jlm}(\theta,\varphi) \tag{D.19}$$

With $(\boldsymbol{\sigma}\cdot\boldsymbol{A})(\boldsymbol{\sigma}\cdot\boldsymbol{B})=\boldsymbol{A}\cdot\boldsymbol{B}+i\boldsymbol{\sigma}\cdot(\boldsymbol{A}\times\boldsymbol{B})$ and $\boldsymbol{r}\cdot\boldsymbol{p}=rp_r=-ir\frac{d}{dr}$, Equation (D.17) can be obtained as follows:

$$\begin{aligned}(\boldsymbol{\sigma}\cdot\boldsymbol{p})=&\frac{1}{r^2}(\boldsymbol{\sigma}\cdot\boldsymbol{r})(\boldsymbol{\sigma}\cdot\boldsymbol{r})(\boldsymbol{\sigma}\cdot\boldsymbol{p})\\ =&\frac{(\boldsymbol{\sigma}\cdot\boldsymbol{r})}{r^2}[(\boldsymbol{r}\cdot\boldsymbol{p})+i\boldsymbol{\sigma}\cdot(\boldsymbol{r}\times\boldsymbol{p})]\\ =&\frac{(\boldsymbol{\sigma}\cdot\hat{r})}{r}[(-ir\frac{d}{dr})+i\boldsymbol{\sigma}\cdot\boldsymbol{l}]\\ =&\frac{(\boldsymbol{\sigma}\cdot\hat{r})}{r}[(-ir\frac{d}{dr})-i\hbar+i(\boldsymbol{\sigma}\cdot\boldsymbol{l}+\hbar)]\\ =&(\boldsymbol{\sigma}\cdot\hat{r})[-i\frac{d}{dr}-\frac{i\hbar}{r}+\frac{i\hat{\kappa}}{r}]\end{aligned} \tag{D.20}$$

Appendix E

A derivation of Eq.(4.34d) and Eq.(4.35) for the matrix elements

E.1 Matrix elements of the vector derivative coupling term

With the $N\Lambda$ vector derivative effective interaction $\hat{V}_D = \delta_V^{N\Lambda}\Big[\overleftarrow{\nabla}^2\delta(\boldsymbol{r}-\boldsymbol{r}_i)+\delta(\boldsymbol{r}-\boldsymbol{r}_i)\overrightarrow{\nabla}^2+2\overleftarrow{\nabla}\cdot\delta(\boldsymbol{r}-\boldsymbol{r}_i)\overrightarrow{\nabla}\Big]$, and the definition of

$$\mathscr{F}_{jlI}^{JM}(\hat{\boldsymbol{r}},\{\boldsymbol{r}_i\}) = \sum_{m_I m} C_{Im_I jm}^{JM}\mathscr{Y}_{jlm}(\hat{\boldsymbol{r}})\Phi_{Im_I}(\{\boldsymbol{r}_i\}), \tag{E.1}$$

where $\mathscr{Y}_{jlm}(\hat{\boldsymbol{r}})$ is the spinor spherical harmonics given by Eq. (D.1). The coupling matrix element of the vector derivative term reads

$$\begin{aligned}
&\langle R_{\alpha l}^k(r)\mathscr{F}_{jlI}^{JM}(\hat{\boldsymbol{r}},\{\boldsymbol{r}_i\})|\hat{V}_D|\mathscr{F}_{j'l'I'}^{JM}(\hat{\boldsymbol{r}},\{\boldsymbol{r}_i\})R_{\alpha' l'}^{k'}(r)\rangle \\
=&\delta_V^{N\Lambda}\sum_{m_I m}\sum_{m'_I m'} C_{Im_I jm}^{JM}C_{I'm'_I j'm'}^{JM}\sum_{\lambda\mu}\int r^2dr\int d\hat{\boldsymbol{r}}\langle\Phi_{Im_I}|\sum_{i=1}^{A_c}\frac{\delta(r-r_i)}{rr_i}Y_{\lambda\mu}(\hat{\boldsymbol{r}}_i)|\Phi_{I'm'_I}\rangle \\
&\times Y_{\lambda\mu}^*(\hat{\boldsymbol{r}})\Delta[\mathscr{Y}_{j\ell m}^*(\hat{\boldsymbol{r}})\mathscr{Y}_{j'\ell' m'}(\hat{\boldsymbol{r}})R_{\alpha l}^k(r)R_{\alpha' l'}^{k'}(r)].
\end{aligned} \tag{E.2}$$

Here, we notice

$$\begin{aligned}
\langle\Phi_{Im_I}|\sum_{i=1}^{A_c}\frac{\delta(r-r_i)}{rr_i}Y_{\lambda\mu}(\hat{\boldsymbol{r}}_i)|\Phi_{I'm'_I}\rangle &= (-1)^{I-m_I}\begin{pmatrix} I & \lambda & I' \\ -m_I & \mu & m'_I\end{pmatrix}\langle\Phi_I||\sum_{i=1}^{A_c}\frac{\delta(r-r_i)}{rr_i}Y_\lambda(\hat{\boldsymbol{r}}_i)||\Phi_{I'}\rangle \\
&= (-1)^{I-m_I}\begin{pmatrix} I & \lambda & I' \\ -m_I & \mu & m'_I\end{pmatrix}\varrho_{\lambda,V}^{II'}(r).
\end{aligned} \tag{E.3}$$

Since $Y_{lm}^*(\theta,\phi) = (-1)^m Y_{l-m}(\theta,\phi)$ (see Eq.(5-1-11) of [159]) and a direct product of two spherical harmonics of the same arguments can be expanded in series as (see Eq.(5-6-9) of [159]

)

$$Y_{l_1m_1}(\theta,\phi)Y_{l_2m_2}(\theta,\phi)=\sum_{LM}\frac{\hat{l}_1\hat{l}_2}{\sqrt{4\pi}\hat{L}}C^{L0}_{l_10l_20}C^{LM}_{l_1m_1l_2m_2}Y_{LM}(\theta,\phi), \tag{E.4}$$

we have

$$\begin{aligned}&\mathscr{Y}^*_{j\ell m}(\hat{\boldsymbol{r}})\mathscr{Y}_{j'\ell'm'}(\hat{\boldsymbol{r}})\\&=\sum_{m_lm_s}\sum_{m'_lm'_s}C^{jm}_{lm_l\frac{1}{2}m_s}C^{j'm'}_{l'm'_l\frac{1}{2}m'_s}\delta_{m_sm'_s}(-1)^{m_l}\sum_{LM}\frac{\hat{l}\hat{l}'}{\sqrt{4\pi}\hat{L}}C^{L0}_{l0l'0}C^{LM}_{l-m_ll'm'_l}Y_{LM}(\hat{\boldsymbol{r}}).\end{aligned} \tag{E.5}$$

We then have

$$\begin{aligned}&\Delta[\mathscr{Y}^*_{j\ell m}(\hat{\boldsymbol{r}})\mathscr{Y}_{j'\ell'm'}(\hat{\boldsymbol{r}})]\\&=\sum_{m_lm_s}\sum_{m'_lm'_s}\sum_{LM}\frac{\hat{l}\hat{l}'}{\sqrt{4\pi}\hat{L}}C^{jm}_{lm_l\frac{1}{2}m_s}C^{j'm'}_{l'm'_l\frac{1}{2}m'_s}\delta_{m_sm'_s}(-1)^{m_l}C^{L0}_{l0l'0}C^{LM}_{l-m_ll'm'_l}\left[\frac{1}{r^2}\frac{d}{dr}\left(r^2\frac{d}{dr}\right)-\frac{L(L+1)}{r^2}\right]Y_{LM}(\hat{\boldsymbol{r}}).\end{aligned} \tag{E.6}$$

The matrix element is then given by

$$\begin{aligned}&\langle R^k_{\alpha l}(r)\mathscr{F}^{JM}_{jlI}(\hat{\boldsymbol{r}},\{\boldsymbol{r}_i\})|\hat{V}_D|\mathscr{F}^{JM}_{j'l'I'}(\hat{\boldsymbol{r}},\{\boldsymbol{r}_i\})R^{k'}_{\alpha'l'}(r)\rangle\\&=\delta^{N\Lambda}_V\sum_{m_Im}\sum_{m'_Im'}C^{JM}_{Im_Ijm}C^{JM}_{I'm'_Ij'm'}\sum_{\lambda\mu}\int r^2dr(-1)^{I-m_I}\begin{pmatrix}I&\lambda&I'\\-m_I&\mu&m'_I\end{pmatrix}\varrho^{II'}_{\lambda,V}(r)\\&\times\sum_{m_lm_s}\sum_{m'_lm'_s}\frac{\hat{l}\hat{l}'}{\sqrt{4\pi}\hat{\lambda}}C^{jm}_{lm_l\frac{1}{2}m_s}C^{j'm'}_{l'm'_l\frac{1}{2}m'_s}\delta_{m_sm'_s}(-1)^{m_l}C^{\lambda0}_{l0l'0}C^{\lambda\mu}_{l-m_ll'm'_l}\\&\times\left[\frac{1}{r^2}\frac{d}{dr}\left(r^2\frac{d}{dr}\right)-\frac{\lambda(\lambda+1)}{r^2}\right]R^k_{\alpha l}(r)R^{k'}_{\alpha'l'}(r),\end{aligned} \tag{E.7}$$

where we have used the orthogonalization of the spherical harmonics $\int Y^*_{\lambda\mu}(\hat{\boldsymbol{r}})Y_{LM}(\hat{\boldsymbol{r}})d\hat{\boldsymbol{r}}=\delta_{\lambda,L}\delta_{\mu,M}$.

According to the relation between the Wigner $3j$ symbols and the Clebsch-Gordan coefficients, $C^{j_3m_3}_{j_1m_1j_2m_2}=(-1)^{j_1-j_2+m_3}\hat{j}_3\begin{pmatrix}j_1&j_2&j_3\\m_1&m_2&-m_3\end{pmatrix}$, we have

$$\begin{aligned}&\sum_{m_Im}\sum_{m'_Im'}\sum_{\mu}\sum_{m_lm_s}\sum_{m'_lm'_s}C^{JM}_{Im_Ijm}C^{JM}_{I'm'_Ij'm'}C^{jm}_{lm_l\frac{1}{2}m_s}C^{j'm'}_{l'm'_l\frac{1}{2}m'_s}C^{\lambda\mu}_{l-m_ll'm'_l}(-1)^{I-m_I}\begin{pmatrix}I&\lambda&I'\\-m_I&\mu&m'_I\end{pmatrix}\\&=(-1)^{I'+j'+J+j+1/2}\hat{j}'\hat{j}\hat{\lambda}\begin{Bmatrix}j&l&1/2\\l'&j'&\lambda\end{Bmatrix}\begin{Bmatrix}I&\lambda&I'\\j'&J&j\end{Bmatrix}.\end{aligned} \tag{E.8}$$

Together with $C^{\lambda 0}_{l0l'0} = (-1)^{\lambda}\hat{\lambda}\begin{pmatrix} l & \lambda & l' \\ 0 & 0 & 0 \end{pmatrix}$ and

$$\begin{aligned}\langle \mathcal{Y}_{j\ell}||Y_\lambda||\mathcal{Y}_{j'\ell'}\rangle =& \ (-1)^{l+1/2+j'+\lambda}\hat{j}'\hat{j}\begin{Bmatrix} l & j & 1/2 \\ j' & l' & \lambda \end{Bmatrix}\langle Y_l||Y_\lambda||Y_{l'}\rangle \\ =& \ (-1)^{1/2+j'+\lambda}\frac{\hat{l}\hat{l}'\hat{\lambda}}{\sqrt{4\pi}}\hat{j}'\hat{j}\begin{Bmatrix} j & l & 1/2 \\ l' & j' & \lambda \end{Bmatrix}\begin{pmatrix} l & \lambda & l' \\ 0 & 0 & 0 \end{pmatrix} \end{aligned} \tag{E.9}$$

(see Eq.(7.1.7) of [160]), then we have

$$\begin{aligned}&\langle R^k_{\alpha l}(r)\mathscr{F}^{JM}_{jlI}(\hat{\boldsymbol{r}},\{\boldsymbol{r}_i\})|\hat{V}_D|\mathscr{F}^{JM}_{j'l'I'}(\hat{\boldsymbol{r}},\{\boldsymbol{r}_i\})R^{k'}_{\alpha' l'}(r)\rangle \\ =&\delta^{N\Lambda}_V(-1)^{j'+I+J}\sum_\lambda \begin{Bmatrix} J & I & j \\ \lambda & j' & I' \end{Bmatrix}\langle j\ell||Y_\lambda||j'\ell'\rangle \\ &\times\int r^2dr\varrho^{II'}_{\lambda,V}(r)\left[\frac{1}{r^2}\frac{d}{dr}\left(r^2\frac{d}{dr}\right)-\frac{\lambda(\lambda+1)}{r^2}\right][R^k_{\alpha l}(r)R^{k'}_{\alpha' l'}(r)].\end{aligned} \tag{E.10}$$

E.2 Matrix elements of the tensor coupling term

The matrix elements of the tensor coupling term is given by

$$\begin{aligned}T^{kk'}_{\alpha\alpha'} \equiv& \langle R^k_{\alpha l}(r)\mathscr{F}^{JM}_{jlI}(\hat{\boldsymbol{r}},\{\boldsymbol{r}_i\})|\alpha^{N\Lambda}_T\sum_{i=1}^{A_c}\left[\overleftarrow{\nabla}\delta(\boldsymbol{r}-\boldsymbol{r}_i)+\delta(\boldsymbol{r}-\boldsymbol{r}_i)\overrightarrow{\nabla}\right]\cdot\boldsymbol{\sigma}|\mathscr{F}^{JM}_{j'\tilde{l}'I'}(\hat{\boldsymbol{r}},\{\boldsymbol{r}_i\})R^{k'}_{\alpha'\tilde{l}'}(r)\rangle \\ =&\alpha^{N\Lambda}_T\sum_{m'_I m'}\sum_{m_I m}C^{JM}_{I'm'_I j'm'}C^{JM}_{Im_I jm} \\ &\times\sum_{\lambda\mu}\int r^2drd\hat{\boldsymbol{r}}\langle\Phi_{Im_I}|\sum_i^{A_c}\frac{\delta(r-r_i)}{rr_i}Y_{\lambda\mu}(\hat{\boldsymbol{r}}_i)|\Phi_{I'm'_I}\rangle Y^*_{\lambda\mu}(\hat{\boldsymbol{r}})\nabla\cdot[R^{k*}_{\alpha l}(r)\mathscr{Y}^*_{jlm}(\hat{\boldsymbol{r}})\boldsymbol{\sigma}R^{k'}_{\alpha'\tilde{l}'}(r)\mathscr{Y}_{j'\tilde{l}'m'}(\hat{\boldsymbol{r}})].\end{aligned} \tag{E.11}$$

With the relation of Eqs.(D.5,D.6), Eqs.(D.11,D.12) and Eqs.(D.18,D.19), we have

$$\begin{aligned}&\nabla\cdot[R^{k*}_{\alpha l}(r)\mathscr{Y}^*_{jlm}(\hat{\boldsymbol{r}})\boldsymbol{\sigma}R^{k'}_{\alpha'\tilde{l}'}(r)\mathscr{Y}_{j'\tilde{l}'m'}(\hat{\boldsymbol{r}})] \\ &=\Big[-\frac{dR^k_{\alpha l}(r)}{dr}-\frac{\kappa+1}{r}R^k_{\alpha l}(r)\Big][R^{k'}_{\alpha'\tilde{l}'}(r)\mathscr{Y}^*_{j\tilde{l}m}(\hat{\boldsymbol{r}})\mathscr{Y}_{j'\tilde{l}'m'}(\hat{\boldsymbol{r}})] \\ &-\Big[\frac{dR^{k'}_{\alpha'\tilde{l}'}(r)}{dr}-\frac{\kappa'-1}{r}R^{k'}_{\alpha'\tilde{l}'}(r)\Big][R^{k*}_{\alpha l}(r)\mathscr{Y}^*_{jlm}(\hat{\boldsymbol{r}})\mathscr{Y}_{j'l'm'}(\hat{\boldsymbol{r}})].\end{aligned} \tag{E.12}$$

With the Wigner-Eckart theorem, one obtains

$$\int d\hat{\boldsymbol{r}}\mathscr{Y}^*_{jlm}(\hat{\boldsymbol{r}})Y^*_{\lambda\mu}(\hat{\boldsymbol{r}})\mathscr{Y}_{j'l'm'}(\hat{\boldsymbol{r}}) = (-1)^{\mu+j-m}\begin{pmatrix} j & \lambda & j' \\ -m & -\mu & m' \end{pmatrix}\langle jl||Y_\lambda||j'l'\rangle. \tag{E.13}$$

With the relation

$$\begin{Bmatrix} j_1 & j_2 & j_3 \\ j_4 & j_5 & j_6 \end{Bmatrix} = \sum_{m_1 m_2 m_3 m_4 m_6} (2j_5+1)(-1)^{j_1+j_2-j_3+j_4+j_5+j_6-m_1-m_4} \begin{pmatrix} j_1 & j_2 & j_3 \\ m_1 & m_2 & -m_3 \end{pmatrix} \begin{pmatrix} j_4 & j_5 & j_3 \\ m_4 & m_5 & m_3 \end{pmatrix} \begin{pmatrix} j_2 & j_4 & j_6 \\ m_2 & m_4 & -m_6 \end{pmatrix} \begin{pmatrix} j_5 & j_1 & j_6 \\ m_5 & m_1 & m_6 \end{pmatrix} \tag{E.14}$$

we have

$$\begin{aligned} &\sum_{m_I' m'} \sum_{m_I m} \sum_{\mu} C^{JM}_{I' m_I' j' m'} C^{JM}_{I m_I j m} (-1)^{I-m_I} \begin{pmatrix} I & \lambda & I' \\ -m_I & \mu & m_I' \end{pmatrix} (-1)^{\mu+j-m} \begin{pmatrix} j & \lambda & j' \\ -m & -\mu & m' \end{pmatrix} \\ &= (-1)^{I'+J+j} \begin{Bmatrix} J & I & j \\ \lambda & j' & I' \end{Bmatrix}, \end{aligned} \tag{E.15}$$

from which

$$\begin{aligned} T^{kk'}_{\alpha\alpha'} = -\alpha_T^{N\Lambda} (-1)^{j+I'+J} \sum_{\lambda} \begin{Bmatrix} J & I & j \\ \lambda & j' & I' \end{Bmatrix} \int r^2 dr \varrho^{I'I}_{\lambda,V}(r) \\ \times \Big\{ \Big[\frac{dR^k_{\alpha l}(r)}{dr} + \frac{\kappa+1}{r} R^k_{\alpha l}(r) \Big] R^{k'}_{\alpha' \tilde{l}'}(r) \langle j \tilde{l} || Y_\lambda || j' \tilde{l}' \rangle \\ + \Big[\frac{dR^{k'}_{\alpha' \tilde{l}'}(r)}{dr} - \frac{\kappa'-1}{r} R^{k'}_{\alpha' \tilde{l}'}(r) \Big] R^k_{\alpha l}(r) \langle j l || Y_\lambda || j' l' \rangle \Big\}. \end{aligned} \tag{E.16}$$

Appendix F

Generator coordinate method for hypernuclear spectroscopy with a covariant density functional

In this appendix, we apply the generator coordinate method (GCM) to describe low-lying states of odd-mass Λ hypernuclei which consist of a Λ particle and an even-even nuclear core. In contrast to the unpaired nucleon in ordinary odd-mass nuclei, the unpaired Λ hyperon in the hypernucleus is free from the Pauli exclusion principle from the nucleons inside the nuclear core. Therefore, the numerical calculation is much simpler than the GCM calculations for ordinary odd-mass nuclei, which has recently been developed based on a Skyrme energy density functional [161].

F.1 Framework

The wave function of hypernuclear states are constructed as a superposition of quantum-number projected hypernuclear reference states with different quadrupole deformation β,

$$|\Psi^{JM}_{n\alpha}\rangle = \sum_{\beta} f^{J}_{n\alpha}(\beta)\hat{P}^{J}_{MK}\hat{P}^{N}\hat{P}^{Z}|\Phi^{(N\Lambda)}_{n}(\beta)\rangle, \tag{F.1}$$

where the index n refers to a different hyperon orbital state, and the index α labels the quantum numbers of the state other than the angular momentum. For simplicity, we take the adiabatic approximation and do not mix different n in the total wave function, $|\Psi^{JM}_{n\alpha}\rangle$. The mean-field states $|\Phi^{(N\Lambda)}_{n}(\beta)\rangle$ are projected onto states with good quantum numbers with the operators $\hat{P}^{N}$ ($\hat{P}^{Z}$), and $\hat{P}^{J}_{MK}$, which project out the component with good neutron (proton) numbers and the angular momentum (see Eqs.(2.46) and (2.50)). The weight function $f^{J}_{n\alpha}(\beta)$ in the GCM states given by Eq. (F.1) is determined by the variational principle, which leads to the Hill-Wheeler-Griffin (HWG) equation, (see Eq.(2.56))

In Eq. (F.1), the mean-field states $|\Phi^{(N\Lambda)}_{n}(\beta)\rangle$, serving as nonorthonormal basis, are generated with deformation constrained relativistic mean-field (RMF) calculations for Λ hypernuclei [43, 45,

46]. Since the hyperon and the nucleons are not mixed, the mean-field states can be decomposed as

$$|\Phi_n^{(N\Lambda)}(\beta)\rangle = |\Phi^N(\beta)\rangle \otimes |\varphi_n^\Lambda(\beta)\rangle, \tag{F.2}$$

where $|\Phi^N(\beta)\rangle$ and $|\varphi_n^\Lambda(\beta)\rangle$ are the mean-field wave functions for the nuclear core and the hyperon, respectively. With this wave function, the deformation parameter β is related to the mass quadrupole moment of the whole hypernucleus ${}^A_\Lambda Z$ as

$$\beta = \frac{4\pi}{3AR^2}\langle\Phi_n^{(N\Lambda)}(\beta)|r^2Y_{20}|\Phi_n^{(N\Lambda)}(\beta)\rangle, \tag{F.3}$$

with $R = 1.2 \times A_c^{1/3}$ fm, $A_c = A - 1$ being the mass number of the core nucleus. In order to reduce the computation burden, we restrict all the reference states to be axially deformed.

The total angular momentum J is a half-integer number and K is its projection on the z-axis in the body-fixed frame. We assume that all the nucleons fill time-reversal states and thus do not contribute to the total angular momentum along the symmetric axis. In this case, the K quantum number is identical to Ω, that is, the component of the angular momentum of the hyperon along the z-axis, and thus can be adopted to characterize the wave function $|\varphi_n^\Lambda(\beta)\rangle$. From the mean-field states with the hyperon in a Ω^π configuration, the angular momentum J takes the value of $|\Omega|, |\Omega|+1, \cdots$. Notice that, in the angular momentum projection, the integrals over the two Euler angles ϕ and ψ can be performed analytically because of the axial symmetry.

F.2 Results and discussion

As an illustration of the method, we apply the GCM approach to ${}^{21}_{\Lambda}$Ne. We first generate a set of hypernuclear reference states $|\Phi_n^{(N\Lambda)}(\beta)\rangle$, by putting the hyperon on the four lowest single-particle states with $\Omega^\pi = 1/2_1^+, 1/2_1^-, 3/2_1^-$, and $1/2_2^-$. To this end, we perform the deformation constrained RMF+BCS calculation using the PC-F1 force [68] for the nucleon-nucleon interaction and the PCY-S2 force [130] for the nucleon-Λ interaction. A density-independent δ force is used in the pairing channel for the nucleons, supplemented with an energy-dependent cutoff [84]. The Dirac equations are solved by expanding the Dirac spinors with harmonic oscillator wave functions with 10 oscillator shells. The number of Euler angle in the interval $[0, \pi]$ and gauge angle in the interval $[0, 2\pi]$ are chosen as 16 and 9 for the angular momentum and the particle number projections, respectively.

F.2.1 Mean-field calculation

Figure F.1(a) shows the mean-field energies for the reference states so obtained as a function of deformation parameter β. One can see that the energies for the three negative-parity configurations (that is, $\Omega^\pi = 1/2_1^-, 3/2_1^-$, and $1/2_2^-$), corresponding to the hyperon occupying the three "p-orbital" states, are close to each other at $\beta = 0$ due to a weak hyperon spin-orbit interaction, and are well separated from the energy of the positive parity configuration ($\Omega^\pi = 1/2_1^+$), which

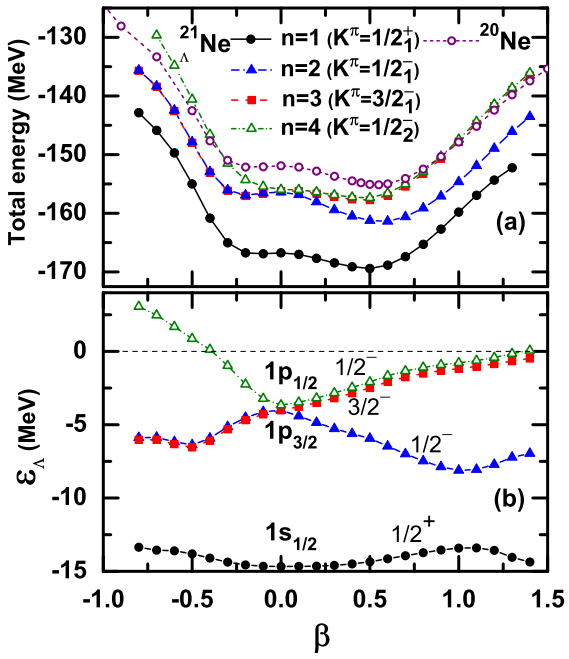

Fig. F.1 (a) The total energy curves for $^{21}_{\Lambda}$Ne obtained in the mean-field approximation as a function of quadrupole deformation β. These are calculated by putting the Λ hyperon in different single-particle orbitals shown in the lower panel. For comparison, the energy curve for the core nucleus ^{20}Ne is also plotted. (b) The single-particle energies of the Λ hyperon in $^{21}_{\Lambda}$Ne as a function of quadrupole deformation. These are labeled with the Ω^{π} number, that is the projection of the angular momentum onto the z-axis in the body fixed frame.

corresponds to the hyperon occupying the "s-orbital" state. The energy difference between the positive- and the negative-parity energy configurations at $\beta = 0$ is about 10.4 MeV, which is consistent with the 2/3 of the energy scale $\hbar\omega = 41A^{-1/3}$ MeV for nucleons. This energy corresponds to the excitation energy of hyperon from the s-orbital to the p-orbital. Moreover, one can also see that the energy minimum appears at $\beta \sim 0.6$ for $K^{\pi} = 1/2^{-}_{1}$, which is larger than the deformation of the energy minimum for the $1/2^{+}_{1}$ configuration ($\beta = 0.49$). This is consistent with the findings in Refs. [38, 46] that the hyperon in the "p-orbital" tends to develop a pronounced energy minima with a larger deformation.

Figure F.1(b) shows the Nilsson diagram for the hyperon in $^{21}_{\Lambda}$Ne. The single-particle level with the $\Omega^{\pi} = 3/2^{-}_{1}$ configuration is approximately degenerate with the $\Omega^{\pi} = 1/2^{-}_{1}$ and $1/2^{-}_{2}$ configurations at the oblate and the prolate sides, respectively. This is a characteristic feature of the Nilsson diagram without the spin-orbit interaction [81], and is responsible for the approximate degeneracy of the corresponding total energy curves shown in Fig. F.1(a). We note that the second $1/2^{-}$ single-particle level becomes unbound on the oblate side with deformation parameter of $\beta < -0.3$. In the following discussions, we therefore focus on the hypernuclear states generated by the Λ hyperon occupying the $\Omega^{\pi} = 1/2^{+}_{1}, 1/2^{-}_{1}$, and $3/2^{-}_{1}$ configurations.

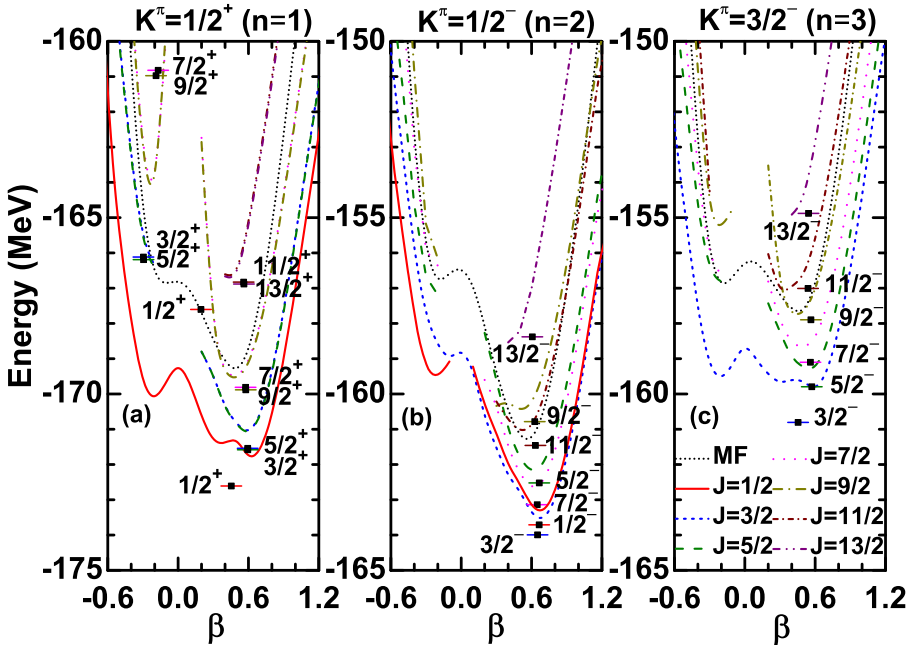

Fig. F.2 The projected energy curves for ${}^{21}_{\Lambda}$Ne obtained by putting the Λ hyperon on the three lowest single-particle orbitals labeled by $\Omega^\pi (= K^\pi)$. The corresponding mean-field energy curves are also shown for a comparison. The solutions of the GCM calculations are indicated by the squares and the horizontal bars placed at the average deformation.

F.2.2 Quantum-number projections

The energy curves shown in Fig. F.1(a) are the results of the mean-field approximation, in which the reference states are not the eigen-states of the angular momentum and the nucleon numbers. The projected energy curves, after the projection procedures, are obtained by taking the diagonal element of the Hamiltonian and the norm kernels as $E^J_n(\beta) = \mathcal{H}^J_n(\beta,\beta)/\mathcal{N}^J_n(\beta,\beta)$. Those energy curves are plotted in Fig. F.2 as a function of β. For the $K^\pi = 1/2^+_1$ configuration shown in Fig. F.2(a), the projected energy curves for $J^\pi = 3/2^+$ and $5/2^+$ almost overlap with each other, indicating a weak coupling of the Λ hyperon to the nuclear core. This is the case also for the pairs of $J^\pi = (7/2^+, 9/2^+)$ and $J^\pi = (11/2^+, 13/2^+)$. It is seen that the prolate minimum in the projected energy curves becomes more pronounced and thus the nuclear shape becomes more stable as the angular momentum increases. Moreover, the energy minimum for the $J^\pi = 1/2^+$ energy curve appears at deformation $\beta = 0.62$, that is somewhat larger than the deformation at the minimum of the corresponding mean-field curve, $\beta = 0.49$, due to the energy gain originated from the angular momentum projection. On the other hand, if one compares it to the projected energy curve for the 0^+ configuration of ^{20}Ne, which has a minimum at $\beta = 0.65$, one finds that the minimum is slightly shifted towards the spherical configuration both on the oblate and the prolate sides, similarly to the finding of the microscopic particle rotor model.

In contrast to the $J^\pi = 1/2^+$ configuration, the deformation at the energy minimum for the $J^\pi = 1/2^-$ configuration increases to $\beta = 0.69$ (see Fig. F.2(b)). Moreover, for this configuration, the energy difference between the prolate and the oblate minima significantly increases as

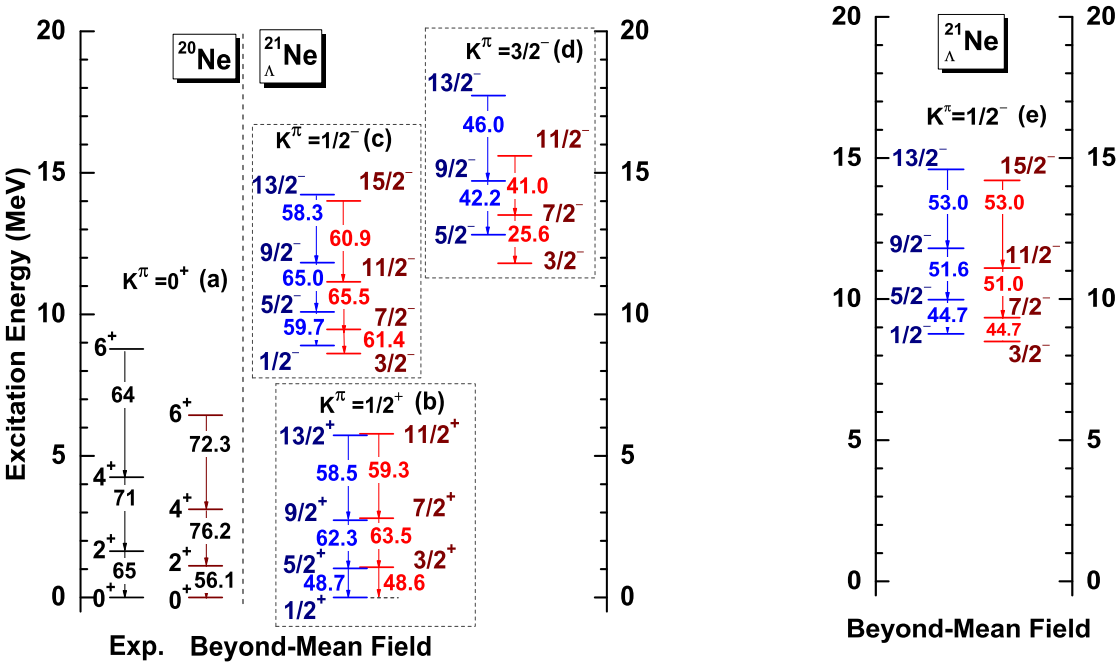

Fig. F.3 The left panel: The low-lying excitation spectra of ^{20}Ne (a) and $^{21}_{\Lambda}$Ne [(b)-(d)] constructed with the GCM approach. The numbers with the arrows indicate the $E2$ transition strengths, given in units of e^2 fm^4. The experimental data for ^{20}Ne are taken from Ref. [162]. The right panel: For comparison, the states of $K^\pi = 1/2^-$ band obtained with GCM calculation by mixing the $\Omega^\pi = 1/2^-_1$ and $\Omega^\pi = 1/2^-_2$ configurations.

compared to the $J^\pi = 1/2^+$ configuration. For this reason, the collective wave function for the $J^\pi = 1/2^-$ state is expected to be more localized on the prolate side than that of the $J^\pi = 1/2^+$ state. As a consequence, the average deformation for the $J^\pi = 1/2^-$ state is close to the minimum point of the energy curve while that for the $J^\pi = 1/2^+$ configuration is shifted towards the oblate side due to a cancellation between the prolate and the oblate contributions (see the filled squares in Fig. F.2(a) and F.2(b)).

The projected energy curves for the $K^\pi = 3/2^-_1$ configuration are shown in Fig. F.2(c). These are several MeV higher than those for the $K^\pi = 1/2^-_1$ configuration. Besides, the energy curve for the $J^\pi = 3/2^-$ is considerably different from that for the $J^\pi = 5/2^-$ configuration, and one would not expect a (quasi-)degeneracy between these two states.

F.2.3 Low-lying spectrum of $^{21}_{\Lambda}$Ne

By mixing all the projected mean-field states for each K^π configuration, we construct the low-lying states of ^{20}Ne and $^{21}_{\Lambda}$Ne with the GCM method. The calculated spectra are shown in Fig. F.3. One can see that the rotational character of the yrast states of ^{20}Ne is well reproduced, although the moment of inertia is somewhat overestimated due to the pairing collapse in the reference states for $\beta > 0.5$. This problem is expected to be improved by introducing the method of particle-number projection before variation while generating the reference states. The Λ binding energy of $^{21}_{\Lambda}$Ne, defined as the energy difference between the 0^+_1 state of ^{20}Ne and

the $1/2^+_1$ state of ${}^{21}_{\Lambda}$Ne, is calculated to be $B_\Lambda = 14.11$ MeV, which is slightly smaller than the mean-field result of 14.27 MeV.

According to a naive picture of a deformed rotor coupled to a hyperon moving in the deformed potential, one may expect several rotational bands with angular momenta in the order of $J = |\Omega|, |\Omega|+1, \cdots$ built on top of each single-particle state of Λ hyperon with Ω^π. This picture is indeed realized for the $K^\pi = 3/2^-$ band shown in Fig. F.3 (d), but is somewhat distorted for the $K^\pi = 1/2^+$ (b) and $1/2^-$ (c) bands due to a large decoupling factor originated from the Coriolis interaction [81]. According to the particle-rotor model in the strong coupling limit, the energy of the state with the angular momentum J in a $K = 1/2$ band reads [81],

$$E_{K=1/2}(J) = \epsilon + \frac{1}{2\mathcal{J}}\left\{J(J+1) - \frac{1}{4} + (-1)^{J+1/2}\left(J+\frac{1}{2}\right)a\right\}, \tag{F.4}$$

where ϵ is the energy of the valence particle, $\mathcal{J}$ is the moment of inertia, and a is the decoupling factor. For an axially deformed even-even core nucleus, one may expect that the decoupling factor a is close to ± 1 [163]. For $a = 1$, the ground state in the band has a spin $J = 1/2$ and the doublets (3/2, 5/2), (7/2, 9/2), $\cdots$ are degenerate in energy. On the other hand, for $a = -1$, the doublets (1/2, 3/2), (5/2, 7/2), $\cdots$ are degenerate. These features are approximately realized in the $K^\pi = 1/2^+$ and $1/2^-$ bands shown in Figs. F.3 (b) and (c).

For the $K^\pi = 1/2^-$ band, the decoupling factor seems somewhat smaller than -1, and the spin-parity of the bandhead state appears to be $J^\pi = 3/2^-$. That is, due to the decoupling factor, the energy ordering of the states in the $K^\pi = 1/2^-$ band is inverted by shifting up the states with odd value of $J + 1/2$ and pulling down the states with even values of $J + 1/2$. As a result, two rotational bands having $\Delta J = 2$ and with similar electric quadrupole transition strengths are formed. A similar feature has also been found in the microscopic particle-rotor model calculation, where the energy displacement between the two bands is, however, much smaller. To be more specific, the energy difference between the $1/2^-$ and $3/2^-$ states is less than 40 keV with the microscopic particle-rotor model, while it is 270 keV with the present GCM calculation. We have confirmed that this feature remains the same even if we mix the $\Omega^\pi = 1/2^-_1$ and $1/2^-_2$ configurations in the GCM calculations, as shown in Figure F.3(e) , which alters the excitation energies only by $\sim$2%.

The $K^\pi = 1/2^+$ band is mainly formed by the Λ hyperon in the "s-orbital" coupled to the ground-state band of the nuclear core, ^{20}Ne. For each core state, except for the ground state, two states appear in this band due to the angular momentum coupling with $j = 1/2$, and two rotational series are formed. The energy splitting in the double states is predicted to be small, which is consistent with the decoupling factor of $a \sim 1$. That is, the energy splitting is 41.5 keV, 71.2 keV and 53.8 keV, for the doublets $(3/2^+, 5/2^+)$, $(7/2^+, 9/2^+)$ and $(11/2^+, 13/2^+)$, respectively. The magnitude of these energy splittings is comparable to the empirical energy splitting of ${}^{9}_{\Lambda}$Be, for which the energy of the $5/2^+$ state is lower than the energy of the state $3/2^+$ by 43 keV [148].

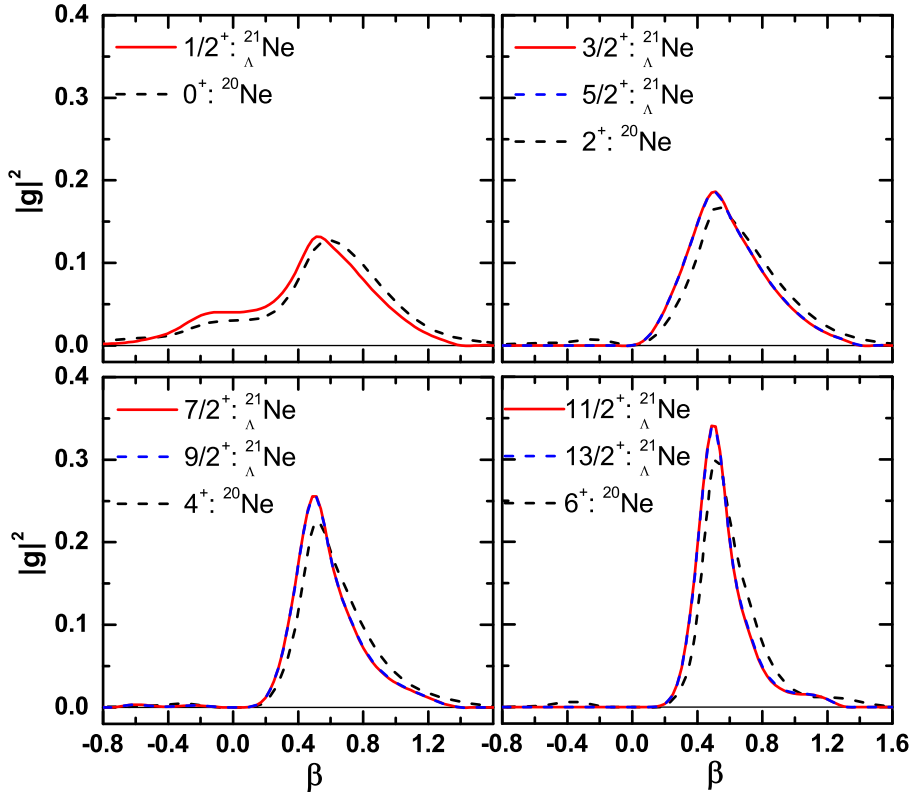

Fig. F.4 The distribution of collective wave functions of the positive-parity states in $K^\pi = 1/2^+$ band of ${}^{21}_{\Lambda}$Ne as a function of deformation β, in comparison with the collective wave functions of some relevant states in ^{20}Ne.

For the E2 transition strength for $3/2^+ \to 1/2^+$ in ${}^{21}_{\Lambda}$Ne, we find that it is smaller than the E2 strength for $2^+ \to 0^+$ in ^{20}Ne by 13.37%. This implies that the Λ hyperon in the "s-orbital" decreases the quadrupole collectivity of ^{20}Ne, which is consistent with the findings in recent theoretical studies [38, 46, 59]. We notice that this is consistent also with the distribution of the collective wave functions, which are shifted towards the small deformation region as compared to those of ^{20}Ne, as shown in Fig. F.4.. On the other hand, the impurity effect for the Λ hyperon in the "p-orbital" is more difficult to assess, because several configurations are admixtured in the wave functions, as has been shown in the calcuation with the microscopic particle-rotor model.

F.3 Comparison with MPRM

The GCM approach presented in this appendix is complementary to the MPRM. The wave functions for hypernuclear states are expressed in different ways in these approaches. In the MPRM, hypernuclear states are expanded in terms of the low-lying states of the core nucleus, while they are generated from intrinsic states for the whole system in the present GCM approach. Meanwhile, the non-adiabatic effects of Λ particle is automatically taken into account in the MPRM, while the Λ particle is restricted to a specific single-particle configuration in the present GCM approach, although this restriction may be easily removed.

Another point is that the cut-off of the nuclear core states has to be introduced in MPRM, while one does not need to worry about it in the GCM approach. From a physics point of view, the MPRM provides a convenient way to analyze the components of hypernuclear wave function, while the GCM approach offers an intuitive way to study the hypernuclear shape fluctuation as well as the nuclear shape polarization due to the Λ hyperon. From a numerical point of view, the GCM approach is numerically more expensive than the MPRM.

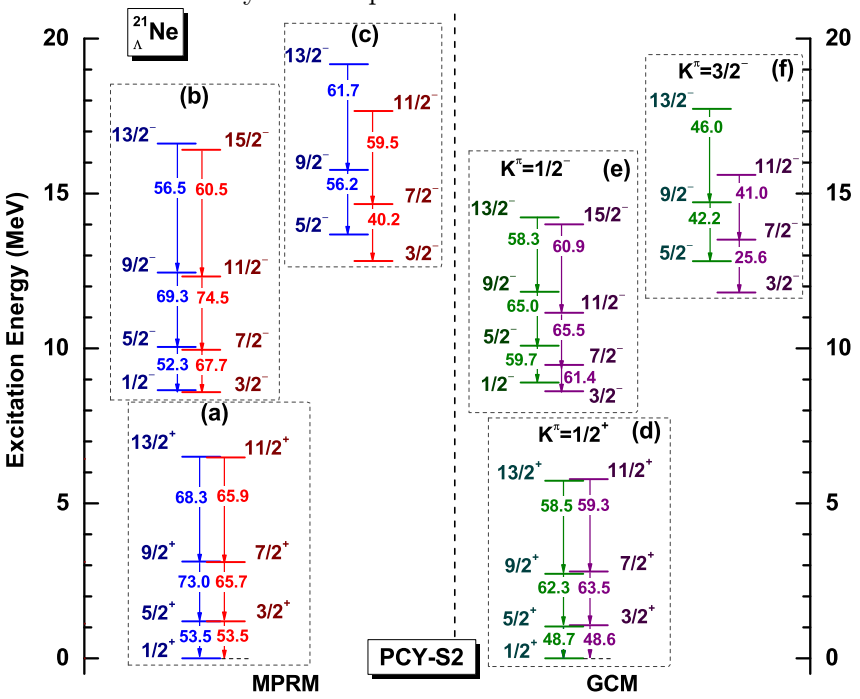

Fig. F.5 A comparison of the low-lying excitation spectra of $^{21}_{\Lambda}$Ne obtained with MPRM [(a)-(c)] and GCM [(d)-(f)](see Appendix F) calculations, where K indicate the projection of the angular momentum J on the z-axis in the body-fixed frame. The numbers with the arrows indicate the $E2$ transition strengths, given in units of e^2 fm^4.

We compare the spectra of $^{21}_{\Lambda}$Ne constructed with the MPRM and the GCM approach by using PCY-S2 force in Figure F.5. The levels in Fig. F.5(a) are the yrast positive parity states showing similar structure as GCM calculation shown in Fig. F.5(d). These states correspond to the configuration of $\Lambda_{s1/2}$ weakly coupled to the ground rotational band in ^{20}Ne with the decoupling factor ~ 1.

Figure F.5(b) shows the yrast negative-parity band constructed with MPRM which share similar structure as GCM calculation Fig. F.5(e) corresponding to $K^\pi = 1/2^-$. This band is dominated by the hyperon in the p state strongly coupled to the ground band in ^{20}Ne. Fig. F.5(c) shows the second negative-parity states for each J constructed with MPRM which share similar structure as GCM calculation Fig. F.5(f) corresponding to $K^\pi = 3/2^-$. The second $1/2^-_2$ state is not shown in Fig. F.5(c) because the E2 transition strength between $5/2^-_2$ and $1/2^-_2$ is 11.4 e^2fm^4, which is much smaller than other B(E2) values in this band.

References

[1] N. Ishii, S. Aoki and T. Hatsuda, *Phys. Rev. Lett.*, 2007, **99**, 022001.

[2] M. Danysz and J. Pniewski, *Phil. Mag.*, 1953, **44**, 348.

[3] H. J. Pirner, *Phys. Lett. B*, 1979, **85**, 190 – 192.

[4] W. Brückner, M. Faessler, T. Ketel, K. Kilian, J. Niewisch, B. Pietrzyk, B. Povh, H. Ritter, M. Uhrmacher, P. Birien, H. Catz, A. Chaumeaux, J. Durand, B. Mayer, J. Thirion, R. Bertini and O. Bing, *Phys. Lett. B*, 1978, **79**, 157–160.

[5] M. May, H. Piekarz, R. E. Chrien, S. Chen, D. Maurizio, H. Palevsky, R. Sutter, Y. Xu, P. Barnes, B. Bassalleck, N. J. Colella, R. Eisenstein, R. Grace, P. Pile, F. Takeutchi, W. Wharton, M. Deutsch, J. Piekarz, S. Bart, R. Hackenburg, E. V. Hungerford, B. Mayes, L. Pinsky, R. Cester and R. L. Stearns, *Phys. Rev. Lett.*, 1981, **47**, 1106–1109.

[6] H. Tamura, K. Tanida, D. Abe, H. Akikawa, K. Araki, H. Bhang, T. Endo, Y. Fujii, T. Fukuda, O. Hashimoto, K. Imai, H. Hotchi, Y. Kakiguchi, J. H. Kim, Y. D. Kim, T. Miyoshi, T. Murakami, T. Nagae, H. Noumi, H. Outa, K. Ozawa, T. Saito, J. Sasao, Y. Sato, S. Satoh, R. I. Sawafta, M. Sekimoto, T. Takahashi, L. Tang, H. H. Xia, S. H. Zhou and L. H. Zhu, *Phys. Rev. Lett.*, 2000, **84**, 5963–5966.

[7] K. Tanida, H. Tamura, D. Abe, H. Akikawa, K. Araki, H. Bhang, T. Endo, Y. Fujii, T. Fukuda, O. Hashimoto, K. Imai, H. Hotchi, Y. Kakiguchi, J. H. Kim, Y. D. Kim, T. Miyoshi, T. Murakami, T. Nagae, H. Noumi, H. Outa, K. Ozawa, T. Saito, J. Sasao, Y. Sato, S. Satoh, R. I. Sawafta, M. Sekimoto, T. Takahashi, L. Tang, H. H. Xia, S. H. Zhou and L. H. Zhu, *Phys. Rev. Lett.*, 2001, **86**, 1982–1985.

[8] H. Akikawa, S. Ajimura, R. E. Chrien, P. M. Eugenio, G. B. Franklin, J. Franz, L. Gang, K. Imai, P. Khaustov, M. May, P. H. Pile, B. Quinn, A. Rusek, J. Sasao, R. I. Sawafta, H. Schmitt, H. Tamura, L. Tang, K. Tanida, L. Yuan, S. H. Zhou, L. H. Zhu and X. F. Zhu, *Phys. Rev. Lett.*, 2002, **88**, 082501.

[9] H. Tamura, *Nucl. Phys. A*, 1998, **639**, 83c – 92c.

[10] K. Tanida, H. Akikawa, Y. Fukao, H. Hotchi, K. Imai, Y. Miura, K. Miwa, K. Mizunuma, S. Nakamura, M. Niiyama, S. Ohta, P. Saha, H. Takahashi, T. Takahashi, H. Tamura, S. Terashima, M. Togawa and M. Ukai, *Nucl. Phys. A*, 2003, **721**, C999 – C1002.

[11] K. Miwa, K. Tanida, H. Akikawa, Y. Fukao, E. Hiyama, H. Hotchi, K. Imai, Y. Miura, K. Mizunuma, S. Nakamura, M. Niiyama, S. Ota, P. Saha, H. Takahashi, T. Takahashi, H. Tamura, S. Terashima, M. Togawa and M. Ukai, *Nucl. Phys. A*, 2005, **754**, 80 – 85.

[12] T. Miyoshi, M. Sarsour, L. Yuan, X. Zhu, A. Ahmidouch, P. Ambrozewicz, D. Androic, T. Angelescu, R. Asaturyan, S. Avery, O. K. Baker, I. Bertovic, H. Breuer, R. Carlini, J. Cha, R. Chrien, M. Christy, L. Cole, S. Danagoulian, D. Dehnhard, M. Elaasar, A. Empl, R. Ent, H. Fenker, Y. Fujii, M. Furic, L. Gan, K. Garrow, A. Gasparian, P. Gueye,

M. Harvey, O. Hashimoto, W. Hinton, B. Hu, E. Hungerford, C. Jackson, K. Johnston, H. Juengst, C. Keppel, K. Lan, Y. Liang, V. P. Likhachev, J. H. Liu, D. Mack, A. Margaryan, P. Markowitz, J. Martoff, H. Mkrtchyan, S. N. Nakamura, T. Petkovic, J. Reinhold, J. Roche, Y. Sato, R. Sawafta, N. Simicevic, G. Smith, S. Stepanyan, V. Tadevosyan, T. Takahashi, K. Tanida, L. Tang, M. Ukai, A. Uzzle, W. Vulcan, S. Wells, S. Wood, G. Xu, H. Yamaguchi and C. Yan, *Phys. Rev. Lett.*, 2003, **90**, 232502.

[13] L. Yuan, M. Sarsour, T. Miyoshi, X. Zhu, A. Ahmidouch, D. Androic, T. Angelescu, R. Asaturyan, S. Avery, O. K. Baker, I. Bertovic, H. Breuer, R. Carlini, J. Cha, R. Chrien, M. Christy, L. Cole, S. Danagoulian, D. Dehnhard, M. Elaasar, A. Empl, R. Ent, H. Fenker, Y. Fujii, M. Furic, L. Gan, K. Garrow, A. Gasparian, P. Gueye, M. Harvey, O. Hashimoto, W. Hinton, B. Hu, E. Hungerford, C. Jackson, K. Johnston, H. Juengst, C. Keppel, K. Lan, Y. Liang, V. P. Likhachev, J. H. Liu, D. Mack, A. Margaryan, P. Markowitz, H. Mkrtchyan, S. N. Nakamura, T. Petkovic, J. Reinhold, J. Roche, Y. Sato, R. Sawafta, N. Simicevic, G. Smith, S. Stepanyan, R. Sutter, V. Tadevosyan, T. Takahashi, K. Tanida, L. Tang, M. Ukai, A. Uzzle, W. Vulcan, S. Wells, S. Wood, G. Xu, H. Yamaguchi and C. Yan, *Phys. Rev. C*, 2006, **73**, 044607.

[14] O. Hashimoto, A. Chiba, D. Doi, Y. Fujii, T. Gogami, H. Kanda, M. Kaneta, D. Kawama, K. Maeda, T. Maruta, A. Matsumura, S. Nagao, S. Nakamura, A. Shichijo, H. Tamura, N. Taniya, T. Yamamoto, K. Yokota, S. Kato, Y. Sato, T. Takahashi, H. Noumi, T. Motoba, E. Hiyama, I. Albayrak, O. Ates, C. Chen, M. Christy, C. Keppel, M. Kohl, Y. Li, A. Liyanage, L. Tang, T. Walton, Z. Ye, L. Yuan, L. Zhu, P. Baturin, W. Boeglin, S. Dhamija, P. Markowitz, B. Raue, J. Reinhold, E. Hungerford, R. Ent, H. Fenker, D. Gaskell, T. Horn, M. Jones, G. Smith, W. Vulcan, S. Wood, C. Johnston, N. Simicevic, S. Wells, C. Samanta, B. Hu, J. Shen, W. Wang, X. Zhang, Y. Zhang, J. Feng, Y. Fu, J. Zhou, S. Zhou, Y. Jiang, H. Lu, X. Yan, Y. Ye, L. Gan, A. Ahmidouch, S. Danagoulian, A. Gasparian, M. Elaasar, F. Wesselmann, A. Asaturyan, A. Margaryan, A. Mkrtchyan, H. Mkrtchyan, V. Tadevosyan, D. Androic, M. Furic, T. Petkovic, T. Seva, G. Niculescu, I. Niculescu, V. Rodriguez, E. Cisbani, F. Cusanno, F. Garibaldi, G. Uuciuoli, R. D. Leo, S. Maronne, P. Achenback and J. Pochodzala, *Nucl. Phys. A*, 2010, **835**, 121 – 128.

[15] S. N. Nakamura, A. Matsumura, Y. Okayasu, T. Seva, V. M. Rodriguez, P. Baturin, L. Yuan, A. Acha, A. Ahmidouch, D. Androic, A. Asaturyan, R. Asaturyan, O. K. Baker, F. Benmokhtar, P. Bosted, R. Carlini, C. Chen, M. Christy, L. Cole, S. Danagoulian, A. Daniel, V. Dharmawardane, K. Egiyan, M. Elaasar, R. Ent, H. Fenker, Y. Fujii, M. Furic, L. Gan, D. Gaskell, A. Gasparian, E. F. Gibson, T. Gogami, P. Gueye, Y. Han, O. Hashimoto, E. Hiyama, D. Honda, T. Horn, B. Hu, E. V. Hungerford, C. Jayalath, M. Jones, K. Johnston, N. Kalantarians, H. Kanda, M. Kaneta, F. Kato, S. Kato, D. Kawama, C. Keppel, K. J. Lan, W. Luo, D. Mack, K. Maeda, S. Malace, A. Margaryan, G. Marikyan, P. Markowitz, T. Maruta, N. Maruyama, T. Miyoshi, A. Mkrtchyan, H. Mkrtchyan, S. Nagao, T. Navasardyan, G. Niculescu, M.-I. Niculescu, H. Nomura, K. Nonaka, A. Ohtani, M. Oyamada, N. Perez, T. Petkovic, S. Randeniya, J. Reinhold, J. Roche, Y. Sato, E. K. Segbefia, N. Simicevic, G. Smith, Y. Song, M. Sumihama, V. Tadevosyan, T. Takahashi, L. Tang, K. Tsukada, V. Tvaskis, W. Vulcan, S. Wells, S. A. Wood, C. Yan and S. Zhamkochyan, *Phys. Rev. Lett.*, 2013, **110**, 012502.

[16] T. Gogami, *Ph.D thesis, Tohoku University*, 2014.

[17] R. Bertini, O. Bing, P. Birien, K. Braune, W. Brčkner, A. Chaumeaux, M. Faessler, R. Frey, D. Garreta, T. Ketel, K. Kilian, B. Mayer, J. Niewisch, B. Pietrzyk, B. Povh, H. Ritter and M. Uhrmacher, *Nucl. Phys. A*, 1981, **368**, 365 – 374.

[18] R. Bertini, O. Bing, P. Birien, K. Braune, W. Brückner, H. Catz, A. Chaumeaux, M. Faessler, R.-W. Frey, D. Garreta, T. Ketel, K. Kilian, B. Mayer, J. Niewisch, B. Pietrzyk, B. Povh, H. Ritter and M. Uhrmacher, *Nucl. Phys. A*, 1981, **360**, 315 – 330.

[19] P. H. Pile, S. Bart, R. E. Chrien, D. J. Millener, R. J. Sutter, N. Tsoupas, J.-C. Peng, C. S. Mishra, E. V. Hungerford, T. Kishimoto, L.-G. Tang, W. von Witsch, Z. Xu, K. Maeda, D. Gill, R. McCrady, B. Quinn, J. Seydoux, J. W. Sleight, R. L. Stearns, H. Plendl, A. Rafatian and J. Reidy, *Phys. Rev. Lett.*, 1991, **66**, 2585–2588.

[20] T. Hasegawa, O. Hashimoto, S. Homma, T. Miyachi, T. Nagae, M. Sekimoto, T. Shibata, H. Sakaguchi, T. Takahashi, K. Aoki, H. Noumi, H. Bhang, M. Youn, Y. Gavrilov, S. Ajimura, T. Kishimoto, A. Ohkusu, K. Maeda, R. Sawafta and R. P. Redwine, *Phys. Rev. C*, 1996, **53**, 1210–1220.

[21] O. Hashimoto and H. Tamura, *Prog. Part. Nucl. Phys.*, 2006, **57**, 564.

[22] B. Gibson, K. Imai, T. Motoba, T. Nagae, A. Ohnishi, O. Hashimoto, A. Chiba, D. Doi, Y. Fujii, T. Gogami, H. Kanda, M. Kaneta, D. Kawama, K. Maeda, T. Maruta, A. Matsumura, S. Nagao, S. Nakamura, A. Shichijo, H. Tamura, N. Taniya, T. Yamamoto, K. Yokota, S. Kato, Y. Sato, T. Takahashi, H. Noumi, T. Motoba, E. Hiyama, I. Albayrak, O. Ates, C. Chen, M. Christy, C. Keppel, M. Kohl, Y. Li, A. Liyanage, L. Tang, T. Walton, Z. Ye, L. Yuan, L. Zhu, P. Baturin, W. Boeglin, S. Dhamija, P. Markowitz, B. Raue, J. Reinhold, E. Hungerford, R. Ent, H. Fenker, D. Gaskell, T. Horn, M. Jones, G. Smith, W. Vulcan, S. Wood, C. Johnston, N. Simicevic, S. Wells, C. Samanta, B. Hu, J. Shen, W. Wang, X. Zhang, Y. Zhang, J. Feng, Y. Fu, J. Zhou, S. Zhou, Y. Jiang, H. Lu, X. Yan, Y. Ye, L. Gan, A. Ahmidouch, S. Danagoulian, A. Gasparian, M. Elaasar, F. Wesselmann, A. Asaturyan, A. Margaryan, A. Mkrtchyan, H. Mkrtchyan, V. Tadevosyan, D. Androic, M. Furic, T. Petkovic, T. Seva, G. Niculescu, I. Niculescu, V. Rodriguez, E. Cisbani, F. Cusanno, F. Garibaldi, G. Uuciuoli, R. D. Leo, S. Maronne, P. Achenback and J. Pochodzala, *Nucl. Phys. A*, 2010, **835**, 121 – 128.

[23] T. Gogami, C. Chen, D. Kawama, P. Achenbach, A. Ahmidouch, I. Albayrak, D. Androic, A. Asaturyan, R. Asaturyan, O. Ates, P. Baturin, R. Badui, W. Boeglin, J. Bono, E. Brash, P. Carter, A. Chiba, E. Christy, S. Danagoulian, R. De Leo, D. Doi, M. Elaasar, R. Ent, Y. Fujii, M. Fujita, M. Furic, M. Gabrielyan, L. Gan, F. Garibaldi, D. Gaskell, A. Gasparian, Y. Han, O. Hashimoto, T. Horn, B. Hu, E. V. Hungerford, M. Jones, H. Kanda, M. Kaneta, S. Kato, M. Kawai, H. Khanal, M. Kohl, A. Liyanage, W. Luo, K. Maeda, A. Margaryan, P. Markowitz, T. Maruta, A. Matsumura, V. Maxwell, A. Mkrtchyan, H. Mkrtchyan, S. Nagao, S. N. Nakamura, A. Narayan, C. Neville, G. Niculescu, M. I. Niculescu, A. Nunez, Nuruzzaman, Y. Okayasu, T. Petkovic, J. Pochodzalla, X. Qiu, J. Reinhold, V. M. Rodriguez, C. Samanta, B. Sawatzky, T. Seva, A. Shichijo, V. Tadevosyan, L. Tang, N. Taniya, K. Tsukada, M. Veilleux, W. Vulcan, F. R. Wesselmann, S. A. Wood, T. Yamamoto, L. Ya, Z. Ye, K. Yokota, L. Yuan, S. Zhamkochyan and L. Zhu, *Phys. Rev. C*, 2016, **93**, 034314.

[24] H. TAMURA, *Int. J. Mod. Phys. A*, 2009, **24**, 2101–2109.

[25] T. O. Yamamoto, M. Agnello, Y. Akazawa, N. Amano, K. Aoki, E. Botta, N. Chiga, H. Ekawa, P. Evtoukhovitch, A. Feliciello, M. Fujita, T. Gogami, S. Hasegawa, S. H. Hayakawa, T. Hayakawa, R. Honda, K. Hosomi, S. H. Hwang, N. Ichige, Y. Ichikawa, M. Ikeda, K. Imai, S. Ishimoto, S. Kanatsuki, M. H. Kim, S. H. Kim, S. Kinbara, T. Koike, J. Y. Lee, S. Marcello, K. Miwa, T. Moon, T. Nagae, S. Nagao, Y. Nakada, M. Nakagawa, Y. Ogura, A. Sakaguchi, H. Sako, Y. Sasaki, S. Sato, T. Shiozaki, K. Shirotori, H. Sugimura, S. Suto, S. Suzuki, T. Takahashi, H. Tamura, K. Tanabe, K. Tanida, Z. Tsamalaidze, M. Ukai, Y. Yamamoto and S. B. Yang, *Phys. Rev. Lett.*, 2015, **115**, 222501.

[26] R. Wirth, D. Gazda, P. Navratil, A. Calci, J. Langhammer and R. Roth, *Phys. Rev. Lett.*, 2001, **113**, 192502.

[27] R. Dalitz and A. Gal, *Ann. Phys. (N.Y.)*, 1978, **116**, 167.

[28] A. Gal, J. Soper and R. Dalitz, *Ann. Phys. (N.Y.)*, 1971, **63**, 53.

[29] D. J. Millener, C. Dover and A. Gal, *Phys. Rev. C*, 1988, **38**, 2700.

[30] D. Millener, *Nucl. Phys. A*, 2012, **881**, 298 – 309.

[31] T. Motoba, H. Bandō and K. Ikeda, *Prog. Theor. Phys.*, 1983, **70**, 189.

[32] E. Hiyama, M. Kamimura, K. Miyazaki and T. Motoba, *Phys. Rev. C*, 1999, **59**, 2351.

[33] H. Bandō, T. Motoba and J. Zofka, *Int. J. Mod. Phys. A*, 1990, **5**, 4021.

[34] E. Hiyama, Y. Kino and M. Kamimura, *Prog. Part. Nucl. Phys.*, 2003, **51**, 223 – 307.

[35] E. Cravo, A. C. Fonseca and Y. Koike, *Phys. Rev. C*, 2002, **66**, 014001.

[36] V. M. Suslov, I. Filikhin and B. Vlahovic, *J. Phys. G: Nucl. Part. Phys.*, 2004, **30**, 513.

[37] M. Shoeb and Sonika, *Phys. Rev. C*, 2009, **79**, 054321.

[38] M. Isaka, M. Kimura, A. Dote and A. Ohnishi, *Phys. Rev. C*, 2011, **83**, 044323.

[39] M. Isaka, H. Homma, M. Kimura, A. Dote and A. Ohnishi, *Phys. Rev. C*, 2012, **85**, 034303.

[40] M. Isaka, M. Kimura, A. Dote and A. Ohnishi, *Phys. Rev. C*, 2013, **87**, 021304(R).

[41] M. Isaka, K. Fukukawa, M. Kimura, E. Hiyama, H. Sagawa and Y. Yamamoto, *Phys. Rev. C*, 2014, **89**, 024310.

[42] X.-R. Zhou, H.-J. Schulze, H. Sagawa, C.-X. Wu and E.-G. Zhao, *Phys. Rev. C*, 2007, **76**, 034312.

[43] M. T. Win and K. Hagino, *Phys. Rev. C*, 2008, **78**, 054311.

[44] M. T. Win, K. Hagino and T. Koike, *Phys. Rev. C*, 2011, **83**, 014301.

[45] B.-N. Lu, E.-G. Zhao and S.-G. Zhou, *Phys. Rev. C*, 2011, **84**, 014328.

[46] W. X. Xue, J. M. Yao, K. Hagino, Z. P. Li, H. Mei and Y. Tanimura, *Phys. Rev. C*, 2015, **91**, 024327.

[47] A. Li, E. Hiyama, X.-R. Zhou and H. Sagawa, *Phys. Rev. C*, 2013, **87**, 014333.

[48] B.-N. Lu, E. Hiyama, H. Sagawa and S.-G. Zhou, *Phys. Rev. C*, 2014, **89**, 044307.

[49] R. Yen, L. Cardman, D. Kalinsky, J. Legg and C. Bockelman, *Nucl. Phys. A*, 1974, **235**, 135 – 153.

[50] T. Motoba, H. Bandō, K. Ikeda and T. Yamada, *Prog. Theor. Phys. Suppl.*, 1985, **81**, 42.

[51] E. Hiyama and T. Yamada, *Prog. Part. Nucl. Phys.*, 2009, **63**, 339 – 395.

[52] M. Jurič, G. Bohm, J. Klabuhn, U. Krecker, F. Wysotzki, G. Coremans-Bertrand, J. Sacton, G. Wilquet, T. Cantwell, F. Esmael, A. Montwill, D. Davis, D. Kielczewska, T. Pniewski, T. Tymieniecka and J. Zakrzewski, *Nucl. Phys. B*, 1973, **52**, 1 – 30.

[53] E. Hiyama, M. Kamimura, T. Motoba, T. Yamada and Y. Yamamoto, *Phys. Rev. C*, 1996, **53**, 2075–2085.

[54] E. Hiyama, Y. Yamamoto, T. Motoba and M. Kamimura, *Phys. Rev. C*, 2009, **80**, 054321.

[55] X.-R. Zhou, A. Polls, H.-J. Schulze and I. Vidaña, *Phys. Rev. C*, 2008, **78**, 054306.

[56] D. Vretenar, W. Pöschl, G. Lalazissis and P. Ring, *Phys. Rev. C*, 1998, **57**, R1060.

[57] H. Sugimura, M. Agnello, J. Ahn, S. Ajimura, Y. Akazawa, N. Amano, K. Aoki, H. Bhang, N. Chiga, M. Endo, P. Evtoukhovitch, A. Feliciello, H. Fujioka, T. Fukuda, S. Hasegawa, S. Hayakawa, R. Honda, K. Hosomi, S. Hwang, Y. Ichikawa, Y. Igarashi, K. Imai, N. Ishibashi, R. Iwasaki, C. Joo, R. Kiuchi, J. Lee, J. Lee, K. Matsuda, Y. Matsumoto, K. Matsuoka, K. Miwa, Y. Mizoi, M. Moritsu, T. Nagae, S. Nagamiya, M. Nakagawa, M. Naruki, H. Noumi, R. Ota, B. Roy, P. Saha, A. Sakaguchi, H. Sako, C. Samanta, V. Samoilov, Y. Sasaki, S. Sato, M. Sekimoto, Y. Shimizu, T. Shiozaki, K. Shirotori, T. Soyama, T. Takahashi, T. Takahashi, H. Tamura, K. Tanabe, T. Tanaka, K. Tanida, A. Tokiyasu, Z. Tsamalaidze, M. Ukai, T. Yamamoto, Y. Yamamoto, S. Yang and K. Yoshida, *Phys. Lett. B*, 2014, **729**, 39 – 44.

[58] M. Isaka, M. Kimura, A. Dote and A. Ohnishi, *Phys. Rev. C*, 2011, **83**, 044323.

[59] J. Yao, Z. Li, K. Hagino, M. Win, Y. Zhang and J. Meng, *Nucl. Phys. A*, 2011, **868-869**, 12 – 24.

[60] J.-W. Cui, X.-R. Zhou and H.-J. Schulze, *Phys. Rev. C*, 2015, **91**, 054306.

[61] J. W. Negele, *Phys. Rev. C*, 1970, **1**, 1260–1321.

[62] R. Brockmann and R. Machleidt, *Phys. Rev. C*, 1990, **42**, 1965–1980.

[63] Y. Gambhir, P. Ring and A. Thimet, *Ann. of Phys.*, 1990, **198**, 132.

[64] P. Ring, *Prog. Part. Nucl. Phys.*, 1996, **37**, 193 – 263.

[65] S.-G. Zhou, J. Meng and P. Ring, *Phys. Rev. Lett.*, 2003, **91**, 262501.

[66] H. Liang, P. Zhao, Y. Zhang, J. Meng and N. V. Giai, *Phys. Rev. C*, 2011, **83**, 041301.

[67] B. A. Nikolaus, T. Hoch and D. G. Madland, *Phys. Rev. C*, 1992, **46**, 1757–1781.

[68] T. Bürvenich, D. G. Madland, J. A. Maruhn and P.-G. Reinhard, *Phys. Rev. C*, 2002, **65**, 044308.

[69] J. Maruhn, T. Büvenich and D. Madland, *J. Comput. Phys.*, 2001, **169**, 238 – 245.

[70] A. Sulaksono, T. Büvenich, J. Maruhn, P.-G. Reinhard and W. Greiner, *Ann. Phys.*, 2003, **306**, 36 – 57.

[71] T. Nikšić, D. Vretenar and P. Ring, *Phys. Rev. C*, 2008, **78**, 034318.

[72] P. W. Zhao, Z. P. Li, J. M. Yao and J. Meng, *Phys. Rev. C*, 2010, **82**, 054319.

[73] D. Vautherin and D. M. Brink, *Phys. Rev. C*, 1972, **5**, 626–647.

[74] P. Bonche, H. Flocard, P. Heenen, S. Krieger and M. Weiss, *Nucl. Phys. A*, 1985, **443**, 39 – 63.

[75] A. Valor, P.-H. Heenen and P. Bonche, *Nucl. Phys. A*, 2000, **671**, 145 – 164.

[76] B. A. Nikolaus, T. Hoch and D. G. Madland, *Phys. Rev. C*, 1992, **46**, 1757–1781.

[77] T. Bürvenich, D. G. Madland, J. A. Maruhn and P.-G. Reinhard, *Phys. Rev. C*, 2002, **65**, 044308.

[78] J. König and P. Ring, *Phys. Rev. Lett.*, 1993, **71**, 3079–3082.

[79] J. Bardeen, L. N. Cooper and J. R. Schrieffer, *Phys. Rev.*, 1957, **108**, 1175.

[80] J. M. Eisenberg and W. Greiner, *Nuclear Theory Vol. III: Microscopic theory of the nucleus*, (North-Holland, Amsterdam, London, 1972).

[81] P. Ring and P. Schuck, *The Nuclear Many-Body Problem*, (Springer-Verlag, New York, 1980).

[82] S. G. Nilsson and I. Ragnarsson, *Shapes and Shells in Nuclear Structure*, (Cambridge University Press, Cambridge,1995).

[83] J. Dobaczewski, H. Flocard and J. Treiner, *Nucl. Phys. A*, 1984, **422**, 103.

[84] M. Bender, K. Rutz., P. G. Reinhard. and J. A. Maruhn, *Eur. Phys. J. A*, 2000, **8**, 59.

[85] D. L. Hill and J. A. Wheeler, *Phys. Rev.*, 1953, **89**, 1102–1145.

[86] P. Arumugam, B. K. Sharma, S. K. Patra and R. K. Gupta, *Phys. Rev. C*, 2005, **71**, 064308.

[87] A. R. Edmonds, *Angular Momentum in Quantum Mechanics*, (Princeton University Press, 1957).

[88] V. N. Fomenko, *J. Phys. A*, 1970, **3**, 8.

[89] M. Anguiano, J. L. Egido and L. Robledo, *Nucl. Phys. A*, 2001, **696**, 467.

[90] T. Nikšić, D. Vretenar and P. Ring, *Phys. Rev. C*, 2006, **74**, 064309.

[91] M. Bender, P.-H. Heenen and P.-G. Reinhard, *Rev. Mod. Phys.*, 2003, **75**, 121–180.

[92] R. Rodríguez-Guzmán, J. Egido and L. Robledo, *Nucl. Phys. A*, 2002, **709**, 201 – 235.

[93] R. R. Rodríguez-Guzmán, J. L. Egido and L. M. Robledo, *Phys. Rev. C*, 2004, **69**, 054319.

[94] T. Nikšić, D. Vretenar and P. Ring, *Phys. Rev. C*, 2006, **73**, 034308.

[95] T. Nikšić, D. Vretenar and P. Ring, *Phys. Rev. C*, 2006, **74**, 064309.

[96] J. J. Griffin and J. A. Wheeler, *Phys. Rev.*, 1957, **108**, 311–327.

[97] J. M. Yao, J. Meng, P. Ring and D. Vretenar, *Phys. Rev. C*, 2010, **81**, 044311.

[98] F. Ajzenberg-Selove, *Nucl. Phys. A*, 1990, **506**, 1 – 158.

[99] T. Kibédi and R. Spear, *Atomic Data and Nuclear Data Tables*, 2005, **89**, 77 – 100.

[100] J. M. Yao, N. Itagaki and J. Meng, *Phys. Rev. C*, 2014, **90**, 054307.

[101] J. M. Yao, M. Bender and P.-H. Heenen, *Phys. Rev. C*, 2015, **91**, 024301.

[102] J. Yao, H. Mei and Z. Li, *Phys. Lett. B*, 2013, **723**, 459 – 463.

[103] A. Nakada, Y. Torizuka and Y. Horikawa, *Phys. Rev. Lett.*, 1971, **27**, 745–748.

[104] L. Cardman, J. Lightbody, S. Penner, S. Fivozinsky, X. Maruyama, W. Trower and S. Williamson, *Phys. Lett. B*, 1980, **91**, 203 – 206.

[105] M. Chernykh, H. Feldmeier, T. Neff, P. von Neumann-Cosel and A. Richter, *Phys. Rev. Lett.*, 2007, **98**, 032501.

[106] Y. Fukuoka, S. Shinohara, Y. Funaki, T. Nakatsukasa and K. Yabana, *Phys. Rev. C*, 2013, **88**, 014321.

[107] J. M. Yao, M. Bender and P.-H. Heenen, *Phys. Rev. C*, 2015, **91**, 024301.

[108] M. Chernykh, H. Feldmeier, T. Neff, P. von Neumann-Cosel and A. Richter, *Phys. Rev. Lett.*, 2007, **98**, 032501.

[109] Y. Kanada-En'yo, *Prog. Theor. Phys.*, 2007, **117**, 655–680.

[110] Y. Funaki, A. Tohsaki, H. Horiuchi, P. Schuck and G. Röpke, *Phys. Rev. C*, 2003, **67**, 051306.

[111] I. Angeli, *Atomic Data and Nuclear Data Tables*, 2004, **87**, 185 – 206.

[112] T. Kibédi and R. Spear, *Atomic Data and Nuclear Data Tables*, 2005, **89**, 77 – 100.

[113] F. Ajzenberg-Selove, *Nuclear Physics A*, 1990, **506**, 1 – 158.

[114] M. M. Nagels, T. A. Rijken and J. J. de Swart, *Phys. Rev. D*, 1977, **15**, 2547–2564.

[115] M. M. Nagels, T. A. Rijken and J. J. de Swart, *Phys. Rev. D*, 1979, **20**, 1633–1645.

[116] P. M. M. Maessen, T. A. Rijken and J. J. de Swart, *Phys. Rev. C*, 1989, **40**, 2226–2245.

[117] T. A. Rijken, V. G. J. Stoks and Y. Yamamoto, *Phys. Rev. C*, 1999, **59**, 21–40.

[118] T. Rijken, P. Maessen and J. de Swart, *Nucl. Phys. A*, 1992, **547**, 245 – 254.

[119] Y. Yamamoto, T.Motoba, H.Himeno, K.Ikeda and S.Nagata, *Prog. Theor. Phys. Suppl.*, 1994, **117**, 361–389.

[120] Y. Yamamoto, T.Motoba and T. A. Rijken, *Prog. Theor. Phys. Suppl.*, 1020, **185**, 72–105.

[121] A. Bouyssy and J. HÜner, *Phys. Lett. B*, 1976, **64**, 276 – 278.

[122] R. H. Dalitz, *Nucl. Phys.*, (Gordon and Breach, New York,1969), 701.

[123] A. Gal, *Advances in Nuclear Physics*, (Plenum, New York,1975), **8**, 1.

[124] J. V. Noble, *Phys. Lett. B*, 1980, **89B**, 325.

[125] J. Mareš and B. K. Jennings, *Phys. Rev. C*, 1994, **49**, 2472–2478.

[126] R. Brockmann and W. Weise, *Physics Letters B*, 1977, **69**, 167 – 169.

[127] N. Kaiser and W. Weise, *Phys. Rev. C*, 2005, **71**, 015203.

[128] P. Finelli, N. Kaiser, D. Vretenar and W. Weise, *Nucl. Phys. A*, 2009, **831**, 163 – 183.

[129] M. Rayet, *Nucl. Phys. A*, 1981, **367**, 381 – 397.

[130] Y. Tanimura and K. Hagino, *Phys. Rev. C*, 2012, **85**, 014306.

[131] E. Hiyama, Y. Funaki, N. Kaiser and W. Weise, *Prog. Theo. Exp. Phys.*, 2014, 013D01.

[132] J. Cohen and H. J. Weber, *Phys. Rev. C*, 1991, **44**, 1181–1187.

[133] M. Isaka, M. Kimura, A. Dote and A. Ohnishi, *Phys. Rev. C*, 2011, **83**, 044323.

[134] A. Bohr and B. R. Mottelson, *Mat. Fys. Medd. Dan. Vid. Selsk.*, 1953, **27**, 12,97,107.

[135] H. Esbensen, B. A. Brown and H. Sagawa, *Phys. Rev. C*, 1995, **51**, 1274–1279.

[136] F. Nunes, I. Thompson and R. Johnson, *Nucl. Phys. A*, 1996, **596**, 171 – 186.

[137] T. Tarutina and M. S. Hussein, *Phys. Rev. C*, 2004, **70**, 034603.

[138] Y. Urata, K. Hagino and H. Sagawa, *Phys. Rev. C*, 2011, **83**, 041303.

[139] *National Nuclear Data Center (NNDC),[http://www.nndc.bnl.gov/].*

[140] S. Ajimura, H. Hayakawa, T. Kishimoto, H. Kohri, K. Matsuoka, S. Minami, T. Mori, K. Morikubo, E. Saji, A. Sakaguchi, Y. Shimizu, M. Sumihama, R. E. Chrien, M. May, P. Pile, A. Rusek, R. Sutter, P. Eugenio, G. Franklin, P. Khaustov, K. Paschke, B. P. Quinn, R. A. Schumacher, J. Franz, T. Fukuda, H. Noumi, H. Outa, L. Gan, L. Tang, L. Yuan, H. Tamura, J. Nakano, T. Tamagawa, K. Tanida and R. Sawafta, *Phys. Rev. Lett.*, 2001, **86**, 4255–4258.

[141] H. Kohri, S. Ajimura, H. Hayakawa, T. Kishimoto, K. Matsuoka, S. Minami, Y. S. Miyake, T. Mori, K. Morikubo, E. Saji, A. Sakaguchi, Y. Shimizu, M. Sumihama, R. E. Chrien, M. May, P. Pile, A. Rusek, R. Sutter, P. M. Eugenio, G. Franklin, P. Khaustov, K. Paschke, B. P. Quinn, R. A. Schumacher, J. Franz, T. Fukuda, H. Noumi, H. Outa, L. Gan, L. Tang, L. Yuan, J. Nakano, T. Tamagawa, K. Tanida, R. Sawafta, H. Tamura and H. Akikawa, *Phys. Rev. C*, 2002, **65**, 034607.

[142] L. Canton, K. Amos, S. Karataglidis and J. P. Svenne, *Int. J. Mod. Phys. E*, 2010, **19**, 1435–1450.

[143] E. Hiyama, M. Kamimura, T. Motoba, T. Yamada and Y. Yamamoto, *Phys. Rev. Lett.*, 2000, **85**, 270–273.

[144] Y. Sugahara and H. Toki, *Prog. Theor. Phys.*, 1994, **92**, 803.

[145] Y. Kanada-En'yo, H. Horiuchi and A. Ono, *Phys. Rev. C*, 1995, **52**, 628–646.

[146] V. M. Datar, S. Kumar, D. R. Chakrabarty, V. Nanal, E. T. Mirgule, A. Mitra and H. H. Oza, *Phys. Rev. Lett.*, 2005, **94**, 122502.

[147] V. M. Datar, D. R. Chakrabarty, S. Kumar, V. Nanal, S. Pastore, R. B. Wiringa, S. P. Behera, A. Chatterjee, D. Jenkins, C. J. Lister, E. T. Mirgule, A. Mitra, R. G. Pillay, K. Ramachandran, O. J. Roberts, P. C. Rout, A. Shrivastava and P. Sugathan, *Phys. Rev. Lett.*, 2013, **111**, 062502.

[148] H. Tamura, S. Ajimura, H. Akikawa, D. Alburger, K. Aoki, A. Banu, R. Chrien, G. Franklin, J. Franz, Y. Fujii, Y. Fukao, T. Fukuda, O. Hashimoto, T. Hayakawa, E. Hiyama, H. Hotchi, K. Imai, W. Imoto, Y. Kakiguchi, M. Kameoka, T. Kishimoto, A. Krutenkova, T. Maruta, A. Matsumura, M. May, S. Minami, Y. Miura, K. Miwa, T. Miyoshi, K. Mizunuma, T. Nagae, S. Nakamura, K. Nakazawa, M. Niiyama, H. Nomura, H. Noumi, Y. Okayasu, S. Ota, T. Ohtaki, H. Outa, P. Pile, B. Quinn, A. Rusek, P. Saha, Y. Sato, T. Saitoh, M. Sekimoto, R. Sutter, H. Takahashi, T. Takahashi, L. Tang, K. Tanida, S. Terashima, M. Togawa, A. Toyoda, M. Ukai, H. Yamauchi, L. Yuan and S. Zhou, *Nucl. Phys. A*, 2005, **754**, 58 – 69.

[149] K. Hagino and T. Koike, *Phys. Rev. C*, 2011, **84**, 064325.

[150] H. Polinder, J. Haidenbauer and U.-G. Meißner, *Nucl. Phys. A*, 2006, **779**, 244 – 266.

[151] T. Yamada, K. Ikeda, H. Bandō and T. Motoba, *Prog. Theor. Phys.*, 1984, **71**, 985–1004.

[152] Meng, J., Zhang, W., Zhou, S. G., Toki, H. and Geng, L. S., *Eur. Phys. J. A*, 2005, **25**, 23–27.

[153] T. Nikšić, D. Vretenar, G. A. Lalazissis and P. Ring, *Phys. Rev. Lett.*, 2007, **99**, 092502.

[154] Z. P. Li, T. Nikšić, D. Vretenar, J. Meng, G. A. Lalazissis and P. Ring, *Phys. Rev. C*, 2009, **79**, 054301.

[155] P. Cejnar, J. Jolie and R. F. Casten, *Rev. Mod. Phys.*, 2010, **82**, 2155–2212.

[156] T. Nikšić, D. Vretenar, G. A. Lalazissis and P. Ring, *Phys. Rev. Lett.*, 2007, **99**, 092502.

[157] Z. P. Li, T. Nikšić, D. Vretenar, J. Meng, G. A. Lalazissis and P. Ring, *Phys. Rev. C*, 2009, **79**, 054301.

[158] M. Borrajo, T. R. Rodríguez and J. L. Egido, *Phys. Lett. B*, 2015, **746**, 341 – 346.

[159] D. A. Varshalovich, A. N. Moskalev and V. K. Khersonskii, *Quantum theory of angular momentum*, (World Scientific, 1988).

[160] A. R. Edmonds, *Angular momentum in quantum mechanics*, (Princeton, new Jersey, Princeton University Press, 1957).

[161] B. Bally, B. Avez, M. Bender and P.-H. Heenen, *Phys. Rev. Lett.*, 2014, **113**, 162501.

[162] J. Tauren and R. B. Firest, *Evaluated Nuclear Structure Data File (ENSDF)*.

[163] A. Bohr and B. Mottelson, *Nuclear Structure 2*, (Benjaming, New York, 1975).